

**Oxidation phenomena in advanced high strength steels  
Modelling and experiment**

Mao, William

**DOI**

[10.4233/uuid:3e978189-4fd7-4358-840e-b995416bedef](https://doi.org/10.4233/uuid:3e978189-4fd7-4358-840e-b995416bedef)

**Publication date**

2018

**Document Version**

Final published version

**Citation (APA)**

Mao, W. (2018). *Oxidation phenomena in advanced high strength steels: Modelling and experiment*. [Dissertation (TU Delft), Delft University of Technology]. <https://doi.org/10.4233/uuid:3e978189-4fd7-4358-840e-b995416bedef>

**Important note**

To cite this publication, please use the final published version (if applicable).  
Please check the document version above.

**Copyright**

Other than for strictly personal use, it is not permitted to download, forward or distribute the text or part of it, without the consent of the author(s) and/or copyright holder(s), unless the work is under an open content license such as Creative Commons.

**Takedown policy**

Please contact us and provide details if you believe this document breaches copyrights.  
We will remove access to the work immediately and investigate your claim.

# **Oxidation Phenomena in Advanced High Strength Steels: Modelling and Experiment**

**Dissertation**

for the purpose of obtaining the degree of doctor  
at Delft University of Technology  
by the authority of the Rector Magnificus Prof.dr.ir. T.H.J.J. van der Hagen,  
chair of the Board for Doctorates,  
to be defended publicly on  
Wednesday 11 April 2018 at 12:30 o'clock

by

Weichen MAO  
Master of Science in Materials Science and Engineering,  
Delft University of Technology, The Netherlands  
born in Jiangsu, China

This dissertation has been approved by the promotor.

Composition of the doctoral committee:

Rector Magnificus,	chairman
Prof.dr. B.J. Thijsse	Delft University of Technology, promotor
Dr.ir. W.G. Sloof	Delft University of Technology, promotor

Independent members:

Prof.dr. I.M. Richardson	Delft University of Technology
Prof.dr.ir. S. van der Zwaag	Delft University of Technology
Prof.dr.ir. B.J. Kooi	University of Groningen
Prof. Dr.-Ing. habil. U. Krupp	Osnabrück University of Applied Sciences, Germany
Dr. W. Melfo	Tata Steel research and development, The Netherlands

This research was carried out under project number M22.3.11439 in the framework of the Research Program of the Materials innovation institute (M2i) in the Netherlands ([www.M2i.nl](http://www.M2i.nl)). This research was also financially supported by International Zinc Association (IZA).



Keywords: Mn steels, annealing, internal oxidation, thermodynamics, kinetics

Copyright © 2018 by Weichen Mao

ISBN: 978-94-91909-50-4

Printed by: Delft Academic Press

Author email: [williammao\\_tud@126.com](mailto:williammao_tud@126.com)

*To all those who have faith in me*





# Table of contents

<b>Chapter 1: Introduction .....</b>	<b>1</b>
1.1 Introduction.....	1
1.2 Outline of the thesis .....	5
References .....	6
<b>Chapter 2: Prediction of oxide phases formed upon internal oxidation of advanced high strength steels .....</b>	<b>7</b>
2.1 Introduction.....	8
2.2 Experiments.....	9
2.2.1 Samples .....	9
2.2.2 Annealing.....	9
2.2.3 Characterization .....	10
2.3 Results and discussion.....	11
2.3.1 Phase diagrams and oxide phases.....	11
2.3.2 Composition of oxide phases .....	18
2.3.3 Internal and external oxides .....	21
2.4 Conclusions.....	24
References .....	25
<b>Chapter 3: Effect of solute interaction on the solubility product of internal precipitates of carbon, nitrogen and oxygen in iron alloys .....</b>	<b>27</b>
3.1 Introduction.....	28
3.2 Solubility product of oxides in non-ideal solution .....	29
3.3 Estimation of interaction parameters.....	32
3.4 Results and discussion.....	34
3.5 Conclusions.....	43
References .....	44
<b>Chapter 4: Effect of solid solute interaction on the internal precipitation kinetics during nitriding or oxidizing of alloys .....</b>	<b>47</b>
4.1 Introduction.....	48
4.2 Coupled thermodynamic-kinetic model .....	49
4.3 Solid solute interactions.....	54
4.4 Results and discussion.....	57
4.4.1 Internal oxidation .....	57
4.4.2 Internal nitriding .....	62

4.5	Conclusions .....	70
	References .....	70
<b>Chapter 5: Relation between oxygen activity gradient in the internal oxidation zone of Mn alloyed steel and the composition of oxide precipitates .....</b>		<b>73</b>
5.1	Introduction .....	74
5.2	Experiments .....	75
5.3	Results and discussion .....	76
5.4	Conclusions .....	82
	References .....	82
<b>Chapter 6: Internal oxidation of Fe-Mn-Cr steel alloys, simulations and experiments .....</b>		<b>85</b>
6.1	Introduction .....	86
6.2	Modelling of internal oxidation of Fe-Mn-Cr alloys .....	86
6.3	Experiments .....	88
6.3.1	Samples .....	88
6.3.2	Annealing .....	89
6.3.3	Characterization .....	89
6.4	Results and discussion .....	90
6.4.1	Transition from external to internal oxidation .....	90
6.4.2	Concentration depth profiles .....	91
6.4.3	Kinetics of internal oxidation .....	97
6.5	Conclusions .....	100
	References .....	101
<b>Chapter 7: Wüstite formation kinetics on pure iron and low alloyed Mn steels during annealing in H<sub>2</sub>O + H<sub>2</sub> and CO<sub>2</sub> + CO gas mixtures .....</b>		<b>103</b>
7.1	Introduction .....	104
7.2	Experiments .....	105
7.2.1	Samples .....	105
7.2.2	Annealing .....	105
7.2.3	Characterization .....	107
7.3	Results .....	108
7.3.1	Kinetics of Wüstite formation on pure iron in H <sub>2</sub> O + H <sub>2</sub> and CO <sub>2</sub> + CO gas mixtures .....	108
7.3.2	Kinetics of Wüstite formation on Mn alloyed steels in H <sub>2</sub> O + H <sub>2</sub> and CO <sub>2</sub> + CO gas mixtures .....	115
7.4	Discussion .....	118

7.5	Conclusions .....	120
	References .....	121
<b>Chapter 8: Reduction kinetics of Wüstite scale on pure iron and steel sheets in Ar and H<sub>2</sub> gas mixture.....</b>		<b>123</b>
8.1	Introduction .....	124
8.2	Kinetics of steady state Wüstite reduction .....	125
8.3	Experiments and methods of investigation.....	128
8.3.1	Samples .....	128
8.3.2	Annealing.....	128
8.3.3	Characterization .....	130
8.4	Results and discussion.....	130
8.4.1	Growth of Wüstite scale.....	130
8.4.2	Growth of iron layer.....	132
8.4.3	Kinetics of Wüstite reduction.....	134
8.5	Conclusions .....	139
	References .....	139
<b>Appendix A.....</b>		<b>143</b>
<b>Appendix B.....</b>		<b>145</b>
<b>Appendix C.....</b>		<b>147</b>
<b>Appendix D.....</b>		<b>149</b>
<b>Appendix E.....</b>		<b>154</b>
<b>Summary .....</b>		<b>155</b>
<b>Samenvatting.....</b>		<b>159</b>
<b>Acknowledgement.....</b>		<b>163</b>
<b>List of publications .....</b>		<b>165</b>
<b>Curriculum vitae.....</b>		<b>166</b>



# Chapter 1

## Introduction

### 1.1 Introduction

In order to reduce the weight of car bodies and thereby reducing fuel consumption and CO<sub>2</sub> emissions, Advanced High Strength Steels (AHSS) are the most competitive structural materials for automotive applications [1, 2]. The superior combination of high strength and formability as well as the low greenhouse gas emission during production make AHSS more promising than other low-density materials such as aluminium alloys and carbon fibre reinforced polymers. Usage of AHSS for automotive applications will continue growing for the next decade [2]. The mechanical properties of AHSS is obtained by increasing the concentration of alloying elements and carefully controlled microstructures. Typical alloying elements in AHSS include C (below 0.3 wt%), Mn (1 to 15 wt%), Si (up to 5 wt%), Cr (up to 1 wt%) and Al (up to 2 wt%). Since the corrosion resistance of AHSS is of equal importance as the mechanical properties required by the automotive industry, the final product of AHSS is usually galvanized for cathodic protection against corrosion. Therefore, producing galvanized AHSS with high quality at low cost has been the area of interest for automotive steel making companies. The main challenge is not only to design novel AHSS grades with controlled bulk microstructures and mechanical properties, but also to improve the zinc coating quality required by automotive companies.

A zinc or zinc alloy protective coating is applied onto the surface of AHSS usually by the continuous hot-dip galvanizing process [3]. Figure 1.1 shows the schematic of a section of an industrial continuous galvanizing line. Before entering the liquid zinc bath where the zinc coating is applied, the steel strip is annealed primarily in radiant tube furnaces. In many European galvanizing lines, before entering the radiant tube furnace the steel strip passes through the direct fired furnace where the steel strip is heated up rapidly. Figure 1.2 shows an example of the temperature profile of steel strip in a continuous galvanizing line. The peak temperature of steel strip during annealing can reach up to about 820 °C. The time of annealing at temperatures above 600 °C is about three minutes. One objective for the continuous annealing treatment of the steel strip in the galvanizing line is to achieve desired final microstructures and mechanical properties. Another objective for the continuous annealing process is to create a clean and metallic steel surface suitable for

galvanizing [4]. Therefore, the annealing atmosphere used in the radiant tube furnace is usually a gas mixture of nitrogen with 3 to 15 vol.% hydrogen [5], so that the surface iron oxide film which originates from the pickling and cold rolling process can be reduced. The annealing atmosphere in the radiant tube furnace also contains small amount of water vapour whose concentration is usually expressed in terms of dew point. The dew point of the annealing atmosphere in the radiant tube furnace usually ranges from -50 to 10 °C [5].

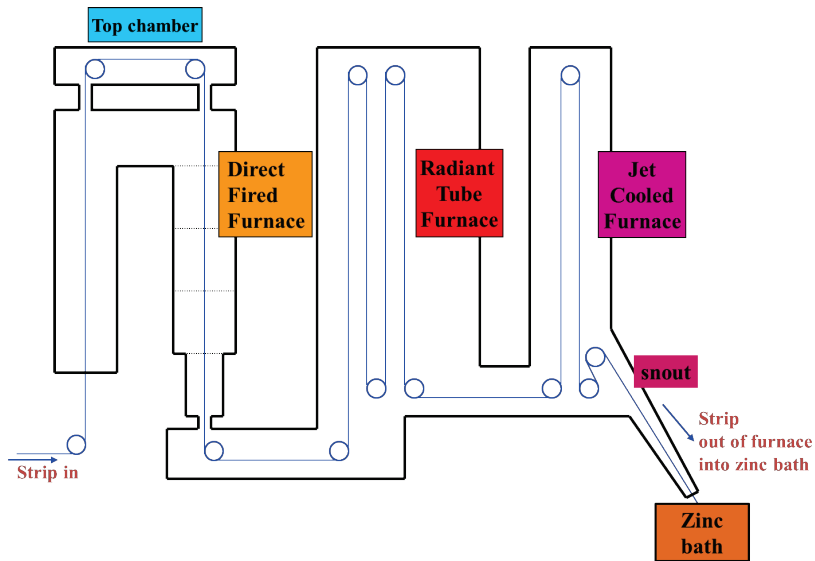


Figure 1.1: Schematic presentation of the annealing section of an industrial continuous galvanizing line.

Although oxidation of iron does not take place during annealing in a gas mixture of nitrogen with hydrogen and dew point below about 20 °C, the alloying elements in AHSS (e.g. Mn, Si, Cr and Al etc.) have high affinity to oxygen and oxidation of those alloying elements is thermodynamically favourable under industrial annealing conditions; see Figure 1.3. The final galvanizing quality of AHSS is to a large extent influenced by its high temperature oxidation behaviour during the annealing process. Because oxides of alloying elements formed at steel surface can significantly reduce the wettability of liquid zinc [6], and thus impair the adhesion between zinc coating and steel substrate. Therefore, one of the biggest challenge for automotive steel makers is to prevent the formation of alloying element oxides at steel surface prior to galvanizing. To date, one common approach for mitigating oxide formation at surface is by increasing dew point in the annealing atmosphere so that internal oxidation of AHSS is promoted during annealing [7]. Another approach to create an oxide-free steel surface is by first forming and subsequently reducing

a Wüstite (FeO) layer which buries the oxides of alloying elements underneath; see Figure 1.4. The formation of FeO layer on AHSS occurs in the direct fire furnace where the oxygen partial pressure of the atmosphere (rich in CO<sub>2</sub> and H<sub>2</sub>O gases) is above the dissociation oxygen partial pressure of FeO. The FeO layer was then reduced in the radiant tube furnace with a reduction atmosphere, producing a pure iron surface. Thus, knowledge on the behaviour of high temperature oxidation and reduction of AHSS is pivotal for improving the quality of the final galvanized steel product.

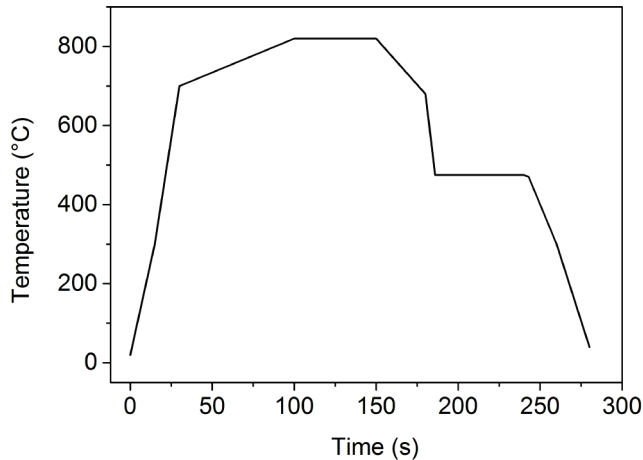


Figure 1.2: Typical temperature profile of a steel strip in an industrial continuous galvanizing line.

A modern steel making company requires the capability of modelling the process-structure-property relationships of steel alloys during the entire production process. For example, simulation tools for microstructure evolution of dual phase steels during continuous annealing are under development [8]. However, the oxidation phenomena of steels during the production process as well as its influence on the surface quality and the subsurface alloy composition have not been taken into account. The industrial aim of this research project is to develop a physical model that quantitatively predicts the oxidation behaviour of AHSS during the continuous annealing process prior to galvanizing. The predictions include the type of oxide phases formed and the concentration depth profiles of oxides and solute alloying elements at the (sub) surface of a steel strip after annealing. The oxidation model can be typically used for developing new AHSS product (e.g. finding the optimum alloy composition and defining alloy composition limits for existing galvanizing lines) and optimizing the process parameters (e.g. defining the desired annealing parameters in galvanizing lines for a particular steel grade). The predicting power of the model can significantly benefit the automotive steel makers by minimizing the number of laboratory and industrial trials and thereby reducing the time and cost for product and process



development. Moreover, the oxidation model can be easily generalized to describe also the internal nitridation and carburization behaviour of steel alloys, and hence can be potentially applied for nitriding and carburizing process.

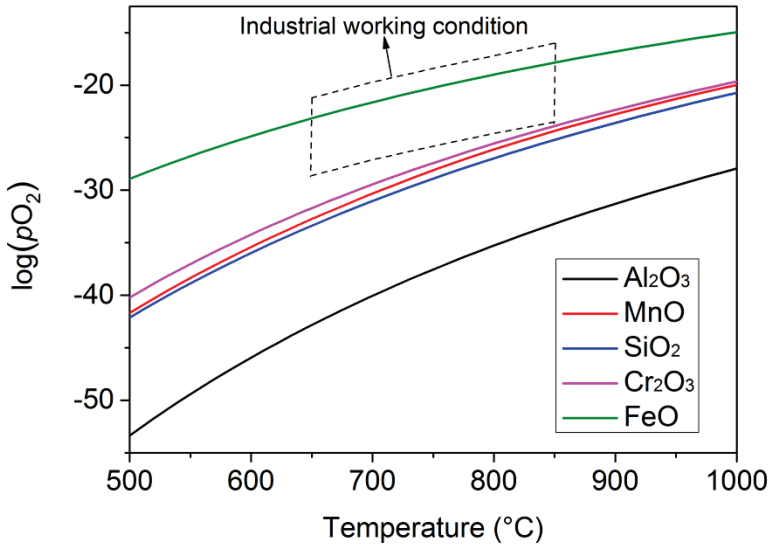


Figure 1.3: Temperature dependence of dissociation oxygen partial pressure of FeO, Cr<sub>2</sub>O<sub>3</sub>, MnO, SiO<sub>2</sub> and Al<sub>2</sub>O<sub>3</sub> for pure iron and Fe – 1 at.% M (M = Cr, Mn, Si and Al) binary alloys, respectively.

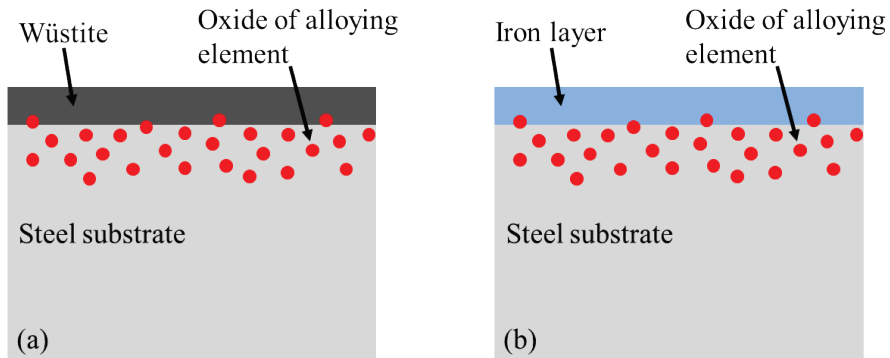


Figure 1.4: Schematic representation of ideal surface conditions during annealing prior to galvanizing. (a) Oxidation of steel sheet to form a layer of iron oxide in the early stage (heating) of the annealing process. (b) Reduction of the layer of iron oxide during annealing in the final stage of the annealing process.

Development of the model requires fundamental understanding of the internal oxidation behaviour of multi-element alloyed steels. The classical Wagner internal oxidation theory

[9, 10] is a generic approach for quantitative description of the internal oxidation behaviour of alloys. Recently it has been reported that the classical Wagner internal oxidation theory can be successfully applied to predict the kinetics of internal oxidation of Fe-Mn binary steel alloys [11, 12]. However, the classical Wagner internal oxidation theory is limited to binary ideal alloys where only one type of oxide precipitates, while a typical AHSS always contains multiple alloying elements. A comprehensive model that considers the formation of multiple types of oxides as well as the non-ideal behaviour of solution induced by adding more alloying elements is not yet available. Experimental studies on internal oxidation kinetics for ternary or higher Fe-Mn based steel alloys have not been reported. Therefore, the challenge and the primary academic focus of this thesis is to extend the classical Wagner internal oxidation theory for oxidation of multi-element alloyed steels with multiple types of oxides formed. The research activities for this thesis comprise the following aspects. The thermodynamics of oxide formation in multi-element (Mn, Cr and Si) alloyed AHSS is first investigated in order to know the type of oxide phases formed during annealing as a function of alloy compositions and oxygen partial pressures. Then, the effect of non-ideal behaviour of solution, i.e. the solute interaction, on the solubility product of internal oxides and the diffusivity of solute atoms in multi-component iron alloys is studied. Next, a generic numerical model for internal oxidation of multi-component alloys is devised, considering the non-ideal behaviour of solution and the precipitation of multiple oxide phases. The internal oxidation behaviour of Fe-Mn-Cr ternary steel alloys is studied as an example to testify the model. Finally, the kinetics of Wüstite formation on Mn alloyed steels in  $\text{CO}_2 + \text{CO}$  and  $\text{H}_2\text{O} + \text{H}_2$  gas mixtures as well as the reduction kinetics of Wüstite in  $\text{Ar} + \text{H}_2$  gas mixtures are investigated, since the kinetic data for Wüstite formation and reduction in the gas environment are lacking, yet important for galvanizing industries.

## 1.2 Outline of the thesis

Chapter 2 focuses on the thermodynamics of oxide formation in selected AHSS alloyed with Mn, Cr and Si. The type of oxides formed upon annealing of AHSS as a function of alloy composition and ambient oxygen partial pressure is predicted with thermodynamic tools and validated by experiments. The effect of non-ideal behaviour of solution on the solubility product of internal oxides in iron alloys is dealt with in Chapter 3. A generic method is proposed to estimate the interaction parameters pertaining to carbon, nitrogen and oxygen in non-ideal iron alloys. A multi-element coupled thermodynamic-kinetic model is presented in Chapter 4 for internal precipitation due to inward diffusion of a foreign element. The effect of non-ideal behaviour of solution on internal oxidation and nitridation of alloys is investigated with simulations and experiments. In Chapter 5, the

composition depth profiles of internal (Mn,Fe)O precipitates formed upon internal oxidation of a Mn alloyed steel is investigated in order to demonstrate that local thermodynamic equilibrium is established within the internal oxidation zone of Mn alloyed steels during annealing. Chapter 6 focuses on the internal oxidation behaviour of Fe-Mn-Cr ternary steel alloys. The kinetics of internal oxidation as well as the concentration depth profiles of internal oxides for Fe-Mn-Cr steel alloys are predicted based on the coupled thermodynamic-kinetic model and validated by experiments. In Chapter 7, kinetics of Wüstite formation on pure iron and Mn alloyed steels in  $\text{CO}_2 + \text{CO}$  and  $\text{H}_2\text{O} + \text{H}_2$  gas mixtures are studied, while the kinetics of Wüstite reduction in  $\text{Ar} + \text{H}_2$  gas mixtures are investigated in Chapter 8.

## References

- [1] N. Fonstein, *Advanced High Strength Sheet Steels*, Springer International Publishing, Switzerland, 2015.
- [2] *Advanced High-Strength Steels Application Guidelines Version 6.0*, WorldAutoSteel, 2017.
- [3] A.R. Marder, *Progress in Materials Science*, **45** (2000), 191.
- [4] J. McDermid, Tutorial lecture, Galvatech 2017, Tokyo, Japan, 2017.
- [5] M. Hamman, personal communication, 2017.
- [6] G.M. Song, T. Vystavel, N. van der Pers, J.T.M. De Hosson and W.G. Sloof, *Acta Materialia*, **60** (2012), 2973.
- [7] H. Liu, Y. He, S. Swaminathan, M. Rohwerder and L. Li, *Surface and Coatings Technology*, **206** (2011), 1237.
- [8] K. Bos, Steel strip through process microstructure evolution modelling, presentation at M2i annual conference, 2017.
- [9] D.J. Young, *High Temperature Oxidation and Corrosion of Metals*, Elsevier, Oxford, 2008.
- [10] R.A. Rapp, *Corrosion*, **21** (1965), 382.
- [11] V.A. Lashgari, G. Zimbitas, C. Kwakernaak and W.G. Sloof, *Oxidation of Metals*, **82** (2014), 249.
- [12] V.A. Lashgari, *Internal and External Oxidation of Manganese in Advanced High Strength Steels*, PhD Dissertation, Delft University of Technology, 2014.

## Chapter 2

# Prediction of oxide phases formed upon internal oxidation of advanced high strength steels<sup>1</sup>

### Abstract

The effect of Cr on the oxidation of Fe-Mn based steels during isothermal annealing at different dew points was investigated. The Fe-Mn-Cr-(Si) phase diagrams for oxidizing environments were computed to predict the oxide phases. Various Fe-Mn steels with different concentrations of Cr and Si were annealed at 950 °C in a gas mixture of Ar or N<sub>2</sub> with 5 vol.% H<sub>2</sub> and dew points ranging from -45 to 10 °C. The identified oxide species after annealing match with those predicted based on the phase diagrams. (Mn,Fe)O is the only oxide phase formed during annealing of Fe-Mn binary steel alloys. Adding Cr leads to the formation of (Mn,Cr,Fe)<sub>3</sub>O<sub>4</sub> spinel. The dissociation oxygen partial pressure of (Mn,Cr,Fe)<sub>3</sub>O<sub>4</sub> in the Fe-Mn-Cr steels is lower than that of (Mn,Fe)O. The Si in the steels results in the formation (Mn,Fe)<sub>2</sub>SiO<sub>4</sub>, and increasing the Si concentration suppresses the formation of (Mn,Cr,Fe)<sub>3</sub>O<sub>4</sub> and (Mn,Fe)O during annealing.

### Keywords

Advanced high strength steels, Annealing, Oxidation, Thermodynamics

---

<sup>1</sup> This chapter is based on:

W. Mao, R.W.A. Hendrikx and W.G. Sloof, *Prediction of oxide phases formed upon internal oxidation of advanced high-strength steels*, Oxidation of Metals, 2017.

## 2.1 Introduction

Advanced High Strength Steels (AHSS) are widely used for automotive applications to reduce the weight of car bodies and thereby reducing fuel consumption and CO<sub>2</sub> emissions; see e.g. [1]. To protect AHSS against corrosion, a zinc coating is applied onto the steel surface usually by hot-dip galvanizing [2]. Before entering the zinc bath the steel strip passes through continuous annealing furnaces. The annealing atmosphere is usually a gas mixture of N<sub>2</sub> and H<sub>2</sub> with dew point ranging from -60 to 10 °C, whose oxygen partial pressure level is below the dissociation oxygen partial pressure of Wüstite (FeO). However, the alloying elements (e.g. Mn, Cr, Si, Al) in AHSS have a higher affinity to oxygen than iron, leading to the formation of oxides of these elements during the annealing process prior to galvanizing. The presence of these alloying element oxides at the steel surface reduces the zinc wettability [3] and thus impairs the galvanizing quality [4]. Therefore, it is imperative to understand the oxidation behaviour of AHSS in N<sub>2</sub> plus H<sub>2</sub> gas mixtures with various dew points, and to find conditions to mitigate the formation of external oxides after annealing.

The oxidation behaviour of Fe-Mn binary and Fe-Mn-Si ternary steel alloys below the dissociation oxygen partial pressure of FeO has been studied in detail (see e.g. Refs [5-9]). However, only a few studies have been reported on the oxidation of Cr alloyed Fe-Mn based steels [10, 11]. The study on the effect of Cr on the type of oxides formed in AHSS during annealing is not complete, and the type of oxides formed during annealing of Fe-Mn-Cr ternary and Fe-Mn-Cr-Si quaternary steel alloys has not been confirmed by X-ray diffraction analysis. Since Cr is often added to AHSS to enhance the hardenability of austenite [1], the primary aim of the present investigation is to understand the effect of Cr on the type of oxides formed in Fe-Mn based steels during annealing. Also, the effect of Si on the type of oxide species formed in steels alloyed with both Mn and Cr is studied. The type and composition of the oxides formed in Fe-Mn-Cr-(Si) steel alloys as a function of annealing temperature, alloy composition and the annealing dew points are first predicted with thermodynamic computation. Then, the experimentally identified oxide phases formed after annealing different Fe-Mn-Cr-(Si) steel alloys in gas mixtures of Ar or N<sub>2</sub> with 5 vol.% H<sub>2</sub> and different dew points are compared with the thermodynamic predictions. Finally, the effect of Cr and Si on the internal and external oxidation of Fe-Mn based steels is discussed.

## 2.2 Experiments

### 2.2.1 Samples

The chemical composition in atom percent of the steel alloys investigated are listed in Table 2.1. The Fe-1.7Mn, Fe-1.8Mn-0.6Cr-0.5Si, Fe-1.8Mn-1.1Cr-0.5Si and Fe-2.8Mn-0.6Cr-0.5Si steel samples were cut with a plate cutter from a cold-rolled steel sheet. The Fe-1.8Mn-0.5Cr and Fe-1.7Mn-1.5Cr alloys were cut from ingots and the Fe-1.9Mn-1.0Cr-0.1Si and Fe-1.9Mn-1.6Cr-0.1Si steels were cut from hot rolled steel plates by electric discharge machining (EDM). Before annealing, the surface of specimens was ground with SiC emery paper and then polished with 1 micron diamond grains. Finally, the samples were cleaned ultrasonically in isopropanol and dried by blowing with pure nitrogen (purity better than 5N). The samples were stored in air tight membrane boxes (Agar Scientific G3319, UK).

Table 2.1: Steel composition in atom percent (weight percent between brackets).

Sample	C	Mn	Cr	Si	Al
Fe-1.7Mn	0.48 (0.10)	1.72 (1.70)	-	0.10 (0.05)	0.004 (0.002)
Fe-1.8Mn-0.5Cr	-	1.75 (1.72)	0.53 (0.49)	-	-
Fe-1.7Mn-1.5Cr	-	1.70 (1.67)	1.49 (1.39)	-	-
Fe-1.8Mn-0.6Cr-0.5Si	0.46 (0.10)	1.82 (1.80)	0.57 (0.53)	0.49 (0.25)	0.006 (0.003)
Fe-1.8Mn-1.1Cr-0.5Si	0.47 (0.10)	1.82 (1.80)	1.09 (1.02)	0.51 (0.26)	0.039 (0.019)
Fe-1.9Mn-1.0Cr-0.1Si	0.46 (0.10)	1.90 (1.88)	0.97 (0.91)	0.12 (0.06)	0.053 (0.026)
Fe-1.9Mn-1.6Cr-0.1Si	0.46 (0.10)	1.85 (1.83)	1.63 (1.53)	0.10 (0.05)	0.049 (0.024)
Fe-2.8Mn-0.6Cr-0.5Si	0.47 (0.10)	2.83 (2.80)	0.59 (0.55)	0.49 (0.25)	0.010 (0.005)

### 2.2.2 Annealing

The oxidation experiments below the dissociation oxygen partial pressure of Wüstite were carried out in a horizontal quartz tube furnace (Carbolite MTF 12/38/850, UK) with an inner tube diameter of 30 mm. The temperature in the furnace tube was measured with a NiCr/NiAl (type K) thermocouple at the sample location. A gas mixture of N<sub>2</sub> or Ar with 5 vol.% H<sub>2</sub> was passed the furnace tube at atmospheric pressure. De-aerated and deionized water (18.2 MΩ.cm at 25 °C) was evaporated with a controlled evaporator mixer (CEM, Bronkhorst, The Netherlands) to create specific dew points of -45, -37, -30, -10 and 10 °C (corresponding oxygen partial pressure of  $8.1 \times 10^{-22}$ ,  $5.0 \times 10^{-21}$ ,  $2.2 \times 10^{-20}$ ,  $1.0 \times 10^{-18}$  and  $2.3 \times 10^{-17}$  atm. at 950 °C; see Appendix A) in the furnace. The pure water was de-aerated with nitrogen gas in a closed pressurized stainless-steel vessel and the dissolved oxygen gas in the pure water was below 100 ppb, as measured with an O<sub>2</sub> sensor (InPro 6850i, Mettler Toledo, USA). The dew points of -10 and 10 °C were monitored with a cooled mirror analyser (Optidew, Michell Instruments, UK). The dew points of -45, -37 and -30 °C were monitored with another cooled mirror analyser (S4000 TRS, Michell Instruments, UK). The

fluctuation of dew points during annealing was within  $\pm 2$  °C. The partial pressure of evaporated H<sub>2</sub>O in the gas mixture is related to dew point according to the formula given in the Appendix A. The gas mixture with dew points of -10 and 10 °C consists of N<sub>2</sub> + 5 vol.% H<sub>2</sub>, while the gas mixture with dew points of -45, -37 and -30 °C was created with Ar + 5 vol.% H<sub>2</sub>. However, the oxidation behaviour of the steel alloys used in this study is not affected by the type of carrier gas (i.e. Ar or N<sub>2</sub>), because formation of nitride is not thermodynamically favourable for our samples and our annealing conditions. The flow rate of gas mixture with dew points of -30 to 10 °C was 1500 sccm, while the flow rate of gas mixture with dew points of -45 and -37 °C was 3000 sccm. Before annealing, the sample was placed onto a quartz boat located at the cold zone of the furnace tube. Then, the furnace was closed and flushed with the reaction gas for more than 30 minutes. Next, the sample was moved to the hot zone of the furnace with a quartz rod to start an annealing cycle. At the end of the annealing cycle, the sample was moved in the reverse direction, i.e. to the cold zone. The heating and cooling of the sample was relatively fast, about 140 and 180 °C/min, respectively.

The oxidation experiments above the dissociation oxygen partial pressure of Wüstite were carried out with the Fe-1.9Mn-1.6Cr-0.1Si steel alloy in the same horizontal quartz tube, but with an infrared furnace (Model 4069-12R-05L, Research Inc.) at 950 °C for 8 hours in a gas mixture of Ar + 20 vol.% CO<sub>2</sub> + 20 vol.% CO (oxygen partial pressure of  $8.8 \times 10^{-16}$  atm.; see Appendix A) at atmospheric pressure with a total gas flow of 500 sccm. The temperature of the sample during annealing was determined by measuring the temperature of a dummy sample which was spot welded to a thermocouple. The dummy sample has the same dimensions and chemical composition as the target sample.

Prior to admitting the gas mixtures to any of the furnaces, each gas, i.e. Ar, N<sub>2</sub>, H<sub>2</sub>, CO<sub>2</sub> and CO (all with a purity better than 5N vol.%), was filtered to remove any residual hydrocarbons, moisture and oxygen, with Accosorb (< 10 ppb hydrocarbons), Hydrosorb (<10 ppb H<sub>2</sub>O) and Oxysorb (< 5 ppb O<sub>2</sub>) filters (Messer Griesheim, Germany), respectively. The flow of each gas was regulated and monitored using mass flow controllers (Bronkhorst, The Netherlands).

### 2.2.3 Characterization

Grazing Angle X-ray Diffractometry (GA-XRD) was used to identify the oxide phases present at the surface of the oxidized samples. The XRD patterns were recorded, with a Bruker D8 Discover diffractometer in the grazing incidence geometry using Co K $\alpha$  radiation, in the  $2\theta$  region between 20° and 60° with a step size of 0.03°  $2\theta$  and a dwell time of 10 s. The incidence angle of the X-ray beam was fixed at 3° with respect to the

sample surface. In this grazing incidence geometry, the depth below the surface corresponding with 70 % of the diffracted intensity of pure iron is 1.27 to 1.34  $\mu\text{m}$  for  $2\theta$  ranging from  $30^\circ$  to  $60^\circ$  [12]. When the incidence angle of the X-ray beam was at  $2^\circ$  with respect to the sample surface, the depth below the surface corresponding with 70 % of the diffracted intensity of FeO is 1.4 to 1.5  $\mu\text{m}$  for  $2\theta$  ranging from  $30^\circ$  to  $60^\circ$ . Also, XRD measurements in the Bragg-Brentano geometry were performed with the same diffractometer in the  $2\theta$  region between  $10^\circ$  and  $110^\circ$  with a step size of  $0.03^\circ 2\theta$  and a dwell time of 2 s. Then, the depth below the surface corresponding with 70 % of the diffracted intensity of FeO for Bragg-Brentano geometry is about 5.7 to 10.9  $\mu\text{m}$  for  $2\theta$  from  $30^\circ$  to  $60^\circ$  [12].

The surface and cross-section of the annealed samples were observed with scanning electron microscopy (SEM) using a JSM-6500F (JEOL, Japan) operated with an accelerating voltage of 5 or 15 kV. X-ray microanalysis (XMA) using Energy Dispersive Spectroscopy (EDS) was performed with the same SEM instrument, but equipped with an UltraDry 30  $\text{mm}^2$  detector (Thermo Fisher Scientific, USA) to determine the chemical composition of oxides qualitatively.

X-ray photoelectron spectroscopy (XPS) was used to analyse the chemical composition of the oxides at the steel surfaces. The photoelectron spectra were recorded with a PHI 5400 ESCA equipped with an X-ray source operated at 200 W and 13 kV using an Al anode. The pass energy of the spherical capacitor analyser was set at 35.75 eV. Prior to the recording of the spectra, the steel sample surface was sputtered mildly with a 3 keV Ar-ion beam with ion flux of  $2 \times 10^{-13} \text{ mol mm}^{-2} \text{ s}^{-1}$ , rastering over an area of  $5 \times 5 \text{ mm}$  for 10 minutes.

## 2.3 Results and discussion

### 2.3.1 Phase diagrams and oxide phases

The phase diagrams of Fe-Mn, Fe-Mn-Cr and Fe-Mn-Cr-Si alloys in an oxidizing environment at  $950^\circ\text{C}$  are shown in Figures 2.1 to 2.6. These phase diagrams were constructed with FactSage [13]. The thermodynamic data of the stoichiometric compounds  $\text{Cr}_2\text{O}_3$  and  $\text{SiO}_2$  as well as the solid solution oxides, namely:  $(\text{Mn,Cr,Fe})_3\text{O}_4$  spinel,  $(\text{Mn,Fe})\text{O}$ ,  $(\text{Mn,Fe})_2\text{SiO}_4$  and  $(\text{Mn,Fe})\text{SiO}_3$  were taken from the FToxid database [14]. A solid solution of Fe-Mn binary, Fe-Mn-Cr ternary and Fe-Mn-Cr-Si quaternary alloy with fcc or bcc crystal lattice was created with the thermodynamic data in the FSstel database [14]. A gas mixture of Ar and  $\text{O}_2$  with increasing oxygen partial pressure (in atm.) was



created using the thermodynamic data in the FactPS database [15] to be in equilibrium with the alloy phase and the oxides.

First the oxide phase that can be formed in a Fe-Mn binary alloy is considered; see Figure 2.1 and Table 2.2. The dissociation oxygen partial pressure of MnO is lower than FeO. However, since both FeO and MnO have the same rock-salt crystal structure, FeO and MnO can form a continuous solid solution [16] denoted as (Mn,Fe)O. The Fe concentration in the (Mn,Fe)O increases with oxygen partial pressure, which agrees with the results reported in Refs. [17, 18]. Above an oxygen partial pressure of about  $1.6 \times 10^{-16}$  atm. at 950 °C, all the Fe and Mn in the alloy are oxidized to (Mn,Fe)O. The prediction with the computed phase diagram is in agreement with our experimental results (see Table 2.2) and the results reported in Ref. [5], that (Mn,Fe)O is the only type of oxide phase that can be formed in a Fe-Mn binary alloy below an oxygen partial pressure of  $1.6 \times 10^{-16}$  atm. However, when annealing the Fe-1.7Mn steel at the dew point of -45 °C (oxygen partial pressure of  $8.1 \times 10^{-22}$  atm.), the (Mn,Fe)O cannot be identified with GA-XRD because the amount of oxides formed is too small.

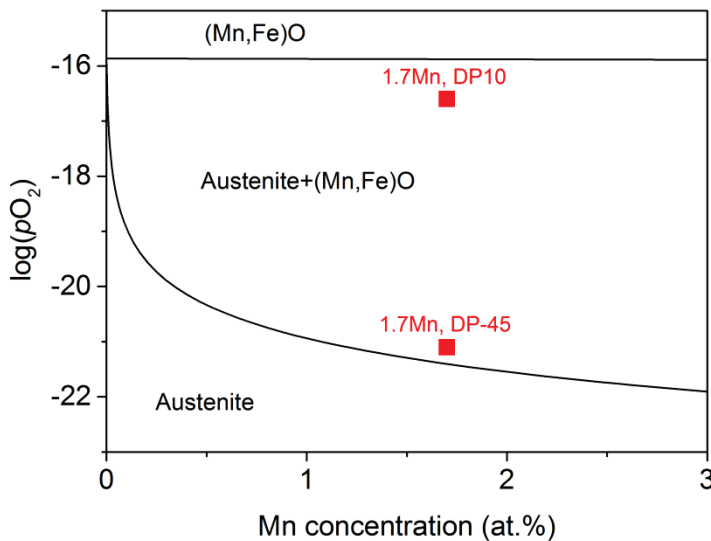


Figure 2.1: Computed phase diagram of Fe-Mn binary alloys in an oxidizing environment at 950 °C. The squares indicate the Fe with 1.7 at.% Mn alloy oxidized at dew points of -45 and 10 °C, respectively.

Table 2.2: Identified oxide species from XRD measurements<sup>1</sup> (in black) after annealing the Fe-Mn and Fe-Mn-Cr-(Si) steel alloys at 950 °C for 1 hour in a gas mixture of Ar or N<sub>2</sub> with 5 vol.% H<sub>2</sub> and dew points (DP) of: -45, -37, -30, -10 and 10 °C (corresponding with oxygen partial pressure ( $pO_2$ ) of  $8.1 \times 10^{-22}$ ,  $5.0 \times 10^{-21}$ ,  $2.2 \times 10^{-20}$ ,  $1.0 \times 10^{-18}$  and  $2.3 \times 10^{-17}$  atm., respectively). Predicted oxide phases are denoted in blue and indicated with an asterisk.

Sample	$pO_2$ $8.1 \times 10^{-22}$ (atm.)	$pO_2$ $5.0 \times 10^{-21}$ (atm.)	$pO_2$ $2.2 \times 10^{-20}$ (atm.)	$pO_2$ $1.0 \times 10^{-18}$ (atm.)	$pO_2$ $2.3 \times 10^{-17}$ (atm.)
Fe-1.7Mn	NA <sup>2</sup>	(Mn,Fe)O	(Mn,Fe)O	(Mn,Fe)O	(Mn,Fe)O
Fe-1.8Mn-0.5Cr	(Mn,Cr,Fe) <sub>3</sub> O <sub>4</sub> (Mn,Fe)O	(Mn,Cr,Fe) <sub>3</sub> O <sub>4</sub> * (Mn,Fe)O*	(Mn,Cr,Fe) <sub>3</sub> O <sub>4</sub> * (Mn,Fe)O*	(Mn,Cr,Fe) <sub>3</sub> O <sub>4</sub> * (Mn,Fe)O*	(Mn,Cr,Fe) <sub>3</sub> O <sub>4</sub> * (Mn,Fe)O*
Fe-1.7Mn-1.5Cr	(Mn,Cr,Fe) <sub>3</sub> O <sub>4</sub>	(Mn,Cr,Fe) <sub>3</sub> O <sub>4</sub> (Mn,Fe)O	(Mn,Cr,Fe) <sub>3</sub> O <sub>4</sub> * (Mn,Fe)O*	(Mn,Cr,Fe) <sub>3</sub> O <sub>4</sub> * (Mn,Fe)O*	(Mn,Cr,Fe) <sub>3</sub> O <sub>4</sub> * (Mn,Fe)O*
Fe-1.8Mn-0.6Cr-0.5Si	(Mn,Fe) <sub>2</sub> SiO <sub>4</sub>	(Mn,Cr,Fe) <sub>3</sub> O <sub>4</sub> (Mn,Fe) <sub>2</sub> SiO <sub>4</sub>	(Mn,Cr,Fe) <sub>3</sub> O <sub>4</sub> (Mn,Fe)O (Mn,Fe) <sub>2</sub> SiO <sub>4</sub>	(Mn,Cr,Fe) <sub>3</sub> O <sub>4</sub> (Mn,Fe)O (Mn,Fe) <sub>2</sub> SiO <sub>4</sub>	(Mn,Cr,Fe) <sub>3</sub> O <sub>4</sub> (Mn,Fe)O (Mn,Fe) <sub>2</sub> SiO <sub>4</sub>
Fe-1.8Mn-1.1Cr-0.5Si	(Mn,Fe) <sub>2</sub> SiO <sub>4</sub>	(Mn,Cr,Fe) <sub>3</sub> O <sub>4</sub> (Mn,Fe) <sub>2</sub> SiO <sub>4</sub>	(Mn,Cr,Fe) <sub>3</sub> O <sub>4</sub> (Mn,Fe) <sub>2</sub> SiO <sub>4</sub>	(Mn,Cr,Fe) <sub>3</sub> O <sub>4</sub> (Mn,Fe)O (Mn,Fe) <sub>2</sub> SiO <sub>4</sub>	(Mn,Cr,Fe) <sub>3</sub> O <sub>4</sub> (Mn,Fe)O
Fe-1.9Mn-1.0Cr-0.1Si	(Mn,Cr,Fe) <sub>3</sub> O <sub>4</sub>	(Mn,Cr,Fe) <sub>3</sub> O <sub>4</sub> (Mn,Fe)O	(Mn,Cr,Fe) <sub>3</sub> O <sub>4</sub> * (Mn,Fe)O*	(Mn,Cr,Fe) <sub>3</sub> O <sub>4</sub> * (Mn,Fe)O*	(Mn,Cr,Fe) <sub>3</sub> O <sub>4</sub> * (Mn,Fe)O*
Fe-1.9Mn-1.6Cr-0.1Si	(Mn,Cr,Fe) <sub>3</sub> O <sub>4</sub>	(Mn,Cr,Fe) <sub>3</sub> O <sub>4</sub> (Mn,Fe)O	(Mn,Cr,Fe) <sub>3</sub> O <sub>4</sub> * (Mn,Fe)O*	(Mn,Cr,Fe) <sub>3</sub> O <sub>4</sub> * (Mn,Fe)O*	(Mn,Cr,Fe) <sub>3</sub> O <sub>4</sub> * (Mn,Fe)O*
Fe-2.8Mn-0.6Cr-0.5Si	(Mn,Cr,Fe) <sub>3</sub> O <sub>4</sub> (Mn,Fe)O (Mn,Fe) <sub>2</sub> SiO <sub>4</sub>	(Mn,Cr,Fe) <sub>3</sub> O <sub>4</sub> * (Mn,Fe)O* (Mn,Fe) <sub>2</sub> SiO <sub>4</sub> *	(Mn,Cr,Fe) <sub>3</sub> O <sub>4</sub> (Mn,Fe)O (Mn,Fe) <sub>2</sub> SiO <sub>4</sub>	(Mn,Cr,Fe) <sub>3</sub> O <sub>4</sub> (Mn,Fe)O (Mn,Fe) <sub>2</sub> SiO <sub>4</sub>	(Mn,Cr,Fe) <sub>3</sub> O <sub>4</sub> (Mn,Fe)O (Mn,Fe) <sub>2</sub> SiO <sub>4</sub>

The oxide species formed in Fe-Mn-Cr ternary alloys at 950 °C as a function of oxygen partial pressure and Cr concentration in the range of 0 to 1.5 at.% for a fixed Mn concentration of 1.8 at.% were predicted; see Figure 2.2. Adding Cr to the Fe-Mn alloy leads to the formation of MnCr<sub>2</sub>O<sub>4</sub> spinel with a cubic crystal lattice. However, Fe cations can substitute with Mn and Cr cations in the spinel to form an oxide solution denoted as (Mn,Cr,Fe)<sub>3</sub>O<sub>4</sub>. For the alloy compositions considered here, changing the Cr concentration and oxygen partial pressure does not result in the formation of Cr<sub>2</sub>O<sub>3</sub>, which is in agreement with our experimental results; see Table 2.2. Considering the Mn concentration in the alloy fixed, the dissociation oxygen partial pressure of (Mn,Cr,Fe)<sub>3</sub>O<sub>4</sub> spinel decreases, while the dissociation oxygen partial pressure of (Mn,Fe)O slightly increases with the Cr concentration in the alloy; see Figure 2.2. The dissociation partial pressure of (Mn,Cr,Fe)<sub>3</sub>O<sub>4</sub> spinel is lower than the dissociation oxygen partial pressure of (Mn,Fe)O, when the Cr concentration in the bulk alloy is higher than about 0.2 at.%. This is confirmed by the observation that (Mn,Cr,Fe)<sub>3</sub>O<sub>4</sub> spinel is formed during annealing at low dew points,

<sup>1</sup> All XRD results obtained from measurements using Co K $\alpha$  radiation with grazing incidence geometry.

<sup>2</sup> Data not available because the amount of oxides formed is below the detection limit of the XRD measurements.

\* Predicted oxide phases.

while (Mn,Fe)O appears at high dew points in the Fe-1.7Mn-1.5Cr, Fe-1.9Mn-1.0Cr-0.1Si and Fe-1.9Mn-1.6Cr-0.1Si steel alloys; see Table 2.2. The increase of the dissociation oxygen partial pressure of (Mn,Fe)O with the Cr concentration is evidenced by the identification of (Mn,Fe)O in the Fe-1.8Mn-0.5Cr, but is not detected in the Fe-1.7Mn-1.5Cr alloy annealed at dew point of -45 °C; see Table 2.2. This is due to the fact that the dissociation oxygen partial pressure of (Mn,Fe)O decreases with the concentration of Mn dissolved in the alloy. At certain oxygen partial pressure and concentration of Mn in the alloy, the amount of Mn that reacts with Cr to form (Mn,Cr,Fe)<sub>3</sub>O<sub>4</sub> spinel increases, and hence, the concentration of Mn that remains in the alloy decreases with Cr concentration.

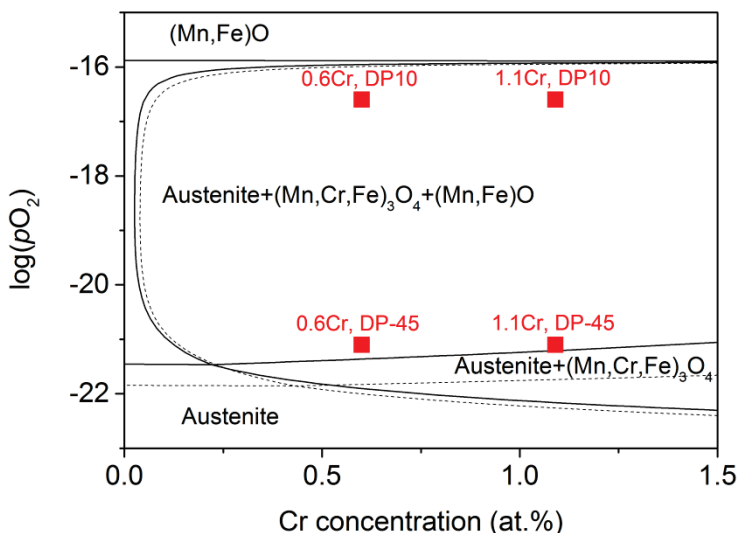


Figure 2.2: Computed phase diagram of Fe-Mn-Cr alloys with Mn concentration fixed at 1.8 or 2.8 (dashed lines) at.% in an oxidizing environment at 950 °C. Note that dissociation oxygen partial pressure of (Mn,Fe)O slightly increases with Cr concentration in the alloy. The squares indicate the alloy with 0.6 or 1.1 at.% Cr oxidized at dew points of -45 and 10 °C.

The addition of Si to the Fe-Mn-Cr alloys leads to the formation of (Mn,Fe)<sub>2</sub>SiO<sub>4</sub>. The dissociation oxygen partial pressure of (Mn,Fe)<sub>2</sub>SiO<sub>4</sub> is lower than that of (Mn,Cr,Fe)<sub>3</sub>O<sub>4</sub> for the alloy compositions considered here; see Figures 2.3 and 2.4. This is consistent with the oxide phase identified in the annealed Fe-1.8Mn-0.6Cr-0.5Si and Fe-1.8Mn-1.1Cr-0.5Si steels, i.e. a single (Mn,Fe)<sub>2</sub>SiO<sub>4</sub> oxide phase is formed at the dew point of -45 °C; see Table 2.2. However, according to the phase diagram (Figure 2.4), the formation of (Mn,Cr,Fe)<sub>3</sub>O<sub>4</sub> spinel is also predicted for the Fe-1.8Mn-0.6Cr-0.5Si and Fe-1.8Mn-1.1Cr-0.5Si alloys after annealing at a dew point of -45 °C. This shows that adding Si to the Fe-Mn-Cr steel alloys suppresses the formation of (Mn,Cr,Fe)<sub>3</sub>O<sub>4</sub> spinel. Apparently, Si in the

steel lowers the oxygen partial pressure at steel surface. But, after annealing of the Fe-1.8Mn-0.6Cr-0.5Si and Fe-1.8Mn-1.1Cr-0.5Si alloys at higher dew points than  $-45\text{ }^{\circ}\text{C}$  up to  $10\text{ }^{\circ}\text{C}$ , also  $(\text{Mn,Cr,Fe})_3\text{O}_4$  spinel is observed; see Table 2.2. This is in agreement with the phase diagram; see Figure 2.4.

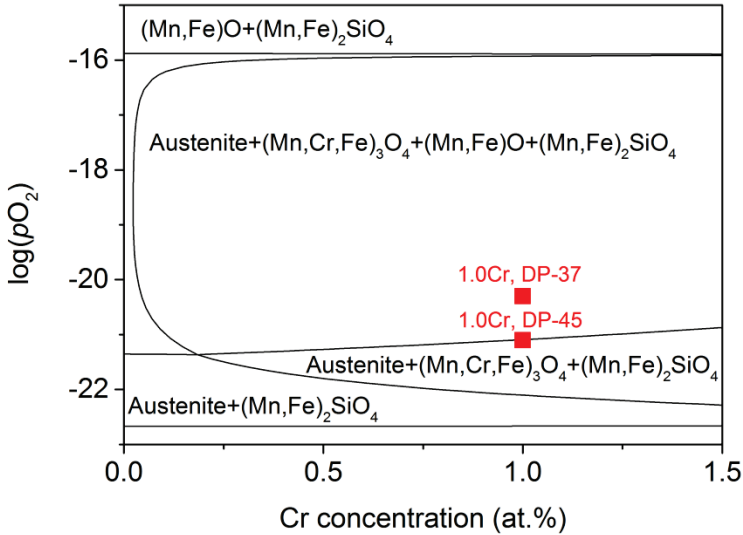


Figure 2.3: Phase diagram of Fe-Mn-Cr-Si alloys with Si concentration fixed at 0.1 at.% and Mn concentration fixed at 1.8 at.% in an oxidizing environment at  $950\text{ }^{\circ}\text{C}$ . The squares indicate the alloy with 1.0 at.% Cr oxidized at dew points of  $-45$  and  $-37\text{ }^{\circ}\text{C}$ , respectively.

With 1.8 at.% Mn and 0 to 1.5 at.% Cr in the bulk alloy, the dissociation oxygen partial pressure of  $(\text{Mn,Fe})\text{O}$  in the Fe-Mn-Cr-Si ternary alloys increases with Si concentration; see Figures 2.3 and 2.4. For example, for a fixed Mn and Cr concentration of 1.8 and 1.0 at.%, respectively, the dissociation oxygen partial pressure of  $(\text{Mn,Fe})\text{O}$  increases from about  $8.1 \times 10^{-22}$  to  $1.0 \times 10^{-20}$  atm. with increasing Si concentration from 0.1 to 0.5 at.% at  $950\text{ }^{\circ}\text{C}$ . This corresponds to the experimental observation that  $(\text{Mn,Fe})\text{O}$  is formed in the Fe-1.8Mn-1.0Cr-0.5Si at a higher annealing dew point than in the Fe-1.9Mn-1.0Cr-0.1Si steel alloy; see Table 2.2. The effect of Si on the dissociation oxygen partial pressure of  $(\text{Mn,Fe})\text{O}$  can be explained as follows. Since  $(\text{Mn,Fe})_2\text{SiO}_4$  is much more stable than both  $(\text{Mn,Cr,Fe})_3\text{O}_4$  spinel and  $(\text{Mn,Fe})\text{O}$ , the concentration of Si in the alloy matrix is practically zero at the dissociation oxygen partial pressure of  $(\text{Mn,Cr,Fe})_3\text{O}_4$  spinel and  $(\text{Mn,Fe})\text{O}$ . Thus, the concentration of Mn that remains in the alloy matrix decreases with the amount of Si added to the alloy due to the formation of  $(\text{Mn,Fe})_2\text{SiO}_4$ . Hence, the dissociation oxygen partial pressure of  $(\text{Mn,Fe})\text{O}$  increases.

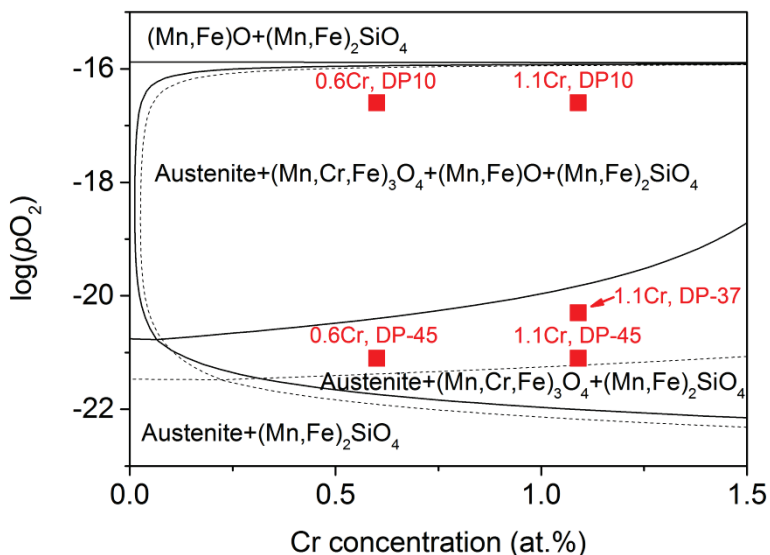


Figure 2.4: Computed phase diagram of Fe-Mn-Cr-Si alloys with Si concentration fixed at 0.5 at.% and Mn concentration fixed at 1.8 or 2.8 (dashed lines) at.% in an oxidizing environment at 950 °C. The squares indicate the alloy with 0.6 or 1.1 at.% Cr oxidized at dew points of -45, -37 and 10 °C, respectively. (It is noted that when the Mn concentration in the steel alloy equals 1.8 at.% and the  $p_{O_2}$  is below  $3.2 \times 10^{-23}$  atm., the formation of  $(Mn,Fe)SiO_3$  is also predicted, but is not shown here.)

Adding Mn in the Fe-Mn-Cr-(Si) alloy decreases the dissociation oxygen partial pressure of  $(Mn,Fe)O$  and  $(Mn,Cr,Fe)_3O_4$  spinel; see Figures 2.2 and 2.4. Both  $(Mn,Cr,Fe)_3O_4$  spinel and  $(Mn,Fe)O$  are formed in the Fe-2.8Mn-0.5Cr-0.5Si steel after annealing at 950 °C in the gas mixture with the dew point of -45 °C, while only  $(Mn,Fe)_2SiO_4$  is formed in the Fe-1.8Mn-0.5Cr-0.5Si steel after annealing under the same condition. This clearly shows that increasing Mn concentration in the steel alloy promotes the formation of  $(Mn,Cr,Fe)_3O_4$  spinel and  $(Mn,Fe)O$ .

Between the dissociation oxygen partial pressure of  $(Mn,Fe)O$  and  $2.3 \times 10^{-17}$  atm. (dew point of 10 °C) at 950 °C, the effect of oxygen partial pressure has no effect on the type of oxides formed during annealing of Fe-Mn-Cr-(Si) steel alloys. For example, both  $(Mn,Fe)O$  and  $(Mn,Cr,Fe)_3O_4$  spinel were identified on Fe-1.8Mn-0.6Cr-0.5Si, Fe-1.8Mn-1.1Cr-0.5Si and Fe-2.8Mn-0.6Cr-0.5Si steels after annealing at -10 and 10 °C; see Table 2.2. It is expected that annealing the Fe-1.8Mn-0.5Cr, Fe-1.7Mn-1.5Cr, Fe-1.9Mn-1.0Cr-0.1Si, Fe-1.9Mn-1.6Cr-0.1Si and Fe-2.8Mn-0.6Cr-0.5Si steel alloys above the dissociation oxygen partial pressure of  $(Mn,Fe)O$ , results in formation of both  $(Mn,Fe)O$  and  $(Mn,Cr,Fe)_3O_4$  spinel; cf. Figures 2.2 and 2.3.

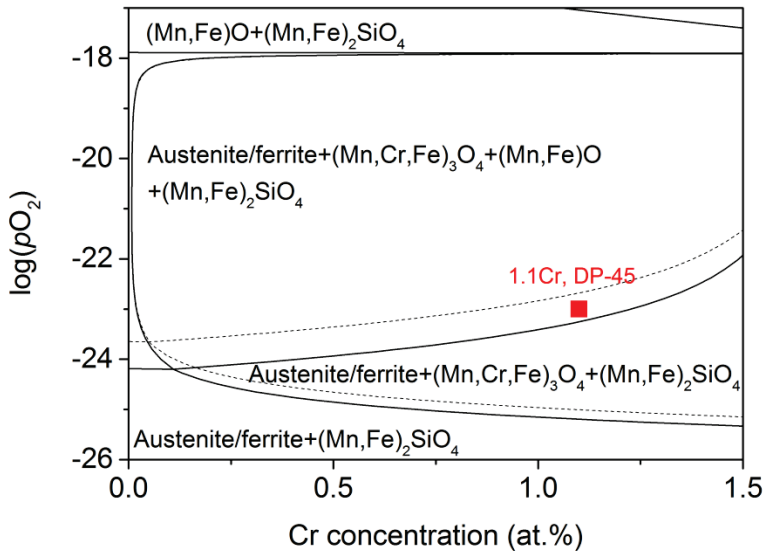


Figure 2.5: Computed phase diagram of Fe-Mn-Cr-Si alloys with bcc (ferrite) or fcc (austenite, dashed lines) crystal lattice with Mn and Si concentration fixed at 1.8 and 0.5 at.%, respectively, in an oxidizing environment at 850 °C. The square indicate the alloy with 1.1 at.% Cr oxidized at the dew point of -45 °C. (It is noted that when the alloy matrix is in austenite and the  $pO_2$  is below  $3.2 \times 10^{-26}$  atm., the formation of  $(Mn,Fe)SiO_3$  is also predicted, but is not shown here.)

The effect of the crystal lattice of the steel matrix on the equilibrium oxide phases formed in advanced high strength steels is small. Figure 2.5 shows the computed phase diagrams of the Fe-Mn-Cr-Si quaternary alloys in an oxidizing gas atmosphere at 850 °C with the concentration of Mn and Si fixed at 1.8 and 0.5 at.%, respectively. The constitution of the steel alloy matrix was fixed in either bcc or fcc phase in the computation, and thus the effect of alloy composition on the austenite-ferrite phase transformation was not considered. The dissociation oxygen partial pressure of  $(Mn,Cr,Fe)_3O_4$  spinel and  $(Mn,Fe)O$  at 850 °C in austenite is only slightly higher than in ferrite. This is due to the fact that the chemical potential of the alloying elements Mn and Cr in ferrite is higher than that in austenite. For example, according to the computation results for a Fe – 1.8 at.% Mn – 1.5 at.% Cr alloy at 850 °C, the chemical potential of Mn and Cr in ferrite are -92.0 and -73.5 kJ/mol, respectively, while the chemical potential of Mn and Cr in austenite are -97.3 and -74.5 kJ/mol, respectively. For the same crystal lattice of the steel matrix, the dissociation oxygen partial pressure of both  $(Mn,Cr,Fe)_3O_4$  spinel and  $(Mn,Fe)O$  increases with temperature; see Figures 2.5 and 2.6. The oxides identified in the Fe-1.8Mn-1.0Cr-0.5Si steel alloy after annealing at 750 °C in a gas mixture with the dew point of -45 °C are:  $(Mn,Fe)_2SiO_4$ ,  $(Mn,Cr,Fe)_3O_4$  spinel and  $(Mn,Fe)O$ . However, the oxides identified in the same steel annealed at 850 °C at the same dew point are  $(Mn,Fe)_2SiO_4$  and  $(Mn,Cr,Fe)_3O_4$

spinel. The type of identified oxide phases is in agreement with the predictions from the computed phase diagrams; see Figures 2.5 and 2.6.

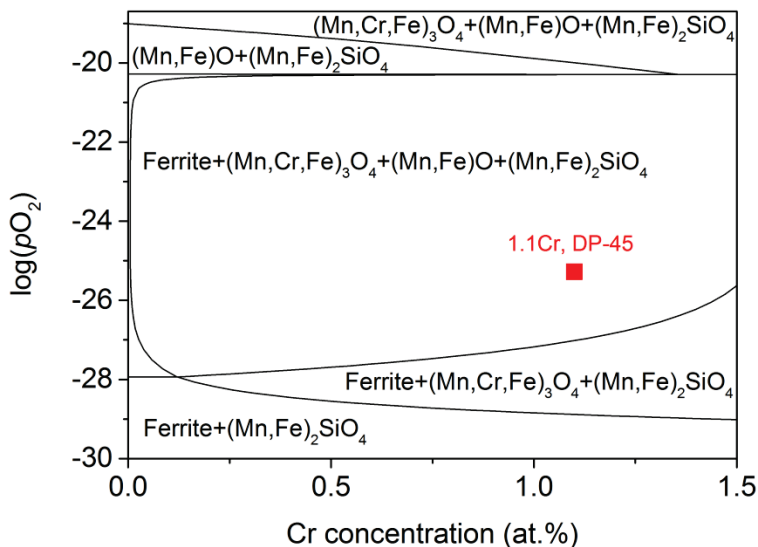


Figure 2.6: Computed phase diagram of Fe-Mn-Cr-Si alloys with bcc (ferrite) crystal lattice with Mn and Si concentration fixed at 1.8 and 0.5 at.%, respectively, in an oxidizing environment at 750 °C. The square indicate the alloy with 1.1 at.% Cr oxidized at the dew point of -45 °C.

### 2.3.2 Composition of oxide phases

The Fe concentration in the  $(\text{Mn,Cr,Fe})_3\text{O}_4$  spinel formed during oxidation of Fe-Mn-Cr steel alloys increases with ambient oxygen partial pressure. A spinel oxide can be written in the general form of  $\text{AB}_2\text{O}_4$  [19]. For  $\text{MnCr}_2\text{O}_4$  spinel, Fe cations can substitute both Mn cations at A-site and Cr cations at B-site [20]. The lattice constant of  $(\text{Mn}_{1-x}\text{Fe}_x)(\text{Cr}_{2-y}\text{Fe}_y)\text{O}_4$  spinel increases with the value of  $y$  while decreases with the value of  $x$  [20]. The amount of Fe dissolved in the  $(\text{Mn,Cr,Fe})_3\text{O}_4$  spinel (i.e. the value of  $(x+y)/3$  in  $(\text{Mn}_{1-x}\text{Fe}_x)(\text{Cr}_{2-y}\text{Fe}_y)\text{O}_4$ ) can be predicted [13, 15]. For example, the amount of Fe in  $(\text{Mn,Cr,Fe})_3\text{O}_4$  increases from 0 to 0.12 when annealing a Fe - 1.8 at.% Mn - 1.1 at.% Cr alloy at 950 °C in Ar + 5 vol.%  $\text{H}_2$  gas mixture while increasing the dew point from -45 to 10 °C; see Figure 2.7. Moreover, the calculations show that non-stoichiometry of the spinel is negligible and that the Fe dissolved in the  $(\text{Mn}_{1-x}\text{Fe}_x)(\text{Cr}_{2-y}\text{Fe}_y)\text{O}_4$  spinel mainly resides at the A-site after annealing at 950 °C with an oxygen partial pressure of  $2.3 \times 10^{-17}$  atm. (i.e. corresponding to a dew point of 10 °C in Ar + 5 vol.%  $\text{H}_2$  gas mixture). The measured stress-free lattice constant of  $(\text{Mn,Cr,Fe})_3\text{O}_4$  spinel formed in the Fe-1.9Mn-1.6Cr-0.1Si steel is  $843.1 \pm 0.2$  and  $841.3 \pm 0.1$  pm after annealing at 950 °C for 16 hours in a gas mixture of Ar + 5 vol.%  $\text{H}_2$  with dew points of -45 and 10 °C, respectively. This decrease of the lattice constant of

the  $(\text{Mn,Cr,Fe})_3\text{O}_4$  spinel with increasing annealing dew point is attributed to an increasing amount of Fe dissolved into the  $(\text{Mn,Cr,Fe})_3\text{O}_4$  spinel [20]. It is also predicted that the concentration of Fe in  $(\text{Mn,Fe})\text{O}$  formed during oxidation of Fe-Mn-Cr steel alloys increases with the dew point of the annealing ambient; see Figure 2.7.

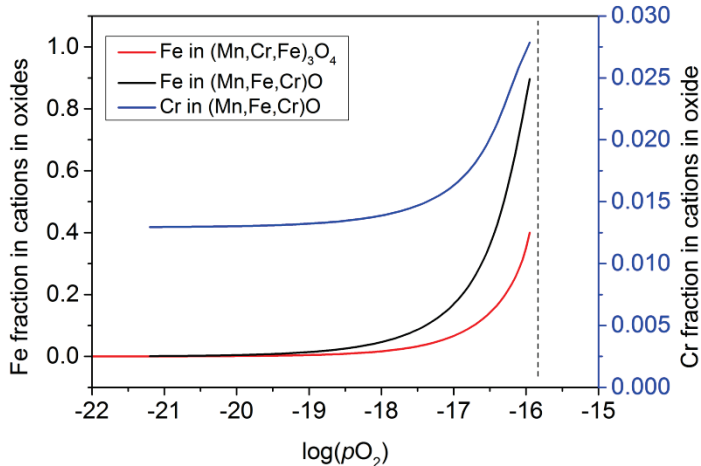


Figure 2.7: Computed composition of  $(\text{Mn,Cr,Fe})_3\text{O}_4$  spinel and  $(\text{Mn,Fe,Cr})\text{O}$  mono-oxide as a function of oxygen partial pressure (in atm.) formed in the Fe - 1.8 at.% Mn - 1.1 at.% Cr alloy at 950 °C. Dashed line indicates the dissociation oxygen partial pressure of FeO (Wüstite).

The  $(\text{Mn,Cr,Fe})_3\text{O}_4$  spinel transforms into  $(\text{Mn,Fe})_{1-x}\text{Cr}_x\text{O}$  at high oxygen partial pressures, close to the dissociation oxygen partial pressure of Wüstite; see Figures 2.2 to 2.6. For example, the  $(\text{Mn,Cr,Fe})_3\text{O}_4$  spinel starts to transform into  $(\text{Mn,Fe})_{1-x}\text{Cr}_x\text{O}$  above an oxygen partial pressure of about  $6.3 \times 10^{-17}$  atm. (dew point of 18 °C) at 950 °C for a Fe - 1.8 at.% Mn - 1.1 at.% Cr alloy; see Figure 2.8. This is because  $(\text{Mn,Fe})\text{O}$  can dissolve small amount of Cr ( $x$  below about 0.03 in  $(\text{Mn,Fe})_{1-x}\text{Cr}_x\text{O}$  at 950 °C). The value of  $x$  in  $(\text{Mn,Fe})_{1-x}\text{Cr}_x\text{O}$  increases from about 0.013 to 0.027 with increasing oxygen partial pressure from  $10^{-20}$  to  $10^{-16}$  atm. at 950 °C; see Figure 2.7. At relatively low oxygen partial pressure (say below  $10^{-17}$  atm.) the amount of  $(\text{Mn,Fe})\text{O}$  formed in the alloy is small and the oxidized Cr is mainly present as  $(\text{Mn,Cr,Fe})_3\text{O}_4$  spinel. However, with increasing oxygen partial pressure the amount of  $(\text{Mn,Fe})\text{O}$  increases due to the increasing amount of Fe in the matrix being oxidized; see Figures 2.7 and 2.8. Hence, the amount of Cr dissolved in  $(\text{Mn,Fe})\text{O}$  increases while the amount of Cr in  $(\text{Mn,Cr,Fe})_3\text{O}_4$  spinel decreases. Above oxygen partial pressure of about  $1.3 \times 10^{-16}$  atm. (dew point of 23 °C),  $(\text{Mn,Fe})_{1-x}\text{Cr}_x\text{O}$  is the only type of oxide formed.



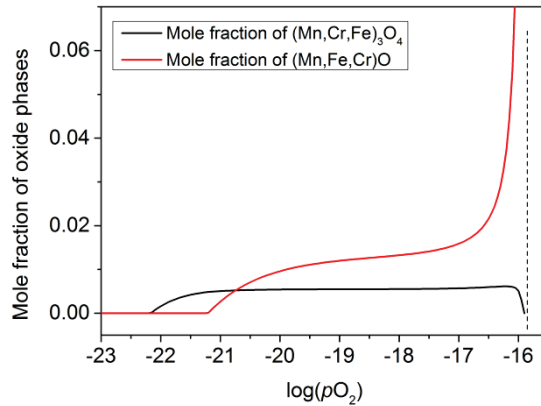


Figure 2.8: Computed mole fraction of  $(\text{Mn,Cr,Fe})_3\text{O}_4$  spinel and  $(\text{Mn,Fe,Cr})\text{O}$  monoxide as a function of oxygen partial pressure (in atm.) in the Fe - 1.8 at.% Mn - 1.1 at.% Cr alloy at 950 °C. Dashed line indicates the dissociation oxygen partial pressure of Wüstite.

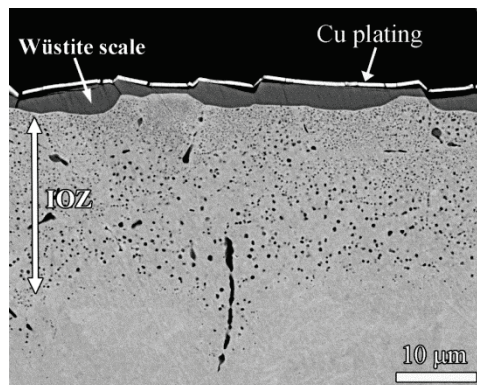


Figure 2.9: SEM backscattered electron image of cross-section of the Fe-1.9Mn-1.6Cr-0.1Si steel annealed at 950 °C for 8 hours in a gas mixture of Ar + 20 vol.%  $\text{CO}_2$  + 20 vol.% CO (oxygen partial pressure of  $8.8 \times 10^{-16}$  atm.). A Wüstite scale fully covers the steel surface after oxidation. An internal oxidation zone (IOZ) is formed beneath the Wüstite scale.

An oxide scale is formed at the surface of the Fe-1.9Mn-1.6Cr-0.1Si steel after annealing at 950 °C for 8 hours in the Ar + 20 vol.%  $\text{CO}_2$  + 20 vol.% CO gas mixture, i.e. at an oxygen partial pressure of  $8.8 \times 10^{-16}$  atm. This oxide scale fully covers the steel surface, but the scale thickness is not uniform; see Figure 2.9. An internal oxidation zone is formed underneath the oxide scale.  $(\text{Mn,Cr,Fe})_3\text{O}_4$  spinel, MnO and Wüstite were identified from the diffraction pattern obtained by XRD with Bragg-Brentano geometry. However, in the diffraction pattern recorded by XRD using the grazing incidence geometry (having a smaller analysis depth),  $(\text{Mn,Cr,Fe})_3\text{O}_4$  spinel and MnO can hardly be observed and the relative intensity of the diffraction peak of iron is significantly lower; see Figure 2.10. This

shows that the diffraction pattern recorded by XRD using the grazing incidence geometry mainly contains the information of the oxide scale at steel surface. These observations suggest that the external oxide scale is composed by Wüstite only, while the  $(\text{Mn,Cr,Fe})_3\text{O}_4$  spinel and  $(\text{Mn,Fe})\text{O}$  are formed as internal oxide precipitates. Moreover, the Cr 2p and Mn 2p lines observed with XPS suggests that both Cr and Mn are dissolved in the Wüstite. Thus the scale is composed of  $(\text{Mn,Fe})_{1-x}\text{Cr}_x\text{O}$  oxide solid solution. According to the XPS analysis the value of  $x$  in the  $(\text{Mn,Fe})_{1-x}\text{Cr}_x\text{O}$  scale is about 0.02, which is in reasonable agreement with thermodynamic prediction; see Figure 2.7.

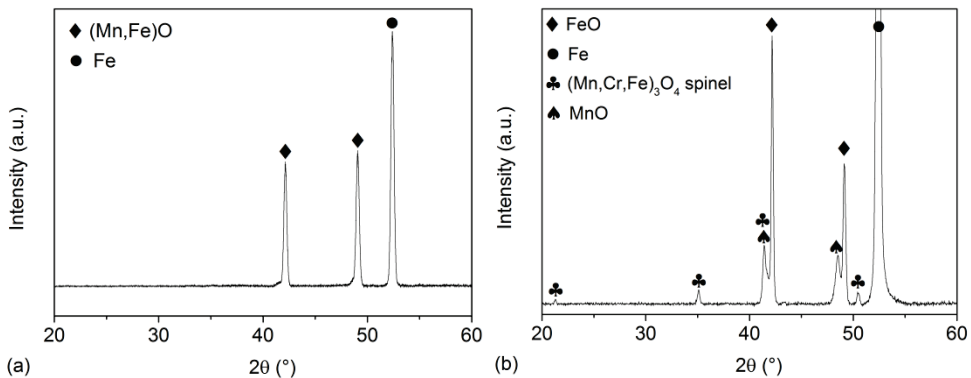


Figure 2.10: XRD patterns of the Fe-1.9Mn-1.6Cr-0.1Si steel annealed at 950  $^\circ\text{C}$  for 8 hours in a gas mixture of Ar + 20 vol.%  $\text{CO}_2$  + 20 vol.% CO (oxygen partial pressure of  $8.8 \times 10^{-16}$  atm.; cf. Figure 2.9); measured with (a) grazing incidence geometry and (b) Bragg-Brentano geometry.

The establishment of local thermodynamic equilibrium between oxide precipitates and dissolved oxygen in alloy matrix upon internal oxidation of Fe-Mn binary steel alloys has been reported [18]. For Fe-Mn-Cr-(Si) steel alloys, the agreement between the computed phase diagrams and the experimentally identified oxide species formed during annealing at different temperatures and oxygen partial pressure indicates that (local) thermodynamic equilibrium between the gas ambient and the steel surface was established. Finally, the thermodynamic data used allowed prediction of the oxide formed in advanced high strength steels having a complex composition and microstructure.

### 2.3.3 Internal and external oxides

The oxidation mode of Fe-Mn-Cr steel alloys annealed at 950  $^\circ\text{C}$  in a gas mixture of Ar or  $\text{N}_2 + 5$  vol.%  $\text{H}_2$  changes from external to internal oxidation with increasing dew point from  $-45$  to 10  $^\circ\text{C}$ , which is similar as for Fe-Mn steels [5]. For example, when annealing the Fe-1.9Mn-1.6Cr-0.1Si steel in an Ar + 5 vol.%  $\text{H}_2$  gas mixture with the dew point of  $-45$   $^\circ\text{C}$  the oxides are formed mainly at the sample surface; see Figure 2.11. Increasing the dew point

of the annealing gas mixture to 10 °C, an internal oxidation zone is observed below the Fe-1.9Mn-1.6Cr-0.1Si steel surface. According to XMA and thermodynamic computations, the internal oxide precipitates should be composed of (Mn,Fe)O and (Mn,Cr,Fe)<sub>3</sub>O<sub>4</sub> spinel. Adding Si to the Fe-Mn-Cr steel promotes formation of (Mn,Fe)<sub>2</sub>SiO<sub>4</sub> along original austenite grain boundaries; see Figure 2.12. However, (Mn,Fe)<sub>2</sub>SiO<sub>4</sub> also forms inside grains, and an individual precipitate can be composed by more than one type of oxide species; see Figure 2.13.

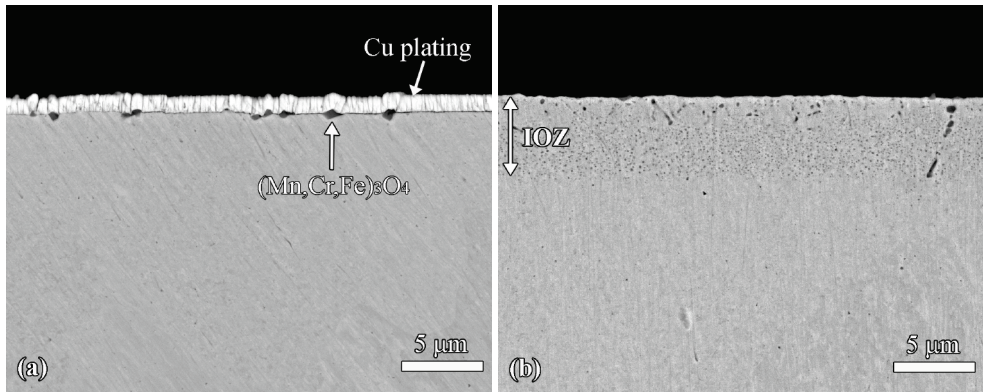


Figure 2.11: SEM backscattered electron images of cross-section of the Fe-1.9Mn-1.6Cr-0.1Si steel annealed for 1 hour at 950 °C in a gas mixture of Ar or N<sub>2</sub> with 5 vol.% H<sub>2</sub> and dew points of (a) -45 °C and (b) 10 °C (oxygen partial pressure of  $8.1 \times 10^{-22}$  and  $2.3 \times 10^{-17}$  atm., respectively). At the dew point of -45 °C (Mn,Cr,Fe)<sub>3</sub>O<sub>4</sub> is formed and at the dew point of 10 °C both (Mn,Cr,Fe)<sub>3</sub>O<sub>4</sub> and (Mn,Fe)O are formed.

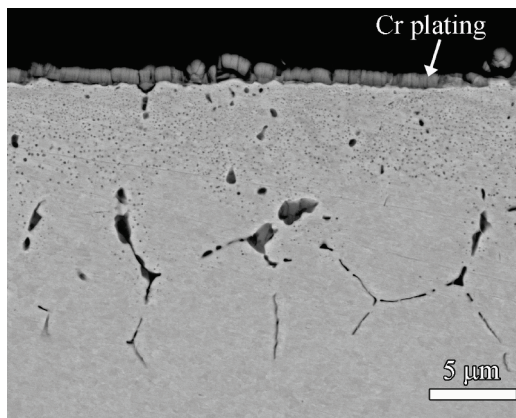


Figure 2.12: SEM backscattered electron image of cross-section of the Fe-1.8Mn-1.1Cr-0.5Si steel annealed for 1 hour at 950 °C in a gas mixture of N<sub>2</sub> + 5 vol.% H<sub>2</sub> at the dew point of 10 °C (oxygen partial pressure of  $2.3 \times 10^{-17}$  atm.). (Mn,Cr,Fe)<sub>3</sub>O<sub>4</sub> and (Mn,Fe)O are formed and (Mn,Fe)<sub>2</sub>SiO<sub>4</sub> along the grain boundaries.

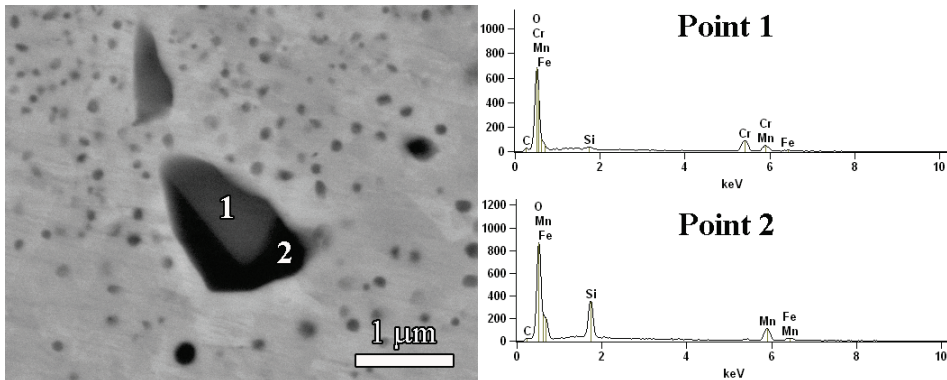


Figure 2.13: Backscattered electron image of cross-section of the Fe-1.8Mn-1.1Cr-0.5Si steel annealed for 1 hour at 950 °C in a gas mixture of N<sub>2</sub> + 5 vol.% H<sub>2</sub> at the dew point of 10 °C (oxygen partial pressure of  $2.3 \times 10^{-17}$  atm.), and spectrums of characteristic X-rays measured with XMA analysis on two different location on an oxide precipitate. Oxide precipitates in Fe-Mn-Cr-Si quaternary steel alloys may consist of both (Mn,Cr,Fe)<sub>3</sub>O<sub>4</sub> spinel and (Mn,Fe)<sub>2</sub>SiO<sub>4</sub>.

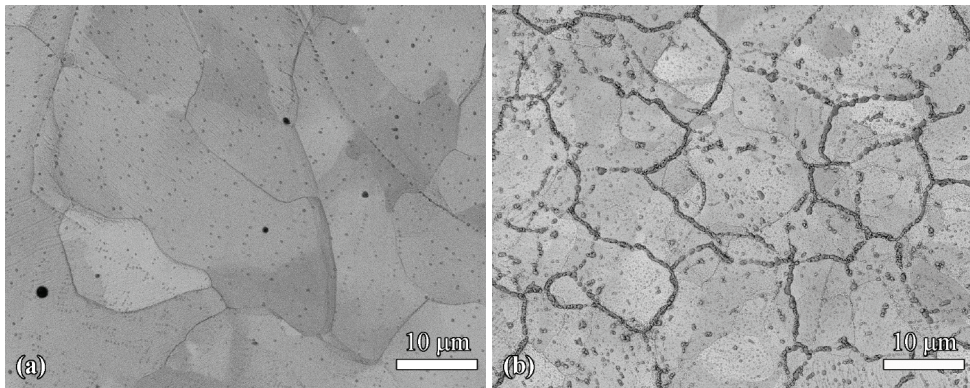


Figure 2.14: SEM backscattered electron images of surface of (a) Fe-1.7Mn and (b) Fe-1.9Mn-1.6Cr-0.1Si steel annealed for 1 hour at 950 °C in a mixture of Ar + 5 vol.% H<sub>2</sub> gases at the dew point of -45 °C (oxygen partial pressure of  $8.1 \times 10^{-22}$  atm.). Cr promotes formation of (Mn,Cr,Fe)<sub>3</sub>O<sub>4</sub> along the grain boundaries at the surface.

Adding Cr to a Fe-Mn binary steel alloy increases the amount of oxides formed at the steel surface; see e.g. Figure 2.14. Oxides at the surface of the Fe-1.9Mn-1.6Cr-0.1Si steel are formed both along grain boundaries and inside grains during annealing; see Figure 2.14. According to the results of XMA, XRD and thermodynamic computations, the oxides at the surface of the Fe-1.9Mn-1.6Cr-0.1Si steel (along grain boundaries and inside grains) annealed at dew point -45 °C are composed by (Mn,Cr,Fe)<sub>3</sub>O<sub>4</sub> spinel. A small amount of (Mn,Fe)<sub>2</sub>SiO<sub>4</sub> is also formed along grain boundaries at the surface of the Fe-1.9Mn-1.6Cr-



0.1Si steel as confirmed with XMA. The tendency of oxides formation along grain boundaries at the Fe-1.9Mn-1.6Cr-0.1Si steel surface decreases with dew point; see Figure 2.14 and 2.15.

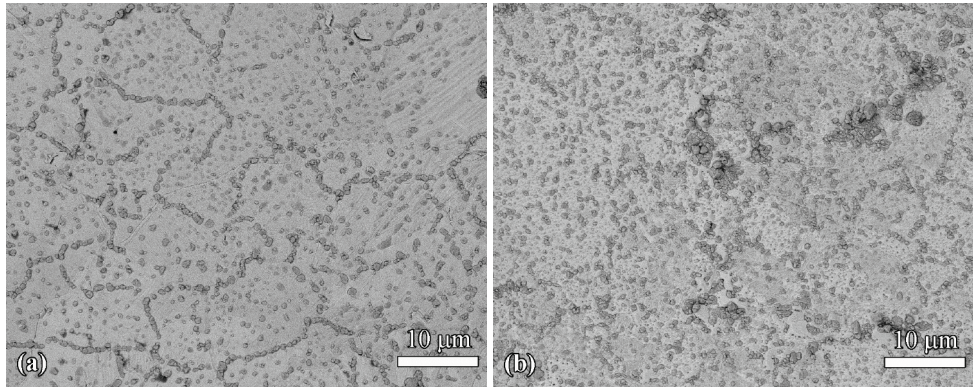


Figure 2.15: SEM backscattered electron images of surface of (a) Fe-1.7Mn and (b) Fe-1.9Mn-1.6Cr-0.1Si steels annealed for 1 hour at 950 °C in a gas mixture of Ar + 5 vol.% H<sub>2</sub> at dew point of 10 °C (oxygen partial pressure of  $2.3 \times 10^{-17}$  atm.).

## 2.4 Conclusions

The oxide species formed during annealing of advanced high strength steel can be well predicted by thermodynamic computation, since (local) thermodynamic equilibrium is established between the annealing gas ambient and the steel surface. Adding Cr to the Fe-Mn based steel alloys results in the formation of (Mn,Cr,Fe)<sub>3</sub>O<sub>4</sub> spinel during annealing. The dissociation oxygen partial pressure of (Mn,Cr,Fe)<sub>3</sub>O<sub>4</sub> spinel is lower than that of (Mn,Fe)O. Increasing the Mn concentration in the alloy promotes the formation of (Mn,Cr,Fe)<sub>3</sub>O<sub>4</sub> spinel and (Mn,Fe)O, which is associated with a decreasing dissociation oxygen partial pressures. The Si in the Fe-Mn-Cr steel alloys leads to the formation of (Mn,Fe)<sub>2</sub>SiO<sub>4</sub> both along grain boundaries and inside grains during annealing. Increasing the Si concentration in the Fe-Mn-Cr steel alloy suppresses the formation of (Mn,Cr,Fe)<sub>3</sub>O<sub>4</sub> spinel and (Mn,Fe)O. However, the formation of (Mn,Fe)<sub>2</sub>SiO<sub>4</sub> can be mitigated by increasing the Mn concentration in the steel alloy. The amount of Fe dissolved in (Mn,Cr,Fe)<sub>3</sub>O<sub>4</sub> spinel formed in Fe-Mn-Cr steels increases with annealing dew point. (Mn,Fe)O can dissolve only a small amount of Cr. Adding Cr to the Fe-Mn steel has no effect on the transition from external to internal oxidation, but increases the amount of oxides formed at steel surface during annealing.

---

**References**

- [1] N. Fonstein, *Advanced High Strength Sheet Steels*, Springer International Publishing, Switzerland, 2015.
- [2] A. R. Marder, *Progress in Materials Science*, **45** (2000), 191.
- [3] G. M. Song, T. Vystavel, N. van der Pers, J. T. M. De Hosson, and W. G. Sloof, *Acta Materialia*, **60** (2012), 2973.
- [4] E. M. Bellhouse and J. R. McDermid, *Metallurgical and Materials Transactions A*, **42** (2011), 2753.
- [5] V. A. Lashgari, C. Kwakernaak, and W. G. Sloof, *Oxidation of Metals*, **81** (2014), 435.
- [6] V. A. Lashgari, G. Zimbitas, C. Kwakernaak, and W. G. Sloof, *Oxidation of Metals*, **82** (2014), 249.
- [7] Y. Suzuki, T. Yamashita, Y. Sugimoto, S. Fujita, and S. Yamaguchi, *ISIJ International*, **49** (2009), 564.
- [8] L. Cho, G. S. Jung, and B. C. De Cooman, *Metallurgical and Materials Transactions A*, **45** (2014), 5158.
- [9] Y. F. Gong, H. S. Kim, and B. C. De Cooman, *ISIJ International*, **49** (2009), 557.
- [10] S. Swaminathan and M. Spiegel, *Surface and Interface Analysis*, **40** (2008), 268.
- [11] S. Swaminathan and M. Spiegel, *Applied Surface Science*, **253** (2007), 4607.
- [12] B. D. Cullity and S. R. Stock, *Elements of X-ray Diffraction*, 3rd ed, Prentice Hall, New York, 2001.
- [13] C. Bale, P. Chartrand, S. A. Degterov, G. Eriksson, K. Hack, R. Ben Mahfoud, J. Melancon, A. D. Pelton, and S. Petersen, *Calphad*, **26** (2002), 189.
- [14] Y. F. Gong and B. C. De Cooman, *Steel Research International*, **82** (2011), 1310.
- [15] Factsage Database Documentation,  
<http://www.crct.polymtl.ca/fact/documentation/>.
- [16] P. Franke and R. Dieckmann, *Journal of Physics and Chemistry of Solids*, **51** (1990), 49.
- [17] V. A. Lashgari, *Internal and External Oxidation of Manganese in Advanced High Strength Steels*, Ph.D. thesis, Delft University of Technology, 2014.
- [18] W. Mao and W. G. Sloof, *Scripta Materialia*, **135** (2017), 29.
- [19] K. E. Sickafus, J. M. Wills, and N. W. Grimes, *Journal of the American Ceramic Society*, **82** (1999), 3279,.
- [20] N. Sakai, T. Horita, Y. P. Xiong, K. Yamaji, H. Kishimoto, M. E. Brito, H. Yokokawa, T. Maruyama, *Solid State Ionics*, **176** (2005), 681.
- [21] D. Huin, P. Flauder, and J. B. Leblond, *Oxidation of Metals*, **64** (2005), 131.



## Chapter 3

# Effect of solute interaction on the solubility product of internal precipitates of carbon, nitrogen and oxygen in iron alloys

### Abstract

In a non-ideal alloy, the compositional dependence of the solubility product of internal oxides can be quantified with the so-called interaction parameters, which are defined according to the Wagner formalism. A generic approach based on the macroscopic atom model is developed in order to calculate the interaction parameters for any element in an alloy. In this study, the interaction parameters pertaining to carbon and nitrogen in iron alloys were estimated and compared with either experimental or computed results from thermodynamic tools. The reasonable to good agreement is promising for estimating unknown interaction parameters of alloying elements for oxygen in iron alloys. The effect of alloying element on solubility product of  $\text{Al}_2\text{O}_3$  in iron alloys is demonstrated.

### Keywords

Solubility product, Interaction parameter, Non-ideal solution, Macroscopic atom model



### 3.1 Introduction

Precipitation of compounds (e.g. oxide, nitride and carbide) of reactive solute metals in an alloy may occur during annealing at high temperature in a gas phase environment containing oxygen, nitrogen and carbon. These precipitates influence to a large extent the final properties of the alloy. For example, formation of these precipitates may increase the number of crack initiation sites and deplete the strengthening alloying elements in the alloy matrix, thereby leading to embrittlement of surface layer and deterioration of the strength and creep resistance of materials [1]. On the other hand, precipitation hardening can be obtained when the precipitates are finely distributed in the alloy matrix; see e.g. refs [2, 3]. Therefore, predicting the kinetics of internal precipitation process during annealing is important for monitoring the material degradation and controlling the final properties of materials.

A numerical finite-difference model has been developed to simulate the internal oxidation behaviour of Fe-Mn binary steel alloys [4, 5]. This model was extended to simulate the internal oxidation of multi-element alloyed steels [4, 6]. In the model, the local precipitation of internal oxides is governed by the solubility product. The solubility product of internal oxides was taken as a constant for simulating the isothermal oxidation of steel alloys [4-6], assuming that the iron alloy is an ideal solution or a solution that strictly obeys Henry's law (i.e. activity coefficient of each solute species is constant). The effect of non-ideal behaviour of iron alloys, i.e. the variation of solubility product of oxide precipitates with alloy composition, has not yet been investigated and may influence the internal oxidation behaviour of steel alloys.

To date, no experimental data are available for composition dependence of the solubility product of oxide precipitates in iron alloys. In principle, the solubility product of a precipitate in a non-ideal alloy as a function of alloy composition can be obtained either by thermodynamic computation based on the Calphad formalism [7], or with ab initio calculations [8]. However, to the authors' knowledge, the thermodynamic data for ternary Fe-O-M solid solution have not been well assessed yet in the available thermodynamic databases [9, 10]. Hence, reliable computation results cannot be obtained for the composition dependence of the solubility product of oxides in non-ideal steel alloys. Moreover, evaluation of the solubility product of oxides in steels with ab initio calculations has not been reported.

The aim of this study is to evaluate quantitatively the influence of alloy composition on the solubility product of internal oxides in steel alloys in the absence of any experimental data.

First, the thermodynamics of oxide precipitation in alloys is presented. The change in the solubility product due to the non-ideal behaviour of solution is quantified by interaction parameters which are defined according to the Wagner formalism [11]. Next, a generic method based on a macroscopic atom model [12] is proposed in order to compute the interaction parameters pertaining to oxygen in iron alloys. The validity of the approach is confirmed by studying the interaction parameters pertaining to nitrogen and carbon for iron alloys for which reliable experimental data or thermodynamic data are known. Finally, the interaction parameters for oxygen in iron alloys are predicted, and the effect of adding alloying elements on solubility product of oxides is estimated.

### 3.2 Solubility product of oxides in non-ideal solution

Oxidation of a pure metal B as  $\alpha$  phase at a constant temperature and pressure proceeds according to:



The standard free energy change of this reaction,  $\Delta G_{B_nO_\nu}^0$ , equals:

$$\Delta G_{B_nO_\nu}^0 = G_{B_nO_\nu}^0 - nG_B^{0,\alpha} - \frac{\nu}{2}G_{O_2}^0 \quad (3.2)$$

where  $G_{B_nO_\nu}^0$ ,  $G_B^{0,\alpha}$  and  $G_{O_2}^0$  are the molar free energies of the species in their standard states. Usually, the  $\Delta G_{B_nO_\nu}^0$  is a linear function of temperature [13] and its value can be obtained from thermodynamic database for pure substance; see e.g. ref. [14].

When B is a solute element in a multi-component alloy A-B-M (A represents solvent and more noble than B, and M does not participate in any reaction) with  $\beta$  phase, formation of internal precipitate  $B_nO_\nu$  in the alloy proceeds according to:



in which the underscore indicates the element as solid solute. The driving force for reaction (3.3) to occur, is the change in Gibbs free energy,  $\Delta G_{B_nO_\nu}$ , which equals:

$$\Delta G_{B_nO_\nu} = \mu_{B_nO_\nu} - n\mu_B^\beta - \nu\mu_O^\beta \quad (3.4)$$

in which  $\mu_{B_nO_\nu}$ ,  $\mu_B^\beta$  and  $\mu_O^\beta$  are chemical potential of the oxide precipitate, solute elements B and O in the alloy, respectively. Here, the following three equations hold:

$$\begin{aligned}
 \mu_{B_nO_v} &= G_{B_nO_v}^0 + RT \ln a_{B_nO_v} \\
 \mu_B^\beta &= G_B^{0,\beta} + RT \ln a_B^\beta \\
 \mu_O^\beta &= G_O^0 + RT \ln a_O
 \end{aligned} \tag{3.5}$$

in which  $a_{B_nO_v}$ ,  $a_B^\beta$  and  $a_O$  are activities of the oxide precipitate, solute elements B and O in the alloy, respectively, with respect to the chosen standard state.  $G_B^{0,\beta}$  is the molar free energy of pure element B in  $\beta$  phase and  $G_O^0$  is the molar free energy of oxygen at a chosen standard state. Since the choice of standard state for a component in a solution is arbitrary, but for convenience the pure oxygen gas at atmospheric pressure is chosen as the standard state for solute oxygen in the alloy, i.e.  $G_O^0 = 1/2 G_{O_2}^0$ , and the activity of solute O can be expressed in terms of oxygen partial pressure  $p_{O_2}$  in atm., i.e.  $a_O = (p_{O_2})^{1/2}$ . Then, the chemical potential of solute oxygen can be expressed as:

$$\mu_O^\beta = \frac{1}{2} G_{O_2}^0 + \frac{1}{2} RT \ln p_{O_2} \tag{3.6}$$

Substituting the chemical potentials in Eq. (3.4) with Eqs (3.5) and (3.6) obtains:

$$\Delta G_{B_nO_v} = G_{B_nO_v}^0 - nG_B^{0,\beta} - \frac{v}{2} G_{O_2}^0 + RT \ln \frac{a_{B_nO_v}}{(a_B^\beta)^n (p_{O_2})^{v/2}} \tag{3.7}$$

At equilibrium,  $\Delta G_{B_nO_v}$  is zero, and hence:

$$G_{B_nO_v}^0 - nG_B^{0,\beta} - \frac{v}{2} G_{O_2}^0 = -RT \ln \frac{a_{B_nO_v}}{(a_B^\beta)^n (p_{O_2})^{v/2}} \tag{3.8}$$

Combining Eq. (3.2) and rewriting Eq. (3.8) gives:

$$\frac{a_{B_nO_v}}{(a_B^\beta)^n (p_{O_2})^{v/2}} = \exp \left[ -\frac{\Delta G_{B_nO_v}^0 + n(G_B^{0,\alpha} - G_B^{0,\beta})}{RT} \right] \tag{3.9}$$

When  $B_nO_v$  is a pure stoichiometric compound,  $a_{B_nO_v}$  is unity. The activity of element B in the alloy is related to its concentration through:

$$a_B^\beta = \gamma_B^\beta N_B \tag{3.10}$$

in which  $N_B$  is the mole fraction of element B in the alloy, and  $\gamma_B^\beta$  is the activity coefficient with respect to the selected standard state (i.e. pure metal B in  $\beta$  phase). The mole fraction of solute O ( $N_O$ ) in the alloy is related to oxygen partial pressure according to:

$$\gamma_O N_O = (p_{O_2})^{1/2} \tag{3.11}$$

Yet, substituting with Eqs (3.10) and (3.11) in Eq. (3.9) results in:

$$\frac{1}{(\gamma_B^\beta N_B)^n (\gamma_O N_O)^v} = \exp \left[ -\frac{\Delta G_{B_n O_v}^0 + n(G_B^{0,\alpha} - G_B^{0,\beta})}{RT} \right] \quad (3.12)$$

Usually, the solubility product of  $B_n O_v$  is defined as:

$$K_{sp(B_n O_v)} = (N_B)^n (N_O)^v \quad (3.13)$$

Therefore, rewriting Eq. (3.12) obtains:

$$K_{sp(B_n O_v)} = \frac{1}{(\gamma_B^\beta)^n (\gamma_O)^v} \exp \left[ \frac{\Delta G_{B_n O_v}^0 + n(G_B^{0,\alpha} - G_B^{0,\beta})}{RT} \right] \quad (3.14)$$

The exponential term on the right-hand side of Eq. (3.14) is a constant at a certain temperature, independent of alloy composition. Usually, the solubility product is considered as a constant at a certain temperature, implying that the solution is ideal or obeys Henry's law, i.e. both the activity coefficient  $\gamma_B^\beta$  and  $\gamma_O$  are constant. However, in reality both  $\gamma_B^\beta$  and  $\gamma_O$  may be a function of alloy composition. Thus, the effect of non-ideal behaviour of a solution on the solubility product of  $B_n O_v$  lies in the composition dependence of the activity coefficients  $\gamma_B^\beta$  and  $\gamma_O$ .

For a dilute solution, the activity coefficient of solute elements B and O can be expressed as a function of alloy composition according to the Wagner formalism [11], namely:

$$\ln \gamma_B^\beta = \ln \gamma_B^{0,\beta} + \varepsilon_B^B N_B + \varepsilon_B^M N_M + \varepsilon_B^O N_O \quad (3.15)$$

and

$$\ln \gamma_O = \ln \gamma_O^0 + \varepsilon_O^O N_O + \varepsilon_O^B N_B + \varepsilon_O^M N_M \quad (3.16)$$

in which  $\varepsilon_i^j$  and  $\varepsilon_i^i$  are the first-order interaction parameters. By definition,  $\varepsilon_j^i$  equals  $\varepsilon_i^j$ .  $\gamma_B^{0,\beta}$  and  $\gamma_O^0$  are the activity coefficient of solute B and O at infinite dilution, respectively.

When the concentration of O in the alloy is very small (say below  $10^{-4}$ ), the  $\varepsilon_B^O N_O$  and  $\varepsilon_O^O N_O$  term can be neglected. Then, Eqs (3.15) and (3.16) can be reduced to:

$$\ln \gamma_B^\beta = \ln \gamma_B^{0,\beta} + \varepsilon_B^B N_B + \varepsilon_B^M N_M \quad (3.17)$$

and

$$\ln \gamma_O = \ln \gamma_O^0 + \varepsilon_O^B N_B + \varepsilon_O^M N_M \quad (3.18)$$

Hence, the effect of solute interaction on the solubility product of  $B_n O_v$  is expressed by the interaction parameters  $\varepsilon_B^M$  and  $\varepsilon_O^M$ .

In order to quantify the effect of alloying element M on the solubility product of  $B_n O_v$ , the parameter  $\alpha$  is introduced as the ratio between the solubility product of  $B_n O_v$  with and

without the presence of alloying element M. Combining Eqs (3.14), (3.17) and (3.18) it is obtained that:

$$\alpha = \frac{K_{sp(B_nO_v)A-B-M}}{K_{sp(B_nO_v)A-B}} = \exp[-(n\varepsilon_B^M + v\varepsilon_O^M)N_M] \quad (3.19)$$

Thus, if  $\alpha$  equals to 1, the element M does not influence the solubility product of  $B_nO_v$ . When  $\alpha < 1$ , adding M to the alloy reduces the solubility product of  $B_nO_v$ , i.e. enhances precipitation of  $B_nO_v$  in the alloy. When  $\alpha > 1$ , the addition of M increases the solubility product of  $B_nO_v$ , i.e. suppresses the precipitation of  $B_nO_v$ .

### 3.3 Estimation of interaction parameters

The interaction parameters  $\varepsilon_j^i$  ( $i \neq j$ ) for any alloy are estimated using a quasi-chemical description of alloys coupled with the macroscopic atom model [12]. Consider a binary regular solution A-B as an example, the enthalpy of mixing equals [15]:

$$\Delta H_{mix} = L_{AB}N_B(1 - N_B) \quad (3.20)$$

in which  $L_{AB}$  is a constant, independent of temperature and alloy composition. According to the quasi-chemical model [16] it holds that:

$$L_{AB} = N^A Z \omega_{AB} \quad (3.21)$$

and

$$\omega_{AB} = u_{AB} - \frac{u_{AA} + u_{BB}}{2} \quad (3.22)$$

where  $N^A$  is Avogadro's number,  $Z$  is the coordination number of solvent A.  $u_{AB}$ ,  $u_{AA}$  and  $u_{BB}$  are the bond energy of the A-B, A-A and B-B atom pairs, respectively. The activity coefficient of solute B at infinite dilution equals [17]:

$$\ln \gamma_B^0 = \frac{L_{AB}}{RT} = \frac{N^A Z \omega_{AB}}{RT} \quad (3.23)$$

When an element M is added and form an A-B-M ternary regular solution, the activity coefficient of B can be expressed as [17]:

$$\ln \gamma_B = N_A(N_A + N_M) \frac{L_{AB}}{RT} + N_M(N_M + N_A) \frac{L_{MB}}{RT} - N_M N_A \frac{L_{AM}}{RT} \quad (3.24)$$

The constants  $L_{MB}$  and  $L_{AM}$  are, according to Eq. (3.20), related to the enthalpy of mixing for binary regular solution M-B and A-M, respectively. Note that the sum of  $N_A$ ,  $N_B$  and  $N_M$  equals one. In the regular solution model it is assumed that the bond energy of a certain atom pair in a binary solution is the same as that in a ternary solution [17]. Neglecting the

second-order terms in Eq. (3.24), the following relation is obtained (cf. Eqs (3.15) and (3.24)) [17]:

$$\varepsilon_B^M = \frac{L_{MB} - L_{AB} - L_{AM}}{RT} \quad (3.25)$$

To take configurational excess entropy into account, Eq. (3.25) should be modified. This entropy arises from the non-random distribution of atoms due to the difference in the bond energies between different atomic pairs. However, the vibrational excess entropy and also any magnetic contribution to the Gibbs free energy of solution is not considered here. Lupis and Elliott (L&E) [18] proposed for a multi-element system that the first-order interaction parameter in the Wagner formalism can be expressed as:

$$\varepsilon_i^j = Z \left[ 1 - \exp\left(\frac{\omega_{Ai} + \omega_{Aj} - \omega_{ij}}{kT}\right) \right] \quad (3.26)$$

where  $\omega$  is related to the bond energies of appropriate atomic pairs (cf. Eq. (3.22)), and  $k$  is the Boltzmann constant. The coordination number  $Z$  is taken as 12 and 8 for solid FCC and BCC crystal lattice, respectively, and 10 for liquid [18]. Thus, for A-B-M ternary solution  $\varepsilon_B^M$  equals (cf. Eq. (3.21)):

$$\varepsilon_B^M = Z \left[ 1 - \exp\left(\frac{L_{AB} + L_{AM} - L_{MB}}{RTZ}\right) \right] \quad (3.27)$$

Both Eqs (3.25) and (3.27) holds for substitutional solutions. But if the solute element B occupies interstitial sites, Wagner [19] proposed that the activity coefficient of solute element B in the A-B-M ternary alloy,  $\gamma_B^0$ , can be predicted according to:

$$\gamma_B^0 = \left[ \frac{1 - N_M}{(\gamma_{B(A)}^0)^{1/Z}} + \frac{N_M}{(\gamma_{B(M)}^0)^{1/Z}} \right]^{-Z} \quad (3.28)$$

where  $\gamma_{B(A)}^0$  and  $\gamma_{B(M)}^0$  denote the activity coefficient of solute B in A-B and M-B binary solutions, respectively, at infinite dilution. Here,  $Z$  is the coordination number of the interstitial B atom. When the solute B is at octahedral interstitial sites,  $Z$  equals 6. From Eq. (3.28), the interaction parameter  $\varepsilon_B^M$  is obtained:

$$\varepsilon_B^M = \left. \frac{\partial \ln \gamma_B}{\partial N_M} \right|_{N_M=0} = Z \left[ 1 - \left( \frac{\gamma_{B(A)}^0}{\gamma_{B(M)}^0} \right)^{1/Z} \right] \quad (3.29)$$

Substituting  $\gamma_{B(A)}^0$  and  $\gamma_{B(M)}^0$  respectively with  $\exp(L_{AB}/RT)$  and  $\exp(L_{MB}/RT)$  (cf. Eq. (3.23)) it follows that:

$$\varepsilon_B^M = Z \left[ 1 - \exp\left(\frac{L_{AB} - L_{MB}}{ZRT}\right) \right] \quad (3.30)$$

Comparing Eq. (3.30) with Eq. (3.27), the difference is the  $L_{AM}$  term. This is because the dissolution of B in the interstitial sites of A-M alloy does not break the bonds between the substitutional A and M atoms.

It can be conceived that  $L_{AB}$ ,  $L_{AM}$  and  $L_{MB}$  are equivalent to the molar solution enthalpies of B in A, M in A and B in M, since it holds for a solute i in an infinite solvent j:

$$\Delta \overline{H}_{i \text{ in } j} = \left. \frac{d(\Delta H_{mix})}{dN_i} \right|_{N_i=0} = L_{ji} \quad (3.31)$$

Thus:

$$\begin{aligned} L_{AB} &= \Delta \overline{H}_{B \text{ in } A} \\ L_{AM} &= \Delta \overline{H}_{M \text{ in } A} \\ L_{MB} &= \Delta \overline{H}_{B \text{ in } M} \end{aligned} \quad (3.32)$$

The solution enthalpies are given by [20]:

$$\begin{aligned} \Delta \overline{H}_{B \text{ in } A} &= \Delta \overline{H}_{B \text{ in } A}^{\text{chemical}} + \Delta \overline{H}_{B \text{ in } A}^{\text{elastic}} + \Delta \overline{H}_{B \text{ in } A}^{\text{structural}} \\ \Delta \overline{H}_{M \text{ in } A} &= \Delta \overline{H}_{M \text{ in } A}^{\text{chemical}} + \Delta \overline{H}_{M \text{ in } A}^{\text{elastic}} + \Delta \overline{H}_{M \text{ in } A}^{\text{structural}} \\ \Delta \overline{H}_{B \text{ in } M} &= \Delta \overline{H}_{B \text{ in } M}^{\text{chemical}} + \Delta \overline{H}_{B \text{ in } M}^{\text{elastic}} + \Delta \overline{H}_{B \text{ in } M}^{\text{structural}} \end{aligned} \quad (3.33)$$

where  $\Delta \overline{H}_{i \text{ in } j}^{\text{chemical}}$ ,  $\Delta \overline{H}_{i \text{ in } j}^{\text{elastic}}$  and  $\Delta \overline{H}_{i \text{ in } j}^{\text{structural}}$  are the chemical, elastic and structural contributions, respectively. The chemical contribution to the solution enthalpy of i in j for an amorphous solution can be estimated with the macroscopic atom model [12]. In this study the chemical contribution to the solution enthalpy of i in j for an amorphous solution is considered to be the same as that for a solid solution, and thus the structural contribution does not play a role. The elastic contribution to the solution enthalpy of i in j is not taken into account.

### 3.4 Results and discussion

Since the thermodynamic data for dissolution of nitrogen and carbon in iron alloys are well established, our approach for calculation of the interaction parameters is first tested for nitrogen and carbon in iron alloys.

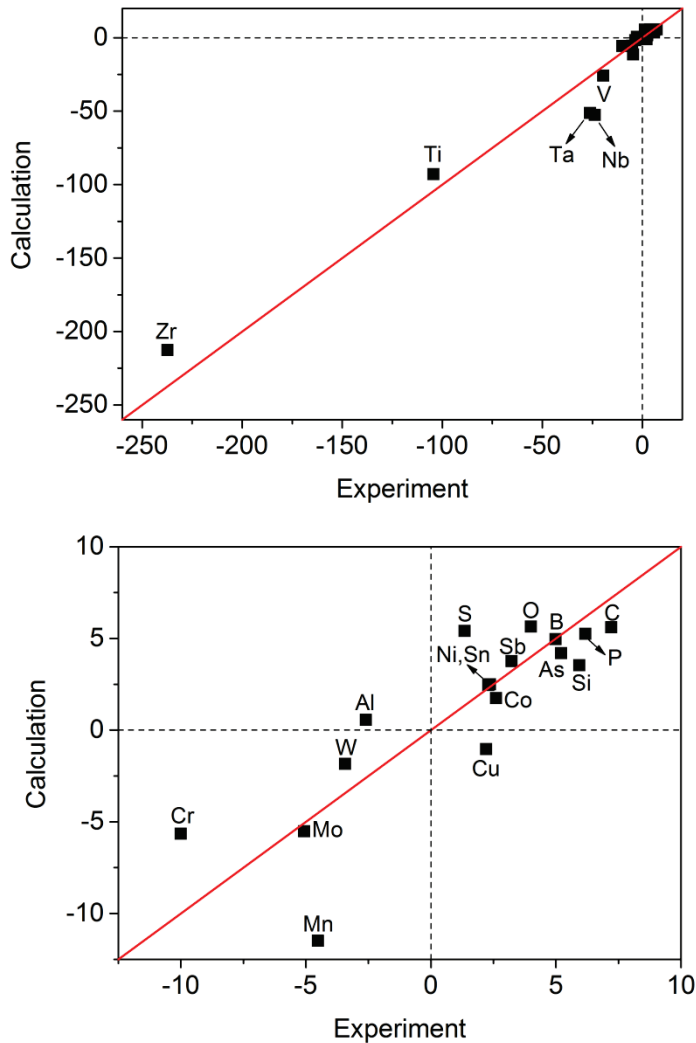


Figure 3.1: Comparison between measured [21] and calculated interaction parameter of alloying element M for nitrogen ( $\varepsilon_N^M$ ) in liquid Fe at 1600 °C. The interaction parameter was calculated with the macroscopic atom model in conjunction the Wagner model.

The interaction parameters for alloying elements M on the dissolution of nitrogen ( $\varepsilon_N^M$ ) in liquid iron alloys at 1600 °C calculated with the macroscopic atom model in conjunction with the Wagner or L&E model are compared with the experimental data summarized in ref. [21]; see Figures 3.1 and 3.2. The predicted sign of the interaction parameter  $\varepsilon_N^M$  with the Wagner model, i.e. the increase or decrease in nitrogen chemical potential due to addition of element M, is the same as the experimental observation except for Al and Cu.



The absolute values of the interaction parameters  $\varepsilon_N^M$  predicted with the Wagner model for liquid iron alloys is in general in better agreement with the experimental results than those calculated with the L&E model. The absolute values of the interaction parameters  $\varepsilon_N^{Zr}$  and  $\varepsilon_N^{Ti}$  predicted with the L&E model is almost an order of magnitude lower than the experimental results. Apparently, dissolution of nitrogen does not significantly influence the bonding between iron and solute Ti and Zr. For other elements, the difference between the  $\varepsilon_N^M$  predicted with Wagner and L&E model is relatively small. The agreement between the predicted and measured interaction parameters  $\varepsilon_N^M$  suggests that the solution enthalpies of nitrogen in liquid metals calculated with the macroscopic atom model are reliable.

The Fe-N-M (M = Ti, Nb, V, Cr, Mo, Mn, W, Ni, Co) ternary solid solutions with FCC crystal lattice has been well assessed in the currently available thermodynamic databases (Fstel [22] and TCFE7 [9]). The interaction parameters  $\varepsilon_N^M$  in solid Fe alloys were estimated with thermodynamic tools in the following manner. The concentration of nitrogen dissolved in Fe and Fe-M binary alloys in equilibrium with a Ar + N<sub>2</sub> gas mixture was computed with the thermodynamic tools [9, 10]. Figure 3.3 shows the computed concentration of nitrogen in Fe and selected Fe + 5 at.% M alloys with FCC crystal lattice at 950 °C as a function of the square root of the nitrogen partial pressure ( $p_{N_2}$ ) in the ambient. The molar fraction of the solute nitrogen increases linearly with  $\sqrt{p_{N_2}}$ , indicating that the dissolution of N<sub>2</sub> in Fe and Fe alloys obeys Sieverts law [13], namely:

$$N_N = K_S (p_{N_2})^{1/2} \quad (3.34)$$

, where  $K_S$  is the Sieverts constant. This constant for dissolution of nitrogen gas in Fe and Fe-M alloys were obtained from the slope of the curves in Figure 3.3. When nitrogen gas at atmospheric pressure is chosen as the standard state for the nitrogen dissolved in Fe and Fe alloys, the reciprocal of the Sieverts constant equals the activity coefficient of solute nitrogen [19], namely:

$$\gamma_N = \frac{1}{K_S} \quad (3.35)$$

Then, the values of the interaction parameters  $\varepsilon_N^M$  for different alloying elements were obtained according to Eq. (3.18). It can be seen from Figure 3 that adding Ti, Nb, Ta, V, Cr, Mo, Mn or W promotes, while adding Ni, Co, Al or Si suppresses the dissolution of nitrogen in iron.

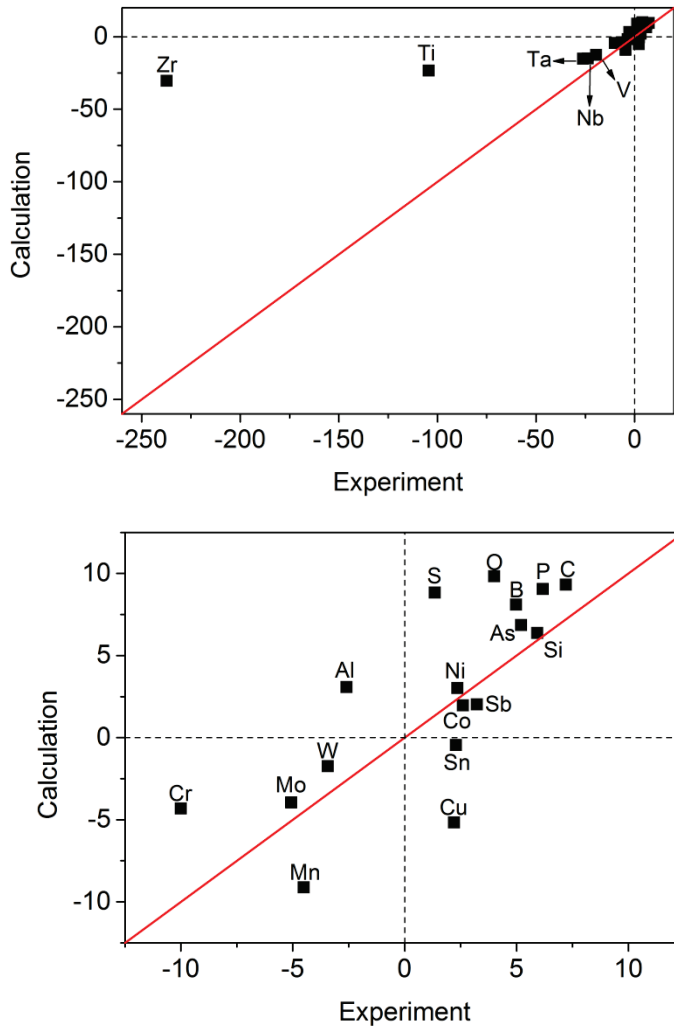


Figure 3.2: Comparison between measured [21] and calculated interaction parameter of alloying element M for nitrogen ( $\epsilon_N^M$ ) in liquid Fe at 1600 °C. The interaction parameter was calculated with the macroscopic atom model in conjunction the L&E model.

The values of the interaction parameters  $\epsilon_N^M$  for solid Fe alloys obtained with the macroscopic atom model in conjunction with the L&E model are in fair agreement with those computed with thermodynamic tools; see Figure 3.4. Compared with the values of the interaction parameters for Ti, Nb and Ta on the dissolution of nitrogen computed with the thermodynamic tools, the Wagner model overestimates these values by an order of magnitude. Apparently, dissolution of nitrogen gas into solid Fe-M (M = Ti, Nb and Ta) alloys significantly influences the bonding between Fe and solute M. However, the

differences between the values of the interaction parameters for Ni, Co, Mn, Mo and Cr on the dissolution of nitrogen, estimated with the Wagner and L&E model are relatively small; see Figures 3.4 and 3.5.

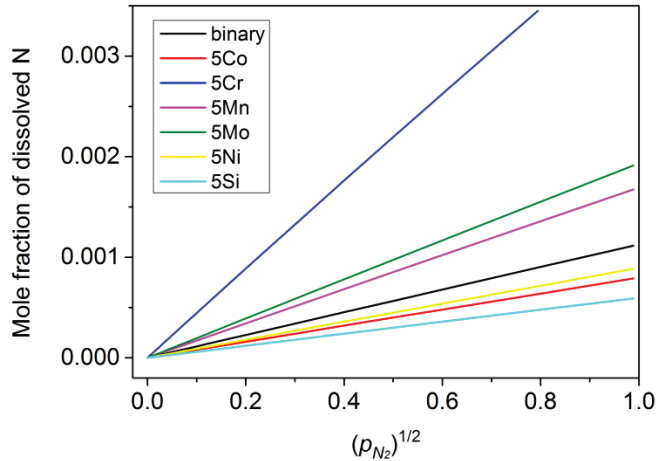


Figure 3.3: Calculated equilibrium concentration of solute nitrogen in iron alloys with 5 at.% alloying element M with FCC crystal lattice at 950 °C as a function of the nitrogen partial pressure ( $p_{N_2}$  in atm.). Dissolution of nitrogen in the iron alloys follows the Sieverts law.

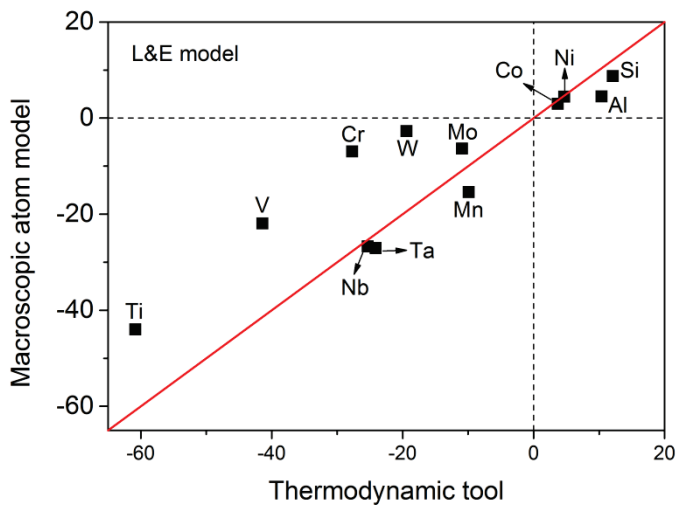


Figure 3.4: Comparison between the interaction parameter of alloying element M for nitrogen ( $\epsilon_N^M$ ) in solid Fe alloys with FCC crystal lattice at 950 °C computed with thermodynamic tools and predicted with the macroscopic atom model adopting the Lupis and Elliot model.

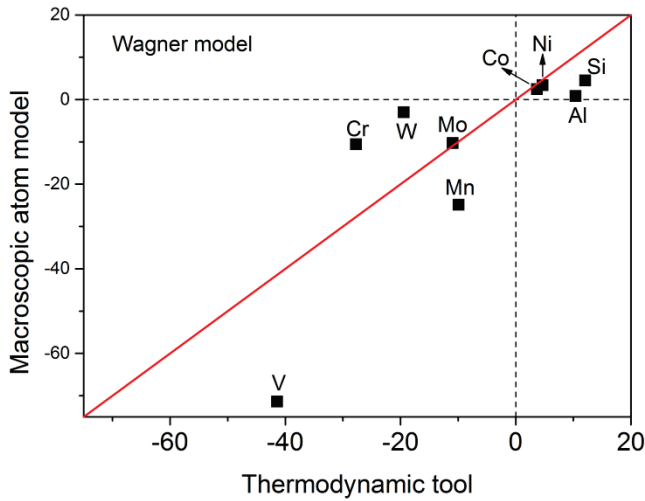


Figure 3.5: Comparison between the interaction parameter of alloying element M for nitrogen ( $\varepsilon_N^M$ ) in solid Fe alloys with FCC crystal lattice at 950 °C computed with thermodynamic tools and predicted with the macroscopic atom model adopting the Wagner model. Data for Nb and Ti are not shown in this figure, namely Nb (-25.3, -190.9) and Ti (-60.8, -433.5).

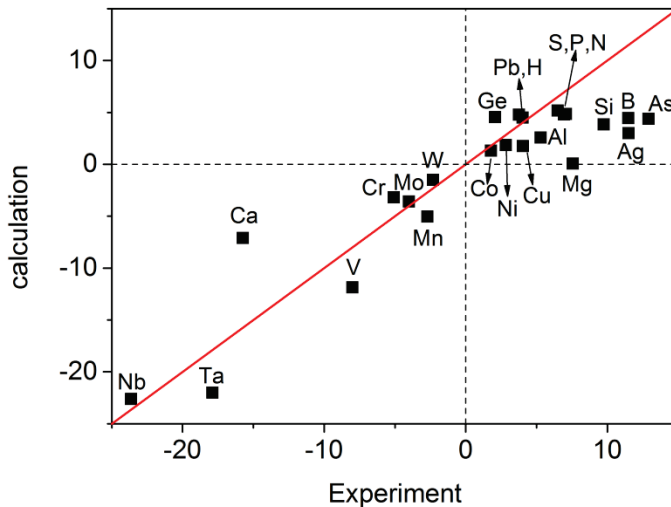


Figure 3.6: Comparison between the measured [21, 23] and calculated interaction parameter of alloying element M for carbon ( $\varepsilon_C^M$ ) in liquid Fe alloys at 1600 °C. The interaction parameter was calculated with the macroscopic atom model adopting the Wagner model.

The interaction parameters of elements M pertaining to carbon ( $\varepsilon_C^M$ ) in liquid iron alloys at 1600 °C were calculated with the macroscopic atom model in conjunction with the Wagner

or L&E model, and compared with the experimental data summarized in refs [21, 23]. These interaction parameters predicted with our approach are in agreement with experimental results; see Figure 3.6. Similar as for nitrogen, the estimated interaction parameters for carbon with the Wagner model are generally in better agreement with experimental data than the L&E model for liquid Fe alloys; see Figures 3.6 and 3.7.

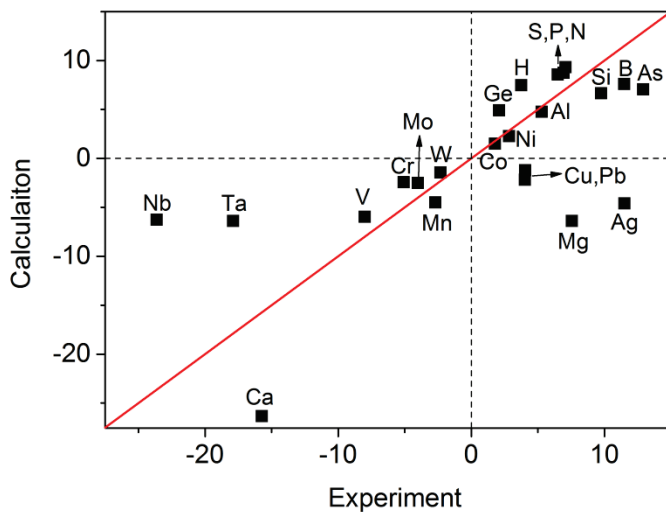


Figure 3.7: Comparison between the measured [21, 23] and calculated interaction parameter of alloying element M for carbon ( $\varepsilon_C^M$ ) in liquid Fe alloys at 1600 °C. The interaction parameter was calculated with the macroscopic atom model adopting the Lupis and Elliot model.

For solid Fe-C-M alloys, however, the L&E model provides a better estimation for the interaction parameters of elements M pertaining to carbon ( $\varepsilon_C^M$ ) than the Wagner model; see Figure 3.8 and 3.9. These interaction parameters were estimated using thermodynamic tools in the similar manner as for nitrogen. The activity of carbon was first calculated as a function of carbon concentration (up to 0.5 at.%) in Fe-C binary and Fe-C-M ternary alloys with FCC or BCC crystal lattice. The concentration of element M in the alloy was fixed at 5 at.%. Then, according to Eq. (3.18), the values of the interaction parameters were obtained by comparing the activity coefficient of carbon in Fe-C and Fe-C-M alloys. These predicted values with the macroscopic atom model in conjunction with the L&E model are in good agreement with the results obtained using the thermodynamic tool for solid Fe alloys; see Figure 3.8. Similar as for the Fe-N-M solid solutions, the prediction with the Wagner model overestimates the interaction parameters for Ti, Zr, V and Nb, while for Co, Ni, Cr, Mn, W and Mo the difference in the prediction between the Wagner and L&E model is relatively small; see Figures 3.8 and 3.9.

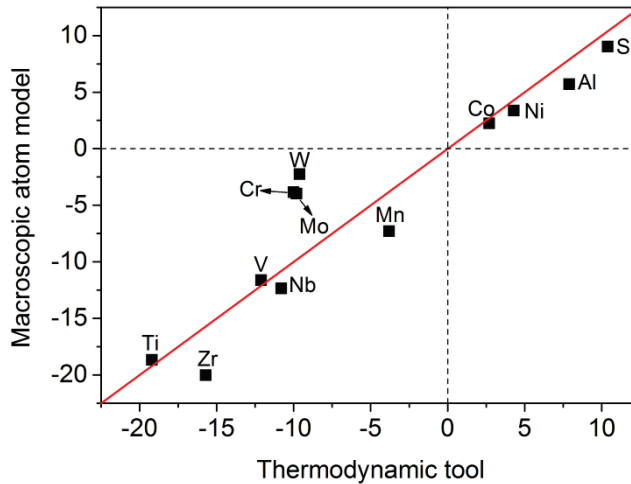


Figure 3.8: Comparison between the interaction parameter of alloying element M for carbon ( $\varepsilon_C^M$ ) in solid Fe alloys at 950 °C computed with thermodynamic tools and predicted with the macroscopic atom model adopting the Lupis and Elliot model. The interaction parameters of Ti, Zr, V, Al and Nb were computed for ferrite and the interaction parameters of other elements were computed for austenite.

For both solid Fe-N-M and Fe-C-M alloys, the predicted interaction parameters using the L&E model are in better agreement with the computed results from thermodynamic tools than using the Wagner model. This suggests that both nitrogen and carbon can be considered simply as substitutional solid solute for estimating the interaction parameters. The reasonable to good agreement between the prediction based on the macroscopic atom model and the computation with thermodynamic tools also suggests that the solution enthalpies of nitrogen and carbon in liquid metals can be regarded equivalent to that for solid metals.

Since oxygen, nitrogen and carbon have similar atomic radii (60, 65, 70 pm, respectively [24]) and also similar diffusivities in iron alloys [25, 26], it is anticipated that the behaviour of oxygen dissolution in iron alloys is similar as that for nitrogen and carbon. For both liquid and solid Fe-N-M and Fe-C-M alloys, it is demonstrated that the interaction parameters for element M pertaining to nitrogen and carbon, respectively, estimated with our approach are in reasonable to good agreement with the experimental or the computed results. This suggests that also the interaction parameters for element M pertaining to oxygen can be estimated well with the approach outlined here. Thus, the effect of alloying elements M on the activity coefficient of dissolved oxygen, i.e.  $\varepsilon_O^M$ , can be determined.

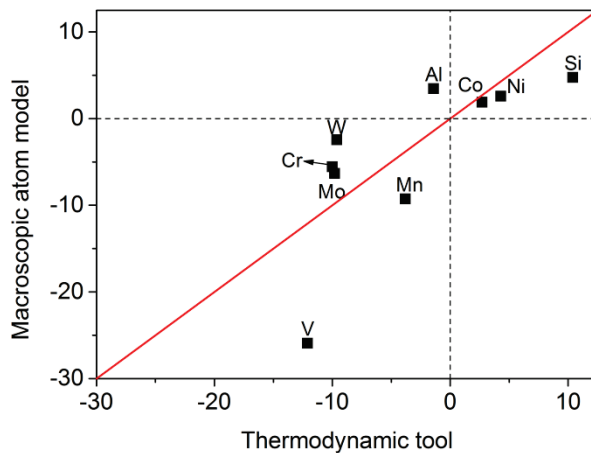


Figure 3.9: Comparison between the interaction parameter of alloying element M for carbon ( $\varepsilon_C^M$ ) in solid Fe alloys at 950 °C computed with thermodynamic tools and predicted with the macroscopic atom model adopting the Wagner model. The interaction parameters of Ti, Zr, V, Al and Nb were computed for ferrite and the interaction parameters of other elements were computed for austenite. Data for Zr (-15.7, -214.8), Nb (-10.8, -59.7) and Ti (-19.2, -94.6) are not shown in this figure.

Figure 3.10 shows the predicted interaction parameters of common alloying elements for oxygen in solid Fe alloys with a FCC crystal lattice at 950 °C. These interaction parameters were calculated with the macroscopic atom model adopting the L&E model. The results show that adding Ti, V, Nb, Ta, Cr, Mo, W, Cu or Mn to steel alloys decreases the activity coefficient of solute oxygen, i.e. promotes the dissolution of oxygen. On the other hand, Co, Si or Ni in steel alloys decreases the solubility of oxygen by increasing the activity coefficient of solute oxygen. Ti, Nb and Ta exert a much larger effect on the activity coefficient of oxygen solute in steel alloys than Cr, W, Mo and Mn.

Yet, the effect of non-ideal behaviour of solution on the solubility product of oxides in steels can be evaluated. As an example, the effect of alloying element M in iron on the precipitation behaviour of  $\text{Al}_2\text{O}_3$  is presented. The change of the solubility product of  $\text{Al}_2\text{O}_3$  in iron due to the addition of an alloying element M is given in terms of the parameter  $\alpha$  as defined by Eq. (3.19). In Figure 3.11, the values of the parameter  $\alpha$  for precipitation of  $\text{Al}_2\text{O}_3$  in Fe-Al-M alloys with FCC crystal lattice are shown taking the concentration of M equal to 5 at.%. It can be seen that adding Ti, V, Nb, Ta, Mo or Mn to a steel alloy increases the solubility product of  $\text{Al}_2\text{O}_3$  and thus suppresses the precipitation of  $\text{Al}_2\text{O}_3$ . Whereas addition of Si or Co to iron enhances the formation of  $\text{Al}_2\text{O}_3$  precipitates in steel alloys by decreasing the solubility product of  $\text{Al}_2\text{O}_3$ . However, the effect of Ni, W, Cu and

Cr in iron on the solubility product of  $\text{Al}_2\text{O}_3$  is relatively small and can be ignored. The same trend is also predicted for iron alloys with BCC crystal lattice, since according to the approach outlined here the effect of crystal structure of alloy matrix on the interaction parameters only depends on the coordination number  $Z$ .

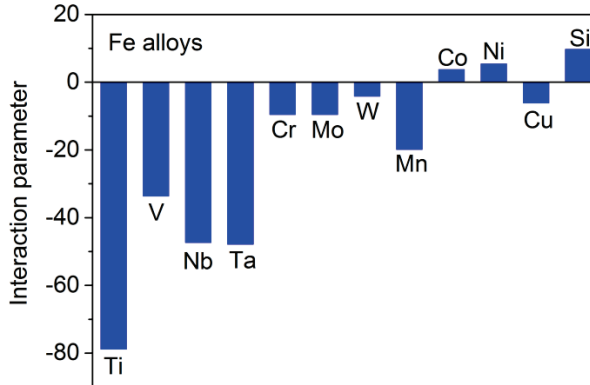


Figure 3.10: Predicted values of the interaction parameter of alloying element M for oxygen ( $\varepsilon_o^M$ ) in solid Fe-M alloys with FCC crystal lattice at 950 °C calculated with the macroscopic atom model in conjunction with the Lupis and Elliot model.

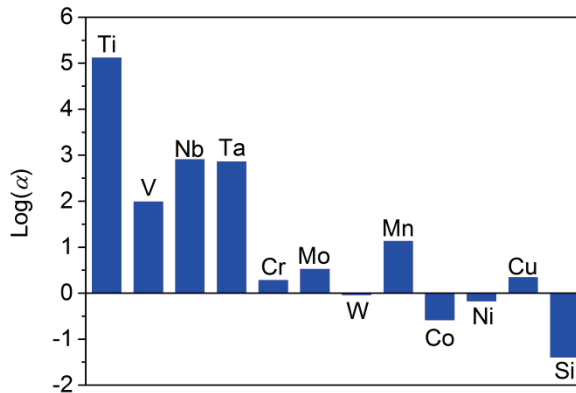


Figure 3.11: Parameter  $\alpha$  describing the non-ideal precipitation behaviour regarding the solubility product of  $\text{Al}_2\text{O}_3$  in Fe-Al-M alloys with FCC crystal lattice at 950 °C; see Eq. (3.19) and text for details. The concentration of alloying element M was taken equal to 5 at.-%.

### 3.5 Conclusions

The change in the solubility product of  $\text{B}_n\text{O}_v$  due to the non-ideal behaviour of solution is determined by the interaction parameters pertaining to B and O as defined according to the



Wagner formalism. The interaction parameters pertaining to nitrogen and carbon for iron alloys can be predicted well with the macroscopic atom model in conjunction with the Wagner or Lupis and Elliot (L&E) model. For liquid iron alloys, the predicted interaction parameters with the Wagner model is in better agreement with experimental results than the L&E model. However, for solid iron alloys, the L&E model provides a more accurate estimation of the interaction parameters. It is shown that adding Ti, V, Nb, Ta, Mo and Mn increases while adding Si and Co decreases the solubility product of  $\text{Al}_2\text{O}_3$  in steel alloys, irrespective of its crystal lattice (i.e. FCC or BCC). Similar prediction can be made for other oxide precipitates as well.

## References

- [1] U. Krupp and H.J. Christ, *Journal of Phase Equilibria and Diffusion*, **26** (2005), 487.
- [2] S.S. Hosmani, R.E. Schacherl, and E.J. Mittemeijer, *Acta Materialia*, **53** (2005), 2069.
- [3] J.L. Meijering, *Advances in materials research*, **5** (1971).
- [4] D. Huin, P. Flauder, and J.B. Leblond, *Oxidation of Metals*, **64** (2005), 131.
- [5] V.A. Lashgari, G. Zimbitas, C. Kwakernaak, and W.G. Sloof, *Oxidation of Metals*, **82** (2014), 249.
- [6] J.B. Brunac, D. Huin, and J.B. Leblond, *Oxidation of Metals*, **73** (2010), 565.
- [7] H.L. Lukas, S.G. Fries and B. Sundman, *Computational thermodynamics: the CALPHAD method*, Cambridge University Press, 2007.
- [8] Z. Liu and Y. Wang, *Computational thermodynamics of materials*, Cambridge University Press, 2016.
- [9] Thermo-Calc Software: Thermodynamic and Mobility Databases Overview, 2017.
- [10] C.W. Bale, E. BÉlisle, P. Chartrand, S.A. Deckerov, G. Eriksson, A.E. Gheribi, et al., *Calphad*, **54** (2016), 35.
- [11] C. Wagner, *Thermodynamics of alloys*, Addison-Wesley Press, 1952.
- [12] F.R.de Boer, R. Boom and W.C.M. Mattens, *Cohesion in metals: transition metal alloys*, Amsterdam, 1988.
- [13] D.J. Young, *High Temperature Oxidation and Corrosion of Metals*, Elsevier, Oxford, 2008.
- [14] M.W.J. Chase, *NIST-JANAF Thermochemical Tables*, American Institute of Physics, New York, 1998.

- 
- [15] D.R. Gaskell, *Introduction to the Thermodynamics of Materials*, 5th ed., Taylor & Francis Group, 2008.
- [16] E.A. Guggenheim, *Mixtures: The Theory of the Equilibrium Properties of Some Simple Classes of Mixtures Solutions and Alloys*, Clarendon Press, 1952.
- [17] M. Hillert, *Phase Equilibria, Phase Diagrams and Phase Transformations: Their Thermodynamic Basis*, Cambridge University Press, 2007.
- [18] C.H.P. Lupis and J.F. Elliott, *Acta Metallurgica*, **14** (1966), 1019.
- [19] C. Wagner, *Acta Metallurgica*, **21** (1973), 1297.
- [20] P.I. Loeff, A.W. Weeber and A.R. Miedema, *Journal of the Less Common Metals*, **140** (1988), 299.
- [21] G.K. Sigworth and J.F. Elliott, *Metal Science J*, **8** (1974), 298.
- [22] Factsage Database Documentation,  
<http://www.crct.polymtl.ca/fact/documentation/>.
- [23] E.H. Foo and C.H.P. Lupis, *Acta Metallurgica*, **21** (1973), 1409.
- [24] J. C. Slater, *The Journal of Chemical Physics*, **41** (1964), 3199.
- [25] H.K.D.H. Bhadeshia and S.R. Honeycombe, *Steels*, 3<sup>rd</sup> ed., Butterworth-Heinemann, Oxford, 2006.
- [26] J.H. Swisher and E.T. Turkdogan, *Transactions of the Metallurgical Society of AIME*, **239** (1967), 426.



## Chapter 4

# Effect of solid solute interaction on the internal precipitation kinetics during nitridation or oxidation of alloys

### Abstract

A general multi-element and multi-phase coupled thermodynamic and kinetic model has been developed for internal precipitation process due to inward diffusion of a foreign element. The model can take into account the non-ideal behaviour of solid solutions. The behaviour of internal nitridation and oxidation in Fe and Ni based alloys is used as an example to study the effect of thermodynamic solute interaction on the internal precipitation process. It is shown that for oxidation and nitridation of binary alloys with a small solubility product of the precipitates, the effect of non-ideal behaviour of solution can be practically ignored. However, for large solubility product of the precipitates, the thermodynamic interaction between nitrogen or oxygen and the alloying element may change the kinetics of internal precipitation and influence the concentration depth profile of dissolved nitrogen or oxygen. In case of ternary alloys, the non-reacting alloying element can significantly affect the kinetics of internal precipitation by changing the solubility of the foreign element in the alloy.

### Keywords

Diffusion, Internal precipitation, Solubility product, Modelling, Solute interaction

## 4.1 Introduction

Wagner's classical theory of internal oxidation [1-3] is a well-known benchmark for estimating the kinetics of internal oxidation quantitatively as well as the concentration depth profiles of internal oxide precipitates, dissolved alloying elements and dissolved oxygen. This internal oxidation theory has also been applied to explain the kinetics of internal nitriding of alloys; see e.g. ref [4]. In principle, this model can be generalized to describe the behaviour of internal precipitation of  $MX_n$ , in any alloys by inward diffusion of a foreign element X. In practice, this occurs for example when boriding, carburizing, oxidizing, nitriding or aluminizing an alloy; see e.g. refs [5-7].

A crucial assumption in the Wagner's classical theory is that the solubility product ( $K_{sp}$ ) of internal precipitates equals zero. The consequence of this condition is: (i) there is a sharp internal precipitation front; (ii) the concentration of the precipitating alloying element within the internal precipitation zone (IPZ) and the concentration of dissolved solute X beyond IPZ are zero; (iii) the process of  $MX_n$  precipitation occurs only at the internal precipitation front; (iv) the concentration of oxide precipitates in IPZ is constant and thus does not change with depth. However, in reality every precipitate exhibits a finite solubility product, even very stable precipitates. Hence, deviation of the actual internal precipitation behaviour of an alloy from that predicted with the Wagner's classical theory increases with the value of the solubility product of the precipitate [8, 9]. To account for the effect of the solubility product on the internal oxide precipitation, a numerical finite-difference model has been developed based on Fick's 2<sup>nd</sup> law [10]. Such a model has been used for simulating internal oxidation of Ni-Al alloys [11] and Fe-Mn steels [10, 12] which showed good agreement with experimental observations. A similar model that considers a finite solubility product of nitrides has been devised to simulate the nitriding behaviour of Ni based alloys [13] and steels [4, 14, 15].

Also, in Wagner's classical internal oxidation theory [1-3] as well as in the numerical model for oxidation [10-12] and nitriding [4, 13, 15], the diffusion coefficients are taken constant, i.e. independent of alloy composition. Further, the solubility product of oxide precipitate and the Sievert's constant [3] for oxygen and nitrogen dissolution in alloy are always considered as a function of temperature only. These assumptions are only valid for ideal solid solutions and solutions that strictly obey Henry's law (i.e. activity of a component increases linearly with its concentration). In real solid solutions, however, the interaction between solute elements can affect the diffusion coefficients [16], the solubility product [17] and the Sievert's constant [17], depending on the alloy composition. This non-

ideal behaviour of solution has been taken into account only in a few studies on oxidation and nitridation [14, 18, 19].

To include the non-ideal behaviour, a coupled thermodynamic-kinetic model based on Fick's 1<sup>st</sup> law is presented to describe internal precipitation of alloys due to inward diffusion of a foreign element X. The model computes the concentration depth profiles of internal precipitates  $MX_v$ , as well as the dissolved X and alloying elements in the alloy matrix as a function of time. Since the depletion of alloying elements in the alloy matrix due to internal precipitation may cause phase transformation of the alloy matrix (e.g. austenite-ferrite transition in iron alloys), the model can also predict the evolution of phase fractions in the alloy matrix as a function of depth and time. Moreover, simultaneous internal precipitation and formation of an external  $MX_v$  scale [20] can be simulated with this model. Also, variations of temperature and ambient activity of X during the course of internal precipitation can be taken into account, which usually happens in practical applications (see e.g. ref. [21]).

A two-step approach is followed for each time lap. In the first step, the change of the alloy composition as a result of solute diffusion is calculated as a function of depth below the alloy surface using a modified flux equation [20, 22-24]. In the second step, the type, amount and composition of the precipitates as well as the phase fractions of the alloy matrix at thermodynamic equilibrium are determined at each depth below the alloy surface. Provided that thermodynamic and kinetic data are available for the case at hand, the model can be applied to the internal precipitation of any type of single or multi phase and multi component alloy systems, as long as the kinetics is diffusion controlled. Although, in this study, the primary interest is in simulating the effect of solute interaction on isothermal internal oxidation and nitridation behaviour of Fe and Ni based alloys, the model is generally applicable to other systems.

## 4.2 Coupled thermodynamic-kinetic model

The coupled thermodynamic-kinetic model is presented for internal precipitation due to inward diffusion of a foreign element X in an alloy composed of elements A, B, C etc. This model is inspired by previous work on external oxidation [20]. Figure 4.1 displays the schematics of the coupled thermodynamic-kinetic model for internal precipitation. Consider that only one of the alloying elements will form a precipitate (e.g.  $BX_v$ ), which is determined by the stability of  $BX_v$  in the alloy and the activity of X in the ambient. Yet, it is assumed that no external  $BX_v$  scale is formed and thus all  $BX_v$  forms internally. The

lateral variation in the alloy composition is assumed to be small, and thus the diffusion process only occurs in the direction perpendicular to the alloy surface. Due to the symmetry along the middle plane of the alloy, only the internal precipitation behaviour of half of the alloy is modelled. Hence, one half of the alloy is divided into a series of slices of original width  $\Delta z^{i,0}$ , where  $i$  is the slice number. The first slice of the alloy is regarded in contact with the ambient while the last slice is at the middle of the alloy. A node point is placed at the middle of each slice. The position of each slice at time zero,  $z^{i,0}$ , is defined as the distance between the node point and alloy surface. At the beginning of internal precipitation process, the average mole fraction of each alloy constituent  $k$  (including the dissolved foreign element X) in each slice  $i$  is denoted as  $N_k^{i,0}$ . The amount of each constituent in each slice is denoted as  $n_k^{i,0}$ , in moles per unit area, which equals to:

$$n_k^{i,0} = \frac{N_k^{i,0}}{V_m} \Delta z^{i,0} \quad (4.1)$$

where  $V_m$  is the molar volume of the alloy, and is taken constant during the whole internal precipitation process, irrespective of the composition or the type of phases of the alloy matrix. When the matrix of alloy contains multiple phases, for each slice  $i$  the relation between the average alloy composition and the composition of each phase is given by:

$$N_k^{i,0} = \sum_{\phi=1}^{\Phi} f^{i,\phi,0} N_k^{i,\phi,0} \quad (4.2)$$

where  $f^{i,\phi,0}$  is the phase fraction and  $N_k^{i,\phi,0}$  is the mole fraction of constituent  $k$  in phase  $\phi$  at time zero.  $\Phi$  is the total number of phases of the alloy matrix excluding the precipitates.

During inward diffusion, the time increment  $\Delta t$  is taken small enough such that the numerical calculation remains stable [25]. At each time increment, the two-step calculation procedure is executed; see Figures 4.1 and 4.2. In the first step, the change in the composition of each slice due to the diffusion process in the alloy is calculated. For example, take the slice  $i$  and the two adjacent slices  $i-1$  and  $i+1$  (slice  $i$  is not the first nor the last slice in the alloy); see Figure 4.2. Adopting the modified flux equations [20, 23], from time  $t$  to time  $t + \Delta t$ , the flux of constituent  $k$  from slice  $i-1$  to  $i$  equals:

$$J_k^{i-1,i,t} = -\frac{RT}{V_m} \left( \frac{\sqrt{M_k^{i,t} N_k^{i,t} M_k^{i-1,t} N_k^{i-1,t}}}{z^{i,t} - z^{i-1,t}} \right) \times 2 \sinh \left( \frac{\mu_k^{i,t} - \mu_k^{i-1,t}}{2RT} \right) \quad (4.3)$$

and the flux from slice  $i$  to  $i+1$  is:

$$J_k^{i/i+1,t} = -\frac{RT}{V_m} \left( \frac{\sqrt{M_k^{i+1,t} N_k^{i+1,t} M_k^{i,t} N_k^{i,t}}}{z^{i+1,t} - z^{i,t}} \right) \times 2 \sinh \left( \frac{\mu_k^{i+1,t} - \mu_k^{i,t}}{2RT} \right) \quad (4.4)$$

Here,  $R$  is the gas constant,  $T$  is temperature in Kelvin,  $M_k^{i,t}$  and  $\mu_k^{i,t}$  are the effective mobility and the chemical potential, respectively, of constituent  $k$  in slice  $i$  at time  $t$ . The effective mobility  $M_k^{i,t}$  can be calculated from the mobilities in the individual phases,  $M_k^{i,\phi,t}$ , through the following relation [20, 24]:

$$M_k^{i,t} = \sum_{\phi=1}^{\Phi} f^{i,\phi,t} M_k^{i,\phi,t} \quad (4.5)$$

The mobilities as used in Eqs (4.3) to (4.5) are related to the tracer diffusion coefficient of constituent  $k$  in phase  $\phi$  in the following equation [26]:

$$M_k^{\phi} = \frac{D_k^{s,\phi}}{RT} \quad (4.6)$$

Both the chemical potential and the mobility of each constituent  $k$  in any slice  $i$  are a function of the alloy composition of that specific slice. Note that the effect of solute interaction on the diffusion of any alloy constituents is actually governed by the dependence of  $M_k$  and  $\mu_k$  on the local alloy compositions. Once the alloy composition in each slice is calculated, the values of chemical potentials and mobilities of all the alloy constituents in the slice can be obtained from thermodynamic computation tools (e.g. ref. [27]) coupled with thermodynamic and mobility databases (e.g. ref. [28]). Then, the solute interaction on diffusion is taken into account when using these tools to obtain the values of  $M_k$  and  $\mu_k$ . One of the advantages of using the modified flux equations described with Eqs (4.3) and (4.4) instead of the regular diffusion equation (Fick's first law) is that the contribution of the alloy constituents' mobility to the mass transport is clearly distinguished from the thermodynamic driving force (i.e. chemical potential gradient). Hence, the effect of mobility solute interaction and the effect of the thermodynamic solute interaction on mass transport can be studied separately. Another advantage of the modified flux equation is that it allows to describe the mass transport between two adjacent slices even if a discontinuous jump in alloy composition between two adjacent slices arises, because of different fractions of phases of alloy matrix [20]. The temporary amount of constituent  $k$  in slice  $i$  after time increment  $\Delta t$  (denoted with a prime, i.e.  $(n_k^{i,t+\Delta t})'$ ) changes as a result of the mass transport between the two adjacent slices (see Figure 4.2), which equals to:

$$(n_k^{i,t+\Delta t})' = n_k^{i,t} + \Delta t (J_k^{i/i+1,t} - J_k^{i-1/i,t}) \quad (4.7)$$

The temporary concentration (mole fraction) of each alloy constituent  $k$  in slice  $i$  at the new time  $t + \Delta t$  after diffusion is defined as:



$$(N_k^{i,t+\Delta t})' = \frac{(n_k^{i,t+\Delta t})'}{(n_{tot}^{i,t+\Delta t})'} \quad (4.8)$$

where  $(n_{tot}^{i,t+\Delta t})'$  is the total amount of all the alloy constituents (including the dissolved foreign element X) in slice  $i$ , which is given by:

$$(n_{tot}^{i,t+\Delta t})' = \sum_{k=1}^K (n_k^{i,t+\Delta t})' \quad (4.9)$$

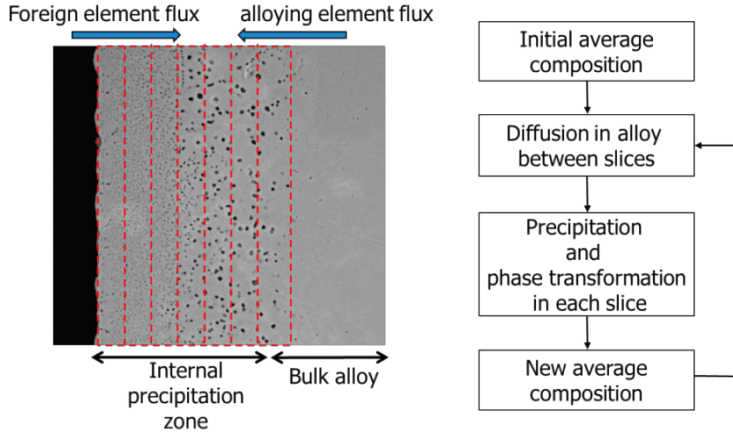


Figure 4.1: Schematics of the coupled thermodynamic-kinetic model for internal precipitation due to inward diffusion of a foreign element and the flow chart of the model's operation.

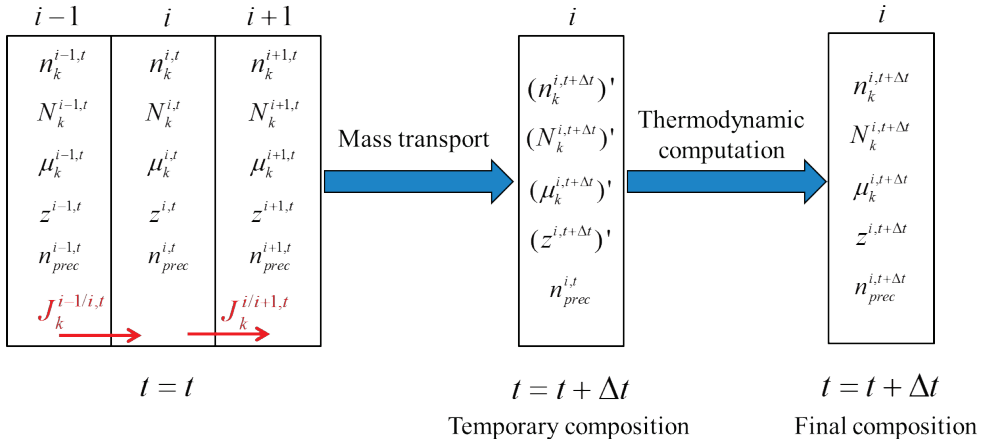


Figure 4.2: Schematic illustration of the calculations on the composition of slice  $i$  after time increment  $\Delta t$ .

After the diffusion process, the alloy matrix with the new composition at time  $t + \Delta t$  may not be in thermodynamic equilibrium. Hence, precipitation of  $BX_v$  and phase transformation of alloy matrix may occur. Therefore, in the second step, a thermodynamic computation is performed for each slice to obtain the final alloy compositions  $N_k^i$ , phase fractions  $f^{i,\phi}$ , phase compositions  $N_k^{i,\phi}$  and the total amount of precipitates  $n_{prec}^i$  at time  $t + \Delta t$ , provided that the local thermodynamic equilibrium is established [29]; see Figure 4.2. Thus, each slice is considered as an entity, which is independent of other slices for precipitation and possible phase transformation of alloy matrix. This happens fast compared to the mass transport in the alloy. In this scheme, contributions of precipitate-matrix interface and phase boundary energies as well as the strain energies associated with volume changes upon precipitation are all discarded.

Three types of boundary conditions can be applied to the first slice ( $i = 1$ ). The first type of boundary condition pertains to thermodynamic equilibrium between the alloy surface (i.e. first slice) and the element X in the ambient maintained during the entire diffusion process, namely the activity of X in the first slice of the alloy is determined by the composition of the ambient. For example, in case that the element X in the ambient is in the form of  $X_w$  gas, the molar fraction of solute X at the first slice of the alloy is determined by the partial pressure of  $X_w$  ( $pX_w$ ) in the annealing atmosphere, independent of the diffusion process, namely:

$$N_X^{1,t>0} = K_S (pX_w)^{1/w} \quad (4.10)$$

where  $K_S$  is the Sievert's constant for  $X_w$  dissolution in the alloy. The second type of boundary condition for the first slice is that the flux of X from ambient into the alloy is a predefined function of time and temperature, i.e.  $J_X^{0/1} = f(t, T)$ . Then, the concentration of X in the first slice (surface) is determined by  $J_X^{0/1}$  and  $J_X^{1/2}$ . This type of boundary condition can be applied, for example, to plasma nitriding [15] or gas-phase nitriding [30] processes in which the nitrogen dissolved at steel surface is not in thermodynamic equilibrium with the ambient. The third type of boundary condition applies to the case that an external  $MX_v$  ( $M = A, B, C$ , etc.) scale is formed and fully covers the alloy surface. Then, the boundary condition can be set as that the flux of M out of the first slice is a predefined function of time and temperature, i.e.  $J_M^{0/1} = g(t, T)$ , and the concentration of M at the first slice is obtained from  $J_M^{0/1}$  and  $J_M^{1/2}$ . The concentration of X in the first slice can be obtained from the concentration of M in the first slice through the law of mass action [3], considering that thermodynamic equilibrium is established at the scale-alloy interface.

For the last slice ( $i = L$ ), it holds that the flux of alloy constituents out of the last slice towards the interior of alloy is always zero ( $J_k^{L/L+1} = 0$ ). An alternative boundary condition for the last slice can be formulated when the “diffusion affected zone” in the alloy is small compared to the sample thickness. Then, it holds that the alloy composition is fixed at the last slice as the bulk composition during the entire internal precipitation process, namely:

$$N_k^{L,t>0} = N_k^{L,0} \quad (4.11)$$

where  $L$  is the total number of slices.

Due to solute element diffusion and precipitates formation the volume of a slice may change. To account for this volume change, the width of each slice at time  $t + \Delta t$  is calculated as follows:

$$\Delta z^{i,t+\Delta t} = V_m n_{tot}^{i,t+\Delta t} + V_{prec} n_{prec}^{i,t+\Delta t} \quad (4.12)$$

where  $V_{prec}$  is the molar volume of precipitates. Next, from the new width of each slice, the position of each slice at  $t + \Delta t$ , i.e.  $z^{i,t+\Delta t}$ , is recalculated:

$$z^{i,t+\Delta t} = \frac{1}{2} \Delta z^{i,t+\Delta t} + \sum_{m=1}^{i-1} \Delta z^{m,t+\Delta t} \quad (4.13)$$

The position, composition of the alloy matrix and the amount of precipitates at each slice and at time  $t + \Delta t$  are used as input for the calculations in the next time step. Such calculation procedure is repeated until the target diffusion time is reached.

### 4.3 Solid solute interactions

The effect of solute interaction on diffusion of alloy constituents and on internal precipitation is considered when the thermodynamic equilibrium in each slice is computed with thermodynamic tools based on the Calphad formalism [31, 32]. The accuracy of the simulation results then depends on the validity of the data in the thermodynamic and mobility databases. However, for example, the ternary Fe-O-M, Ni-O-M and Ni-N-M systems (where M represents an alloying element) with BCC or FCC crystal lattice have not yet been well assessed in the currently available thermodynamic and mobility databases [28, 33] due to the lack of experimental data for oxygen and nitrogen dissolution in binary Fe and Ni based alloys. Besides, the thermodynamic data stored in the commercial thermodynamic databases cannot be modified to study the influence of solute interaction on the internal precipitation kinetics. In order to account for the composition dependence of the chemical potential ( $\mu_k$ ) of each alloy constituent during internal precipitation process for dilute single-phase alloys, the Wagner formalism [34] is used in this study. The

composition dependence of the mobility ( $M_k$ ) of each alloy constituents is taken constant, since data are lacking for oxygen and nitrogen.

In slice  $i$  at time  $t$ , the chemical potential of each alloy constituent  $k$  is:

$$\mu_k^{i,t} = \mu_k^0 + RT \ln N_k^{i,t} + RT \ln \gamma_k^{i,t} \quad (4.14)$$

where  $\gamma_k^{i,t}$  is the activity coefficient in slice  $i$  at time  $t$  and  $\mu_k^0$  is the chemical potential of constituent  $k$  in its standard state. Consider a dilute single-phase ternary alloy A-B-C (A is matrix, B and C are alloying elements), then according to the Wagner formalism, the activity coefficient  $\gamma_k^{i,t}$  for the alloying elements B and C and the dissolved foreign element X can be expressed as a function of alloy composition as:

$$\begin{aligned} \ln \gamma_X^{i,t} &= \ln \gamma_X^0 + \varepsilon_X^X N_X^{i,t} + \varepsilon_X^B N_B^{i,t} + \varepsilon_X^C N_C^{i,t} \\ \ln \gamma_B^{i,t} &= \ln \gamma_B^0 + \varepsilon_B^X N_X^{i,t} + \varepsilon_B^B N_B^{i,t} + \varepsilon_B^C N_C^{i,t} \\ \ln \gamma_C^{i,t} &= \ln \gamma_C^0 + \varepsilon_C^X N_X^{i,t} + \varepsilon_C^B N_B^{i,t} + \varepsilon_C^C N_C^{i,t} \end{aligned} \quad (4.15)$$

in which  $\gamma_k^0$  is the activity coefficient of element  $k$  when its concentration is close to zero, and  $\varepsilon_X^B$ ,  $\varepsilon_X^C$ ,  $\varepsilon_B^C$ ,  $\varepsilon_B^B$ ,  $\varepsilon_C^C$  and  $\varepsilon_X^X$  are the interaction parameters, where the element in the superscript pertains to its interaction on the element in the subscript. By definition the interaction parameter  $\varepsilon_C^B$  is equal to  $\varepsilon_B^C$ , etc. The values of these interaction parameters only depend on temperature, and can be estimated either from thermodynamic databases [28, 33] using the Calphad approach [31, 32] or with a modified macroscopic atom model [17]. Hence, for a non-ideal A-B-C-X solid solution, the solute interaction is specified by the interaction parameters. Note that for an ideal solid solution all interaction parameters are zero. Now, combining Eqs (4.14) and (4.15), the difference in the chemical potentials of B, C and dissolved X between two adjacent slices  $i$  and  $i+1$  at time  $t$  equals:

$$\begin{aligned} \mu_X^{i+1,t} - \mu_X^{i,t} &= RT[\ln N_X^{i+1,t} - \ln N_X^{i,t} + \varepsilon_X^X(N_X^{i+1,t} - N_X^{i,t}) + \varepsilon_X^B(N_B^{i+1,t} - N_B^{i,t}) + \varepsilon_X^C(N_C^{i+1,t} - N_C^{i,t})] \\ \mu_B^{i+1,t} - \mu_B^{i,t} &= RT[\ln N_B^{i+1,t} - \ln N_B^{i,t} + \varepsilon_B^X(N_X^{i+1,t} - N_X^{i,t}) + \varepsilon_B^B(N_B^{i+1,t} - N_B^{i,t}) + \varepsilon_B^C(N_C^{i+1,t} - N_C^{i,t})] \\ \mu_C^{i+1,t} - \mu_C^{i,t} &= RT[\ln N_C^{i+1,t} - \ln N_C^{i,t} + \varepsilon_C^X(N_X^{i+1,t} - N_X^{i,t}) + \varepsilon_C^B(N_B^{i+1,t} - N_B^{i,t}) + \varepsilon_C^C(N_C^{i+1,t} - N_C^{i,t})] \end{aligned} \quad (4.16)$$

Yet, the mass transport of each alloying constituent at each time step can be obtained from Eq. (4.4) by substituting the  $\mu_k^{i+1,t} - \mu_k^{i,t}$  with Eq. (4.16). Next, a temporary alloy composition at time  $t + \Delta t$  (i.e.  $(n_k^{i,t+\Delta t})'$  and  $(N_k^{i,t+\Delta t})'$ ) for each slice before precipitation is obtained from Eqs (4.7) and (4.8). Eq. (4.16) clearly shows that the transport of any alloy constituent between two adjacent slices not only depends on the concentration gradient of the constituent itself, but also depends on the concentration gradient of all the other alloying elements.

The criterion of precipitation in each slice can be determined from the solubility product of the precipitate [3]. Consider that B is the only element that forms a compound  $BX_v$ , the solubility product of this compound (defined as  $K_{sp} = N_B(N_X)^v$ ) in a non-ideal solution equals [17]:

$$K_{sp} = K_{sp}^0 \times \exp\left[-(\varepsilon_B^B N_B + \varepsilon_B^C N_C + \varepsilon_B^X N_X) - v(\varepsilon_X^X N_X + \varepsilon_X^B N_B + \varepsilon_X^C N_C)\right] \quad (4.17)$$

where  $K_{sp}^0$  is the solubility product of  $BX_v$  for an ideal solution. Thus, the solubility product of  $BX_v$  in a solid solution changes with depth and local alloy composition during inward diffusion. After the mass transport at each time step, when the product of the temporary mole fraction of B and dissolved foreign element X is larger than the value of  $K_{sp}'$ , namely:

$$(N_B^{i,t+\Delta t})(N_X^{i,t+\Delta t})' \geq K_{sp}' \quad (4.18)$$

in which  $K_{sp}'$  equals:

$$K_{sp}' = K_{sp}^0 \exp\left[-\varepsilon_B^B(N_B^{i,t+\Delta t})' - \varepsilon_B^C(N_C^{i,t+\Delta t})' - \varepsilon_B^X(N_X^{i,t+\Delta t})' - v\varepsilon_X^X(N_X^{i,t+\Delta t})' - v\varepsilon_X^B(N_B^{i,t+\Delta t})' - v\varepsilon_X^C(N_C^{i,t+\Delta t})'\right] \quad (4.19)$$

, precipitation commences in slice  $i$ . Thermodynamic equilibrium is established after precipitation, and the final alloy composition of slice  $i$  obeys the following relation:

$$N_B^{i,t+\Delta t} N_X^{i,t+\Delta t} = K_{sp}^0 \exp\left[-(\varepsilon_B^B N_B^{i,t+\Delta t} + \varepsilon_B^C N_C^{i,t+\Delta t} + \varepsilon_B^X N_X^{i,t+\Delta t}) - v(\varepsilon_X^X N_X^{i,t+\Delta t} + \varepsilon_X^B N_B^{i,t+\Delta t} + \varepsilon_X^C N_C^{i,t+\Delta t})\right] \quad (4.20)$$

Since each slice is considered as a single entity, the following two equations are obeyed because of conservation of mass:

$$(n_X^{i,t+\Delta t})' + v n_{BX_v}^{i,t} = n_X^{i,t+\Delta t} + v n_{BX_v}^{i,t+\Delta t} \quad (4.21)$$

and

$$(n_B^{i,t+\Delta t})' + n_{BX_v}^{i,t} = n_B^{i,t+\Delta t} + n_{BX_v}^{i,t+\Delta t} \quad (4.22)$$

The final amount of dissolved oxygen, alloying element B and oxide precipitates in slice  $i$  at time  $t + \Delta t$  after the oxide precipitation can be calculated by solving Eqs (4.20) to (4.22). Then, the corresponding mole fraction of X, alloying element B and C dissolved in the alloy matrix after precipitation is calculated according to Eq. (4.8). Here, the mole fraction of oxide precipitates in slice  $i$  is defined as:

$$N_{BX_v}^i = \frac{n_{BX_v}^i}{n_{BX_v}^i + n_{tot}^i} \quad (4.23)$$

In case that the element X in the ambient is of the form of  $X_w$  gas, when the solid solution is non-ideal, also the Sievert's constant for dissolution of element X in the alloy matrix (cf.

Eq. (4.10)) is composition dependent. Then, the mole fraction of dissolved X at alloy surface,  $N_X^s$  (i.e.  $N_X^{1,t>0}$ ), obeys the following relation:

$$N_X^{1,t>0} = K_S^0 (pX_w)^{1/w} \exp(-\varepsilon_X^X N_X^{1,t>0} - \varepsilon_X^B N_B - \varepsilon_X^C N_C) \quad (4.24)$$

where  $K_S^0$  is the Sievert's constant for an ideal alloy.

## 4.4 Results and Discussion

### 4.4.1 Internal oxidation

#### *Solubility product*

Mn, Cr, Al and Si are the typical alloying elements in advanced high strength steels [35]. The binary oxides of those alloying elements formed during oxidation are: MnO, Cr<sub>2</sub>O<sub>3</sub>, Al<sub>2</sub>O<sub>3</sub> and SiO<sub>2</sub>. These oxide precipitates are considered in the form of MO<sub>v</sub>, hence the Cr and Al oxide are formulated as CrO<sub>1.5</sub> and AlO<sub>1.5</sub>, respectively. Since MnO, CrO<sub>1.5</sub>, AlO<sub>1.5</sub> and SiO<sub>2</sub> have different stoichiometry, comparison of the value of their solubility product does not show the tendency of dissociation in an alloy matrix. Therefore, adopting the concept from ref. [9], a solubility parameter  $\alpha$  is used to indicate the stability of oxide precipitate in an alloy matrix. This solubility parameter is defined as:

$$\alpha = \frac{K_{sp}}{N_M^0 (N_O^s)^v} \quad (4.25)$$

where  $N_M^0$  is the bulk concentration of alloying elements and  $N_O^s$  is the surface concentration of oxygen dissolved in alloy matrix in equilibrium with ambient gas. The value of  $\alpha$  lies between 0 to 1. The value of  $\alpha$  for small solubility product oxides is close to zero and increases with the solubility product of an oxide. Since the logarithm of solubility product of an oxide is usually a linear function of reciprocal of absolute temperature, Eq. (4.25) is rewritten as:

$$\ln \alpha = \ln K_{sp} - \ln N_M^0 - v \ln N_O^s \quad (4.26)$$

Considering annealing in a gas mixture of water vapour (H<sub>2</sub>O) and hydrogen (H<sub>2</sub>) with a fixed composition, the temperature dependence of the surface concentration of oxygen dissolved in alloy matrix  $N_O^s$  can be obtained from ref. [36]. The temperature dependence of the solubility product of oxides in steels is given in the Appendix C. As can be seen that the value of  $\ln(\alpha)$  is a linear function of the reciprocal of absolute temperature at fixed  $N_M^0$  and fixed ratio of partial pressure of water vapour and hydrogen ( $p_{H_2O}/p_{H_2}$ ) in the annealing atmosphere. Figure 4.3 shows the temperature dependence of  $\alpha$  for MnO, CrO<sub>1.5</sub>,

$\text{AlO}_{1.5}$  and  $\text{SiO}_2$  precipitates in an ideal austenitic iron alloy. The tendency of dissociation of  $\text{MnO}$  in an ideal austenitic iron alloy is higher than for  $\text{CrO}_{1.5}$ ,  $\text{AlO}_{1.5}$  and  $\text{SiO}_2$ .

#### *Internal oxidation of binary alloys*

The numerical simulation based on the coupled thermodynamic-kinetic model can exactly produce the results as predicted from the analytical solutions of the classical Wagner internal oxidation theory [1-3] (see Appendix B). Since  $\text{AlO}_{1.5}$  is a stable oxide with a very small solubility product in Fe alloys (see Figure 4.3), the internal oxidation of an ideal Fe – 1 at.% Al binary alloy having a austenite matrix at 950 °C under different ambient oxygen partial pressures is used as an example to compare the numerical calculations with analytical solutions. The numerically and analytically obtained concentration depth profiles of internal  $\text{AlO}_{1.5}$ , dissolved Al and dissolved O are matching; see Figure 4.4.

The coupled thermodynamic-kinetic model can well describe the internal oxidation behaviour of Fe-Mn steel alloys. As an example, the kinetics of internal oxidation of Fe – 1.7 at.% Mn steel alloy annealed at 950 °C in a gas mixture of Ar with 5 vol.%  $\text{H}_2$  and dew point of -10 °C (corresponding with an oxygen partial pressure of  $1.0 \times 10^{-18}$  atm.) was simulated based on the coupled thermodynamic-kinetic model and experimentally determined. The Fe-Mn steel alloy is considered as an ideal solution in the simulation. The adopted diffusion coefficient of oxygen and Mn in austenite are  $3.5 \times 10^{-7}$  [37] and  $4.0 \times 10^{-12}$  [12]  $\text{cm}^2/\text{s}$ , respectively. The concentration of oxygen dissolved at steel surface is obtained using the oxygen dissolution data reported in ref. [36]. An internal oxidation zone of  $\text{MnO}$  is formed after annealing at a dew point of -10 °C, and the measured depth profile of volume fraction of internal  $\text{MnO}$  is in agreement with the results of the simulation; see Figure 4.5. The concentration of internal  $\text{MnO}$  slightly decreases with depth in the internal oxidation zone and drops to zero relatively sharply at the internal oxidation front, indicating that  $\text{MnO}$  can be considered as a precipitate in iron with a relatively small solubility product [9] albeit non zero. The growth of internal oxidation zone in the Fe – 1.7 at.% Mn steel alloy follows the parabolic rate law, which also agrees with the results of the simulation; see Figure 4.6.

#### *Effect of solute interaction on internal oxidation of binary alloys*

Since the tendency of  $\text{MnO}$  dissociation in iron alloys is the lowest among those oxides of interest (see Figure 4.3), Fe-Mn steel alloy having an austenitic matrix is used as an example to study the effect of solute interaction on the oxidation behaviour. The interaction parameter  $\varepsilon_{\text{O}}^{\text{Mn}}$  for a Fe based alloy is adopted from ref. [17]; see Table 4.1. The interaction parameter  $\varepsilon_{\text{Mn}}^{\text{Mn}}$  estimated with thermodynamic computation [38] is about 0.1 at 950 °C,

indicating that the Mn-Mn solute interaction in steel alloys can practically be ignored. Assuming that the Fe-O solid solution follows Henrian behaviour, the interaction parameter  $\varepsilon_{\text{O}}^{\text{O}}$  equals zero. The simulated concentration depth profiles of MnO, solute Mn and oxygen considering the Mn-O solute interaction are compared with that for an ideal Fe – 1.7 at.% Mn steel alloy after annealing at 950 °C in a gas ambient with oxygen partial pressures of  $1.0 \times 10^{-18}$  and  $2.3 \times 10^{-17}$  atm. (corresponding with an Ar gas mixture with 5 vol.% H<sub>2</sub> and a dew point of -10 and 10 °C, respectively). The solute interaction between Mn and O clearly has a negligible influence on the internal oxidation behaviour of Fe-Mn steel alloys; see Figure 4.7. The negligible influence of Mn-O solute interaction can be explained as follows: (i) the solubility product of MnO is relatively small ( $2.4 \times 10^{-10}$  at 950 °C), and increasing the solubility product of MnO by a factor of 1.6 in steel by alloying 1.7 at.% Mn does not significantly influence the oxidation behaviour; (ii) the concentration of dissolved Mn at surface is almost zero due to the small solubility product of MnO, hence the change in  $N_{\text{O}}^s$  due to the un-oxidized Mn is negligible (cf. Eq. (4.24)), and the  $N_{\text{O}}^s$  is almost the same as in an ideal solution; (iii) there is no concentration gradient of dissolved Mn in the internal oxidation zone, which exerts negligible effect on the oxygen flux within the internal oxidation zone (cf. e.g. Eq. (4.3)). Since the solubility parameter of CrO<sub>1.5</sub>, AlO<sub>1.5</sub> and SiO<sub>2</sub> are even smaller than that of MnO for steel alloys, it is expected that the solute interaction between M (M = Si, Cr and Al) and dissolved oxygen has practically no influence on the internal oxidation behaviour of these binary steel alloys.

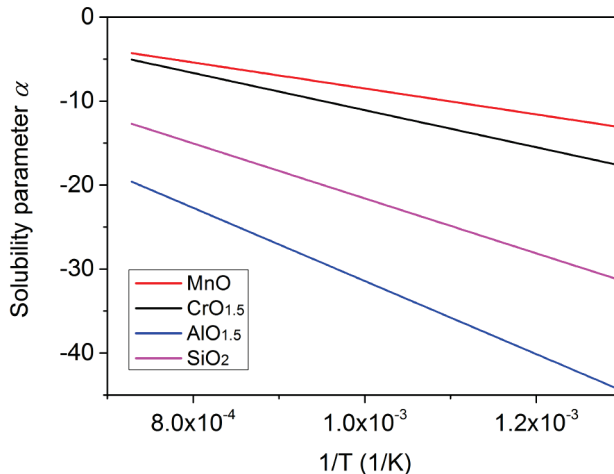


Figure 4.3: Temperature dependence of solubility parameter  $\alpha$  (cf. Eq. (4.26)) for oxides in ideal Fe – 2 at. % M (M = Mn, Cr, Al and Si) binary alloys having an austenite matrix in H<sub>2</sub>O + H<sub>2</sub> gas ambient with  $p_{\text{H}_2\text{O}}/p_{\text{H}_2}$  equal to 0.24.



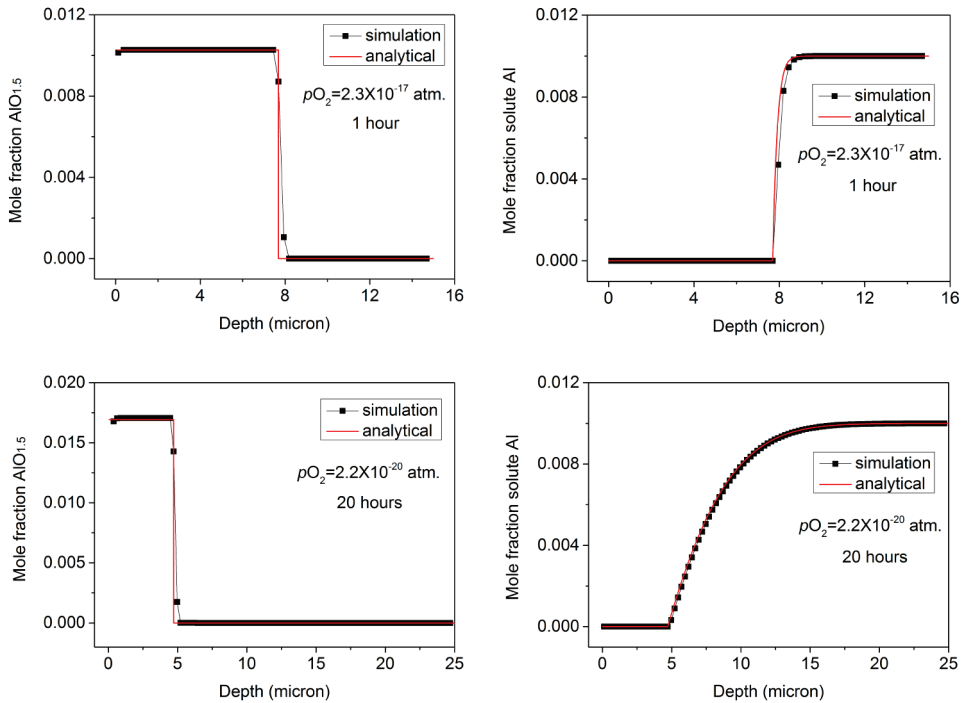


Figure 4.4: Predicted concentration depth profiles of  $\text{AlO}_{1.5}$  and dissolved Al in an ideal Fe – 1 at.% Al alloy having an austenite matrix after oxidizing at 950 °C for 1 and 20 hours at ambient oxygen partial pressures ( $p_{\text{O}_2}$ ) of  $2.3 \times 10^{-17}$  and  $2.2 \times 10^{-20}$  atm., respectively. Calculated using classical Wagner internal oxidation theory (analytical) and with coupled thermodynamic-kinetic model (simulation).

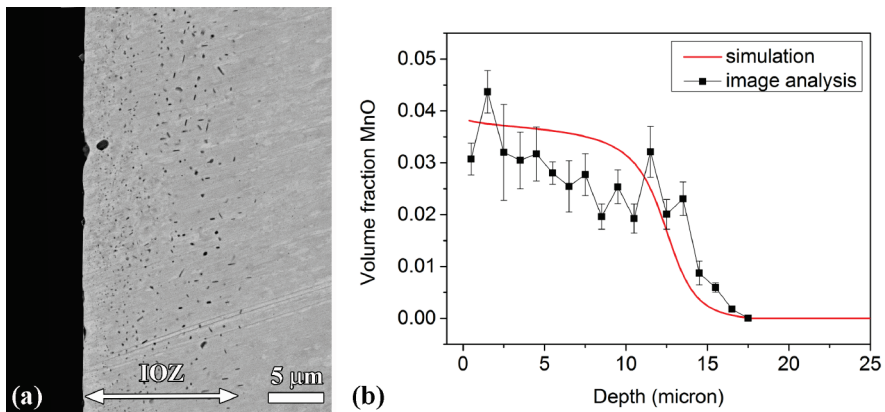


Figure 4.5: (a) SEM image (backscattered electrons) of a cross-section of a Fe - 1.7 at.% Mn steel, and (b) simulated and measured (using image analysis) depth profiles of internal MnO in the steel alloy, after annealing for 16 hours at 950 °C in a gas mixture of Ar with 5 vol.%  $\text{H}_2$  and a dew point of -10 °C (i.e. oxygen partial pressure of  $1.0 \times 10^{-18}$  atm.).

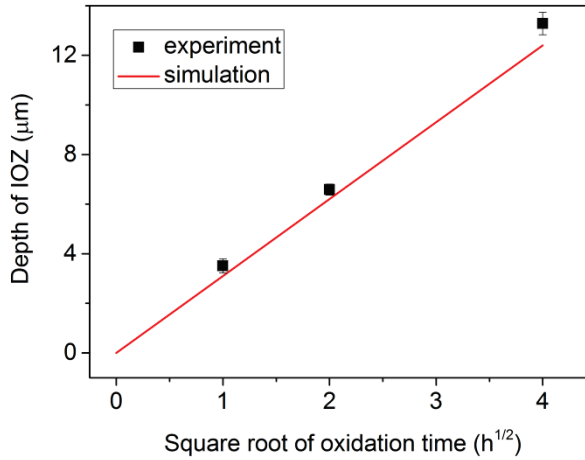


Figure 4.6: Predicted and measured internal oxidation kinetics (in terms of depth of the internal oxidation zone (IOZ) versus the square root of oxidation time) of Fe - 1.7 at.% Mn steel alloy annealed at 950 °C in a gas mixture of Ar with 5 vol.% H<sub>2</sub> and a dew point of -10 °C (i.e. oxygen partial pressure of  $1.0 \times 10^{-18}$  atm.).

Table 4.1: Interaction parameters for Fe and Ni alloys.

	Temperature (°C)	Interaction coefficient (-)	Ref.
$\varepsilon_{\text{O}}^{\text{Mn}}$ in austenite	950	-20	[17]
$\varepsilon_{\text{Mn}}^{\text{Mn}}$ in austenite	950	0.1	[38]
$\varepsilon_{\text{N}}^{\text{Cr}}$ in ferrite	580	-30	[38]
$\varepsilon_{\text{N}}^{\text{Cr}}$ in ferrite	860	-22	[38]
$\varepsilon_{\text{N}}^{\text{Cr}}$ in austenite	1050	-25	[38]
$\varepsilon_{\text{Cr}}^{\text{Cr}}$ in ferrite	580	-3	[38]
$\varepsilon_{\text{N}}^{\text{V}}$ in ferrite	580	-36.2	[38]
$\varepsilon_{\text{N}}^{\text{Ti}}$ in ferrite	580	-44.8	[38]
$\varepsilon_{\text{N}}^{\text{Cr}}$ in Ni	1125	-24	[17]
$\varepsilon_{\text{N}}^{\text{Cr}}$ in Ni	1000	-29	[17]
$\varepsilon_{\text{N}}^{\text{V}}$ in Ni	1000	-22	[17]
$\varepsilon_{\text{N}}^{\text{Nb}}$ in Ni	1000	-21	[17]
$\varepsilon_{\text{N}}^{\text{Ti}}$ in Ni	1000	-30	[17]
$\varepsilon_{\text{Ti}}^{\text{Cr}}$ in Ni	1000	8	[17]

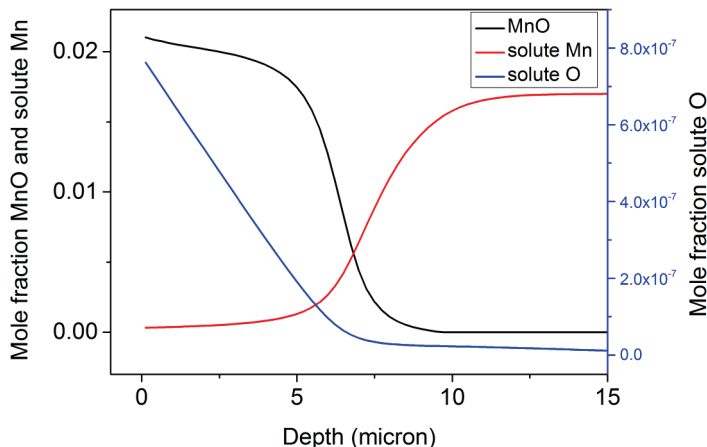


Figure 4.7: Simulated concentration depth profiles of MnO, dissolved Mn and O after oxidizing a Fe – 1.7 at.% Mn alloy at 950 °C for 4 hours in a gas mixture of Ar with 5 vol.% H<sub>2</sub> and a dew point of – 10 °C (i.e. oxygen partial pressure of  $1.0 \times 10^{-18}$  atm.). Effect of Mn-O interaction is negligible, since data for ideal and non-ideal behaviour overlap. The following interaction parameters were used in simulation:  $\varepsilon_{\text{O}}^{\text{Mn}} = -20$ ,  $\varepsilon_{\text{Mn}}^{\text{Mn}} = 0.1$  and  $\varepsilon_{\text{O}}^{\text{O}} = 0$ .

#### 4.4.2 Internal nitriding

Since the nitride precipitates in Fe and Ni alloys generally have a higher tendency of dissociation in alloy matrix, the significance of the effect of thermodynamic solute interaction on internal nitridation behaviour may be different from internal oxidation. The nitrides of interest in this study have the same stoichiometry, and thus the solubility product of those nitrides can be used to compare their tendency of dissociation in alloys. The temperature dependence of the solubility product of common nitrides in iron and nickel is given in the Appendix C and shown in Figure 4.8. To compare the tendency of dissociation of these nitrides with oxides, the solubility product of MnO in austenitic iron as a function of temperature is also shown in Figure 4.8. For all nitrides in iron and nickel, the solubility product increases with temperature. In both iron and nickel, at certain temperature, the nitrides have larger solubility product than that of MnO except for TiN. For each type of nitride in iron, its solubility product for austenite is larger than that for ferrite.

##### *Effect of solute interaction on internal nitridation of binary alloys*

Since the focus here is on the effect of solute interaction between nitrogen and the nitrated elements M (M = Cr, Ti, Al and V), the M-M solute interaction is not considered and thus  $\varepsilon_{\text{M}}^{\text{M}}$  is taken equal to zero. The  $\varepsilon_{\text{N}}^{\text{N}}$  is also considered to be zero for concentrations of the solute nitrogen below 1 at.%. First, the internal nitriding behaviour of binary Fe – M alloys from 500 to 600 °C is analysed. The solubility product of CrN is much higher than that of

VN, AlN and TiN; see Figure 4.8. The nitriding of Fe – 7.0 at.% Cr binary alloy is taken as an example to simulate the effect of solute interaction under the nitriding conditions reported in ref. [39]. The estimated interaction parameter  $\varepsilon_N^{\text{Cr}}$  by thermodynamic computation [38] at 580 °C in ferrite is about -30; see Table 4.1. However, there is practically no influence of the Cr-N interaction on the nitriding kinetics or the concentration depth profiles of CrN and dissolved nitrogen and Cr; see Figure 4.9. This negligible influence of solute interaction can be explained similarly as for the oxidation of Fe – Mn alloys; see above. As can be expected, the effect of solute interaction on nitriding behaviour of Fe - V and Fe - Ti alloys for the same experimental conditions as mentioned in ref. [40] is not significant according to the simulation results (not shown here), although the absolute values for the interaction parameters  $\varepsilon_N^{\text{V}}$  and  $\varepsilon_N^{\text{Ti}}$  are larger than that of  $\varepsilon_N^{\text{Cr}}$ ; see Table 4.1.

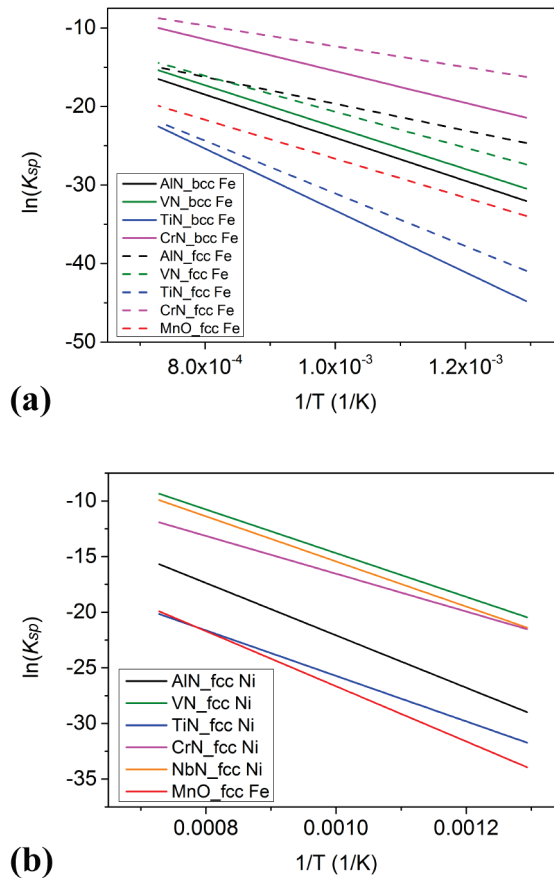


Figure 4.8: Temperature dependence of the solubility product ( $K_{sp}$ ) of common nitrides in (a) ferritic and austenitic Fe alloys, and in (b) Ni based alloys, considering ideal solid solutions.

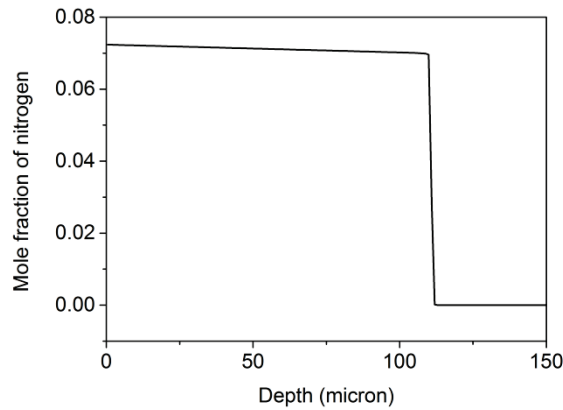


Figure 4.9: Simulated depth profile of total nitrogen concentration (i.e. in nitride and in solid solution) after nitriding a ferritic Fe – 7 at.% Cr binary alloy at 580 °C for 4 hours in  $\text{NH}_3 + \text{H}_2$  gas mixture with a nitriding potential  $p_{\text{NH}_3} / (p_{\text{H}_2})^{3/2}$  equal to  $0.11 \text{ atm}^{-1/2}$ . Effect of Cr-N interaction is negligible, since data for ideal and non-ideal behaviour overlap. The following interaction parameters were adopted in simulation:  $\varepsilon_{\text{N}}^{\text{Cr}} = -30$ ,  $\varepsilon_{\text{Cr}}^{\text{Cr}} = -3.4$  and  $\varepsilon_{\text{N}}^{\text{N}} = 0$ .

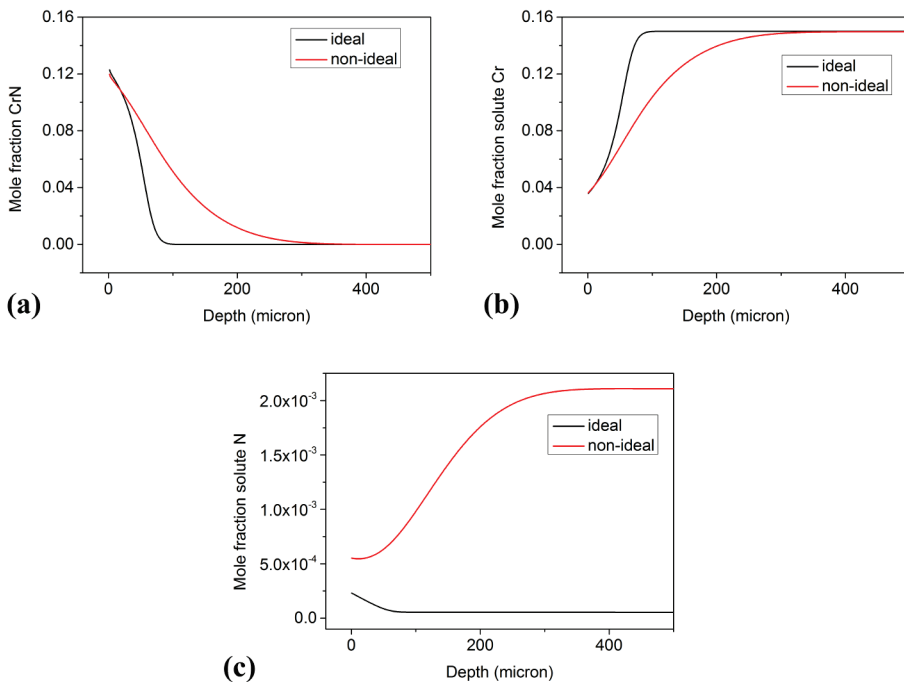


Figure 4.10: Effect of Cr-N solute interaction on concentration depth profiles of (a) CrN, (b) solute Cr and (c) solute nitrogen after nitriding a Ni - 15 at.% Cr binary alloy at 1125 °C for 1 hour in nitrogen gas with a pressure of 900 atm. The following interaction parameters were adopted in simulation:  $\varepsilon_{\text{N}}^{\text{Cr}} = -24$ ,  $\varepsilon_{\text{Cr}}^{\text{Cr}} = 0$  and  $\varepsilon_{\text{N}}^{\text{N}} = 0$ .

In general, it can be stated that for binary alloys where the solubility product of the precipitate is small, the thermodynamic solute interaction between the inward diffusing element and the reactive alloying element does not change the kinetics of internal precipitation. Hence, the analytical solution from the classical Wagner internal oxidation theory can still estimate well the kinetics of internal precipitation due to the inward diffusion of foreign elements. Then, a discrepancy between estimation with the classical theory and experimental results, if any, is not caused by the non-ideal behaviour of solution.

On the contrary, the effect of solute interaction for binary alloys may not be ignored when the solubility product of the precipitate is large. Then, the thermodynamic interaction between the inward diffusing foreign element and the reactive alloying element may change the kinetics of internal precipitation significantly. For example, when nitriding an alloy with a large solubility product of the nitride precipitate at a low nitriding potential (i.e. low  $N_N^s$ ). At temperatures ranging from 1000 to 1100 °C, CrN, VN and NbN are regarded as high solubility product nitrides in Ni based alloys; see Figure 4.8. In the case of a Ni - 15 at.% Cr alloy and considering that the solid solution behaves ideally, then after nitriding at 1125 °C and 900 atm. of pure nitrogen gas the predicted concentration of internal CrN precipitates decreases with depth, while the concentration of solute Cr remaining in the alloy matrix increases with depth within the internal nitridation zone as shown in Figure 4.10. These composition depth profiles are characteristic for an internal precipitation process with large solubility product precipitates [9, 12]. The concentration of solute nitrogen decreases with depth within the internal nitridation zone. But for a non-ideal Ni-Cr-N solid solution, with the value of interaction parameter  $\varepsilon_N^{Cr}$  equal to -24, the extent of the internal nitridation zone is much larger than considering the solid solution as ideal; see Figure 4.10. Moreover, the Cr-N solute interaction causes uphill diffusion of the solute nitrogen in the internal nitridation zone, and the concentration of the solute nitrogen at surface is twice of the value predicted for an ideal Ni-Cr alloy; see Figure 4.10. The effect of Cr-N solute interaction on nitridation of Ni-Cr alloys can be explained as follows. Adding Cr lowers the chemical potential of dissolved nitrogen (i.e. negative  $\varepsilon_N^{Cr}$ ) and hence increases the nitrogen solubility in Ni (cf. Eq. (4.24)). Furthermore, the surface concentration of solute Cr that remains in alloy matrix is about 4 at.%, and the concentration of solute Cr within internal nitridation zone continuously increases with depth. This is due to the large solubility product of CrN. Thus, when thermodynamic equilibrium is established at the alloy surface, the inward flux of nitrogen is enhanced (cf. Eqs (4.4), (4.16) and (4.24)) and the internal nitridation is promoted. However, if the absolute value of the interaction parameter  $\varepsilon_N^{Cr}$  is large enough, the difference between

bulk and surface Cr concentration can lead to an increasing nitrogen concentration with depth, although the chemical potential of nitrogen decreases always with depth. The experimental observation of nitrogen uphill diffusion during nitridation of Ni-Cr alloys has been reported in ref. [41]. Since the solubility product of VN and NbN are larger than that of CrN for Ni alloys and the values of the interaction parameters  $\varepsilon_N^V$  and  $\varepsilon_N^{Nb}$  are close to that of  $\varepsilon_N^{Cr}$  (see Table 4.1), it is expected that the nitrogen uphill diffusion will also occur during nitridation of Ni-V and Ni-Nb alloys.

*Effect of solute interaction on internal nitridation of ternary alloys*

For a ternary A-B-C alloy, the effect of a non-reacting element ‘C’ may significantly influence the internal precipitation process of  $BX_v$ , by changing the solubility of the inward diffusing element X in the alloy, i.e. the surface concentration of solute X in the alloy, when thermodynamic equilibrium is established at alloy surface. Here, internal nitridation of Ni-Ti-Cr and Fe-Al-Cr alloys are taken as examples.

Nitridation of Ni - Ti alloys takes place during annealing at 1000 °C and 1 atm. of nitrogen gas forming TiN, while nitriding of Ni - Cr alloys does not occur at the same temperature and nitrogen partial pressure; see Figure 4.8. Since the solubility product of TiN in Ni alloys is small, the Ti-N interaction has practically no influence on the nitriding behaviour; see above. However, when adding Cr to the Ni-Ti alloys the internal nitridation kinetics is promoted. According to our prediction, the concentration of dissolved nitrogen at alloy surface increases by a factor of 4 when alloyed with 5 at.% Cr (with the value for the interaction parameter  $\varepsilon_N^{Cr}$  taken equal to -29), and the depth of internal nitridation zone with TiN increases by a factor of two; see Figure 4.11. The higher concentration of solute nitrogen at the surface provides a higher flux of this element into the bulk of the Ni-Ti-Cr alloy, and hence increases the kinetics of internal nitridation. The concentration gradient of TiN at internal nitridation front does not change with the addition of Cr, which indicates that the increase of the solubility product of TiN by a factor of 3 with 5 at.% Cr has practically no influence on the nitridation behaviour. Although the Ti-Cr interaction is considered in simulation (the value for the interaction parameter  $\varepsilon_{Ti}^{Cr}$  taken equal to 8) as well as the possible Cr transport due to depletion of Ti by nitriding, the simulation result shows that the Cr concentration in the alloy matrix is almost constant throughout the alloy after nitriding; see Figure 4.11. The effect of Cr enhancing the internal nitridation rate of a Ni-Ti-Cr alloy was experimentally observed [42, 43].

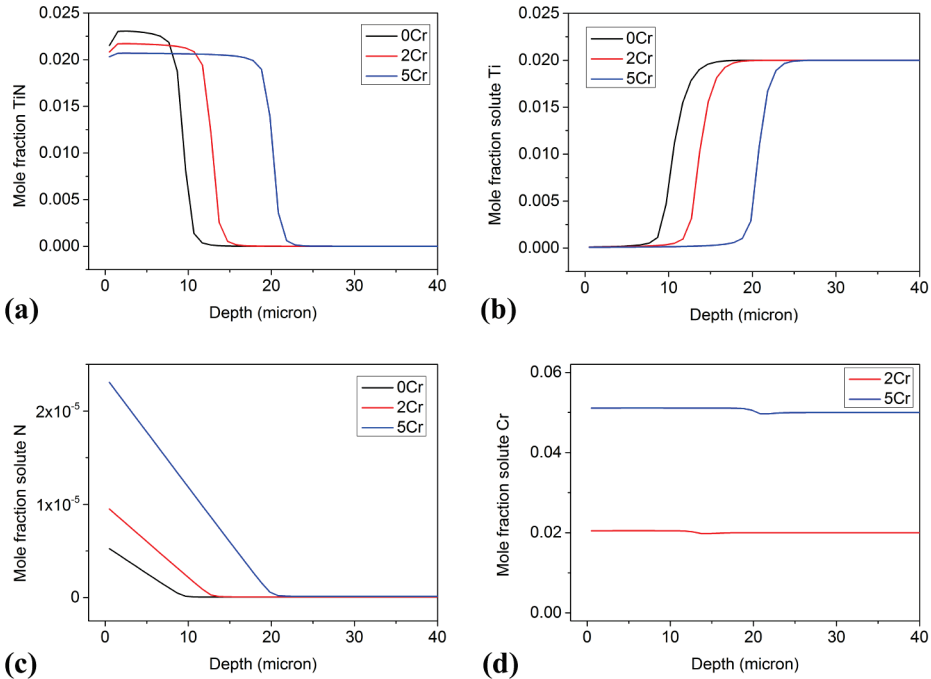


Figure 4.11: Effect of Cr content on the concentration depth profiles of (a) TiN, (b) solute Ti, (c) solute nitrogen and (d) solute Cr after nitriding Ni - 2 at.% Ti - X at.% Cr (with X = 0, 2, 5) alloys at 1000 °C for 1 hour in nitrogen gas at 1 atm. The interaction parameters were taken from Table 4.1, i.e.:  $\varepsilon_N^{\text{Cr}} = -29$ ,  $\varepsilon_N^{\text{Ti}} = -30$ ,  $\varepsilon_{\text{Ti}}^{\text{Cr}} = 8$ ,  $\varepsilon_{\text{Cr}}^{\text{Cr}} = 0$ ,  $\varepsilon_{\text{Ti}}^{\text{Ti}} = 0$  and  $\varepsilon_N^{\text{N}} = 0$ .

The internal nitridation behaviour of Fe-Al-Cr alloys having a ferrite matrix between 800 to 900 °C has not been reported yet, and hence is analysed in this study. AlN can be considered as a small solubility product precipitate in Fe alloys below 900 °C; see Figure 4.8. The estimated value of the interaction parameter  $\varepsilon_N^{\text{Cr}}$  in ferrite at 860 °C is about -22; see Table 4.1. Hence, according to our simulation result (not shown here) adding Cr to Fe – Al alloys enhances the internal nitridation kinetics by increasing the nitrogen concentration dissolved at the alloy surface, as long as Cr is not nitrided. The predicted effect of Cr on nitridation of Fe – Al alloys is similar as for the Ni – Ti alloys. The formation of internal nitridation zone with AlN is experimentally observed in both Fe – 2 at.% Al and Fe – 2 at.% Al – 2 at.% Cr alloys after annealing at 860 °C for 1 hour in Ar + 30 vol.% N<sub>2</sub> gas mixture; see Figure 4.12. The internal nitridation front is relatively sharp, indicating the small solubility product of AlN in ferrite at 860 °C. However, the depth of internal nitridation zone in the Fe – 2 at.% Al – 2 at.% Cr alloy is almost twice of that in the Fe – 2 at.% Al alloy for the same annealing condition; see Figure 4.12. According to electron probe X-ray micro analysis (EPMA) [44], the solute Al in the alloy matrix is practically



depleted by forming AlN while the Cr concentration remains the same as in the bulk alloy within the internal nitridation zone; see Figure 4.13. According to the results computed with the currently available mobility databases [27, 28], adding Cr does not change the mobility of N in ferrite. Thus, if that is the case, the difference in the nitridation kinetics between the two alloys is solely attributed to the thermodynamic solute interaction between nitrogen and Cr. The observed increase of the internal nitridation rate due to Cr addition has also been reported for austenitic Fe-Mn-Al based alloys annealed in nitrogen gas at temperatures from 1000 to 1100 °C [45, 46].

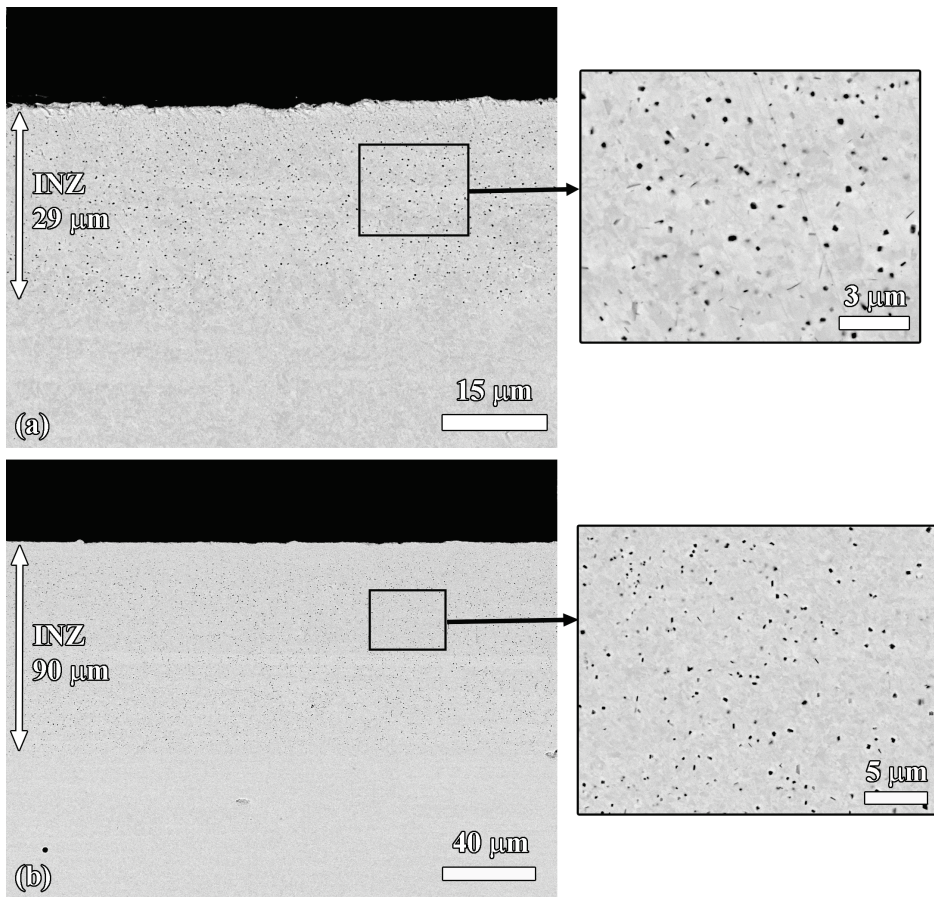


Figure 4.12: Internal nitridation zone (INZ) of (a) Fe – 2 at.% Al and (b) Fe – 2 at.% Al – 2 at.% Cr alloy, having a ferrite matrix, after nitriding at 860 °C for 1 hour in Ar + 30 vol.% N<sub>2</sub> + 5 vol.% H<sub>2</sub> gas mixture.

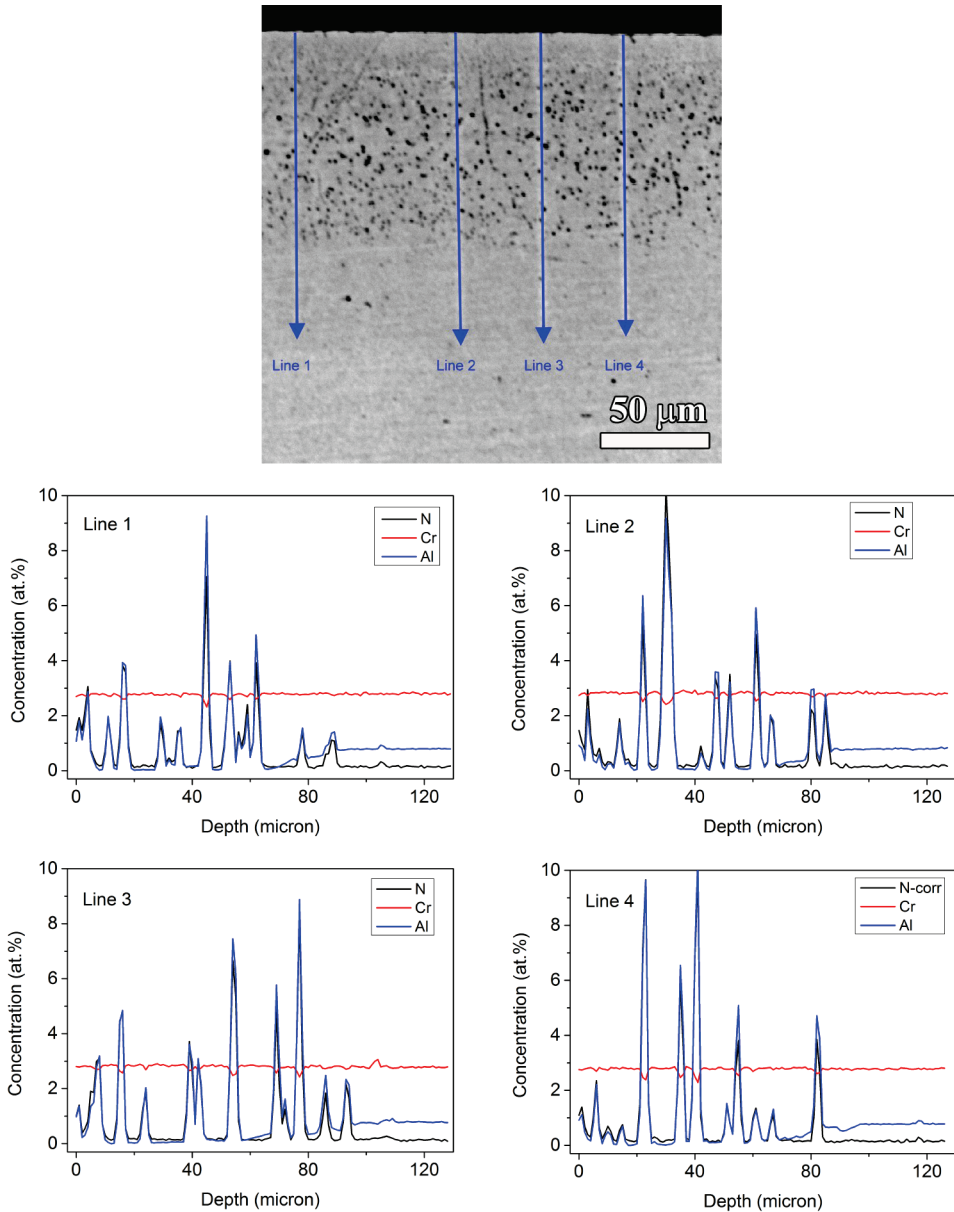


Figure 4.13: Concentration depth profiles of nitrogen, Al and Cr measured with EPMA in Fe – 2 at.% Al – 2 at.% Cr alloy after nitriding at 860 °C for 1 hour in Ar + 30 vol.% N<sub>2</sub> + 5 vol.% H<sub>2</sub> gas mixture. Only Al is nitrided and the concentration of solute Cr within the internal nitridation zone is the same as in the bulk alloy.

## 4.5 Conclusions

A coupled thermodynamic-kinetic model based on Fick's 1<sup>st</sup> law has been developed which allows simulation of the effect of non-ideal behaviour of solid solution on the internal precipitation of alloys due to inward diffusion of a foreign element. For a binary alloy, the effect of solute interaction depends solely on the solubility product of the precipitate. If the solubility product of the precipitated phase is small, the effect of solute interaction on the internal precipitation is negligible. This applies, for example, to internal oxidation of iron alloys with Mn, Cr, Si and Al. However, the solute interaction cannot be ignored, if the solubility product of the precipitates is large. Then, the large solubility product accounted for non-ideal behaviour of the solid solution will affect the internal precipitation behaviour of the alloy. This has been demonstrated for the interaction between nitrogen and the nitrated element in Ni alloys, which enhances internal nitridation and results in uphill diffusion of solute nitrogen in the internal nitridation zone. For a ternary alloy, the solute interaction between a foreign element and the non-reacting alloying element can significantly influence the internal precipitation kinetics due to the non-ideal behaviour of the solubility of the foreign element in the alloy. This, for example, occurs when adding Cr to Fe - Al and to Ni - Ti alloys.

## References

- [1] C. Wagner, *Zeitschrift Fur Elektrochemie*, **63** (1959), 772.
- [2] R.A. Rapp, *Corrosion*, **21** (1965), 382.
- [3] D.J. Young, *High Temperature Oxidation and Corrosion of Metals*, Elsevier, Oxford, 2008.
- [4] R.E. Schacherl, P.C.J. Graat and E.J. Mittemeijer, *Metallurgical and Materials Transactions A*, **35** (2004), 3387.
- [5] I.E. Campos-Silva and G.A. Rodríguez-Castro, Boriding to improve the mechanical properties and corrosion resistance of steels, *Thermochemical Surface Engineering of Steels*, Elsevier, UK, 2015.
- [6] H.J. Grabke, *Materials and Corrosion*, **54** (2003), 736.
- [7] V.A. Ravi, T.K. Nguyen and J.C. Nava, Aluminizing of steel to improve high temperature corrosion resistance, *Thermochemical Surface Engineering of Steels*, Elsevier, UK, 2015.
- [8] H.J. Christ, H. Biermann, F.C. Rizzo and H.G. Sockel, *Oxidation of Metals*, **32** (1989), 111.

- [9] E.K. Ohriner and J.E. Morral, *Scripta Metallurgica*, **13** (1979), 7.
- [10] D. Huin, P. Flauder and J.B. Leblond, *Oxidation of Metals*, **64** (2005), 131.
- [11] G. Zimbitas and W.G. Sloof, *Materials Science Forum*, **696** (2011), 82.
- [12] V.A. Lashgari, G. Zimbitas, C. Kwakernaak and W.G. Sloof, *Oxidation of Metals*, **82** (2014), 249.
- [13] U. Krupp and H.J. Christ, *Oxidation of Metals*, **52** (1999), 299.
- [14] M. Jung, S.R. Meka, B. Rheingans and E.J. Mittemeijer, *Metallurgical and Materials Transactions A*, **47** (2016), 1425.
- [15] Y. Sun and T. Bell, *Materials Science and Engineering A*, **224** (1997), 33.
- [16] J.S. Kirkaldy and D.J. Young, *Diffusion in the Condensed State*, Institute of Metals, London, 1987.
- [17] Chapter 3.
- [18] W.W. Smeltzer and D.P. Whittle, *Journal of the Electrochemical Society*, **125** (1978), 1116.
- [19] S.W. Guan and W.W. Smeltzer, *Oxidation of Metals*, **42** (1994), 375.
- [20] T.J. Nijdam and W.G. Sloof, *Acta Materialia*, **56** (2008), 4972.
- [21] E. Buscarlet, J. Nauzin, X. Cluzel and S. Mehraïn, *Galvatech Conference Proceedings*, Toronto, Canada, 2015.
- [22] M. Hillert, *Scripta Materialia*, **44** (2001), 1095.
- [23] H. Larsson, H. Strandlund and M. Hillert, *Acta Materialia*, **54** (2006), 945.
- [24] H. Larsson and A. Engström, *Acta Materialia*, **54** (2006), 2431.
- [25] C. Vuik, P. van Beek, F. Vermolen and J. van Kan, *Numerical methods for ordinary differential equations*, VSSD, Delft, 2007.
- [26] J.O. Andersson and J. Agren, *Journal of Applied Physics*, **72** (1992), 1350.
- [27] J.O. Andersson, T. Helander, L. Höglund, P. Shi and B. Sundman, *Calphad*, **26** (2002), 273.
- [28] Thermo-Calc Software: Thermodynamic and Mobility Databases Overview, 2017.
- [29] Y.L. Li and J.E. Morral, *Acta Materialia*, **50** (2002), 3683.
- [30] D. Wu, H. Kahn, J.C. Dalton, G.M. Michal, F. Ernst and A.H. Heuer, *Acta Materialia*, **79** (2014), 339.
- [31] H.L. Lukas, S.G. Fries and B. Sundman, *Computational thermodynamics: the CALPHAD method*, Cambridge University Press, 2007.
- [32] M. Hillert, *Phase Equilibria, Phase Diagrams and Phase Transformations: Their Thermodynamic Basis*, Cambridge University Press, 2007.
- [33] Factsage Database Documentation,  
<http://www.crct.polymtl.ca/fact/documentation/>.
- [34] C. Wagner, *Thermodynamics of alloys*, Addison-Wesley Press, 1952.

- [35] N. Fonstein, *Advanced High Strength Sheet Steels*, Springer International Publishing, Switzerland, 2015.
- [36] V.A. Lashgari, PhD Dissertation, Delft University of Technology, 2014.
- [37] J.H. Swisher and E.T. Turkdogan, *Transactions of the Metallurgical Society of AIME*, **239** (1967), 426.
- [38] C. Bale, P. Chartrand, S.A. Degterov, G. Eriksson, K. Hack, R. Ben Mahfoud, et al., *Calphad*, **26** (2002), 189.
- [39] S.S. Hosmani, R.E. Schacherl and E.J. Mittemeijer, *Materials Science and Technology*, **21** (2005), 113.
- [40] S.S. Hosmani, R.E. Schacherl and E.J. Mittemeijer, *Metallurgical and Materials Transactions A*, **38** (2007), 7.
- [41] A.A. Kodentsov, J.H. Gulpen, C. Cserhati, J.K. Kivilahti and F.J.J. VanLoo, *Metallurgical and Materials Transactions A*, **27** (1996), 59.
- [42] U. Krupp and H.J. Christ, *Oxidation of Metals*, **52** (1999), 277.
- [43] H.J. Christ, S.Y. Chang and U. Krupp, *Materials and Corrosion*, **54** (2003), 887.
- [44] V.D. Scott and G. Love, *Quantitative electron-probe microanalysis*, Ellis Horwood, 1983.
- [45] J.G. Duh and C.J. Wang, *Journal of Materials Science*, **25** (1990), 2615.
- [46] J.G. Duh and S.C. Lin, *Journal of Materials Science*, **28** (1993), 5975.

## Chapter 5

# Relation between oxygen activity gradient in the internal oxidation zone of Mn alloyed steel and the composition of oxide precipitates<sup>1</sup>

### Abstract

An internal oxidation zone with  $(\text{Mn}_{1-x}\text{Fe}_x)\text{O}$  mixed oxide precipitates occurs after annealing a Fe – 1.7 at.% Mn steel at 950 °C in a  $\text{N}_2$  plus 5 vol.%  $\text{H}_2$  gas mixture with dew point of 10 °C. Local thermodynamic equilibrium in the internal oxidation zone is established during annealing of the Mn alloyed steel. As a result, the composition of  $(\text{Mn}_{1-x}\text{Fe}_x)\text{O}$  precipitates depends on the local oxygen activity. The oxygen activity decreases as a function of depth below steel surface, and consequently the concentration of Fe decreases in the  $(\text{Mn}_{1-x}\text{Fe}_x)\text{O}$  precipitates.

### Keywords

Mn alloyed steel, Internal oxidation,  $(\text{Mn}_{1-x}\text{Fe}_x)\text{O}$  mixed oxide, Composition depth profile, Local thermodynamic equilibrium

---

<sup>1</sup> This chapter is based on:

W. Mao and W.G. Sloof, *Relation between oxygen activity gradient in the internal oxidation zone of Mn alloyed steel and the composition of oxide precipitates*, Scripta Materialia, vol. 135, p. 29, 2017.

## 5.1 Introduction

Mn is one of the major alloying elements in advanced high strength steels, which are used for automotive applications to reduce the weight of car bodies and thereby reducing fuel consumption and CO<sub>2</sub> emissions. To protect these steels against corrosion a zinc coating is applied, usually by hot-dip galvanizing. However, during annealing of these steels prior to galvanizing the Mn can be oxidized easily, which may impair the zinc coating adhesion [1]. Then, it is beneficial if the oxides are formed beneath rather than at the steel surface.

The kinetics of internal oxidation of Fe-Mn binary steel alloys has been studied experimentally [2] and a numerical model has been developed to simulate the internal oxidation behaviour of Fe-Mn binary alloys [2, 3]. Extension of this model to simulate internal oxidation of multi-element alloyed steels has also been reported [3, 4]. A vital assumption in all internal oxidation models [2, 3, 5], as in the model adopted here [2], is that local thermodynamic equilibrium is reached between dissolved oxygen, alloying elements, iron matrix and oxide precipitates. However, experimental proof for the establishment of local thermodynamic equilibrium inside alloy matrix during internal oxidation of Mn alloyed steels is lacking. In this work, it will be shown from the observed composition depth profile of the internal oxide precipitates formed during internal oxidation of Mn alloyed steel that local thermodynamic equilibrium indeed occurs.

FeO and MnO, which are known as Wüstite and manganosite respectively, have the same rock salt crystal structure. Hence, FeO and MnO can form a continuous solid solution also known as manganowüstite, henceforth denoted as  $(\text{Mn}_{1-x}\text{Fe}_x)\text{O}$ ; see e.g. [6]. When annealing steels alloyed with Mn,  $(\text{Mn}_{1-x}\text{Fe}_x)\text{O}$  mixed oxide can be formed at the steel surface even below the dissociation oxygen partial pressure of FeO [7]. The concentration of Fe-ions dissolved in the external  $(\text{Mn}_{1-x}\text{Fe}_x)\text{O}$  increases with dew point (i.e. oxygen partial pressure) in the annealing atmosphere [7]. When these Mn steel alloys are oxidized internally,  $(\text{Mn}_{1-x}\text{Fe}_x)\text{O}$  precipitates are formed in the internal oxidation zone (IOZ). However, the composition of these precipitates depends on the local activity (i.e. chemical potential) of dissolved oxygen. Upon internal oxidation a gradient of oxygen activity in the IOZ exists which results in the inward diffusion of dissolved oxygen. Hence, if local thermodynamic equilibrium between dissolved oxygen and oxide precipitates is established, it is expected that the concentration of Fe in the  $(\text{Mn}_{1-x}\text{Fe}_x)\text{O}$  decreases with depth.

In this work, the concentration and activity depth profiles of dissolved oxygen are predicted quantitatively for steels alloyed with Mn using a numerical internal-oxidation simulation

tool [2]. Since the thermodynamic data of the Fe-Mn-O ternary system have been well assessed in the currently available thermodynamic databases [8], the corresponding composition of the internal  $(\text{Mn}_{1-x}\text{Fe}_x)\text{O}$  as a function of depth is calculated using a thermodynamic computation tool [9]. The actual composition depth profile of the internal oxide precipitates is determined experimentally from their lattice parameter as obtained from X-ray diffractometry (XRD).

## 5.2 Experiments

The steel alloyed with 1.7 at.% Mn was annealed for 1 hour at 950 °C in a  $\text{N}_2 + 5 \text{ vol.}\% \text{H}_2$  gas mixture at a dew point of 10 °C, corresponding with an oxygen partial pressure of  $2.3 \times 10^{-17}$  atm. This dew point was realized by adding de-aerated and deionized water vapour to the gas flow of 1500 sccm passing through a 30 mm inner diameter quartz tube in a horizontal furnace (Carbolite MTF 12/38/850, UK). Based on the fluctuation of the dew point during annealing observed with a cooled mirror analyzer (Optidew, Michell Instruments, UK), the uncertainty of the dew point in the annealing atmosphere is about 2 °C. The annealing process is terminated by moving the steel sample to the cold zone of the quartz tube, allowing the steel sample to be cooled down to room temperature. The cooling rate from the annealing temperature to about 400 °C is about 180 °C/min. Further details of the experimental setup are described elsewhere [2]. Under these annealing conditions internal oxidation of the Mn alloyed steel will prevail [10]. The composition of the steel used is: 0.48 at.% C, 1.72 at.% Mn, 0.097 at.% Si, 0.004 at.% Al and balance Fe.

To obtain the composition depth profile of internal  $(\text{Mn}_{1-x}\text{Fe}_x)\text{O}$  with X-ray diffractometry (XRD), the surface of sample after annealing was mechanically polished to remove a layer with certain thickness. The polishing was done with 1  $\mu\text{m}$  diamond grains using a soft cloth (Lam Plan MM431, UK). After each polishing step the sample was thoroughly cleaned ultrasonically with isopropanol. The thickness of the surface layer removed was determined from the measured weight loss of the sample after polishing and considering the polished surface area. For the density of the steel 7.87  $\text{g}/\text{cm}^3$  is taken. The sample was weighted with an analytical balance (Mettler M5SA, Switzerland) having an accuracy of  $\pm 10 \mu\text{g}$ .

After each polishing step, the lattice constant of the  $(\text{Mn}_{1-x}\text{Fe}_x)\text{O}$  precipitates in the alloy matrix was determined from XRD measurements. XRD patterns were recorded with a Bruker D8 Discover diffractometer in the grazing incidence geometry using  $\text{Co } K\alpha$  radiation, in the  $2\theta$  region between  $37^\circ$  and  $57^\circ$  with a step size of  $0.01^\circ 2\theta$  and a dwell time of 30 s. The incidence angle of the X-ray beam was fixed at  $3^\circ$  with respect to the



sample surface. As the analysis depth, the depth below the surface corresponding with 70 % of the diffracted intensity of pure iron was taken, which is 1.27 to 1.34  $\mu\text{m}$  [11] for  $2\theta$  from  $30^\circ$  to  $60^\circ$ . The data evaluation was done with the Bruker software Diffrac.EVA version 4.0. The position of the (111) and (200) diffraction lines of  $(\text{Mn}_{1-x},\text{Fe}_x)\text{O}$  was determined by fitting a parabola to the top of the diffracted intensity peak after smoothing and stripping  $K\alpha_2$  contribution [12]. The peak positions were corrected for instrumental errors by measuring reference SRM LaB<sub>6</sub> 660 [13] on a (510)-Si wafer using the same acquisition parameters as used for the sample, except that the dwell time per step was 1 s.

The (111) and (200) peak positions determined of the  $(\text{Mn}_{1-x},\text{Fe}_x)\text{O}$  precipitates were also corrected for any residual stress, as determined by the so-called  $\sin^2\psi$ -method [11].

### 5.3 Results and discussion

The composition of  $(\text{Mn}_{1-x},\text{Fe}_x)\text{O}$  formed in a Fe-Mn binary alloy in thermodynamic equilibrium with a gaseous oxidizing environment as a function of oxygen partial pressure at 850, 950 and 1050  $^\circ\text{C}$  is presented in Figure 5.1(a). This diagram was calculated using Factsage [9] by considering thermodynamic equilibrium between a Fe-Mn alloy,  $(\text{Mn}_{1-x},\text{Fe}_x)\text{O}$  and a gas mixture of Ar + O<sub>2</sub> at atmospheric pressure. First, the thermodynamic data for the solid solution oxide  $(\text{Mn}_{1-x},\text{Fe}_x)\text{O}$  was taken from the FToxid database [8]. Then, a gas mixture of Ar and O<sub>2</sub> with a total pressure of 1 atm. at different oxygen partial pressures was created with thermodynamic data from the FactPS database [8]. Finally, a solid solution of Fe-Mn binary alloy with fcc crystal lattice was created with the thermodynamic data in the FSstel database [8].

Since MnO is more stable than FeO, the dissociation oxygen partial pressure of MnO is lower than that of FeO. Below the dissociation oxygen partial pressure of MnO, Fe and Mn form a solid solution. Above the dissociation oxygen partial pressure of MnO,  $(\text{Mn}_{1-x},\text{Fe}_x)\text{O}$  mixed oxide is formed and the concentration of Fe dissolved in the  $(\text{Mn}_{1-x},\text{Fe}_x)\text{O}$  increases with the ambient oxygen partial pressure. Above the dissociation oxygen partial pressure of FeO the entire alloy phase will oxidize and hence the concentration of Fe in  $(\text{Mn}_{1-x},\text{Fe}_x)\text{O}$  is constant. The dissociation oxygen partial pressure of both MnO and FeO increases with temperature; see Figure 5.1(b). Between the dissociation oxygen partial pressures of MnO and FeO, the concentration of Fe in the  $(\text{Mn}_{1-x},\text{Fe}_x)\text{O}$  decreases with temperature. Increasing Mn concentration in the Fe-Mn alloy from 1.0 to 2.5 at.% has a negligible effect on the Fe concentration in  $(\text{Mn}_{1-x},\text{Fe}_x)\text{O}$ . Also, the Fe concentration in  $(\text{Mn}_{1-x},\text{Fe}_x)\text{O}$  is

practically independent of the crystal lattice of the Fe-Mn alloy phase (i.e. ferrite or austenite).

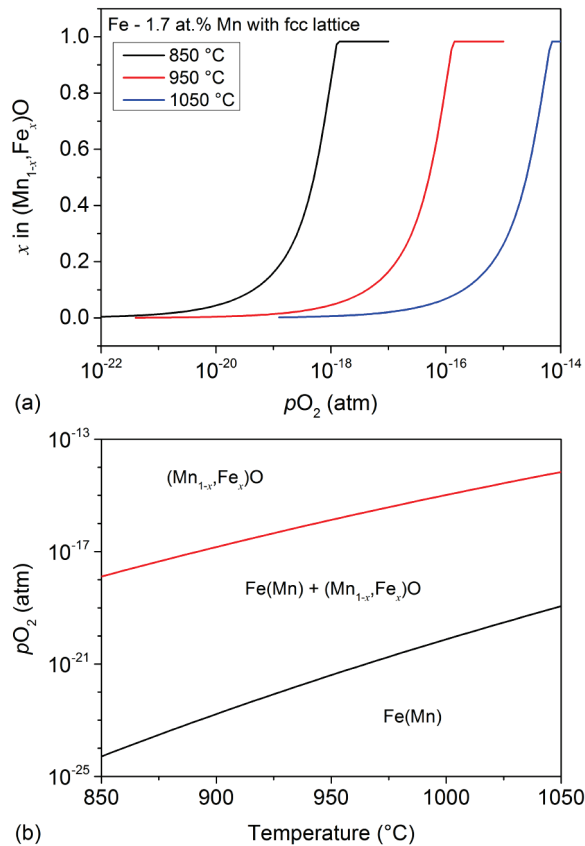


Figure 5.1: (a) Computed Fe concentration in  $(\text{Mn}_{1-x}\text{Fe}_x)\text{O}$  mixed oxide as a function of oxygen partial pressure (logarithm scale) at 850, 950 and 1050 °C in the Fe - Mn alloys with fcc crystal lattice at thermodynamic equilibrium with oxidizing gas atmosphere; (b) Computed phase diagram of Fe – 1.7 at.% Mn alloy with fcc crystal lattice in oxidizing gas atmosphere, black and red lines represent the dissociation oxygen partial pressure of MnO and FeO, respectively.

The concentration depth profiles of dissolved oxygen in the IOZ of steels alloyed with 1.0, 1.7 and 2.5 at.% Mn after annealing at 950 °C in a gas mixture of  $\text{N}_2$  plus 5 vol.%  $\text{H}_2$  with a dew point of 10 °C were calculated using a finite difference method considering the precipitation of oxides [2]. At 950 °C the mole fraction of dissolved oxygen at steel surface in equilibrium with the gas mixture of  $\text{N}_2$  plus 5 vol.%  $\text{H}_2$  with a dew point of 10 °C is about  $3.6 \times 10^{-6}$  [7]. For the diffusion coefficient of oxygen a value of  $3.5 \times 10^{-7} \text{ cm}^2/\text{s}$  [14] was adopted. As can be seen in Figure 5.2(a), the concentration of dissolved oxygen decreases almost linearly with depth. The concentration of dissolved oxygen at internal

oxidation front is practically zero. Since the depth of IOZ decreases with the bulk Mn concentration in the alloy, the concentration gradient of dissolved oxygen across the IOZ increases with the Mn concentration in the base alloy under the same ambient oxygen partial pressure.

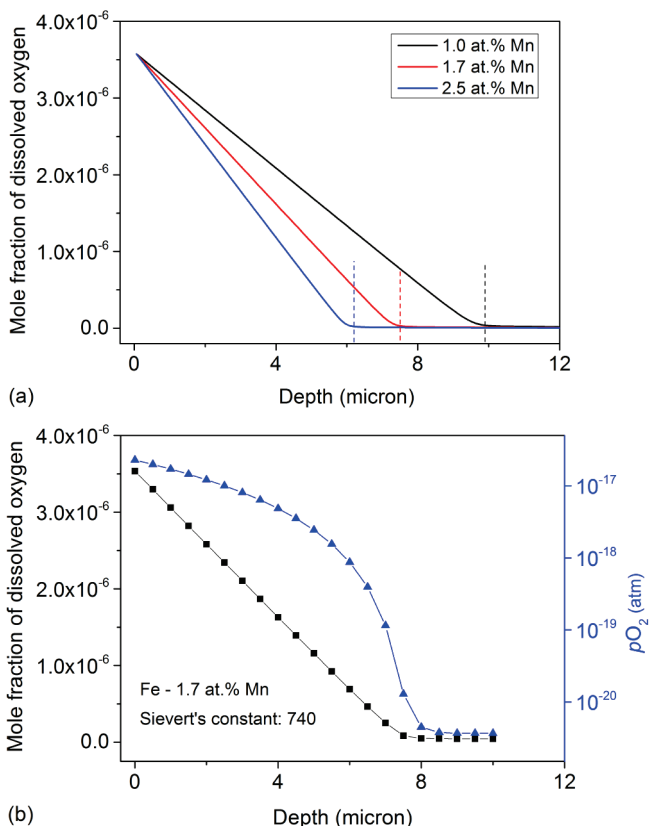


Figure 5.2: (a) Simulated concentration depth profiles of dissolved oxygen in steel alloyed with 1.0, 1.7 and 2.5 at.% Mn, respectively, after annealing at 950 °C for 1 hour in a  $N_2 + 5$  vol.%  $H_2$  gas mixture with a dew point of 10 °C, dashed lines indicate the internal oxidation front where the concentration of oxide precipitate is almost zero. (b) The corresponding oxygen activity depth profile expressed as oxygen partial pressure (logarithm scale) for the 1.7 at.% Mn alloyed steel.

Yet, the composition depth profile of  $(Mn_{1-x}Fe_x)O$  internal precipitates can be calculated using the thermodynamic tool [9] considering local thermodynamic equilibrium with the dissolved oxygen. To this end, the activity of dissolved oxygen is expressed in terms of the oxygen partial pressure ( $pO_2$  in atm.) using the Sievert's law [15]:

$$pO_2 = \left( \frac{N_O}{K_S} \right)^2 \quad (5.1)$$

where  $K_s$  is the Sievert's constant,  $N_{\text{O}}$  is the mole fraction of dissolved oxygen. The value of  $K_s$  for oxygen dissolution in iron is 739 at 950 °C [14]. Thus, the activity depth profile of dissolved oxygen in IOZ of the annealed Mn alloyed steels is obtained; see Figure 5.2(b). Next, the concentration of Fe dissolved in the  $(\text{Mn}_{1-x},\text{Fe}_x)\text{O}$  precipitates as a function of depth is determined from the composition diagram for  $(\text{Mn}_{1-x},\text{Fe}_x)\text{O}$ ; see Figure 5.1(a). It is predicted that the concentration of Fe in the internal  $(\text{Mn}_{1-x},\text{Fe}_x)\text{O}$  precipitates decreases continuously with depth until the Fe concentration in  $(\text{Mn}_{1-x},\text{Fe}_x)\text{O}$  becomes zero near internal oxidation front; see Figure 5.3. The Fe concentration in the  $(\text{Mn}_{1-x},\text{Fe}_x)\text{O}$  at steel surface is independent of bulk Mn concentration in steel; see Figure 5.3. However, the concentration gradient of Fe in the  $(\text{Mn}_{1-x},\text{Fe}_x)\text{O}$  precipitates increases with the bulk Mn concentration in the alloy, because the concentration gradient of dissolved oxygen increases with the bulk Mn concentration.

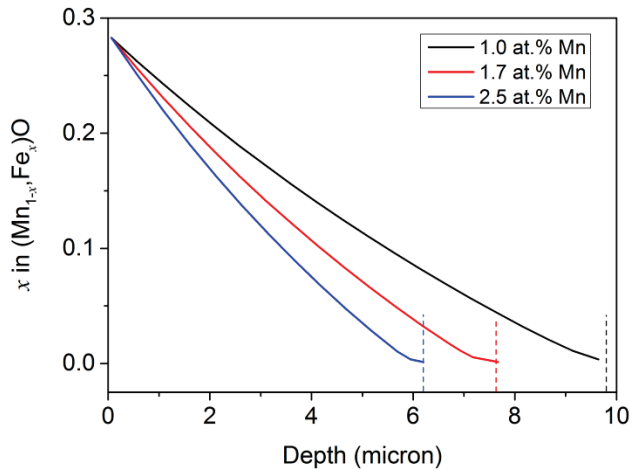


Figure 5.3: Predicted depth profiles of Fe concentration in internal  $(\text{Mn}_{1-x},\text{Fe}_x)\text{O}$  precipitates formed after annealing the 1.0, 1.7 and 2.5 at.% Mn alloyed steels at 950 °C for 1 hour in a  $\text{N}_2 + 5 \text{ vol.}\% \text{H}_2$  gas mixture with a dew point of 10 °C; dashed lines indicate the internal oxidation front where the concentration of oxide precipitate is almost zero.

The observed extent of the IOZ of the steel alloyed with 1.7 at.% Mn after annealing at 950 °C for 1 hour in  $\text{N}_2$  plus 5 vol.%  $\text{H}_2$  with a dew point of 10 °C is about 8.7  $\mu\text{m}$ ; see Figure 5.4(a). The lattice constant derived from XRD measurements of the internal  $(\text{Mn}_{1-x},\text{Fe}_x)\text{O}$  precipitates in the annealed steel alloyed with 1.7 at.% Mn increases with depth; see Table 5.1. The lattice constants of the  $\alpha$ -Fe matrix at different depths (about 2.867 Å) are close to the reported values of the  $\alpha$ -Fe lattice constant, i.e. 2.866 [16], 2.865 [17] and 2.868 Å [18]. Thus the effect of any hydrostatic stress, if present, on  $(\text{Mn}_{1-x},\text{Fe}_x)\text{O}$  precipitates is negligible. An in-plane residual stress in the  $(\text{Mn}_{1-x},\text{Fe}_x)\text{O}$  precipitates and the  $\alpha$ -Fe matrix

of the annealed 1.7 at.% Mn alloyed steel was not observed. The deviation from stoichiometry,  $\Delta$  in  $\text{Mn}_{1-\Delta}\text{O}$ , is small and thus can be neglected. The equilibrium value of  $\Delta$  in  $\text{Mn}_{1-\Delta}\text{O}$  at 950 °C is below 0.001 below an oxygen partial pressure of  $3 \times 10^{-17}$  atm [19] (which corresponds to a dew point of 12 °C in a gas mixture of  $\text{N}_2$  with 5 vol.%  $\text{H}_2$ ). This value of  $\Delta$  in  $(\text{Mn}_{1-x}\text{Fe}_x)_{1-\Delta}\text{O}$  increases with Fe concentration and oxygen partial pressure [6]. However, below an oxygen partial pressure of  $3 \times 10^{-17}$  atm. the equilibrium value of  $\Delta$  in  $(\text{Mn}_{1-x}\text{Fe}_x)_{1-\Delta}\text{O}$  computed with thermodynamic tool [8, 9] is below 0.0025 at 950 °C. Hence, the influence of cation deficiency on the lattice constant of  $(\text{Mn}_{1-x}\text{Fe}_x)\text{O}$  precipitates is negligible. Therefore, the change in the lattice constant of  $(\text{Mn}_{1-x}\text{Fe}_x)\text{O}$  precipitates in the annealed 1.7 at.% Mn alloyed steel is solely attributed to the change in their composition as a function of depth below the surface. The adopted lattice constant of pure MnO is 4.444 Å [7]. The lattice constant of  $\text{Fe}_{1-\Delta}\text{O}$  increases from about 4.28 to 4.31 Å with  $1-\Delta$  increasing from about 0.89 to 0.95 [20]. The extrapolated lattice constant for stoichiometric FeO equals about 4.334 Å [20]. The concentration of Fe in the  $(\text{Mn}_{1-x}\text{Fe}_x)\text{O}$  was then determined by linear interpolation of the measured lattice constant, i.e. adopting Vegard's law [21]. Since the lattice constant of  $(\text{Mn}_{1-x}\text{Fe}_x)\text{O}$  determined with XRD reflects an average value over a certain range of depth below the surface, its value is assigned to the analysis depth of 1.3  $\mu\text{m}$  below the surface; cf. Section Experimental. The thus obtained composition depth profile of the  $(\text{Mn}_{1-x}\text{Fe}_x)\text{O}$  internal precipitates in the annealed 1.7 at.% Mn alloyed steel is shown in Figure 5.4(b).

Table 5.1: Lattice constant of internal  $(\text{Mn}_{1-x}\text{Fe}_x)\text{O}$  and  $\alpha\text{-Fe}$  matrix in Å after each step of surface layer removal measured with grazing-incidence XRD analysis for 1.7 at.% Mn alloyed steel annealed at 950 °C for 1 hour in a  $\text{N}_2 + 5$  vol.%  $\text{H}_2$  gas mixture with a dew point of 10 °C.

Total thickness of removed surface layer ( $\mu\text{m}$ )	lattice constant of $(\text{Mn}_{1-x}\text{Fe}_x)\text{O}$ determined from (200) diffraction peak (Å)	lattice constant of $(\text{Mn}_{1-x}\text{Fe}_x)\text{O}$ determined from (111) diffraction peak (Å)	average lattice constant of $(\text{Mn}_{1-x}\text{Fe}_x)\text{O}$ (Å)	Lattice constant of $\alpha\text{-Fe}$ (Å)
0.0	4.4091±0.0003	4.4083±0.0004	4.4087±0.0007	2.8653±0.0002
0.9	4.4197±0.0003	4.4185±0.0004	4.4191±0.0009	2.8667±0.0002
2.0	4.4259±0.0009	4.4226±0.0011	4.4243±0.0027	2.8676±0.0005
2.8	4.4279±0.0009	4.4301±0.0011	4.4290±0.0021	2.8667±0.0005
3.9	4.4329±0.0009	4.4335±0.0011	4.4332±0.0013	2.8667±0.0005
5.3	4.4403±0.0009	4.4386±0.0011	4.4395±0.0019	2.8670±0.0005
6.7	4.4427±0.0003	4.4435±0.0004	4.4431±0.0007	2.8677±0.0002

As can be seen in Figure 5.1(a), the level of the oxygen partial pressure in the annealing atmosphere may strongly affect the composition depth profile of internal  $(\text{Mn}_{1-x},\text{Fe}_x)\text{O}$ . For example, a slight increase in oxygen partial pressure from  $2.3 \times 10^{-17}$  (corresponding to the oxygen partial pressure level at 950 °C in  $\text{N}_2 + 5 \text{ vol.}\% \text{H}_2$  gas mixture with dew point of 10 °C) to  $3.0 \times 10^{-17}$  atm. (corresponding to the oxygen partial pressure level at 950 °C in  $\text{N}_2 + 5 \text{ vol.}\% \text{H}_2$  gas mixture with dew point of 12 °C) increases the Fe concentration in the  $(\text{Mn}_{1-x},\text{Fe}_x)\text{O}$  from  $x$  of 0.28 to 0.34. Hence, a slight increase of the annealing dew point can significantly increase the Fe concentration in the internal  $(\text{Mn}_{1-x},\text{Fe}_x)\text{O}$  precipitates; see Figure 5.4(b). Considering that the cooling from the annealing temperature is fast (about 180 °C/min), the composition of the oxide precipitates is likely preserved. The experimentally determined profile of Fe concentration in the internal  $(\text{Mn}_{1-x},\text{Fe}_x)\text{O}$  of the annealed 1.7 at.% Mn alloyed steel fits perfectly to the profile predicted for a dew point of 12 °C rather than 10 °C; see Figure 5.4(b). Since this difference in dew point is within the experimental error of about 2 °C (cf. Section Experimental), it can be concluded that local thermodynamic equilibrium is established between the dissolved oxygen and the oxide precipitates in the IOZ of the annealed Mn alloyed steel.

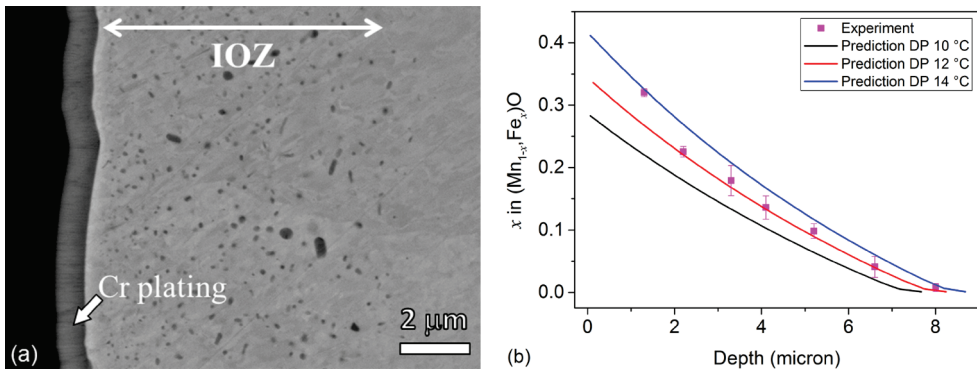


Figure 5.4: (a) SEM image of internal oxidation zone (IOZ) of steel alloyed with 1.7 at.% Mn after annealing at 950 °C for 1 hour in a  $\text{N}_2 + 5 \text{ vol.}\% \text{H}_2$  gas mixture with a dew point of 10 °C showing the oxide precipitates (dark spots in IOZ). (b) Predicted depth profiles of Fe concentration in the  $(\text{Mn}_{1-x},\text{Fe}_x)\text{O}$  precipitates formed after annealing 1.7 at.% Mn alloyed steel at 950 °C for 1 hour in a  $\text{N}_2 + 5 \text{ vol.}\% \text{H}_2$  gas mixture with dew points (DP) of 10, 12 and 14 °C. The dots represent the experimentally determined Fe concentration in the  $(\text{Mn}_{1-x},\text{Fe}_x)\text{O}$  precipitates formed after annealing the 1.7 at.% Mn alloyed steel at 950 °C for 1 hour in a  $\text{N}_2 + 5 \text{ vol.}\% \text{H}_2$  gas mixture with a dew point of about 10 °C.

Hence, the composition of the  $(\text{Mn}_{1-x},\text{Fe}_x)\text{O}$  precipitates in IOZ is determined by the activity of dissolved oxygen. Since the activity of dissolved oxygen decreases from the alloy surface towards the internal oxidation front, the composition of the  $(\text{Mn}_{1-x},\text{Fe}_x)\text{O}$

precipitates changes accordingly; i.e. the concentration of Fe in the  $(\text{Mn}_{1-x},\text{Fe}_x)\text{O}$  precipitates decreases as a function of depth below the surface. Therefore, it is anticipated that when oxidizing multi-element alloyed steels internally, the composition as well as the type of multiple oxide precipitates formed in the IOZ will change as a function of depth, depending on the local oxygen activities. For example, it has been observed that during internal oxidation of Ni-Al-Si alloy different types of oxides (i.e. spinels,  $\text{SiO}_2$ , and  $\text{Al}_2\text{O}_3$ ) are formed in the IOZ at different depths, and the sequence of those oxides formed with increasing depth is consistent with the increasing thermodynamic stability of those oxides [22].

## 5.4 Conclusions

Local thermodynamic equilibrium is established in the internal oxidation zone of Mn alloyed steels during annealing in an oxidizing environment. After internal oxidation of Mn alloyed steels mixed oxide precipitates  $(\text{Mn}_{1-x},\text{Fe}_x)\text{O}$  are formed even at oxygen partial pressures (dew points) in the gas ambient well below the dissociation oxygen partial pressure of Wüstite ( $\text{FeO}$ ). The composition of these  $(\text{Mn}_{1-x},\text{Fe}_x)\text{O}$  precipitates depends on the local activity of oxygen in the IOZ. Consequently, the concentration of Fe in the  $(\text{Mn}_{1-x},\text{Fe}_x)\text{O}$  precipitates decreases similar to the oxygen activity within the IOZ as a function of depth below the steel surface.

## References

- [1] G.M. Song, T. Vystavel, N. van der Pers, J.T.M. De Hosson and W.G. Sloof, *Acta Materialia*, **60** (2012), 2973.
- [2] V.A. Lashgari, G. Zimbitas, C. Kwakernaak and W.G. Sloof, *Oxidation of Metals*, **82** (2014), 249.
- [3] D. Huin, P. Flauder and J.B. Leblond, *Oxidation of Metals*, **64** (2005), 131.
- [4] J.B. Brunac, D. Huin and J.B. Leblond, *Oxidation of Metals*, **73** (2010), 565.
- [5] G. Zimbitas and W.G. Sloof, *Materials Science Forum*, **696** (2011), 82.
- [6] P. Franke and R. Dieckmann, *Journal of Physics and Chemistry of Solids*, **51** (1990), 49.
- [7] V.A. Lashgari, Ph.D. thesis, Delft University of Technology, 2014.
- [8] Factsage Database Documentation, <http://www.crct.polymtl.ca/fact/documentation/>.

- 
- [9] C. Bale, P. Chartrand, S.A. Degterov, G. Eriksson, K. Hack, R. Ben Mahfoud, J. Melancon, A.D. Pelton, S. Petersen, *CALPHAD*, **26** (2002), 189.
- [10] V.A. Lashgari, C. Kwakernaak, W.G. Sloof, *Oxid. Met.* **81** (2014) 435.
- [11] B.D. Cullity and S.R. Stock, *Elements of X-ray Diffraction*, third ed., Prentice Hall, New York, 2001.
- [12] W.A. Rachinger, *Journal of Scientific Instruments and of Physics in Industry*, **25** (1948), 254.
- [13] NIST, SRM 660a, Gaithersburg, 2000.
- [14] J.H. Swisher and E.T. Turkdogan, *Transactions of the Metallurgical Society of AIME*, **239** (1967), 426.
- [15] D.J. Young, *High Temperature Oxidation and Corrosion of Metals*, Elsevier, Oxford, 2008.
- [16] Powder Diffraction File 00-006-0696.
- [17] Powder Diffraction File 04-007-9753.
- [18] Powder Diffraction File 04-014-0360.
- [19] M. Keller and R. Dieckmann, *Berichte der Bunsengesellschaft für Physikalische Chemie*, **89** (1985), 883.
- [20] C. Haavik, S. Stolen, M. Hanfland and C.R.A. Catlow, *Physical Chemistry Chemical Physics*, **2** (2000), 5333.
- [21] L. Vegard, *Zeitschrift für Physik*, **5** (1921), 17.
- [22] H.C. Yi, S.Q. Shi, W.W. Smeltzer and A. Petric, *Oxidation of Metals*, **43** (1995), 115.





## Chapter 6

# Internal oxidation of Fe-Mn-Cr steel alloys, simulations and experiments<sup>1</sup>

### Abstract

A multi-element and multi-phase coupled thermodynamic kinetic internal oxidation model is developed to predict the internal oxidation behaviour of Fe-Mn-Cr steel alloys as a function of annealing time and oxygen partial pressure. To validate the simulation results, selected Fe-Mn-Cr steel alloys were annealed at 950 °C for 1 to 16 hours in a gas mixture of Ar with 5 vol.% H<sub>2</sub> and dew points of -30, -10 and 10 °C. The measured kinetics of internal oxidation as well as the concentration depth profiles of internal oxides in the annealed Fe-Mn-Cr steel alloys are in agreement with the predictions. Internal MnO and MnCr<sub>2</sub>O<sub>4</sub> are formed during annealing and both two oxides have a relatively low solubility product. Local thermodynamic equilibrium is established in the internal oxidation zone of Fe-Mn-Cr steel alloys during annealing and the internal oxidation kinetics are solely controlled by diffusion of oxygen. The internal oxidation of Fe-Mn-Cr steel alloys follows the parabolic rate law. The parabolic rate constant increases with the annealing dew point, but decreases with the concentration of the alloying elements.

### Keywords

FeMnCr steels, Annealing, Internal oxidation, Kinetics, Modelling

---

<sup>1</sup> This chapter is based on:

W. Mao, Y. Ma and W.G. Sloof, *Internal oxidation of Fe-Mn-Cr steels, simulations and experiments*, Oxidation of Metals, 2018.

## 6.1 Introduction

Advanced High Strength Steels (AHSS) are extensively used for automotive applications to reduce the weight of car bodies and thereby reducing fuel consumption and CO<sub>2</sub> emissions; see e.g. [1]. A zinc coating is applied onto the steel surface usually by hot-dip galvanizing [2] in order to protect the AHSS against corrosion. Before entering the zinc bath, the steel strip passes through continuous annealing furnaces. The annealing atmosphere is mostly a gas mixture of N<sub>2</sub> and H<sub>2</sub> with dew points ranging from -60 to 10 °C, whose oxygen partial pressure level is below the dissociation oxygen partial pressure of Wüstite (FeO). However, oxidation of the alloying elements (e.g. Mn, Cr, Si, Al) in AHSS is thermodynamically favourable during annealing process prior to galvanizing. The presence of these alloying element oxides at the steel surface reduces the zinc wettability [3] and thus impairs the quality of the galvanized steel product [4]. Hence, understanding the nature of oxidation of AHSS and predicting the oxidation behaviour of AHSS is essential to the steel industry in terms of designing new steel grades and optimizing annealing parameters.

The transition from internal to external oxidation as well as the kinetics of internal oxidation of Fe-Mn binary steel alloys have been studied extensively [5, 6]. It has been found that the internal oxidation behaviour of Fe-Mn binary steel alloys can be well described by the classical Wagner internal oxidation theory [7]. Recently, the thermodynamics of oxides formation in Fe-Mn-Cr ternary and Fe-Mn-Cr-Si quaternary steel alloys has been reported and the type of oxides formed during annealing of Fe-Mn-Cr steel alloys can be predicted as a function of alloy composition and oxygen partial pressure of annealing atmosphere [8]. However, the kinetics of internal oxidation of Fe-Mn-Cr steel alloys are not reported yet. Therefore, the aim of this study is to investigate the kinetics of internal oxidation of Fe-Mn-Cr ternary steel alloys under different oxygen partial pressures below the dissociation oxygen partial pressure of Wüstite. The internal oxidation behaviour of selected Fe-Mn-Cr steel alloys is first predicted by the newly developed coupled thermodynamic-kinetic internal oxidation model [9]. Then the predicted internal oxidation kinetics as well as the concentration depth profiles of internal oxides formed during oxidation are validated by comparison with experimental results.

## 6.2 Modelling of internal oxidation of Fe-Mn-Cr alloys

The concentration depth profiles of internal oxide precipitates as well as the solute atoms in the Fe-Mn-Cr steel alloys oxidized for different time and at different ambient oxygen partial pressures were simulated with a multi-element and multi-phase coupled

thermodynamic-kinetic (CTK) internal oxidation model [9], which is built on a similar model involving external oxidation [10]. The details of this CTK model are described elsewhere [9]. The schematics of the internal oxidation model and the flow chart of the simulation program are displayed in Figure 6.1. The alloy matrix is divided into a series of thin slices. Mass transport occurs between adjacent slices driven by the gradient of the chemical potential of each alloy constituent (i.e. alloying elements, iron and dissolved oxygen). Each slice is considered as a closed entity when conducting thermodynamic computation. At each time increment during oxidation, a two-step calculation procedure is executed. In the first step, the flux of each element between neighbouring slices is calculated and the change of the composition in each slice is obtained. In the second step, the thermodynamic equilibrium composition of each slice is calculated in terms of concentration of oxide precipitates and concentration of dissolved oxygen and alloying elements in the steel matrix. Thus, at each time step it is assumed that local thermodynamic equilibrium is instantaneously established between oxides, alloying elements and dissolved oxygen. This assumption is valid for the internal oxidation of Fe-Mn based steel alloys [11]. When annealing below dissociation oxygen partial pressure of FeO (Wüstite), the type of oxide phases formed in the Fe-Mn-Cr steel alloys with the compositions used in this study are MnO and MnCr<sub>2</sub>O<sub>4</sub> [8]. Hence, the precipitation of MnO and MnCr<sub>2</sub>O<sub>4</sub> are considered in the simulations. The possible dissolution of Fe in MnO and MnCr<sub>2</sub>O<sub>4</sub> is ignored. The amount of oxide precipitated in each slice and at each time increment is calculated considering mass balance and the solubility product,  $K_{sp}$ , of each oxide. The  $K_{sp}$  of MnO and MnCr<sub>2</sub>O<sub>4</sub> are defined as, respectively:

$$\begin{aligned} K_{sp_{\text{MnO}}} &= N_{\text{Mn}} N_{\text{O}} \\ K_{sp_{\text{MnCr}_2\text{O}_4}} &= N_{\text{Mn}} (N_{\text{Cr}})^2 (N_{\text{O}})^4 \end{aligned} \quad (6.1)$$

in which  $N_{\text{Mn}}$ ,  $N_{\text{Cr}}$  and  $N_{\text{O}}$  denote the local mole fraction of Mn, Cr and O dissolved in the alloy, respectively.

The change in Mn activity coefficient in austenite due to Cr addition is negligible according to thermodynamic computation [12]. Moreover, the effect of thermodynamic solute interaction between Mn and O on internal oxidation behaviour of Fe-Mn alloys is negligible [9]. Thus, the Fe-Mn-Cr steel alloys can be considered as ideal solutions. Hence, the solubility product of MnO and MnCr<sub>2</sub>O<sub>4</sub> as well as the diffusion coefficients of Mn, O and Cr in iron are considered as functions of temperature only, i.e. independent of local alloy composition. The adopted diffusion coefficients of oxygen, Mn and Cr in austenite at 950 °C are:  $3.5 \times 10^{-7}$  [13],  $4.0 \times 10^{-12}$  [6] and  $1.3 \times 10^{-12}$  [14] cm<sup>2</sup>/s, respectively. The solubility

products of  $\text{MnO}$  and  $\text{MnCr}_2\text{O}_4$  in austenite at  $950\text{ }^\circ\text{C}$  are computed with a thermodynamic tool [12], and equal  $2.4 \times 10^{-10}$  and  $3.0 \times 10^{-39}$ , respectively.

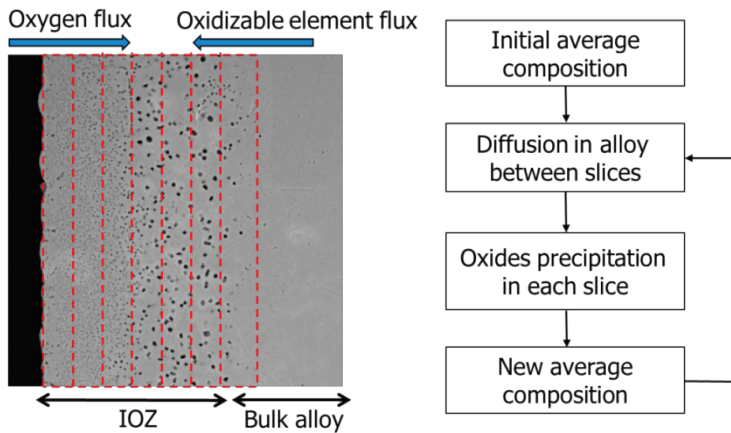


Figure 6.1: Schematics of the coupled thermodynamic-kinetic (CTK) internal oxidation model and the flow chart of the model's operation [9].

During the course of oxidation, the surface of steel alloys is considered to be in equilibrium with the annealing atmosphere. Hence, the concentration of dissolved oxygen at steel surface remains constant throughout the simulation. The concentration of oxygen dissolved at the surface of steel alloys can be calculated as a function of temperature, hydrogen volume fraction and dew point of the annealing atmosphere; see Appendix A.

## 6.3 Experiments

### 6.3.1 Samples

The chemical compositions of the Fe-Mn and Fe-Mn-Cr steel alloys are listed in Table 1. The steel samples were cut from hot rolled steel plates by electric discharge machining (EDM). Before annealing, the surface of all specimens was grinded with SiC emery paper and then polished with 1 micron diamond grains. Next, the samples were cleaned ultrasonically in isopropanol and dried by a flow of pure nitrogen (purity better than 5N). Finally, the samples were stored in air tight membrane boxes (Agar Scientific G3319, UK).

Table 6.1: Steel composition in atom percent (weight percent between brackets).

	C	Mn	Cr	Si	Al
Fe-1.7Mn	0.48 (0.10)	1.72 (1.70)	-	0.10 (0.05)	0.004 (0.002)
Fe-1.9Mn-1.0Cr	0.46 (0.10)	1.90 (1.88)	0.97 (0.91)	0.12 (0.06)	0.053 (0.026)
Fe-1.9Mn-1.6Cr	0.46 (0.10)	1.85 (1.83)	1.63 (1.53)	0.10 (0.05)	0.049 (0.024)

### 6.3.2 Annealing

The oxidation experiments were carried out in a horizontal quartz tube furnace (Carbolite MTF 12/38/850, UK) with tube inner diameter of 30 mm. The temperature in the furnace tube was measured with a NiCr/NiAl (type K) thermocouple at the sample location. A gas mixture of Ar with 5 vol.% H<sub>2</sub> passed the furnace tube at atmospheric pressure. Prior to admitting the gas mixtures to the furnace, the Ar and H<sub>2</sub> gases (all with a purity better than 5N) were filtered to remove any residual hydrocarbons, moisture and oxygen, with Accosorb (< 10 ppb hydrocarbons), Hydrosorb (<10 ppb H<sub>2</sub>O) and Oxsorb (< 5 ppb O<sub>2</sub>) filters (Messer Griesheim, Germany), respectively. De-aerated and deionized water (18.2 MΩ.cm at 25 °C) was evaporated with an in the gas line controlled evaporator mixer (CEM, Bronkhorst, The Netherlands) to create specific dew points of -45, -30, -10 and 10 °C in the furnace. These dew points correspond to oxygen partial pressure of  $8.1 \times 10^{-22}$ ,  $2.2 \times 10^{-20}$ ,  $1.0 \times 10^{-18}$  and  $2.3 \times 10^{-17}$  atm. at 950 °C; see Appendix A. The pure water was de-aerated with nitrogen in a closed pressurized stainless-steel vessel and the concentration of oxygen dissolved in the pure water was below 100 ppb, as measured with an O<sub>2</sub> sensor (InPro 6850i, Mettler Toledo, USA). The dew points of -10 and 10 °C were monitored with a cooled mirror analyser (Optidew, Michell Instruments, UK). The dew points of -45 and -30 °C were monitored with another cooled mirror analyser (S4000 TRS, Michell Instruments, UK). The fluctuation of dew points during annealing was within  $\pm 2$  °C. The partial pressure of evaporated H<sub>2</sub>O in the gas mixture is related to dew point according to the formula given in the Appendix A. The flow of each gas was regulated and monitored using mass flow controllers (Bronkhorst, The Netherlands). The flow rate of gas mixture with dew points of -30 to 10 °C was 1500 sccm, while the flow rate of gas mixture with dew points of -45 was 3000 sccm. Before annealing, the sample was placed onto a quartz boat located at the cold zone of the furnace tube. Then, the furnace was closed and flushed with the Ar + 5 vol.% H<sub>2</sub> gas mixture for more than 30 minutes. Next, the sample was moved to the hot zone of the furnace with a quartz rod to start an annealing cycle. The annealing times were 1, 4 and 16 hours. At the end of the annealing cycle, the sample was moved in the reverse direction to the cold zone of the furnace tube. The heating and cooling of the sample was relatively fast, about 140 and 180 °C/min, respectively.

### 6.3.3 Characterization

X-ray diffractometry (XRD) was used to identify the oxide phases formed in the steel alloys after annealing. The XRD patterns were recorded, with a Bruker D8 Advance diffractometer in the Bragg-Brentano geometry using Co K $\alpha$  radiation, in the 2 $\theta$  region between 10 and 110° with a step size of 0.034° and a dwell time of 4 s. The depth below the

surface corresponding with 70 % of the diffracted intensity of pure iron is about 2.3 to 6.7  $\mu\text{m}$  for  $2\theta$  from  $20^\circ$  to  $60^\circ$  [15].

The surfaces and cross-sections of the annealed samples were observed with scanning electron microscopy (SEM) using a JSM-6500F (JEOL, Japan) operated with an accelerating voltage of 5 and 15 kV, respectively. X-ray microanalysis (XMA) using Energy Dispersive Spectroscopy (EDS) was performed with the same SEM instrument, but equipped with an UltraDry 30  $\text{mm}^2$  detector (Thermo Fisher Scientific, USA) to determine the chemical composition of oxides qualitatively. The depth of internal oxidation zone (IOZ) was measured with SEM on backscattered electron images of cross-section of oxidized samples. The volume fraction of internal oxide precipitates was determined from the backscattered electron images of cross-section of oxidized samples using the image processing software ImageJ (version 1.47s).

The concentration of Fe, Mn, Cr and O was determined with electron probe X-ray microanalysis (EPMA). The analysis was performed with a JXA 8900R (JEOL, Japan) microprobe employing Wavelength Dispersive Spectrometry (WDS). A focussed electron beam was used with an energy of 10 keV and a current of 50 nA. The composition at each analysis location of the sample was determined using the X-ray intensities of the constituting elements after background correction relative to the corresponding intensities of reference materials. In this case, the X-ray intensities of Fe-K $\alpha$ , Mn-K $\alpha$ , Cr-K $\alpha$  and O-K $\alpha$  were measured and pure Fe, Mn, Cr and SiO<sub>2</sub> were used as references. The thus obtained intensity ratios were processed with a matrix correction program CITZAF [16]. The concentration depth profiles of Mn, Cr and O were determined from the cross-section of the oxidized samples. An average concentration of each element at each depth was obtained from a line parallel to the sample surface consisting of 40 measurement points. The distance between adjacent measurement points was 1  $\mu\text{m}$ . The distance between the adjacent lines (i.e. at different depths) parallel to the sample surface was also 1  $\mu\text{m}$ . In order to prevent carbon contamination, an air jet cleaning the surface was employed during the EPMA measurements.

## **6.4 Results and discussion**

### **6.4.1 Transition from external to internal oxidation**

Increasing the oxygen partial pressure in the annealing atmosphere (i.e. the dew point) promotes the internal oxidation of Fe-Mn-Cr steel alloys. Figure 6.2 shows the back scattered electron images of the surface and cross-section of the Fe-1.9Mn-1.6Cr steel

annealed at 950 °C for 16 hours in an Ar + 5 vol.% H<sub>2</sub> gas mixture with dew points from -45 to 10 °C. When annealing at a dew point of -45 °C, the Fe-1.9Mn-1.6Cr steel alloys are externally oxidized, since the oxides are mainly formed at steel surface. The transition from external to internal oxidation of the Fe-1.9Mn-1.6Cr steel alloys occurs at an annealing dew point of -30 °C, with oxides formed both at steel surface and in the alloy matrix. The Fe-1.9Mn-1.6Cr steel alloys are internally oxidized when annealed at dew points of -10 and 10 °C. According to the results of XRD and XMA, the oxide formed during annealing at a dew point of -45 °C is (Mn,Cr,Fe)<sub>3</sub>O<sub>4</sub> spinel, while annealing at dew points of -30, -10 and 10 °C forms both the (Mn,Cr,Fe)<sub>3</sub>O<sub>4</sub> spinel and (Mn,Fe)O at the steel surface and as internal precipitates. The type of oxide species identified in the Fe-Mn-Cr steel alloys annealed at dew points from -45 to 10 °C is in agreement with the phase diagrams and experimental results reported in ref. [8]. Annealing Si free Fe-Mn-Cr ternary alloys does not form internal oxides along grain boundaries [17]. However, the Fe-Mn-Cr steel samples used in this study contain 0.1 at.% Si (see Table 6.1), and the formation of internal (Mn,Fe)<sub>2</sub>SiO<sub>4</sub> and (Mn,Cr,Fe)<sub>3</sub>O<sub>4</sub> along grain boundaries was observed; see Figure 6.2. The penetration depth of oxides along grain boundaries is much larger (by a factor of 2 and more) than that of internal oxides formed inside grains.

#### 6.4.2 Concentration depth profiles

Figure 6.3 shows the simulated concentration depth profiles of internal MnO and MnCr<sub>2</sub>O<sub>4</sub> precipitates as well as the Mn, Cr and O dissolved in iron matrix after annealing a Fe – 1.8 at.% Mn – 1.5 at.% Cr alloy at 950 °C for 16 hours in a Ar + 5 vol.% H<sub>2</sub> gas mixture with a dew point of 10 °C (corresponding oxygen partial pressure of  $2.3 \times 10^{-17}$  atm.). The formation of an internal oxidation zone of MnO and MnCr<sub>2</sub>O<sub>4</sub> beneath the steel surface is predicted, which agrees with the experimental observation; see Figure 6.2. The concentrations of internal MnO and MnCr<sub>2</sub>O<sub>4</sub> are almost constant in the internal oxidation zone, and drop sharply to zero. The width of the internal oxidation zone of MnO is almost the same as that of MnCr<sub>2</sub>O<sub>4</sub>. The solute Mn and Cr in the iron matrix are depleted within the internal oxidation zone, while their concentrations increase to bulk values beyond the internal oxidation front. The concentration depth profiles of MnO, MnCr<sub>2</sub>O<sub>4</sub> and solute Mn and Cr as shown in Figure 6.3 indicate that both MnO and MnCr<sub>2</sub>O<sub>4</sub> can be considered as oxides with a low solubility product [6, 18]. The concentration of oxygen dissolved in iron matrix decreases almost linearly with the depth below the surface to practically zero at internal oxidation front.



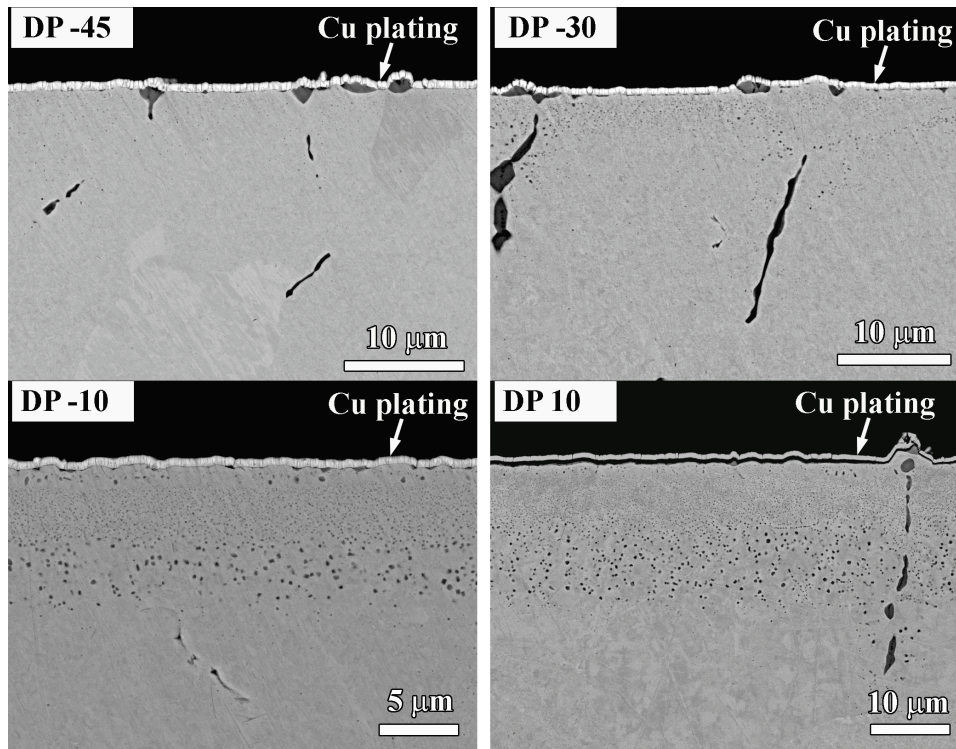


Figure 6.2: SEM backscattered electron images of surface and cross-section of the Fe - 1.9 at.% Mn - 1.6 at.% Cr steels annealed for 16 hours at 950 °C in a gas mixture of Ar with 5 vol.% H<sub>2</sub> and dew points (DP) of -45, -30, -10 and 10 °C (oxygen partial pressure of  $8.1 \times 10^{-22}$ ,  $2.2 \times 10^{-20}$ ,  $1.0 \times 10^{-18}$  and  $2.3 \times 10^{-17}$  atm., respectively). The Fe-Mn-Cr steel alloys are internally oxidized above an annealing dew point of -30 °C. The Si impurity in the steel alloys leads to the formation of  $(\text{Mn,Fe})_2\text{SiO}_4$  and  $(\text{Mn,Cr,Fe})_3\text{O}_4$  along grain boundaries.

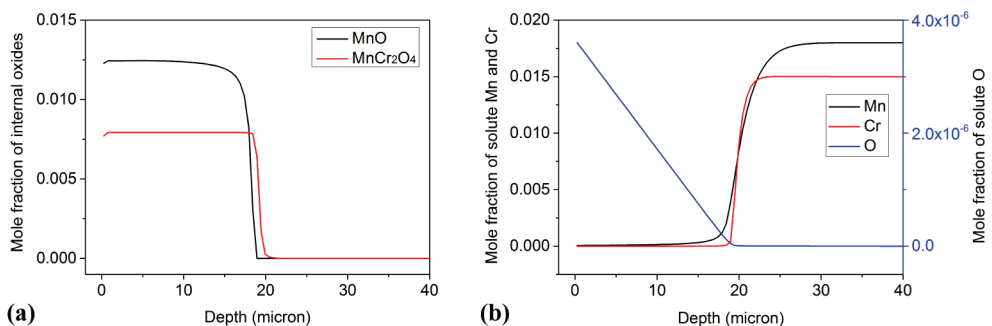


Figure 6.3: Simulated concentration depth profiles of (a) internal oxides and (b) solute Mn, Cr and O after annealing a Fe - 1.8 at.% Mn - 1.5 at.% Cr alloy at 950 °C for 16 hours in a Ar + 5 vol.% H<sub>2</sub> gas mixture with a dew point of 10 °C (corresponding oxygen partial pressure of  $2.3 \times 10^{-17}$  atm.).

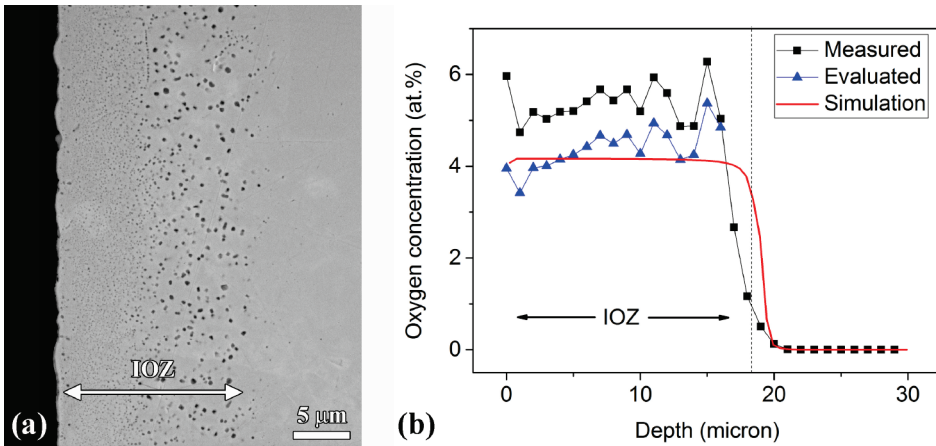


Figure 6.4: (a) SEM image (backscattered electrons) of the cross-section of the Fe - 1.9 at.% Mn - 1.6 at.% Cr steel where EPMA measurements were performed, and (b) simulated and measured (with EPMA) depth profiles of total oxygen concentration (oxygen in oxides and iron matrix) in the steel alloy, after annealing for 16 hours at 950 °C in a gas mixture of Ar with 5 vol.% H<sub>2</sub> and a dew point of 10 °C (oxygen partial pressure of  $2.3 \times 10^{-17}$  atm.). The dashed line indicates the internal oxidation front observed.

The simulated concentration depth profile of oxygen in the Fe-1.9Mn-1.6Cr steel alloy annealed at a dew point of 10 °C is in good agreement with the experimental results; see Figure 6.4. Since the concentration of solute oxygen in the iron matrix (maximum 3.6 ppm, see Figure 6.3) is much below the detection limit of EPMA, the measured oxygen concentration reflects the concentration of internal oxides. Once the ratio of MnO to MnCr<sub>2</sub>O<sub>4</sub> concentration is known (see below), the volume fraction of internal oxides at each depth can be estimated from the oxygen concentration measured with EPMA, taking the molar volume of iron, MnO and MnCr<sub>2</sub>O<sub>4</sub> as: 7.1, 13.1 and 45.0 cm<sup>3</sup>/mol, respectively. The depth profile of volume fraction of internal oxides determined by image analysis agrees with that obtained from the EPMA measurement; see Figure 6.5. Both the results of EPMA measurement and image analysis show that the concentration of oxide precipitates is almost constant in the internal oxidation zone and drops sharply to zero at a depth of about 17 μm; see Figures 6.4 (b) and 6.5. Although the volume fractions (concentrations) of internal oxides at different depths are almost the same, the size and the number density of oxide precipitates may vary with depth; see Figure 6.4 (a). Since the nucleation and growth of oxide precipitates in austenite matrix is beyond the scope of this study, only a qualitative explanation for the variation of size and number density of oxide precipitates with depth is given here. Since the solubility product of MnO and MnCr<sub>2</sub>O<sub>4</sub> in austenite are low, the formation of internal oxides mainly takes place near the internal oxidation front [14]. The driving force for oxide precipitation at internal oxidation front depends on the local

supersaturation of oxygen solute in alloy matrix, and at a small time step the amount of supersaturated solute oxygen increases with the inward oxygen flux at the internal oxidation front. Since the concentration of solute oxygen decreases almost linearly with depth (see Figure 6.2 (b)), the oxygen flux at internal oxidation front can be approximated from the gradient of solute oxygen within internal oxidation zone using the Fick's 1<sup>st</sup> law. Apparently, the gradient of solute oxygen concentration decreases with depth of internal oxidation zone. Hence, the driving force for oxide precipitation at internal oxidation front decreases with the width of the internal oxidation zone, and accordingly the size of the oxide precipitate increases while the number density decreases with depth. The change in the size and number density of oxide precipitates with depth while maintaining an almost constant oxide concentration also indicates that during 16 hours oxidation of the Fe-Mn-Cr steel alloy the precipitation of MnO and MnCr<sub>2</sub>O<sub>4</sub> (reaction between solute O, Mn and Cr) at internal oxidation front is fast compared with the progression of internal oxidation front, and thus the local thermodynamic equilibrium is likely established during the internal oxidation process. The increase of the size and the decrease of the number density of oxide precipitates with depth is also observed for internal oxidation of Fe – 7 at.% Mn binary steel alloys [5].

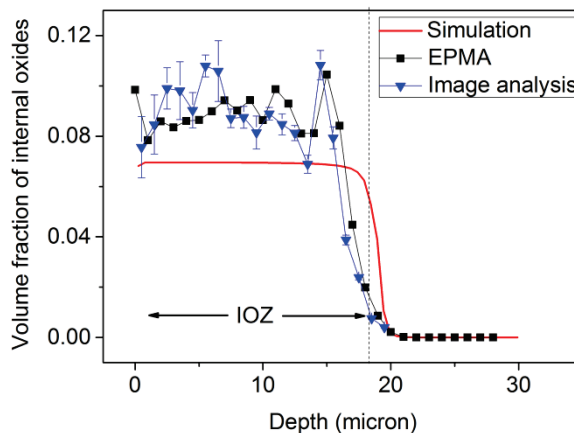


Figure 6.5: Simulated and measured depth profiles of the volume fraction of internal oxides in the Fe - 1.9 at.% Mn - 1.6 at.% Cr steel alloy after annealing for 16 hours at 950 °C in a gas mixture of Ar with 5 vol.% H<sub>2</sub> and a dew point of 10 °C (oxygen partial pressure of  $2.3 \times 10^{-17}$  atm.). The dashed line indicates the internal oxidation front observed; see Figure 6.4 (a).

Since the solubility products of MnO and MnCr<sub>2</sub>O<sub>4</sub> are low, the concentration of both Mn and Cr that remains in the alloy matrix within the internal oxidation zone can be neglected; see Figure 6.3 (b). Hence, the Mn and Cr detected with EPMA within the internal oxidation zone are those present in the oxide precipitates. Since Cr only exists in the MnCr<sub>2</sub>O<sub>4</sub> spinel

and the molar ratio of Mn to Cr in  $\text{MnCr}_2\text{O}_4$  is 1:2, the concentration of MnO and  $\text{MnCr}_2\text{O}_4$  at each depth of the oxidized Fe-Mn-Cr steel alloys can be evaluated from the measured concentration of Mn and Cr with EPMA within the internal oxidation zone. The experimental results show that the concentration of each type of oxides (i.e. MnO and  $\text{MnCr}_2\text{O}_4$ ) within the internal oxidation zone of the annealed Fe-1.9Mn-1.6Cr steel alloy is almost constant with depth, which is in agreement with the above predictions; see Figure 6.6. The concentration ratio of MnO to  $\text{MnCr}_2\text{O}_4$  is almost a constant, equal to 3:2 within the internal oxidation zone, and drops sharply to zero at the internal oxidation front; see Figure 6.6 (b). The experimental results confirm the prediction that the penetration depth of internal MnO is almost the same as that of  $\text{MnCr}_2\text{O}_4$  for internal oxidation of Fe-Mn-Cr steel alloys; see Figures 6.3 (a) and 6.6.

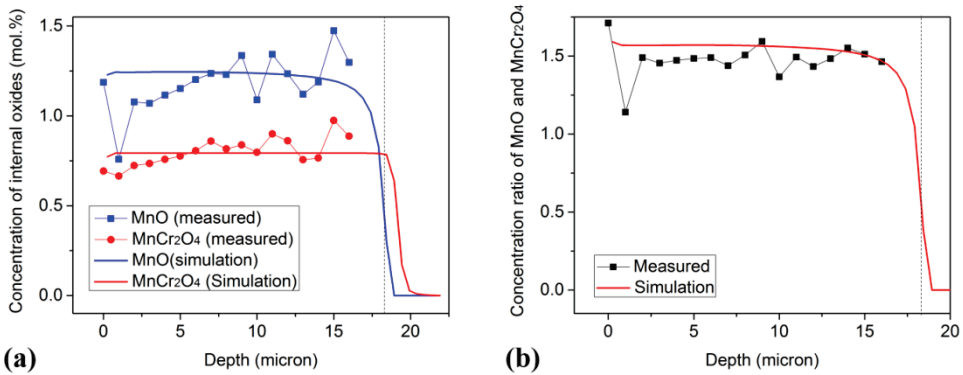


Figure 6.6: (a) Simulated and measured (EPMA) concentration depth profiles of internal MnO and  $\text{MnCr}_2\text{O}_4$ , and (b) the corresponding ratio of concentration of MnO to  $\text{MnCr}_2\text{O}_4$  as a function of depth in Fe - 1.9 at.% Mn - 1.6 at.% Cr steel alloy after annealing for 16 hours at 950 °C in a gas mixture of Ar with 5 vol.%  $\text{H}_2$  and a dew point of 10 °C (oxygen partial pressure of  $2.3 \times 10^{-17}$  atm.). The dashed line indicates the internal oxidation front observed; see Figure 6.4 (a).

The oxygen concentration within the internal oxidation zone can also be evaluated from the measured concentrations of Mn and Cr with EPMA considering the stoichiometry of MnO and  $\text{MnCr}_2\text{O}_4$  and also that all Mn and Cr within the internal oxidation zone are oxidized. However, the evaluated oxygen concentration based on Mn and Cr concentration is slightly lower than the oxygen concentration directly obtained from EPMA; see Figure 6.4 (b). This is caused by the dissolution of Fe in the internal MnO and  $\text{MnCr}_2\text{O}_4$  particles to form  $(\text{Mn,Fe})\text{O}$  and  $(\text{Mn,Cr,Fe})_3\text{O}_4$  oxide solutions, respectively [8, 11]. For example, at 950 °C and with an oxygen partial pressure of  $2.3 \times 10^{-17}$  atm (corresponding to Ar with 5 vol.%  $\text{H}_2$  and dew point of 10 °C), the Fe fraction in cations of  $(\text{Mn,Fe})\text{O}$  and  $(\text{Mn,Cr,Fe})_3\text{O}_4$  for a Fe - Mn - Cr alloy system at equilibrium is about 0.31 and 0.12, respectively, and the amount

of Fe in both oxides increases with the oxygen partial pressure [8]. The concentration of solute oxygen within the internal oxidation zone of the annealed Fe-1.9Mn-1.6Cr steel alloy decreases almost linearly with depth below the surface; cf. Figure 6.3 (b). The corresponding depth profile of oxygen activity expressed in terms of the logarithm of oxygen partial pressure (in atm.) is then obtained adopting Sievert's law [11]; see Figure 6.7 (a). Next, the Fe concentration in  $(\text{Mn,Fe})\text{O}$  and  $(\text{Mn,Cr,Fe})_3\text{O}_4$  as a function of oxygen partial pressure in a Fe – 1.9 at.% Mn – 1.6 at.% Cr alloy system at equilibrium is computed with a thermodynamic tool [12]. Then, the estimated amount of excess oxygen consumed by Fe at each depth is obtained, considering that the concentration ratio of MnO to  $\text{MnCr}_2\text{O}_4$  is 3:2; see above. Figure 6.7 (b) shows the predicted and measured ratio of the total concentration of precipitated oxygen to the concentration of oxygen consumed by Mn and Cr as a function of depth in the annealed Fe-1.9Mn-1.6Cr steel alloy. Both predicted and experimental results show the trend that the concentration of Fe in the internal oxides decreases with depth to almost zero near the internal oxidation front.

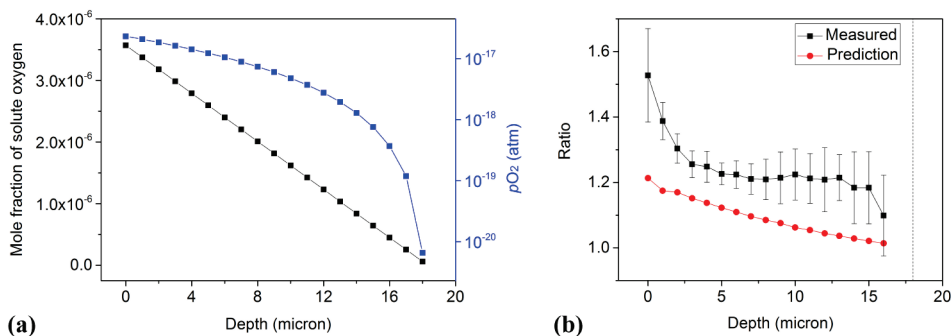


Figure 6.7: (a) Predicted depth profiles of solute oxygen concentration and the corresponding oxygen activity (expressed as oxygen partial pressure ( $p\text{O}_2$ ) on logarithm scale) within the internal oxidation zone, and (b) depth profiles of predicted and measured ratio of the total precipitated oxygen concentration to the concentration of oxygen consumed by Mn and Cr, in Fe - 1.9 at.% Mn - 1.6 at.% Cr steel alloy after annealing for 16 hours at 950 °C in a gas mixture of Ar with 5 vol.%  $\text{H}_2$  and a dew point of 10 °C (oxygen partial pressure of  $2.3 \times 10^{-17}$  atm.). The dashed line indicates the internal oxidation front observed; see Figure 6.4 (a).

The predicted and measured depth profiles of internal oxide volume fraction are in reasonable agreement for the Fe-1.9Mn-1.6Cr steel alloy annealed in a gas mixture of Ar with 5 vol.%  $\text{H}_2$  and a dew point of -10 °C (oxygen partial pressure of  $1.0 \times 10^{-18}$  atm.); see Figure 6.8. According to the EMPA results, the size of the internal oxidation zone of MnO is close to that of  $\text{MnCr}_2\text{O}_4$ . The measured concentration of internal oxides within the internal oxidation zone of the Fe-1.9Mn-1.6Cr steel alloy annealed at a dew point of -10 °C is still almost constant and decreases sharply to zero at the internal oxidation front. A

relatively sharp internal oxidation front can also be observed from the SEM images. Thus, the depth of internal oxidation zone in Fe-Mn-Cr steel alloys annealed at dew points of -10 and 10 °C can be determined precisely, and the kinetics of internal oxidation of Fe-Mn-Cr steel alloys can be quantified accurately.

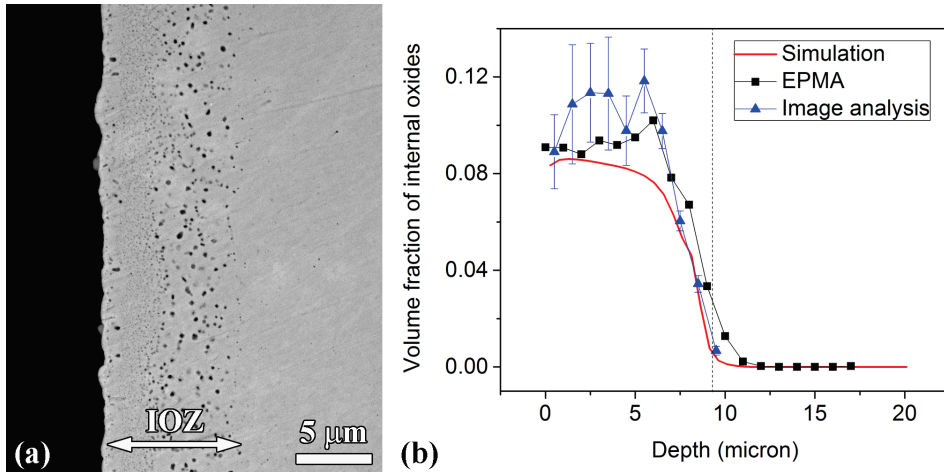


Figure 6.8: (a) SEM backscattered electron image of the cross-section of Fe - 1.9 at.% Mn - 1.6 at.% Cr steel at the location where EPMA measurements were performed, and (b) simulated and measured (EPMA and image analysis) depth profiles of volume fraction of internal oxides in the steel alloy, after annealing for 16 hours at 950 °C in a gas mixture of Ar with 5 vol.% H<sub>2</sub> and a dew point of -10 °C (oxygen partial pressure of  $1.0 \times 10^{-18}$  atm.). The dashed line indicates the internal oxidation front observed.

### 6.4.3 Kinetics of internal oxidation

The measured kinetics of internal oxidation of the Fe-1.9Mn-1.6Cr steel alloy annealed at dew points of -10 and 10 °C are in good agreement with the predictions using the coupled thermodynamic-kinetic model; see Figures 6.5, 6.8 and 6.9. The growth of internal oxidation zone of Fe-Mn-Cr steel alloys during annealing follows the parabolic rate law (see Figure 6.9), which can be described as:

$$\xi^2 = 2k_p t \quad (6.2)$$

where  $\xi$  is the depth of internal oxidation zone,  $t$  is oxidation time and  $k_p$  is the parabolic rate constant. Hence, the internal oxidation kinetics of Fe-Mn-Cr steel alloys are solely controlled by diffusion of the reacting elements (i.e. O, Mn and Cr), while the precipitation of internal oxides can be considered to occur instantaneously. Therefore, local thermodynamic equilibrium between oxides and solute elements (O, Mn and Cr) in alloy matrix within internal oxidation zone is established during internal oxidation of Fe-Mn-Cr steel alloys. The parabolic growth behaviour of internal oxidation zone also shows that the



Fe-Mn-Cr steel surface is in equilibrium with gas ambient during annealing, i.e. the concentration of oxygen dissolved at steel surface is constant with annealing time.

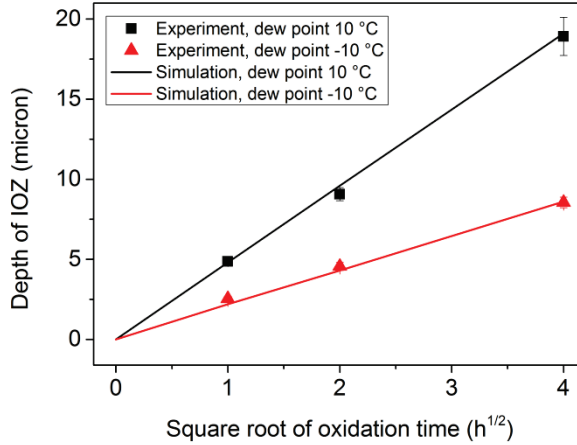


Figure 6.9: Predicted and measured internal oxidation kinetics (in terms of depth of the internal oxidation zone (IOZ) versus the square root of oxidation time) of Fe - 1.9 at.% Mn - 1.6 at.% Cr steel alloy annealed at 950 °C in a gas mixture of Ar with 5 vol.% H<sub>2</sub> and dew points of -10 and 10 °C (oxygen partial pressure of  $1.0 \times 10^{-18}$  and  $2.3 \times 10^{-17}$  atm., respectively).

An alternative method for estimating the parabolic rate constant is the analytical approach using the extended Wagner internal oxidation theory for ternary alloys [19]. The use of this method is justified, since the following three criteria are met for internal oxidation of Fe-Mn-Cr steel alloys annealed at dew points above -10 °C, namely: (i) similar size of internal oxidation zone of MnO and MnCr<sub>2</sub>O<sub>4</sub>, (ii) low solubility product for both MnO and MnCr<sub>2</sub>O<sub>4</sub>, and (iii) the establishment of local thermodynamic equilibrium. The parabolic rate constant  $k_p$  is given by:

$$k_p = 2\gamma^2 D_O \quad (6.3)$$

in which  $\gamma$  is a dimensionless parameter and  $D_O$  is the diffusion coefficient of oxygen in alloy matrix. The value of  $\gamma$  can be obtained by solving the following equation [19]

$$N_O^s = \frac{\nu N_{Mn}^0 G(\gamma)}{F(\gamma \sqrt{D_O / D_{Mn}})} + \frac{w N_{Cr}^0 G(\gamma)}{F(\gamma \sqrt{D_O / D_{Cr}})} \quad (6.4)$$

where  $N_O^s$  is the mole fraction of oxygen dissolved at steel surface,  $N_{Mn}^0$  and  $N_{Cr}^0$  are the mole fraction of the solute Mn and Cr in the bulk alloy,  $D_{Mn}$  and  $D_{Cr}$  are the diffusion coefficient of Mn and Cr in the alloy matrix,  $\nu$  and  $w$  are the stoichiometry oxygen-to-metal ratio of MnO and Cr<sub>2</sub>O<sub>3</sub> (i.e.  $\nu = 1$ ,  $w = 1.5$ ), respectively. Although MnCr<sub>2</sub>O<sub>4</sub> is actually formed instead of Cr<sub>2</sub>O<sub>3</sub> during annealing of Fe-Mn-Cr steel alloys, the amount of

oxygen consumed by oxidizing one mole of Cr equals 1.5 mole O.  $G(r)$  and  $F(r)$  are two auxiliary functions, which reads:

$$\begin{aligned} G(r) &= \pi^{1/2} r \exp(r^2) \operatorname{erf}(r) \\ F(r) &= \pi^{1/2} r \exp(r^2) \operatorname{erfc}(r) \end{aligned} \quad (6.5)$$

When the permeability [14] of oxygen is much higher than that of Mn and Cr, i.e.  $N_{\text{O}}^s D_{\text{O}} \gg N_{\text{Mn}}^0 D_{\text{Mn}}$  and  $N_{\text{O}}^s D_{\text{O}} \gg N_{\text{Cr}}^0 D_{\text{Cr}}$ , Eq. (6.4) can be simplified and  $\gamma$  can be approximated as:

$$\gamma = \left( \frac{N_{\text{O}}^s}{2vN_{\text{Mn}}^0 + 2wN_{\text{Cr}}^0} \right)^{1/2} \quad (6.6)$$

The experimentally determined parabolic rate constants for internal oxidation of Fe-Mn-Cr steel alloys are in good agreement with the calculated results using the extended Wagner approach [19]; see Table 6.2. The parabolic rate constants obtained from Eq. (6.4) and (6.6) are almost the same (see Table 6.2), which indicates that the permeability of oxygen is much higher than the permeability of Mn and Cr for the steel alloys studied here when annealing at dew points of -10 and 10 °C. Hence, the kinetics of internal oxidation of the Fe-Mn and Fe-Mn-Cr steel alloys annealed at dew points of -10 and 10 °C are dominated by the bulk alloy composition and the oxygen permeability; see Eqs (6.3) and (6.6). Adding Cr to the Fe-Mn steels decreases the internal oxidation rate simply because of the consumption of solute oxygen by forming  $\text{MnCr}_2\text{O}_4$ . The growth rate of internal oxidation zone increases with ambient oxygen partial pressure (i.e. annealing dew point) because the inward oxygen flux increases with the concentration of oxygen dissolved at steel surface.

Table 6.2: Measured and calculated parabolic rate constants for internal oxidation of Fe-Mn and Fe-Mn-Cr steel alloys annealed at 950 °C in a gas mixture of Ar with 5 vol.%  $\text{H}_2$  and dew points of -10 and 10 °C.

Dew point (°C)	Sample	Measured $k_p$ ( $\mu\text{m}^2/\text{h}$ )	Calculated $k_p$	Calculated $k_p$
			( $\mu\text{m}^2/\text{h}$ ) (general; cf. Eq. (6.4))	( $\mu\text{m}^2/\text{h}$ ) (simplified; cf. Eq. (6.6))
10	Fe-1.9Mn-1.6Cr	11.1	9.8	10.6
	Fe-1.9Mn-1.0Cr	12.3	13.0	13.5
	Fe-1.7Mn	24.8 [6]	25.5	26.8
-10	Fe-1.9Mn-1.6Cr	2.3	1.7	2.2
	Fe-1.9Mn-1.0Cr	3.0	2.2	2.9
	Fe-1.7Mn	5.5	4.6	5.7

However, the extended Wagner approach may not be valid for estimating the internal oxidation kinetics of Fe-Mn-Cr steel alloys annealed at a dew point of -30 °C, because



MnO and  $\text{MnCr}_2\text{O}_4$  have different internal oxidation fronts. According to the simulation results, the width of the internal oxidation zone of  $\text{MnCr}_2\text{O}_4$  is about two times larger than that of MnO after annealing at a dew point of  $-30\text{ }^\circ\text{C}$  for 16 hours; see Figure 6.10 (b). Thus, the measured internal oxidation kinetics of Fe-Mn-Cr steel alloys annealed at a dew point of  $-30\text{ }^\circ\text{C}$  were only compared with the simulation results. The measured depth of internal oxidation zone (inside grains) in the Fe-1.9Mn-1.6Cr steel alloy annealed for 16 hours at a dew point of  $-30\text{ }^\circ\text{C}$  is about  $3.4\text{ }\mu\text{m}$ , which is in fair agreement with the prediction; see Figure 6.10.

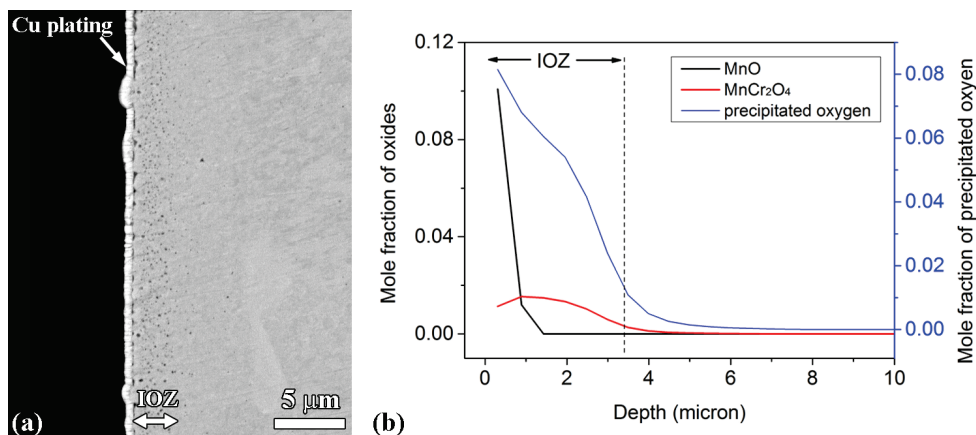


Figure 6.10: (a) SEM image (backscattered electrons) of the cross-section of Fe - 1.9 at.% Mn - 1.6 at.% Cr steel, and (b) simulated concentration depth profiles of internal oxides and precipitated oxygen in a Fe - 1.8 at.% Mn - 1.5 at.% Cr steel alloy, after annealing for 16 hours at  $950\text{ }^\circ\text{C}$  in a gas mixture of Ar with 5 vol.%  $\text{H}_2$  and a dew point of  $-30\text{ }^\circ\text{C}$  (oxygen partial pressure of  $2.2 \times 10^{-20}$  atm.). The dashed line indicates the internal oxidation front observed.

The good agreement between predictions (numerical simulation and analytical approach with extended Wagner theory) and experimental observations in the internal oxidation kinetics of Fe-Mn [6] and Fe-Mn-Cr steel alloys annealed under different ambient oxygen partial pressures also indicates that the adopted data of oxygen diffusivity [13] and oxygen dissolution [20] in austenite matrix are valid. The predicted internal oxidation behaviour of steel alloys adopting the data of oxygen diffusivity and dissolution can be regarded as a benchmark.

## 6.5 Conclusions

The coupled thermodynamic kinetic model allows prediction of the internal oxidation behaviour of Fe-Mn-Cr steel alloys annealed under different ambient oxygen partial

pressures, including the growth kinetics of internal oxidation zone and the concentration depth profiles of multiple internal oxides. The internal oxidation rate of Fe-Mn-Cr steel alloys is controlled by the diffusion of reactants through the iron matrix and thus follows the parabolic rate law. Both MnO and MnCr<sub>2</sub>O<sub>4</sub> exhibit a relatively low solubility product, and local thermodynamic equilibrium is established during internal oxidation of Fe-Mn-Cr steel alloys. When annealing at dew points of -10 and 10 °C, the depth of the internal oxidation zone of MnO is almost the same as that of MnCr<sub>2</sub>O<sub>4</sub>.

## References

- [1] N. Fonstein, *Advanced High Strength Sheet Steels*, Springer International Publishing, Switzerland, 2015.
- [2] A.R. Marder, *Progress in Materials Science*, **45** (2000), 191.
- [3] G.M. Song, T. Vystavel, N. van der Pers, J.T.M. De Hosson and W.G. Sloof, *Acta Materialia*, **60** (2012), 2973.
- [4] E.M. Bellhouse and J.R. McDermid, *Metallurgical and Materials Transactions A*, **41** (2010), 1539.
- [5] V.A. Lashgari, C. Kwakernaak and W.G. Sloof, *Oxidation of Metals*, **81** (2014), 435.
- [6] V.A. Lashgari, G. Zimbitas, C. Kwakernaak and W. G. Sloof, *Oxidation of Metals*, **82** (2014), 249.
- [7] R.A. Rapp, *Corrosion*, **21** (1965), 382.
- [8] W. Mao, R.W.A. Hendrikx and W. G. Sloof, *Oxidation of Metals*, (2017).
- [9] Chapter 4.
- [10] T. J. Nijdam and W. G. Sloof, *Acta Materialia*, **56** (2008), 4972.
- [11] W. Mao and W. G. Sloof, *Scripta Materialia*, **135** (2017), 29.
- [12] C.W. Bale, E. Bélisle, P. Chartrand, S.A. Deckerov, G. Eriksson, A.E. Gheribi, et al., *Calphad*, **54** (2016), 35.
- [13] J.H. Swisher and E.T. Turkdogan, *Transactions of the Metallurgical Society of AIME*, **239** (1967), 426.
- [14] D.J. Young, *High Temperature Oxidation and Corrosion of Metals*, Elsevier, Oxford, 2008.
- [15] B.D. Cullity and S.R. Stock, *Elements of X-ray Diffraction*, 3rd ed, Prentice Hall, New York, 2001.
- [16] J.T. Armstrong, *Electron Probe Quantitation*, Springer US, Boston, 1991.

- [17] Y. Ma, *Kinetics of internal oxidation of Fe-Mn-Cr steel alloys*, Master thesis, Delft University of Technology, 2017.
- [18] E.K. Ohriner and J.E. Morral, *Scripta Metallurgica*, **13** (1979), 7.
- [19] Y. Niu and F. Gesmundo, *Oxidation of Metals*, **60** (2003), 371.
- [20] V.A. Lashgari, *Internal and External Oxidation of Manganese in Advanced High Strength Steels*, Ph.D. thesis, Delft University of Technology, 2014.
- [21] D. Huin, P. Flauder and J.B. Leblond, *Oxidation of Metals*, **64** (2005), 131.

## Chapter 7

# Wüstite formation kinetics on pure iron and low alloyed Mn steels during annealing in $\text{H}_2\text{O} + \text{H}_2$ and $\text{CO}_2 + \text{CO}$ gas mixtures

### Abstract

Knowledge on the kinetics of Wüstite ( $\text{FeO}$ ) formation on Mn alloyed steels is of significant importance for the galvanizing industry. In this study, the linear growth kinetics of Wüstite scale on pure iron and Mn alloyed steels in gas mixtures containing  $\text{H}_2\text{O}$  or  $\text{CO}_2$  are investigated. The classical coupled linear-parabolic model can well describe the kinetics of Wüstite formation on pure iron in  $\text{H}_2\text{O} + \text{H}_2$  and  $\text{CO}_2 + \text{CO}$  gas mixtures as a function of temperature and gas composition. However, this model cannot predict the growth kinetics of Wüstite scale on Mn alloyed steels, since the observed linear growth rate of Wüstite scale on Mn alloyed steel in  $\text{H}_2\text{O} + \text{H}_2$  and  $\text{CO}_2 + \text{CO}$  gas mixtures is much lower than that on pure iron. Possible explanations for the substantially lower Wüstite growth rate on Mn alloyed steels than on pure iron are discussed.

### Keywords

Iron, Mn alloyed steel, Oxidation, Wüstite, Kinetics

## 7.1 Introduction

Advanced high strength steels (AHSS) are widely used in automotive industries to reduce the weight of car bodies and thereby reducing fuel consumption and CO<sub>2</sub> emissions [1]. To protect AHSS against corrosion, a zinc coating is usually applied to the surface by hot-dip galvanizing [2]. During the hot-dip galvanizing process, the steel strip passes through continuous annealing furnaces before entering the zinc bath. The final annealing atmosphere is usually a gas mixture of N<sub>2</sub> and H<sub>2</sub> with some water vapor. However, the alloying elements in AHSS, such as Mn, Si, Cr, Al etc., can form stable oxides at steel surface during annealing in this atmosphere before the steel enters the zinc bath. These alloying element oxides at the steel surface lower the zinc wettability [3] and hence degrade the quality of the galvanized steel product [4]. An attractive approach to create an oxide-free steel surface is by first forming a thin Wüstite (FeO) layer at the steel surface with the oxides of alloying elements being formed internally and buried underneath the layer [5]. Then, the Wüstite layer is fully reduced during the subsequent annealing process in the N<sub>2</sub> plus H<sub>2</sub> gas mixture with only pure iron at steel surface [6]. The formation of a Wüstite scale occurs, for example, when annealing a steel sheet in a direct-fired furnace where the oxygen partial pressure ( $p_{O_2}$ ) is above that for Wüstite formation; see e.g. ref. [5]. A mixture of oxidants as CO<sub>2</sub> and H<sub>2</sub>O as well as reductants CO and H<sub>2</sub> is the typical gas atmosphere in such a furnace. Hence, the kinetics of Wüstite layer formation on Mn alloyed steels in these gas mixtures is of particular interest.

The kinetics of Wüstite growth on pure iron oxidized in H<sub>2</sub>O + H<sub>2</sub> and CO<sub>2</sub> + CO gas mixtures have been studied extensively [7-13]. At the early stage of iron oxidation, the Wüstite growth rate is controlled by gas-oxide boundary reaction, and the scale thickness increases linearly with time. As the oxide layer thickens, the transport of the reacting species through the oxide scale determines the growth rate and then a parabolic growth law is obeyed. Experimental results from Turkdogan et al. [12] and Young & Yin [13] show that during the parabolic growth regime, the parabolic rate constant of Wüstite growth on pure iron in gas mixtures containing H<sub>2</sub>O and H<sub>2</sub> can be predicted well with the classical Wagner theory [14]. However, it is expected that for the annealing conditions and the short exposure time encountered in an industrial galvanizing line, the Wüstite scale formed during annealing will not be thick enough to result in a fully parabolic growth kinetics. Hence, a coupled linear-parabolic model, proposed by Wagner and Pettit [8], is adopted here to quantitatively describe the kinetics of Wüstite growth in gas mixtures containing H<sub>2</sub>O + H<sub>2</sub> or CO<sub>2</sub> + CO.

Recently, it is reported that the Wüstite growth on Mn alloyed steels is significantly slower than on pure iron in  $N_2 + H_2O + H_2$  gas mixtures at temperatures ranging from 800 to 1100 °C [13]. During the parabolic growth regime, the parabolic rate constant of Wüstite formation is much smaller for Mn alloyed steels than for pure iron under the same annealing conditions. To date, an explanation for the difference in oxidation rate between iron and Mn alloyed steels is not conclusive [13, 15]. It is suggested that sulphur in the steel segregates at Wüstite surface and lowers the oxygen partial pressure at Wüstite surface [15], but this is not supported by experimental evidence. Such a comparison between the Wüstite growth kinetics on pure iron and on Mn alloyed steels at the early stages, i.e. in the linear growth regime, has not been reported yet, while this is most relevant for annealing prior to galvanizing.

Hence, in this paper, the kinetics of Wüstite growth on pure iron in  $H_2O + H_2$  and  $CO_2 + CO$  gas mixtures as predicted with the coupled linear-parabolic model [8] are compared with the recently reported experimental results [9-11, 13]. Next, the growth kinetics of Wüstite scale on Mn alloyed steels as observed in our study are compared with that of pure iron during the early stages of oxidation in  $H_2O + H_2$  and  $CO_2 + CO$  gas mixtures. Finally, possible explanations are presented for the discrepancy between the rate of Wüstite scale growth on iron and Mn alloyed steels in the linear growth regime.

## 7.2 Experiments

### 7.2.1 Samples

The chemical compositions of the pure iron, Fe-0.69C alloy, Fe-Mn alloys and Fe-1.7Mn-0.1C steel used in this study are listed in Table 7.1. Rectangular samples of  $15 \times 7 \times 2$  mm for thermogravimetric analysis were cut from ingots by electric discharge machining (EDM). All samples were grinded with SiC emery paper and then polished with 1 micron diamond grains in the final step. The samples were cleaned ultrasonically in isopropanol and dried by blowing with pure nitrogen (purity better than 5N) before storing in air tight membrane boxes (Agar Scientific G3319, UK). The dimension of each sample after preparation was measured with a caliper (accuracy  $\pm 0.05$  mm).

### 7.2.2 Annealing

A first series of oxidation experiments were performed with a symmetrical thermogravimetric analyser (TGA, Setaram TAG 16/18, France) in order to obtain the kinetics of Wüstite formation. The sample was mounted onto a sapphire rod with an alumina pin having a diameter of 2.2 mm through a hole of diameter of 2.5 mm in the

sample. A dummy sample of alumina with the same dimensions was mounted onto a sapphire rod of the counter part of the balance to eliminate any buoyancy effect.

Table 7.1: Chemical composition (in wt%) of iron, Fe-0.69C steel, Fe-Mn alloys and Fe-1.7Mn-0.1C steel determined by Optical Emission Spectrometry. Elements with concentration below 0.001 wt% are not listed here.

	C	Si	P	Cr	Mn	Ni	Nb	Mo	Al
Iron	20 (ppm)	0.003	<0.000	<0.000	<0.005	0.005	<0.001	0.001	<0.040
Fe-0.69C	0.731	0.015	<0.000	0.043	<0.005	0.003	<0.001	<0.001	0.020
Fe-1.7Mn	9 (ppm)	<0.01	0.002	<0.003	1.71	0.002	<0.01	0.002	NA
Fe-3.5Mn	9 (ppm)	<0.01	<0.002	<0.003	3.49	0.002	<0.01	0.002	NA
Fe-7.0Mn	14 (ppm)	<0.01	<0.002	<0.003	6.72	<0.001	<0.01	0.002	NA
Fe-14Mn	16 (ppm)	<0.01	0.002	<0.003	13.3	<0.001	<0.01	0.002	NA
Fe-1.7Mn-0.1C	0.101	0.056	0.006	0.015	1.78	-	-	-	0.021

The whole TGA system was pumped to vacuum (< 50 Pa) and refilled with an Ar + 5 vol.% H<sub>2</sub> gas mixture twice to flush the gas lines, balance and furnaces. Then the dual furnaces were heated up from room temperature to the target temperature with 5 or 10 °C/min, while purging with 200 sccm Ar + 5 vol.% H<sub>2</sub>, i.e. 100 sccm gas in each furnace. 30 minutes after the target temperature for isothermal oxidation was reached, the Ar + 5 vol.% H<sub>2</sub> was switched to oxidation atmosphere while maintaining a total gas flow of 200 sccm. Two types of oxidation atmosphere were used in this study, i.e. Ar + 33 vol.% CO<sub>2</sub> + 17 vol.% CO and Ar + 1.2 vol.% H<sub>2</sub>O gas mixtures. After oxidation, the furnace was cooled down to room temperature with 5 or 10 °C/min in pure Ar. Since no significant decarburisation was observed during oxidation of the steel samples, the TG curves represent the kinetics of oxidation. Because the oxide scale formed on the Mn alloyed steel from 650 to 850 °C is very thin, the growth kinetics of a Wüstite layer cannot be accurately determined from the TG curves because of the significant contribution of internal oxidation of Mn to the mass gain. To solve this problem and to avoid potential influence of mass loss due to decarburization, the Mn alloyed steel was first annealed in the oxidation atmosphere at 950 °C for 8 hours to create a relatively thick oxide scale that fully covered steel surface as well as a thick internal oxidation zone of MnO. Then the furnace temperature was lowered to the

target oxidation temperature and isothermally held for 1 to 4 hours while maintaining the same oxidation atmosphere. The internal oxidation rate of the Mn alloyed steels decreases with the depth of internal oxidation zone [16], and hence the contribution of mass gain due to the internal oxidation during the Wüstite growth will be lowered when annealing at the target oxidation temperature. The mass gain of the Mn alloyed steel increases linearly with time during oxidation at temperatures of 650, 750 and 850 °C. Thus the linear growth rate of Wüstite on the Mn alloyed steel was obtained for different oxidation temperatures.

For characterization of the Wüstite scale formed on iron and steels, a second series of experiments were carried out in a horizontal quartz tube furnace (Carbolite MTF 12/38/850, UK) with an inner tube diameter of 30 mm. The sample was placed onto a quartz boat located at the cold zone of the furnace tube. Then, the furnace was closed and flushed with pure Ar at a flow rate of 500 sccm. Next, the sample was moved to the hot zone of the furnace with a quartz rod. At the end of the annealing experiment the sample was moved in the reverse direction to the cold zone. The heating and cooling of the sample was relatively fast, about 140 and 180 °C/min, respectively. Thus, the transformation of Wüstite into magnetite during cooling was negligible. The gas mixtures passed through the furnace tube at atmospheric pressure at a total flow rate of 500 sccm. The gas composition of the oxidation atmosphere was the same as that for the thermogravimetric analysis.

Prior to admitting the gas mixtures to any of the furnace, each gas, i.e. Ar, H<sub>2</sub>, CO<sub>2</sub> and CO (all with 5N vol.% purity), was filtered to remove any residual hydrocarbons, moisture and oxygen, with Accosorb (< 10 ppb hydrocarbons), Hydrosorb (<10 ppb H<sub>2</sub>O) and Oxysorb (< 5 ppb O<sub>2</sub>) filters (Messer Griesheim, Germany), respectively. The flow of each gas was regulated and monitored using mass flow controllers (Bronkhorst, The Netherlands). H<sub>2</sub>O vapour was added to the gas by evaporating de-aerated and deionized water (18.2 MΩ.cm at 25 °C) with an in the gas line controlled evaporator mixer (CEM, Bronkhorst, The Netherlands). The pure water was de-aerated with nitrogen gas in a closed pressurized stainless steel vessel and the dissolved oxygen gas in the pure water is below 100 ppb, as measured with an O<sub>2</sub> sensor (InPro 6850i, Mettler Toledo).

### 7.2.3 Characterization

X-ray diffraction (XRD) was used to identify the oxide phases formed after annealing. The XRD patterns were recorded with a Bruker D8 Advance diffractometer in the Bragg-Brentano geometry using Co K $\alpha$  radiation, in the 2 $\theta$  region between 10 to 110° with a step size of 0.034° 2 $\theta$  and a dwell time of 2 s.



The surface and cross-section of the annealed samples were examined with scanning electron microscopy (SEM) using a JSM6500F (JEOL, Japan) operated with an accelerating voltage of 5 or 15 kV. X-ray microanalysis (XMA) using Electron Dispersive Spectroscopy (EDS) was performed with the same SEM instrument equipped with an UltraDry 30 mm<sup>2</sup> detector (Thermo Fisher Scientific, USA). The SEM instrument is also equipped with an Oxford Instruments-HKL Nordlys II detector allowing Electron Backscattering Diffraction (EBSD). The EBSD measurements were performed with an electron beam energy of 20 keV. The acquisition and processing of EBSD data was performed using Channel 5 software (version 2011).

The concentration of Mn in the Wüstite formed on Mn alloyed steels was determined with electron probe X-ray microanalysis (EPMA). The analysis was performed with a JXA 8900R (JEOL, Japan) microprobe employing Wavelength Dispersive Spectrometry (WDS). A focussed electron beam was used with an energy of 10 keV and a current of 50 nA. The measurement was performed on cross-sections of samples. The composition at each analysis location of the sample was determined using the X-ray intensities of the constituent elements after background correction relative to the corresponding intensities of reference materials. In this case the X-ray intensities of Fe-K $\alpha$ , Mn-K $\alpha$  and O-K $\alpha$  were measured and pure Fe, Mn and SiO<sub>2</sub>, respectively, were used as references. The thus obtained intensity ratios were processed with a matrix correction program CITZAF [17].

## 7.3 Results

### 7.3.1 Kinetics of Wüstite formation on pure iron in H<sub>2</sub>O + H<sub>2</sub> and CO<sub>2</sub> + CO gas mixtures

The coupled linear-parabolic model [8] is revisited and summarized in the Appendix D. The rate of oxygen incorporation to Wüstite surface ( $J_O$ , in mol cm<sup>-2</sup> s<sup>-1</sup>) equals to:

$$J_O = K_{oxid} (a_O^*)^{-n} \left(1 - \frac{a_O^*}{a_O}\right) p_{oxid} \quad (7.1)$$

in which  $K_{oxid}$  (mol cm<sup>-2</sup> s<sup>-1</sup> atm<sup>-1</sup>) is the rate constant of the overall surface reaction between Wüstite scale and H<sub>2</sub>O vapour ( $K_{H_2O}$ ) or CO<sub>2</sub> ( $K_{CO_2}$ ) in the gas.  $p_{oxid}$  (in atm.) is the partial pressure of the oxidant gas species in the gas mixture, namely H<sub>2</sub>O vapour ( $p_{H_2O}$ ) or CO<sub>2</sub> ( $p_{CO_2}$ ).  $a_O^*$  and  $a_O$  are oxygen activities at the Wüstite scale surface and in the gas ambient, respectively. Both oxygen activities  $a_O^*$  and  $a_O$  are expressed in terms of  $p_{H_2O} / p_{H_2}$  or  $p_{CO_2} / p_{CO}$  ratio in Eq. (7.1). The value of  $n$  ( $0 \leq n \leq 1$  [18]) depends on the

mechanism of oxygen incorporation into the Wüstite surface [10]. In this study, the value of  $n$  adopted for predicting the Wüstite growth kinetics in  $\text{H}_2\text{O} + \text{H}_2$  and  $\text{CO}_2 + \text{CO}$  gas mixtures equals  $2/3$  [8, 19]. Figure 7.1 shows the schematic of the growth mechanism of Wüstite scale on pure iron. At the early stages of Wüstite growth, the oxygen activity  $a_{\text{O}}^*$  almost equals to the value corresponding with the iron-Wüstite equilibrium oxygen activity ( $a_{\text{O}}^{\text{Fe/FeO}}$ ). Then, the kinetics of Wüstite growth is controlled by its surface reaction. Accordingly, the oxygen flux  $J_{\text{O}}$  is almost a constant and the Wüstite scale thickens almost linearly with time. During the Wüstite growth the oxygen activity  $a_{\text{O}}^*$  gradually increases, and hence the growth rate of Wüstite scale decreases with time. When the oxygen activity  $a_{\text{O}}^*$  is close to  $a_{\text{O}}$ , i.e. Wüstite surface is almost equilibrated with gas ambient, the growth of Wüstite scale is controlled by mass transport through the scale and then a parabolic rate law is obeyed. In the coupled linear-parabolic model it is assumed that the defect structure of the Wüstite scale at surface and in the bulk are the same, and that the concentration of cation vacancy depends only on the local oxygen partial pressure. Any formation of pores or defect clusters is excluded. The mechanism of Wüstite growth is considered to be controlled by the inward diffusion of cation vacancies [8]. Moreover, it is assumed that thermodynamic equilibrium is established at Wüstite-iron interface.

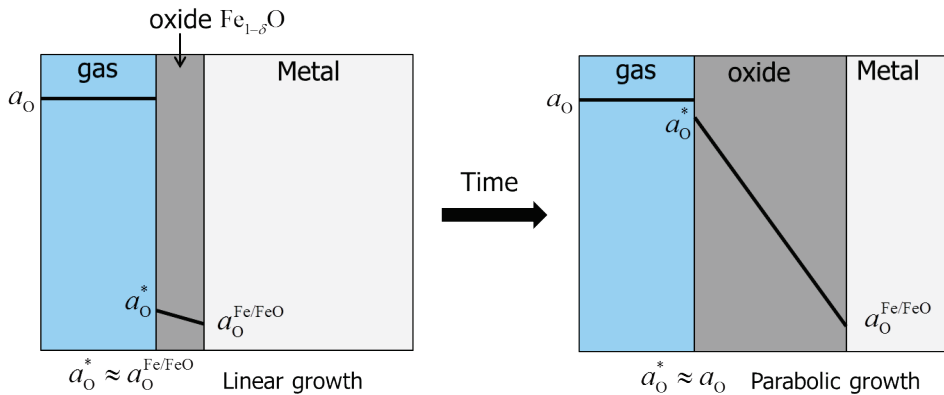


Figure 7.1: Schematic of the growth mechanism of Wüstite scale formed on pure iron according to the coupled linear-parabolic model [8].

The surface reaction rate constant  $K_{\text{oxid}}$  for Wüstite formation can be evaluated from the observed growth kinetics during the linear growth regime as long as the gas composition in annealing atmosphere is known and the value of  $n$  is pre-defined; see Eq. (7.1). The values for the surface reaction rate constant for  $\text{CO}_2 + \text{CO}$  gas mixtures,  $K_{\text{CO}_2}$ , of Wüstite growth

on pure iron in the temperature range from 700 to 1100 °C were reported in ref. [8], and the temperature dependence of the surface reaction rate constant for  $\text{H}_2\text{O} + \text{H}_2$  gas mixtures,  $K_{\text{H}_2\text{O}}$ , of Wüstite growth on pure iron in the temperature range from 850 to 1150 °C was estimated from the experimental data reported in ref. [12]. Adopting these values for the surface reaction rate constant, the thickness of Wüstite scale formed on pure iron in  $\text{H}_2\text{O} + \text{H}_2$  and  $\text{CO}_2 + \text{CO}$  gas mixtures, respectively, can be predicted quantitatively for any annealing condition (i.e. gas composition, temperature and time).

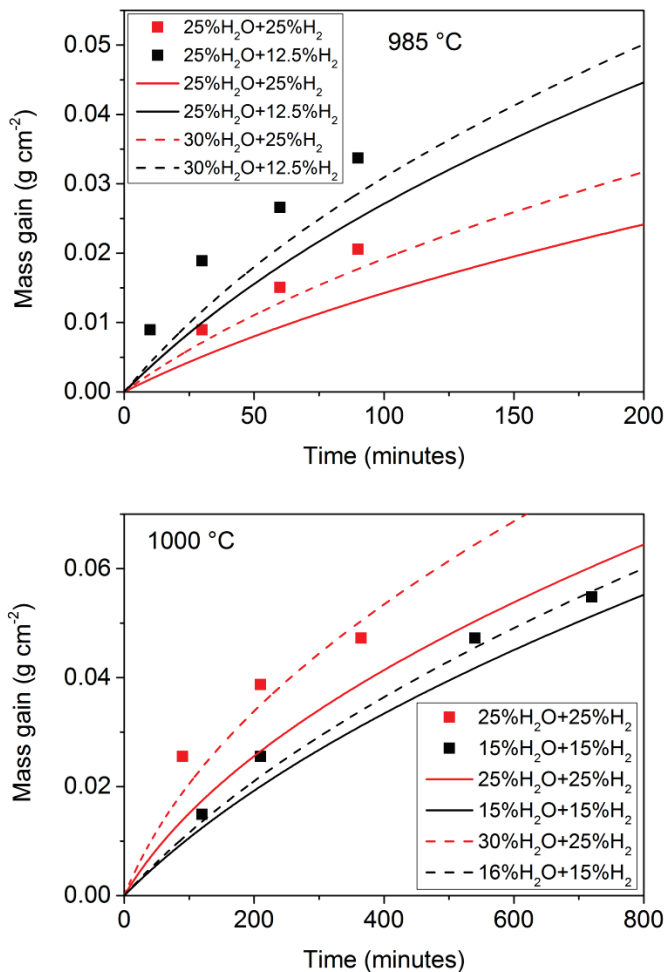


Figure 7.2: Comparison between the measured [13] (solid symbol) and predicted (solid and dashed lines) kinetics of Wüstite scale growth on pure iron in  $\text{N}_2 + \text{H}_2\text{O} + \text{H}_2$  gas mixtures with different composition at 1 atm.

The predicted kinetics of Wüstite growth with the coupled linear-parabolic model are in agreement with the reported growth kinetics for a Wüstite scale on pure iron annealed in  $N_2 + H_2O + H_2$  gas mixtures at 985 and 1000 °C [13]; see Figure 7.2. Both the experimental results [13] and our predictions clearly show that the Wüstite growth rate increases not only with the oxygen partial pressure, but also with partial pressure of  $H_2O$  vapour in the annealing atmosphere. Since the growth rate of Wüstite scale is sensitive to the partial pressure of  $H_2O$  vapour, the somewhat larger values reported for the mass gain of pure iron than predicted may be due to the uncertainty of the  $H_2O$  vapour concentration in the actual annealing atmosphere; see Figure 7.2.

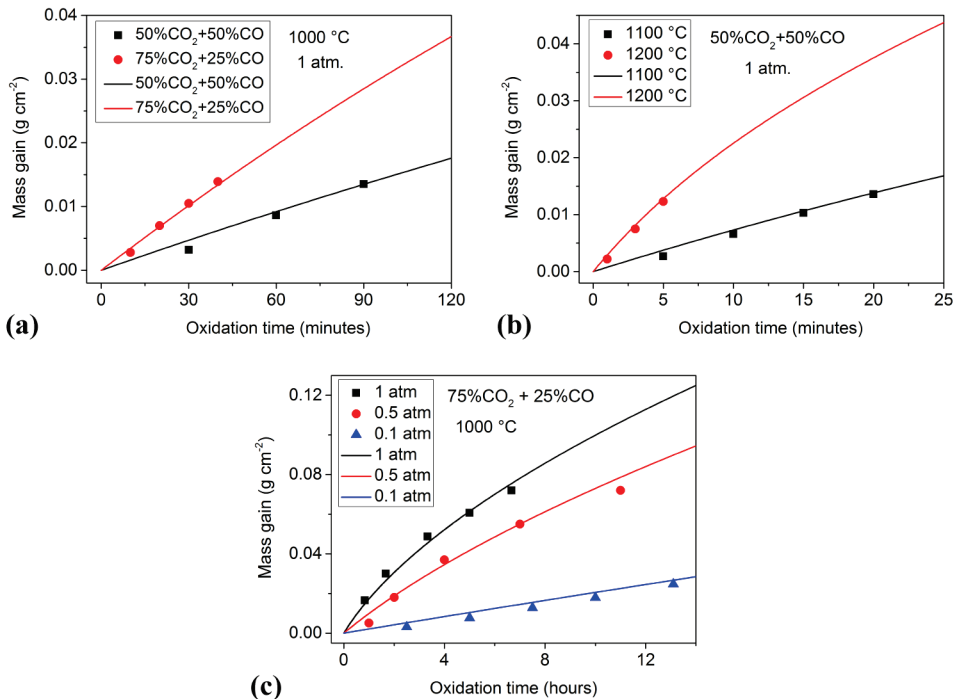


Figure 7.3: Comparison between the measured [9-11] (solid symbol) and predicted (solid lines) kinetics of Wüstite scale growth on pure iron in  $CO_2 + CO$  gas mixtures with different (a) gas compositions, (b) annealing temperatures and (c) total gas pressures.

The kinetics of Wüstite growth on pure iron in  $CO_2 + CO$  gas mixtures predicted with the coupled linear-parabolic model also matches the experimental results; see Figure 7.3. The reported Wüstite growth rate on pure iron in refs [9, 11], determined with thermogravimetric analysis at temperatures ranging from 1000 to 1200 °C, were taken to validate our predictions. For simplicity, only several points from the reported continuous curve of mass gain with time were selected for this comparison. It is worth noting that all

the data adopted (e.g. the surface reaction rate constant  $K_{\text{CO}_2}$ , parabolic rate constant for Wüstite formation in air, defect concentration in Wüstite) for simulating the scale growth kinetics based on the coupled linear-parabolic model are fully independent from the reported experimental results. The growth rate of Wüstite scale on pure iron in CO<sub>2</sub> + CO gas mixtures increases with the oxygen partial pressure, the partial pressure of oxidant gas and the total gas pressure of the annealing atmosphere. This behaviour is similar as for the growth of Wüstite scale on pure iron in H<sub>2</sub>O + H<sub>2</sub> gas mixtures. More importantly, the good agreement between the predicted and observed growth kinetics of a Wüstite scale on pure iron in CO<sub>2</sub> + CO gas mixtures in the temperature range from 1000 to 1200 °C for any given annealing condition, shows that the coupled linear-parabolic model can accurately describe the Wüstite growth kinetics.

Although the experimental data for kinetics of Wüstite formation on pure iron in CO<sub>2</sub> + CO gas mixtures below 900 °C have been reported, also the growth of Wüstite on pure iron in an Ar + 33 vol.% CO<sub>2</sub> + 17 vol.% CO gas mixture (1 atm.) at temperatures ranging from 650 to 950 °C were investigated here for comparison. The experimental results are compared with our predictions; see Figure 7.4. Both thermodynamic computation and XRD analysis confirms that the oxide scale formed for the annealing conditions applied here only consists of Wüstite. According to our predictions, the formation of a Wüstite scale on pure iron within 6 hours of oxidation in the gas mixture at temperatures ranging from 650 to 850 °C is within the linear growth regime. This indicates that the growth kinetics is controlled by the reaction at scale surface. Indeed, the observed growth kinetics of Wüstite at 650 and 750 °C follow a linear rate law, and the growth rate determined matches our predictions. At 850 °C, however, the initial growth rate is smaller than predicted (about 20 % of the predicted value), but continuously increases with time until it exceeds the predicted values; see Figure 7.4. After 8 hours of oxidation the observed linear growth rate is about twice the value predicted. Observation of similar rate curves consisting of two separate linear regions was already reported [8, 9]. It is suggested that in the first linear region, the Wüstite scale nucleates epitaxially onto the iron substrate (with randomly oriented crystal grains) and grows with a relatively small growth rate. Subsequently, a scale texture develops gradually such that the (100) plane of Wüstite (rocksalt crystal structure) is parallel to the iron substrate, corresponding with an increase of the growth rate at the second linear region. Apparently, the surface reaction rate depends on the crystal orientation of the oxide scale. This may be explained by the higher site occupation of Fe cations at the (100) ( $1.1 \times 10^{19}/\text{m}^2$ ) than at the (110) ( $7.5 \times 10^{18}/\text{m}^2$ ) or (111) ( $6.2 \times 10^{18}/\text{m}^2$ )<sup>1</sup> plane of Wüstite. At

---

<sup>1</sup> Since the surface of Wüstite scale with (111) orientation is composed by either Fe cations or O anions, an average value is taken for site occupation of Fe cations.

these sites, oxidant molecules ( $\text{H}_2\text{O}$  or  $\text{CO}_2$ ) adsorbs preferentially and subsequently dissociate leaving an oxygen atom behind. The higher the density of Fe cation sites, the faster Wüstite growth. Thus, the highest Wüstite growth rate is expected to occur at the (100) plane. Since the calculated surface energy of (100) and (110) planes of FeO are almost the same [20], the evolution of scale texture during oxidation is attributed to the uneven growth rate of Wüstite crystals with different orientation.

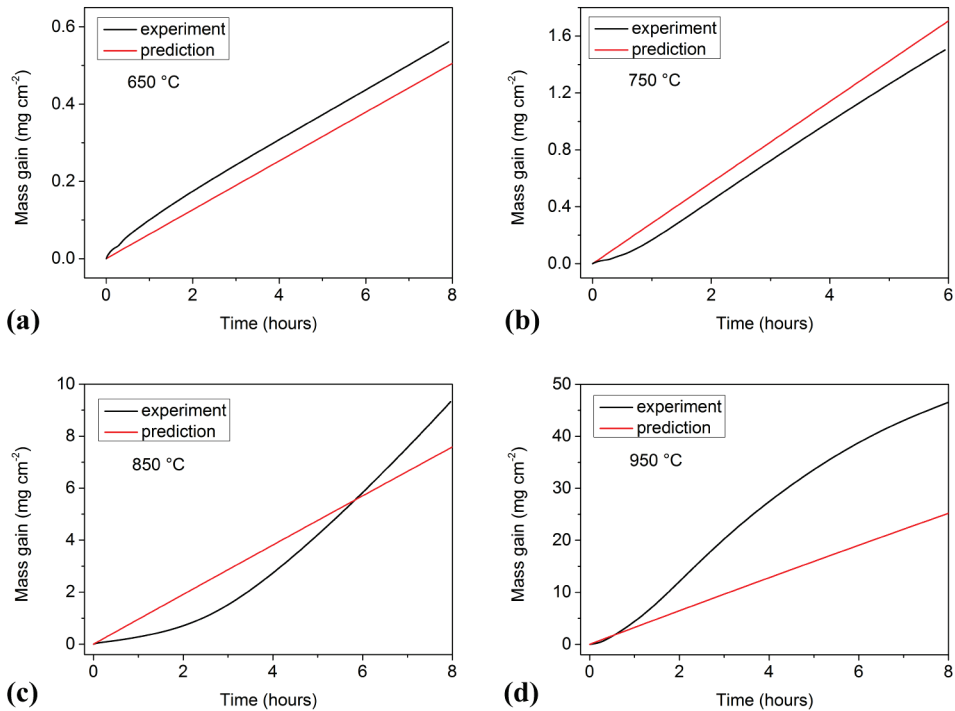


Figure 7.4: Comparison between measured and predicted kinetics of Wüstite scale formation on pure iron at temperatures of (a) 650, (b) 750, (c) 850 and (d) 950 °C in a gas mixture of Ar + 33 vol.%  $\text{CO}_2$  + 17 vol.% CO at 1 atm.

When oxidizing at 950 °C, the oxide growth rate starts to decrease after about 3.5 hours, indicating that then diffusion of species through the scale starts to affect the oxide growth kinetics. The maximum oxide scale growth rate observed in our experiments was taken to evaluate the surface reaction rate constant  $K_{\text{CO}_2}$  for Wüstite formation on pure iron; see Eq. (7.1). The values obtained are larger than those reported in ref. [8] at temperatures of 850 and 950 °C. This is probably due to the difference in purity of the iron used in the experiments, as the Wüstite growth rate is very sensitive for impurities in iron (see below). Also, there may be a difference in texture development in the various Wüstite scales. The

re-evaluated temperature dependence of the surface reaction rate constant  $K_{\text{CO}_2}$  for Wüstite formation on iron from 650 to 950 °C is listed in Table 7.2.

Table 7.2: Surface reaction rate constant  $K$  for Wüstite growth on pure iron and Mn steels in CO<sub>2</sub> + CO and H<sub>2</sub>O + H<sub>2</sub> gas mixtures. The value of  $n$  is taken equal to 2/3 (see Eq. (7.1)).

Material	Temperature range (°C)	Gas mixture	Rate constant $K$ (mol cm <sup>-2</sup> s <sup>-1</sup> atm <sup>-1</sup> )	Reference
Iron	700-880	CO <sub>2</sub> + CO	$1.5 \times 10^{-3} \exp\left(-\frac{98000}{RT}\right)$	[8]
Iron	960-1100	CO <sub>2</sub> + CO	$3.3 \times 10^2 \exp\left(-\frac{221000}{RT}\right)$	[8]
Iron	650-950	CO <sub>2</sub> + CO	$0.17 \exp\left(-\frac{136000}{RT}\right)$	This study
Fe-1.7Mn-0.1C	650-950	CO <sub>2</sub> + CO	$9.7 \times 10^{-3} \exp\left(-\frac{163000}{RT}\right)$	This study
Fe-0.2Mn-0.06C	1000-1150	CO <sub>2</sub> + CO	$1.8 \times 10^4 \exp\left(-\frac{274000}{RT}\right)$	[21]
Iron	850-1150	H <sub>2</sub> O + H <sub>2</sub>	$7.5 \times 10^{-3} \exp\left(-\frac{88000}{RT}\right)$	[12]
Fe-0.2Mn-0.06C	950-1150	H <sub>2</sub> O + H <sub>2</sub>	$2.8 \times 10^4 \exp\left(-\frac{264000}{RT}\right)$	[21]
Fe-1.7Mn-0.1C	650-950	H <sub>2</sub> O + H <sub>2</sub>	$1.0 \exp\left(-\frac{153000}{RT}\right)$	This study

The agreement between predicted and experimentally determined growth kinetics of Wüstite scale on pure iron annealed in H<sub>2</sub>O + H<sub>2</sub> (Figure 7.1) or CO<sub>2</sub> + CO (Figures 7.2 and 7.3) gas mixtures shows that the coupled linear-parabolic kinetic model can be used as a benchmark for estimating the thickness of Wüstite scale on pure iron after oxidation for various annealing conditions.

### 7.3.2 Kinetics of Wüstite formation on Mn alloyed steels in H<sub>2</sub>O + H<sub>2</sub> and CO<sub>2</sub> + CO gas mixtures

Since Mn is the major alloying element in advanced high strength steels at a concentration usually below about 2 wt%, its effect on the Wüstite growth rate is investigated. The linear growth rate of Wüstite scale on Mn alloyed steels is much lower than on pure iron in gas mixtures with H<sub>2</sub>O as the only type of oxidant; see Figure 7.5. All the experimental data reported so far [15, 21-23] on linear growth kinetics of Wüstite on Mn alloyed steels in H<sub>2</sub>O containing atmosphere are summarized and compared with that for pure iron in Figure 7.5. The Mn alloyed steels used in those studies have similar composition, i.e. 0.2 wt% Mn and 0.04 to 0.06 wt% carbon. Because kinetic data on Wüstite scale formation on Mn alloyed steels below 950 °C are lacking, the temperature dependence of the surface reaction rate constant  $K_{\text{H}_2\text{O}}$  from 650 to 950 °C was experimentally evaluated for the steel alloyed with 1.7 wt% Mn and 0.1 wt% carbon. For both Mn alloyed steels and iron, the surface reaction rate constant  $K_{\text{H}_2\text{O}}$  for Wüstite formation follows an Arrhenius type relation with temperature. The activation energies derived for the surface reaction of Wüstite scale on pure iron and the Mn alloyed steel are, however, much different, i.e. about 88 and 153 kJ/mol, respectively; see Table 7.2. The surface reaction rate constant  $K_{\text{H}_2\text{O}}$  for Wüstite formation on Mn alloyed steels is smaller than that for iron below about 1200 °C, and this discrepancy increases with decreasing temperature; see Figure 7.5.

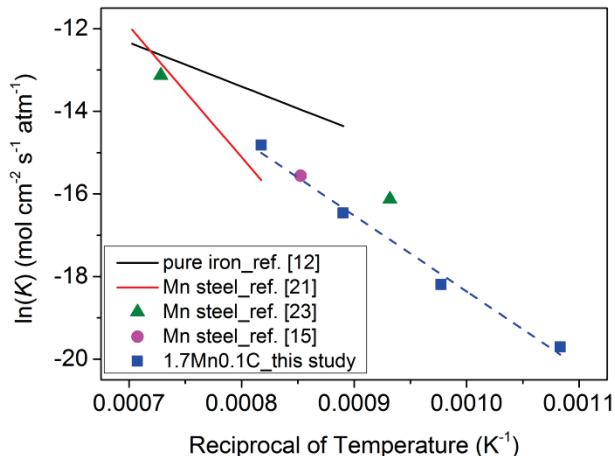


Figure 7.5: Temperature dependence of the surface reaction rate constant  $K$  for Wüstite growth on pure iron and Mn alloyed steels in gas mixtures containing H<sub>2</sub>O as the only oxidant, with the value of  $n$  taken equal to 2/3; cf. Eq. (7.1).



In CO<sub>2</sub> + CO gas mixtures, Wüstite growth on Mn alloyed steels is also much slower than on pure iron during the linear growth regime. Since the available experimental data on linear growth kinetics of a Wüstite scale on Mn alloyed steel (0.2 wt% Mn and 0.05 wt% C) in gas mixtures with CO<sub>2</sub> as the only type of oxidant only cover the temperature range from 1000 to 1150 °C [21], in this study the growth kinetics of a Wüstite scale is determined for a Mn steel alloyed with 1.7 wt% Mn and 0.1 wt% carbon in an Ar + 33 vol.% CO<sub>2</sub> + 17 vol.% CO gas mixture for temperatures ranging from 650 to 950 °C. The temperature dependence of the surface reaction rate constant  $K_{\text{CO}_2}$  is evaluated from the observed linear oxidation kinetics; see Table 7.2. Also, this surface reaction rate constant follows an Arrhenius type relation with temperature; see Figure 7.6. Clearly, the surface reaction rate constant  $K_{\text{CO}_2}$  for Wüstite growth on Mn alloyed steels is much smaller than that for Wüstite growth on pure iron (see Figure 7.6), and this difference can reach up to three orders of magnitude.

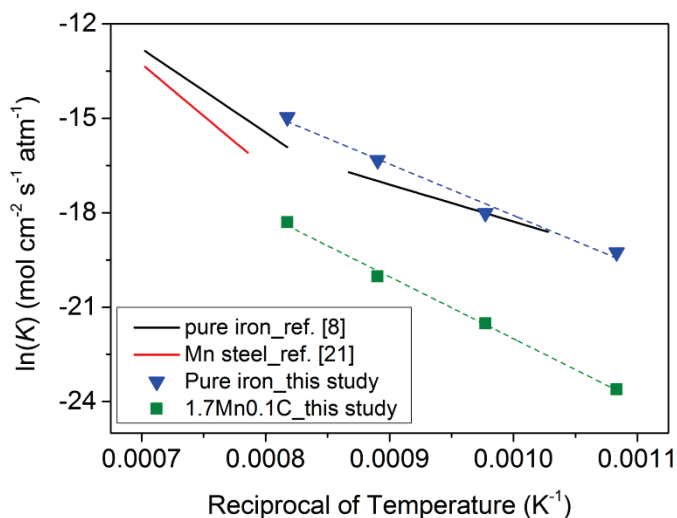


Figure 7.6: Temperature dependence of the surface reaction rate constant  $K$  for Wüstite growth on pure iron and Mn alloyed steels in gas mixtures containing CO<sub>2</sub> as the only oxidant, with the value of  $n$  taken equal to 2/3; cf. Eq. (7.1).

Both Mn and carbon additions to Fe substantially lower the linear growth rate of a Wüstite scale; see Figure 7.7. No clear correlation between oxidation rate and Mn concentration is observed, and the effect of increasing Mn concentration on Wüstite growth rate is relatively small up to 7 wt.%. Only when heavily alloyed with Mn (14 wt%) the Wüstite growth rate further decreases.

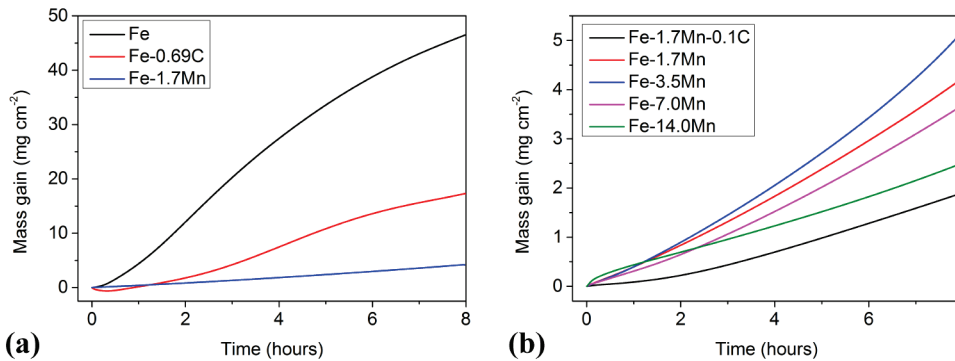


Figure 7.7: Kinetics of Wüstite scale formation on (a) pure iron, Fe-0.69C steel and Fe-1.7Mn-0.1C steel, and (b) Fe-1.7Mn-0.1C steel and Fe-Mn alloys, annealed at 950 °C in an Ar + 33 vol.% CO<sub>2</sub> + 17 vol.% CO gas mixture at 1 atm.

For both pure iron and Mn alloyed steels, a dense Wüstite scale is formed at surface and separates the metal matrix from the gas atmosphere after annealing in an Ar + 33 vol.% CO<sub>2</sub> + 17 vol.% CO gas mixture at 950 °C; see Figure 7.8. The Wüstite scale is well adhered to metal matrix and no delamination of oxide occur during oxidation. According to the composition analysis of the Wüstite scale by EPMA, the Mn is homogeneously dissolved with a concentration of about 3 at.% (among cations) after annealing the Fe-1.7Mn-0.1C steel at 950 °C in Ar + 33 vol.% CO<sub>2</sub> + 17 vol.% CO gas mixture. An internal oxidation zone of MnO is formed in the Mn alloyed steel underneath the Wüstite scale.

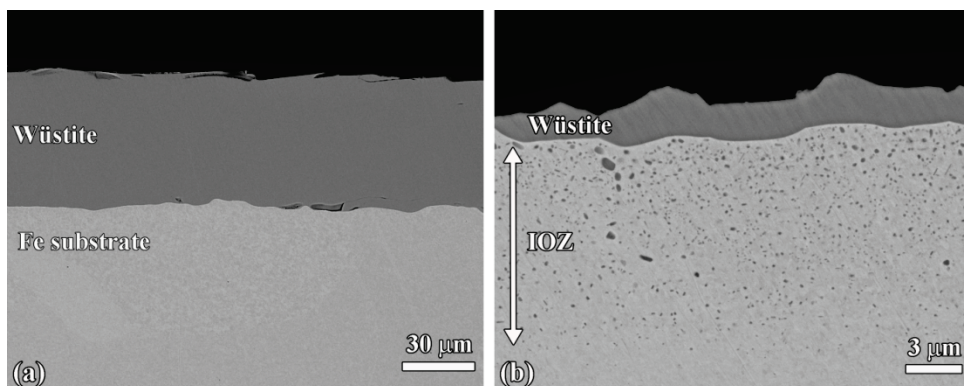


Figure 7.8: Back-scattered electron image of a cross-section of (a) pure iron and (b) Fe-1.7Mn-0.1C steel after annealing at 950 °C for 3 hours in an Ar + 33 vol.% CO<sub>2</sub> + 17 vol.% CO gas mixture at 1 atm. Internal oxidation zone (IOZ) of MnO is formed in the annealed Fe-1.7Mn-0.1C steel.

## 7.4 Discussion

The much slower Wüstite growth on Fe-Mn alloys and Mn alloyed steels than on iron cannot be explained by the influence of Mn on the iron cation diffusivity nor by the influence of Mn on defect concentration in Wüstite [24]. The kinetics of Wüstite formation on pure iron, Fe-Mn alloys and the Mn alloyed steel in Ar + CO<sub>2</sub> + CO gas mixtures within the oxidation time considered are controlled by the surface reaction rather than by the mass transport across the oxide scale. This is evidenced by the observed gradual increase of Wüstite growth rate with time (see Figure 7.6), which is in contrast with oxide scale growth kinetics determined by diffusion.

It has been reported that Si alloyed steels also oxidize much slower than pure iron, because a Fe<sub>2</sub>SiO<sub>4</sub> or SiO<sub>2</sub> layer is formed in between the Wüstite scale and alloy matrix and blocks the iron transport from alloy to Wüstite scale [25]. However, on Fe-Mn alloys, MnO is the only type of oxide that can be formed at the ambient oxygen partial pressure considered here, but between the Wüstite scale and alloy matrix no other type of oxide layer is observed; see Figure 7.8. This suggests that Mn influences the reaction rate at the scale-gas interface.

It has been reported [13, 23] that a preferred orientation of the crystals in Wüstite develops with the (110) lattice planes parallel to the surface for Mn alloyed steels, while a strong preferred orientation of the crystals in Wüstite occurs with the (100) lattice planes parallel to the surface for pure iron, when oxidizing in N<sub>2</sub> + H<sub>2</sub>O + H<sub>2</sub> gas mixtures from 800 to 1100 °C. Also it has been reported [13] that a preferred orientation of the crystals in Wüstite happens with the (100) lattice planes parallel to the surface for pure iron when oxidizing in CO<sub>2</sub> + CO gas mixtures. Then, the linear growth rate of a Wüstite scale with a (100) fibre texture is higher than that of a Wüstite scale with no crystallographic texture. But the observed discrepancy in the linear growth rate of Wüstite scale between iron and Mn alloyed steels is not caused by the difference in scale texture. In our study, no texture is observed in the Wüstite scale formed on both pure iron and the Mn alloyed steel after oxidation at 950 °C for 3 hours in an Ar + 33 vol.% CO<sub>2</sub> + 17 vol.% CO gas mixture, according to the results of EBSD measurements. A columnar structure was observed and the Wüstite crystals are randomly oriented in the scale on both iron and the Mn alloyed steel; see Figures 7.9 and 7.10. The thickness of Wüstite crystals on pure iron is much larger than the thickness of the Wüstite crystals with similar orientation on the Mn alloyed steel. Thus, the discrepancy in scale growth rate between iron and Mn alloyed steels cannot be explained by the texture of the Wüstite crystals.

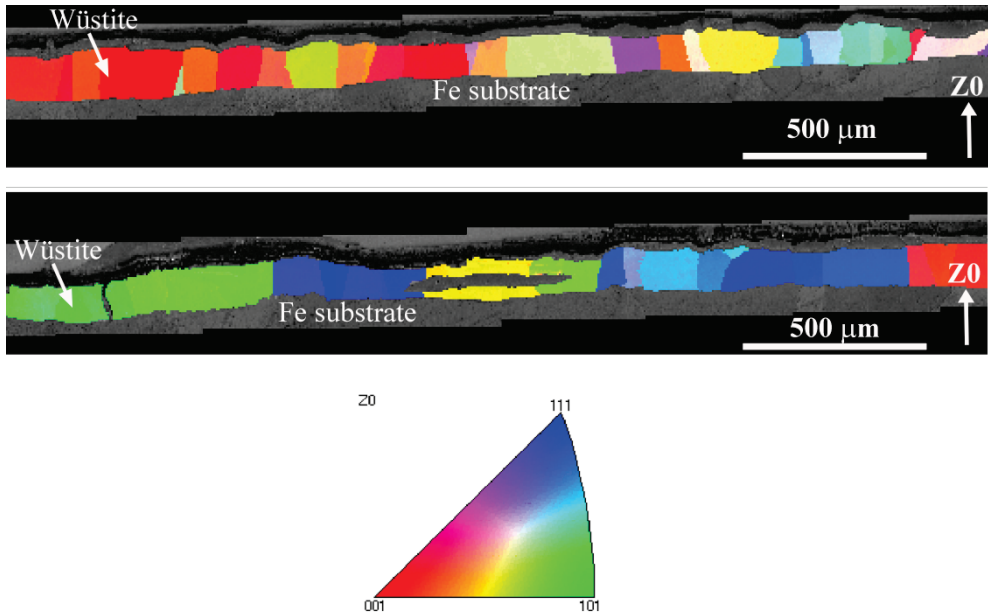


Figure 7.9: Inverse pole figure maps of cross-section of Wüstite scale formed on pure iron after annealing at 950 °C for 3 hours in an Ar + 33 vol.% CO<sub>2</sub> + 17 vol.% CO gas mixture at 1 atm. The crystal orientation is given with respect to the normal to the sample surface. The Wüstite crystals are randomly oriented.

MnO and FeO have the same rock-salt crystal structure and can form a continuous solid solution, denoted as (Fe<sub>1-x</sub>Mn<sub>x</sub>)O with 0 < x < 1 [26]. The lattice constant of MnO (4.444 Å [27]) is close to that of FeO (4.332 Å [11]). The bond dissociation energy of diatomic molecules Mn-O and Fe-O are 362 and 407 kJ/mol, respectively [28]. Based on these values of the bond strength, it is estimated with the Langmuir-McLean segregation equation [29, 30] that Mn cations dissolved in Wüstite significantly segregate at scale surface during annealing. For example, at 927 °C the value of  $x$  for the (100) surface of (Fe<sub>0.97</sub>Mn<sub>0.3</sub>)O can reach up to about 0.7. The Mn cations enriched at the Wüstite surface may act as a barrier between adsorbed gas molecules and the Fe cations, and hence hinder the growth of Wüstite. Moreover, the dissociation rate of CO<sub>2</sub>/H<sub>2</sub>O into CO/H<sub>2</sub> and adsorbed oxygen on Wüstite surface may be lowered with Mn segregation. Then, the surface reaction rate constants ( $K_{\text{H}_2\text{O}}$  and  $K_{\text{CO}_2}$ ) for MnO will be lower than that for FeO. However, the linear growth rate constant of MnO on pure Mn in H<sub>2</sub>O + H<sub>2</sub> or CO<sub>2</sub> + CO gas mixtures has not been reported, and hence the surface reaction rate constants  $K_{\text{H}_2\text{O}}$  and  $K_{\text{CO}_2}$  for MnO are unknown. Carbon may influence the growth kinetics of Wüstite scale on steels in CO<sub>2</sub> +

CO gas mixtures through a different mechanism from Mn. Small amount of carbon can be dissolved in Wüstite [31] and may change the defect structure at Wüstite surface. Hence, the carbon at Wüstite surface may lower the number density of adsorption sites of CO<sub>2</sub> molecules and thereby lowering the growth rate of Wüstite scale. The measurement of the surface reaction rate constants  $K_{\text{H}_2\text{O}}$  and  $K_{\text{CO}_2}$  for MnO as well as the effect of carbon on defect structure at Wüstite surface will be the subject of further studies.

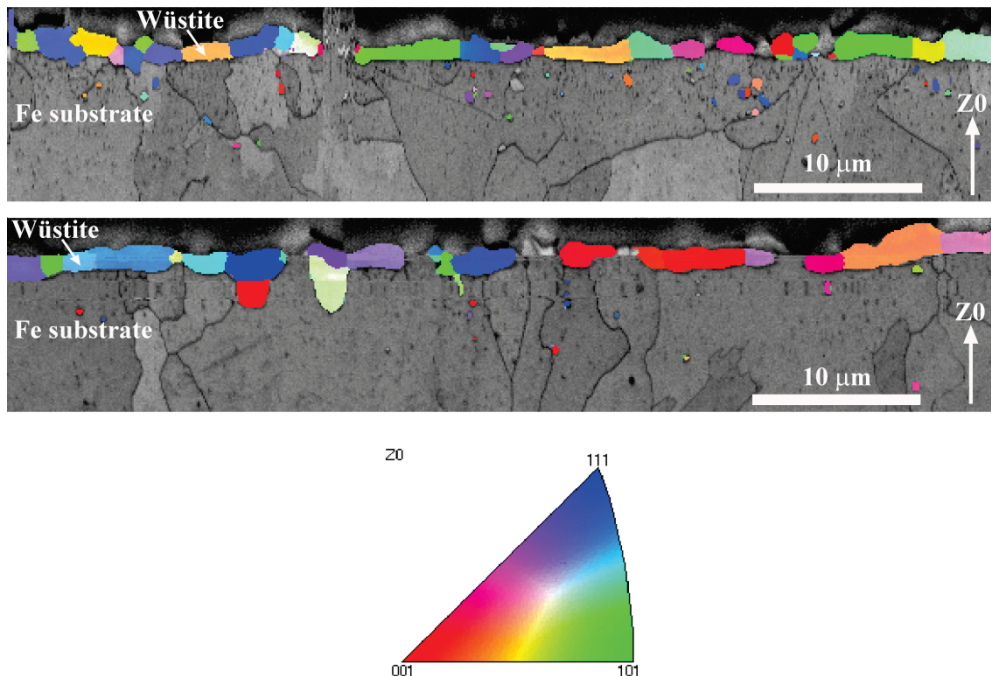


Figure 7.10: Inverse pole figure maps of cross-section of Wüstite scale formed on the Fe-1.7Mn-0.1C steel after annealing at 950 °C for 3 hours in an Ar + 33 vol.% CO<sub>2</sub> + 17 vol.% CO gas mixture at 1 atm. The crystal orientation is given with respect to the normal to the sample surface. The Wüstite crystals are randomly oriented.

## 7.5 Conclusion

The coupled linear-parabolic model can well predict the kinetics of Wüstite formation on pure iron in H<sub>2</sub>O + H<sub>2</sub> and CO<sub>2</sub> + CO gas mixtures as a function of temperature and gas composition. However, when applying this model to predict the growth kinetics of Wüstite scale on Mn alloyed steels in H<sub>2</sub>O + H<sub>2</sub> and CO<sub>2</sub> + CO gas mixtures, the observed linear growth rate is substantially lower. The alloying elements Mn and carbon lower the linear

growth rate of a Wüstite scale. Possibly, the Mn ions segregate to the Wüstite scale surface during oxidation thereby suppressing the reaction between Fe and the oxidant gas species.

## References

- [1] N. Fonstein, *Advanced High Strength Sheet Steels*, Springer International Publishing, Switzerland, 2015.
- [2] A.R. Marder, *Progress in Materials Science*, **45** (2000), 191.
- [3] G.M. Song, T. Vystavel, N. van der Pers, J.T.M. De Hosson and W.G. Sloof, *Acta Materialia*, **60** (2012), 2973.
- [4] E.M. Bellhouse and J.R. McDermid, *Metallurgical and Materials Transactions A*, **41** (2010), 1539.
- [5] M. Blumenau, C.O. Gusek and M. Norden, *AISTech Conference Proceedings*, 2012.
- [6] W. Mao and W. G. Sloof, *Metallurgical and Materials Transactions B*, **48** (2017), 2707.
- [7] F. Pettit, R. Yinger and J.B. Wagner Jr, *Acta Metallurgica*, **8** (1960), 617.
- [8] F.S. Pettit and J.B. Wagner Jr, *Acta Metallurgica*, **12** (1964), 35.
- [9] R. Bredesen and P. Kofstad, *Oxidation of Metals*, **34** (1990), 361.
- [10] R. Bredesen and P. Kofstad, *Oxidation of Metals*, **35** (1991), 107.
- [11] R. Bredesen and P. Kofstad, *Oxidation of Metals*, **36** (1991), 27.
- [12] E.T. Turkdogan, W.M. McKewan and L. Zwell, *Journal of Physical Chemistry*, **69** (1965), 327.
- [13] D.J. Young and H.Y. Yin, *Oxidation of Metals*, **79** (2013), 445.
- [14] D.J. Young, *High Temperature Oxidation and Corrosion of Metals*, Elsevier, Oxford, 2008.
- [15] R.Y. Chen and W.Y.D. Yuen, *Oxidation of Metals*, **85** (2016), 489.
- [16] V.A. Lashgari, G. Zimbitas, C. Kwakernaak and W.G. Sloof, *Oxidation of Metals*, **82** (2014), 249.
- [17] J.T. Armstrong, Quantitative Elemental Analysis of Individual Microparticles with Electron Beam Instruments, in *Electron Probe Quantitation*, Springer US, Boston, 1991.
- [18] H.J. Grabke, K.J. Best and A. Gala, *Werkstoffe und Korrosion*, **21** (1970), 911.
- [19] H.J. Grabke, *Annals of the New York Academy of Sciences*, **213** (1973), 110.

- [20] C. Kwakernaak and W. G. Sloof, Work of adhesion of interfaces between M<sub>2</sub>AlC (M = Ti, V, Cr) MAX phases and α-Al<sub>2</sub>O<sub>3</sub>, submitted to *Journal of Alloys and Compounds*, 2017.
- [21] H.T. Abuluwefa, R.I.L. Guthrie and F. Ajersch, *Metallurgical and Materials Transactions A*, **28** (1997), 1633.
- [22] R.Y. Chen and W.Y.D. Yuen, *Metallurgical and Materials Transactions A*, **40** (2009), 3091.
- [23] H. Yin, S.L.I. Chan, W.Y.D. Yuen and D.J. Young, *Oxidation of Metals*, **77** (2012), 305.
- [24] P. Mayer and W.W. Smeltzer, *Journal of the Electrochemical Society*, **119** (1972), 626.
- [25] S. Chandra-ambhorn, T. Nilsonthi, Y. Wouters and A. Galerie, *Corrosion Science*, **87** (2014), 101.
- [26] P. Franke and R. Dieckmann, *Journal of Physics and Chemistry of Solids*, **51** (1990), 49.
- [27] V.A. Lashgari, *Internal and External Oxidation of Manganese in Advanced High Strength Steels*, PhD Dissertation, Delft University of Technology, 2014.
- [28] *CRC Handbook of Chemistry and Physics*, 88th Edition, Taylor & Francis, 2007.
- [29] P. Wynblatt and R.C. Ku, *Surface Science*, **65** (1977), 511.
- [30] M. Zhao, W.G. Sloof and A.J. Bottger, Modelling of Surface Segregation for Palladium Alloys in Vacuum and Gas Environments, in preparation.
- [31] H. Meurer and H. Schmalzried, *Archiv für das Eisenhüttenwesen*, **42** (1971), 87.

## Chapter 8

# Reduction kinetics of Wüstite scale on pure iron and steel sheets in Ar and H<sub>2</sub> gas mixture<sup>1</sup>

### Abstract

A dense and closed Wüstite scale is formed on pure iron and Mn alloyed steel after oxidation in Ar + 33 vol.% CO<sub>2</sub> + 17 vol.% CO gas mixture. Reducing the Wüstite scale in Ar + H<sub>2</sub> gas mixture forms a dense and uniform iron layer on top of the remaining Wüstite scale, which separates the unreduced scale from the gas mixture. The reduction of Wüstite is controlled by the bulk diffusion of dissolved oxygen in the formed iron layer and follows parabolic growth rate law. The reduction kinetics of Wüstite formed on pure iron and on Mn alloyed steel are the same. The parabolic rate constant of Wüstite reduction obeys an Arrhenius relation with an activation energy of 104 kJ/mol if the formed iron layer is in the ferrite phase. However, at 950 °C parabolic rate constant of Wüstite reduction drops due to the phase transformation of the iron layer from ferrite to austenite. The effect of oxygen partial pressure on the parabolic rate constant of Wüstite reduction is negligible when reducing in a gas mixture with a dew point below 10 °C. During oxidation of the Mn alloyed steel, Mn is dissolved in the Wüstite scale. Subsequently, during reduction of the Wüstite layer, Mn diffuses into the unreduced Wüstite. Ultimately, an oxide-free iron layer is obtained at the surface of the Mn alloyed steel, which is beneficial for coating application.

### Keywords

Wüstite scale, Gaseous reduction, Hydrogen, Kinetics

---

<sup>1</sup> This chapter is based on:

W. Mao and W.G. Sloof, *Reduction kinetics of Wüstite scale on pure iron and steel sheets in Ar and H<sub>2</sub> gas mixture*, Metallurgical and Materials Transactions B, vol. 48, p. 2707, 2017.



## 8.1 Introduction

Advanced high strength steels (AHSS) are used in automotive industries to reduce the weight of car bodies thereby reducing fuel consumption and CO<sub>2</sub> emissions [1]. To protect AHSS against corrosion, a zinc coating is usually applied to the surface by hot-dip galvanizing [2]. During the hot-dip galvanizing process, the steel strip passes through continuous annealing furnaces before entering the zinc bath. The final annealing atmosphere is usually a gas mixture of N<sub>2</sub> and H<sub>2</sub> with some water vapor. However, the alloying elements in AHSS, such as Mn, Si, Cr, Al etc., can form stable oxides during this annealing process prior to galvanizing. These alloying element oxides at the steel surface lower the zinc wettability [3] and hence degrade the quality of the galvanized steel product [4]. One approach to mitigate the formation of external oxides during annealing is by annealing at high dew points to promote internal oxidation of alloying elements [5]. However, alloying element oxides can still be observed at the steel surface after annealing at high dew points, even when the annealing conditions favor internal oxidation [6]. An alternative way to create an oxide-free steel surface during annealing prior to galvanizing is by first forming a uniform thin Fe<sub>1-δ</sub>O (Wüstite) layer at the steel surface that subsequently is reduced into iron [7]. Then the unreduced alloying element oxides are buried underneath the steel surface.

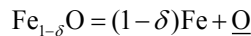
Generally, the reduction process of Wüstite goes through three different stages [8]. First, oxygen of the Wüstite reacts with H<sub>2</sub> at the very surface [9]. Depending on the oxygen partial pressure, Wüstite can accommodate cation vacancies with a relatively large concentration (iron deficiency can reach up to 10 % [10]). However, if the concentration of cation vacancies in the bulk Wüstite before reduction is higher than the equilibrium cation vacancy concentration, the initial reduction of Wüstite only decreases the amount of cation vacancies instead of forming metallic iron [11]. This decrease of concentration of cation vacancies at the Wüstite surface leads to an outward flux of these vacancies [12]. Next, when the surface concentration of oxygen drops below the value given by the Wüstite/iron phase boundary, iron nucleates and grow laterally at the surface [8, 11]. Eventually, iron covers the whole surface. Then, the iron layer separates the Wüstite from the reduction atmosphere. Subsequently, the Wüstite reduction proceeds by oxygen diffusion through the iron layer formed at the surface [13]. This stage is referred to as the steady state reduction of Wüstite.

The kinetics of Wüstite reduction during the three stages are different. The rate of oxygen removal by hydrogen at Wüstite surface in the first stage of reduction as well as the lateral

growth rate of iron nuclei during the second stage have been studied in detail [8, 9, 14, 15]. However, a detailed description of the kinetics of Wüstite reduction in the third stage, i.e. by oxygen diffusion through the occurring dense iron layer, is lacking [16]. First a model will be presented to predict the reduction kinetics of Wüstite quantitatively. Next, the reduction kinetics of a Wüstite scale formed on pure iron and Mn alloyed steel sheet is studied experimentally at different annealing temperatures in the Ar + H<sub>2</sub> atmosphere with different hydrogen partial pressures and dew points. Finally, the composition and microstructure of the surface is analyzed.

## 8.2 Kinetics of steady state Wüstite reduction

The kinetics of steady state reduction of Wüstite has been described in Refs [13, 17] only qualitatively. In this paper, however, the kinetics of steady state reduction of Wüstite is quantified. It is assumed that a closed and dense Fe layer is formed at the surface that separates the Fe<sub>1-δ</sub>O scale from the reducing gas atmosphere; see Figure 8.1. At the interface between the formed iron layer and the remaining Wüstite layer (Fe/Fe<sub>1-δ</sub>O), the Wüstite decomposes into iron and oxygen according to:



, in which  $\underline{\text{O}}$  denotes the oxygen atom dissolved in the formed iron layer as mobile solid solute without any charges. Then the dissolved oxygen diffuses through the reduced iron layer and reacts with the hydrogen at the gas/iron interface. Ultimately, the diffusion of dissolved oxygen across the iron layer governs the rate of Wüstite reduction, and local thermodynamic equilibrium is established at both Fe/Fe<sub>1-δ</sub>O and gas/Fe interfaces. This implies that the reactions at these interfaces and the transport of species in the gas phase are fast compared with the diffusion of species in the iron layer. Also, the oxygen activity is considered to be constant across the remaining Wüstite scale and equals the dissociation oxygen partial pressure of Fe<sub>1-δ</sub>O. Hence, the iron deficiency  $\delta$  (i.e. the concentration of cation vacancies) in the Fe<sub>1-δ</sub>O scale remains constant during reduction process. The concentration of dissolved oxygen in Fe at the surface is determined by the oxygen partial pressure in the gas phase through Sievert's law [18]. While the concentration of dissolved oxygen in Fe at the interface with Fe<sub>1-δ</sub>O is determined by the dissociation oxygen partial pressure of Wüstite. Hence, the mole fraction of dissolved oxygen in Fe at the surface ( $N_{\underline{\text{O}}}^s$ ) and at the Fe/Fe<sub>1-δ</sub>O interface ( $N_{\underline{\text{O}}}^e$ ) reads:

$$\begin{aligned} N_{\underline{\text{O}}}^s &= K_S \times \sqrt{p\text{O}_2^{(\text{ambient})}} \\ N_{\underline{\text{O}}}^e &= K_S \times \sqrt{p\text{O}_2^{(\text{Fe/FeO})}} \end{aligned} \quad (8.1)$$

where  $K_s$  is the Sievert's constant and  $p_{O_2}^{(Fe/FeO)}$  is the dissociation oxygen partial pressure of Wüstite. The ambient oxygen partial pressure ( $p_{O_2}^{(ambient)}$ ) as a function of temperature, hydrogen partial pressure and dew point can be calculated from the data in ref. [19]. Both  $K_s$  and  $p_{O_2}^{(Fe/FeO)}$  are a function of temperature, namely:

$$K_s = \exp\left(\frac{-\Delta G_{O_2}^0}{RT}\right) \quad (8.2)$$

and

$$p_{O_2}^{(Fe/FeO)} = \exp\left(\frac{2\Delta G_{FeO}^0}{RT}\right) \quad (8.3)$$

in which  $\Delta G_{O_2}^0$  is the standard free energy for O<sub>2</sub> dissolution in Fe, and  $\Delta G_{FeO}^0$  is the standard free energy of reaction  $Fe + 1/2O_2 = FeO$ . Further,  $\Delta G_{O_2}^0$  and  $\Delta G_{FeO}^0$  can be expressed in terms of enthalpy  $H$ , entropy  $S$  and temperature  $T$  according to:

$$\Delta G_{O_2}^0 = \Delta H_{O_2}^0 - T\Delta S_{O_2}^0 \quad (8.4)$$

and

$$\Delta G_{FeO}^0 = \Delta H_{FeO}^0 - T\Delta S_{FeO}^0 \quad (8.5)$$

, respectively. Data of  $\Delta G_{O_2}^0$  can be evaluated from ref. [20], and  $\Delta G_{FeO}^0$  is obtained from ref. [18].

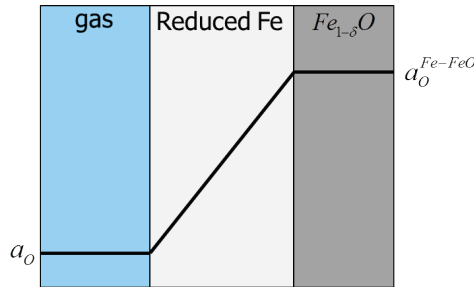


Figure 8.1: Schematic presentation of oxygen activity profile across the iron layer during the steady-state reduction of a Wüstite scale.

Taking the concentration profile of dissolved oxygen in Fe linear, then the flux of oxygen in the iron layer follows from Fick's first law:

$$J_{\underline{O}} = \frac{D_{\underline{O}}}{V_{m(Fe)}} \frac{(N_{\underline{O}}^e - N_{\underline{O}}^s)}{X} \quad (8.6)$$

where  $V_{m(\text{Fe})}$  is the molar volume of Fe and  $X$  is the thickness of the reduced iron layer.  $D_{\text{O}}$  is the bulk diffusion coefficient of oxygen in iron, which equals:

$$D_{\text{O}} = D_{\text{O}}^0 \exp\left(\frac{-Q}{RT}\right) \quad (8.7)$$

Values of  $D_{\text{O}}^0$  and  $Q$  are adopted from ref. [18]. Since the growth rate of the reduced iron layer is coupled to the oxygen flux, it holds that:

$$\frac{dX}{dt} = J_{\text{O}}(1-\delta)V_{m(\text{Fe})} \quad (8.8)$$

Integrating Eq. (8.8) gives:

$$X^2 = 2(1-\delta)D_{\text{O}}(N_{\text{O}}^e - N_{\text{O}}^s)t \quad (8.9)$$

Usually, such a parabolic growth law is expressed as:

$$X^2 = 2kt \quad (8.10)$$

where  $k$  is termed the parabolic growth rate constant, which equals:

$$k = (1-\delta)D_{\text{O}}(N_{\text{O}}^e - N_{\text{O}}^s) \quad (8.11)$$

Alternatively, the kinetics of Wüstite reduction can be expressed in terms of the weight change per unit area as a function of square root of time, namely:

$$(\Delta m / S) = k_w t^{1/2} \quad (8.12)$$

For this parabolic growth rate constant,  $k_w$  can be written:

$$k_w = \frac{\sqrt{2}M_{\text{O}}}{M_{\text{Fe}}} \rho_{\text{Fe}} [(1-\delta)D_{\text{O}}(N_{\text{O}}^e - N_{\text{O}}^s)]^{1/2} \quad (8.13)$$

in which  $M_{\text{O}}$  and  $M_{\text{Fe}}$  are the molar mass of oxygen and iron respectively, and  $\rho_{\text{Fe}}$  is the density of iron, whose values are adopted from ref. [21]. The value of  $\delta$  in Wüstite at thermodynamic equilibrium with iron is typically about 0.05 from 600 to 1000 °C [10]. The value of  $k_w$  at different reduction temperatures and gas compositions (i.e. dew points and hydrogen partial pressure) can then be predicted from Eq. (8.13). When the ambient oxygen partial pressure is low (e.g. low annealing dew point),  $N_{\text{O}}^s$  is practically zero, and Eq. (8.13) can be simplified to:

$$k_w = \frac{\sqrt{2}M_{\text{O}}}{M_{\text{Fe}}} \rho_{\text{Fe}} [(1-\delta)D_{\text{O}}N_{\text{O}}^e]^{1/2} \quad (8.14)$$

Combining Eqs (8.1) to (8.5) and (8.7), the temperature dependence of  $k_w$  can be expressed as:

$$k_w = \frac{M_{\text{O}}\rho_{\text{Fe}}[2(1-\delta)D_{\text{O}}^0]^{1/2}}{M_{\text{Fe}}} \exp\left(\frac{-\Delta S_{\text{O}}^0 - \Delta S_{\text{FeO}}^0}{2R}\right) \exp\left(\frac{-Q - \Delta H_{\text{O}}^0 + \Delta H_{\text{FeO}}^0}{2RT}\right) \quad (8.15)$$

Here, half the sum of  $-Q$ ,  $-\Delta H_{\text{O}}^0$  and  $\Delta H_{\text{FeO}}^0$  represents the activation energy of Wüstite reduction.

## 8.3 Experiments and methods of investigation

### 8.3.1 Samples

The Wüstite scale to study its reduction kinetics was created by oxidizing sheets of pure iron and a Mn alloyed steel in a gas mixture of Ar + 33 vol.% CO<sub>2</sub> + 17 vol.% CO. The chemical composition of the pure iron and the Mn alloyed steel is listed in Table 8.1. Rectangular samples of 15×7×2 mm for thermogravimetric analysis were cut from ingots by electric discharge machining (EDM). Also the Mn alloyed steel samples of 19×10×1 mm were cut, but with a plate cutter from a cold rolled sheet. All samples were grinded with SiC emery paper and then polished with 1 micron diamond grains. Between each preparation step the samples were cleaned ultrasonically in isopropanol and dried by blowing with pure nitrogen (purity better than 5N). The dimension of each sample after preparation was measured with a caliper (accuracy ± 0.05 mm). The samples were stored in air tight membrane boxes (Agar Scientific G3319, UK).

Table 8.1: Chemical composition of iron and Mn alloyed steel as determined by Optical Emission Spectrometry.

	C (wt%)	Mn (wt%)	Si (wt%)	Al (wt%)	Ni (wt%)
Iron	0.002	-	0.003	0.040	0.005
Mn-steel	0.103	1.70	0.049	0.002	-

### 8.3.2 Annealing

A first series of oxidation and reduction experiments were performed with a symmetrical thermogravimetric analyzer (TGA, Setaram TAG 16/18, France). The sample was mounted onto a sapphire rod with an alumina pin having a diameter of 2.2 mm through a hole of diameter of 2.5 mm in the sample. A dummy sample of alumina with the same dimensions is mounted onto a sapphire rod of the counter part of the balance to eliminate any buoyancy effect.

The whole TGA system was pumped to vacuum (< 50 Pa) and refilled with an Ar + 5 vol.% H<sub>2</sub> gas mixture twice to flush the gas lines, balance and furnaces. Then the dual furnaces were heated up from room temperature to the target temperature with 5 °C/min, while purging with 200 sccm Ar + 5 vol.% H<sub>2</sub>, i.e. 100 sccm gas in each furnace. When the target

temperature for isothermal oxidation was reached, the gas composition was switched to Ar + 33 vol.% CO<sub>2</sub> + 17 vol.% CO while maintaining a total gas flow of 200 sccm. After oxidation, the conditions were switched to reduction either at the same temperature as for oxidation or at a specific temperature for isothermal reduction. The gas composition was switched to Ar + 5 or 10 vol.% H<sub>2</sub> while maintaining a total gas flow of 200 sccm. Finally, the furnace was cooled down to room temperature with 5 °C/min, while keeping the gas composition the same as during reduction. Since no significant decarburization was observed during oxidation and reduction of Mn alloyed steels, the TG curves of the Mn-steels during the reduction process represents the kinetics of Wüstite reduction.

A second series of experiments on the Mn alloyed steel samples were carried out in a horizontal quartz tube furnace (Carbolite MTF 12/38/850, UK) with an inner tube diameter of 30 mm. The sample was placed onto a quartz boat located at the cold zone of the furnace tube. Then the furnace was closed and flushed with pure Ar at a flow rate of 500 sccm. Next, the sample was moved to the hot zone of the furnace with a quartz rod. At the end of the annealing experiment the sample was moved in the reverse direction to the cold zone. The heating and cooling of the sample was relatively fast, about 140 and 180 °C/min, respectively. The gas mixtures passed through the furnace tube at atmospheric pressure at a total flow rate of 500 sccm. The Mn alloyed steel samples were first oxidized in the Ar + 33 vol.% CO<sub>2</sub> + 17 vol.% CO gas mixture at 950 °C and then reduced in dry or wet Ar + 10 vol.% H<sub>2</sub> gas mixture at the same temperature. During reduction process the dew point was monitored with a cooled mirror analyzer (Optidew, Michell Instruments, UK). The fluctuation of dew points during reduction process was within ± 2 °C.

Prior to admitting the gas mixtures to any of the furnace, each gas, i.e. Ar, H<sub>2</sub>, CO<sub>2</sub> and CO (all with 5N vol.% purity), was filtered to remove any residual hydrocarbons, moisture and oxygen, with Accosorb (< 10 ppb hydrocarbons), Hydrosorb (<10 ppb H<sub>2</sub>O) and Oxysorb (< 5 ppb O<sub>2</sub>) filters (Messer Griesheim, Germany), respectively. The flow of each gas was regulated and monitored using mass flow controllers (Bronkhorst, The Netherlands). To create a specific dew point in the furnace, de-aerated and deionized water (18.2 MΩ.cm at 25 °C) was evaporated with an in the gas line controlled evaporator mixer (CEM, Bronkhorst, The Netherlands). The pure water was de-aerated with nitrogen gas in a closed pressurized stainless steel vessel and the dissolved oxygen gas in the pure water is below 100 ppb, as measured with an O<sub>2</sub> sensor (InPro 6850i, Mettler Toledo). The partial pressure of evaporated H<sub>2</sub>O in the Ar + H<sub>2</sub> gas mixtures is related to dew point according to the formula given in ref. [19].

### 8.3.3 Characterization

X-ray diffraction (XRD) was used to identify the oxide phases formed after annealing. The XRD patterns were recorded with a Bruker D8 Advance diffractometer in the Bragg-Brentano geometry using Co K $\alpha$  radiation, in the 2 $\theta$  region between 10° to 110° with a step size of 0.034° 2 $\theta$  and a dwell time of 2 s.

The surface and cross-section of the annealed samples were examined with scanning electron microscopy (SEM) using a JSM6500F (JEOL, Japan) operated with an accelerating voltage of 5 or 15 kV. X-ray microanalysis (XMA) using Electron Dispersive Spectroscopy (EDS) was performed with the same SEM instrument equipped with an UltraDry 30 mm<sup>2</sup> detector (Thermo Fisher Scientific, USA).

The concentration of Mn in the Wüstite formed on Mn alloyed steel as well as the Mn concentration in the iron layer formed after Wüstite reduction was determined with electron probe X-ray microanalysis (EPMA). The analysis was performed with a JXA 8900R (JEOL, Japan) microprobe employing Wavelength Dispersive Spectrometry (WDS). A focused electron beam was used with an energy of 10 keV and a current of 50 nA. All measurements were performed on cross-sections of samples. The composition at each analysis location of the sample was determined using the X-ray intensities of the constituent elements after background correction relative to the corresponding intensities of reference materials. In this case the X-ray intensities of Fe-K $\alpha$ , Mn-K $\alpha$  and O-K $\alpha$  were measured and pure Fe, Mn and SiO<sub>2</sub>, respectively, were used as references. The thus obtained intensity ratios were processed with a matrix correction program CITZAF [22].

## 8.4 Results and discussion

### 8.4.1 Growth of Wüstite scale

After oxidation of pure iron and Mn alloyed steel in the Ar + 33 vol.% CO<sub>2</sub> + 17 vol.% CO gas mixture, a dense oxide scale fully covering the surface was formed; see e.g. Figure 8.2. According to XRD, the oxide scale on both pure iron and Mn-steel is composed of Wüstite. However, the oxide scale on Mn-steel contains Mn in solid solution, i.e. (Fe<sub>1-x</sub>Mn<sub>x</sub>)<sub>1- $\delta$</sub> O, as confirmed with EPMA. Mn is homogeneously distributed in the Wüstite scale on Mn-steel with a concentration of about 3 at.% among metallic elements (i.e.  $x$  equals to 0.03 in (Fe<sub>1-x</sub>Mn<sub>x</sub>)<sub>1- $\delta$</sub> O) after annealing in the Ar + 33 vol.% CO<sub>2</sub> + 17 vol.% CO gas mixture at 950 °C for 8 hours. An internal oxidation zone (IOZ) is formed beneath the Wüstite scale after oxidation of the Mn alloyed steel; see Figure 8.2(b). The oxide precipitates in the IOZ comprise (Mn,Fe)O with rock-salt crystal lattice [23].

For both iron and the Mn alloyed steel, the Wüstite growth follows linear kinetics; see e.g. Figures 8.3 and 8.4. This indicates that the level of oxygen partial pressure across the Wüstite scale is uniform and equals to the dissociation oxygen partial pressure of Wüstite [24, 25]. Hence the composition of the Wüstite ( $\text{Fe}_{1-\delta}\text{O}$  or  $(\text{Fe,Mn})_{1-\delta}\text{O}$ ) scale in terms of its metal deficiency  $\delta$  equals to about 0.05 [10]. The initial non-linear growth of Wüstite scale is due to stabilization of the flow and composition of the annealing gas atmosphere after switching to oxidation conditions, which takes about 20 to 30 minutes. Moreover, during the initial oxidation stage the linear growth rate of Wüstite scale on pure iron in  $\text{Ar} + \text{CO}_2 + \text{CO}$  gas mixtures increases with time due to the evolution of the texture of the Wüstite scale [26].

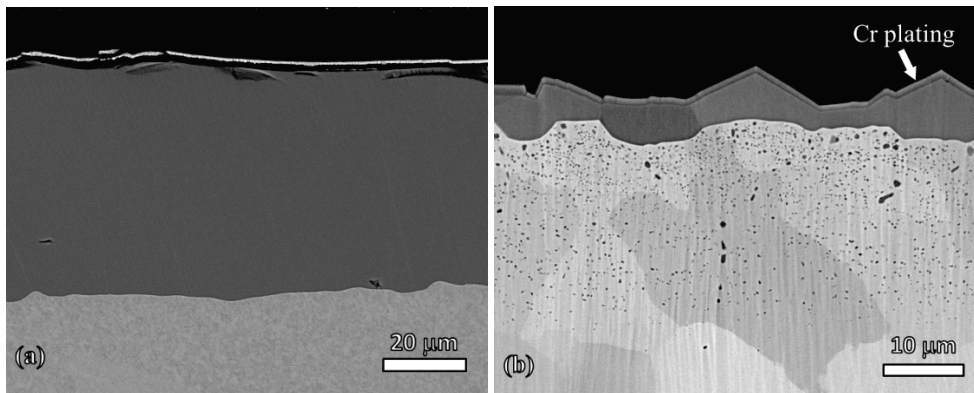


Figure 8.2: SEM images (back scattered electrons) of cross-section of (a) a pure iron and (b) a Mn alloyed steel after oxidizing at 950 °C in  $\text{Ar} + 33 \text{ vol.}\% \text{CO}_2 + 17 \text{ vol.}\% \text{CO}$  gas mixture for 3 and 8 hours, respectively.

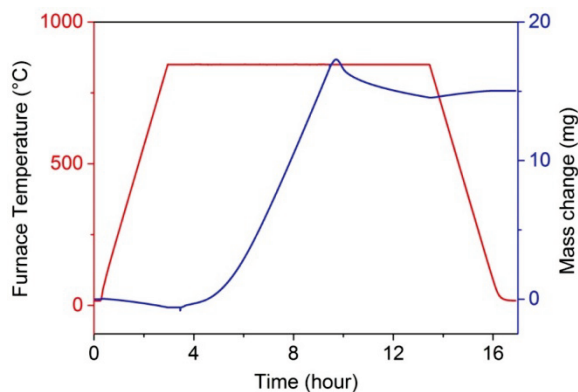


Figure 8.3: Temperature profile and corresponding mass change of iron during first oxidation in  $\text{Ar} + 33 \text{ vol.}\% \text{CO}_2 + 17 \text{ vol.}\% \text{CO}$  gas mixture for 6 hours and next reduction of the formed Wüstite in dry  $\text{Ar} + 5 \text{ vol.}\% \text{H}_2$  gas mixture for 4 hours both at 850 °C.



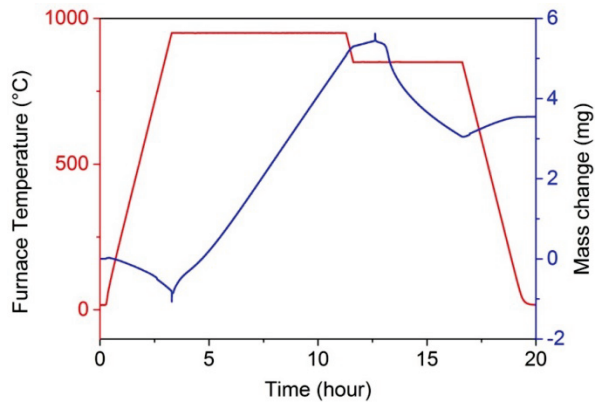


Figure 8.4: Temperature profile and corresponding mass change curve of a Mn alloyed steel (cf. Table 8.1) during first oxidation in Ar + 33 vol.% CO<sub>2</sub> + 17 vol.% CO gas mixture at 950 °C for 8 hours and next at 850 °C for 1 hour. Thereafter, the Wüstite layer on the Mn alloyed steel was reduced in dry Ar + 5 vol.% H<sub>2</sub> gas mixture for 4 hours at 850 °C.

### 8.4.2 Growth of iron layer

When reducing the Wüstite scale, either formed on pure iron or on Mn alloyed steel, in an Ar + H<sub>2</sub> gas mixture, a dense and uniform layer of iron is formed beneath the surface. This iron layer separates the unreduced Wüstite scale from the reduction atmosphere; see e.g. Figure 8.5. The iron layer is well adherent to the unreduced Wüstite scale. In contrast with results reported for the reduction of Wüstite in pure H<sub>2</sub> (see e.g. ref. [27]), no significant cracks or pores were observed in the iron layer nor at the scale-iron interface.

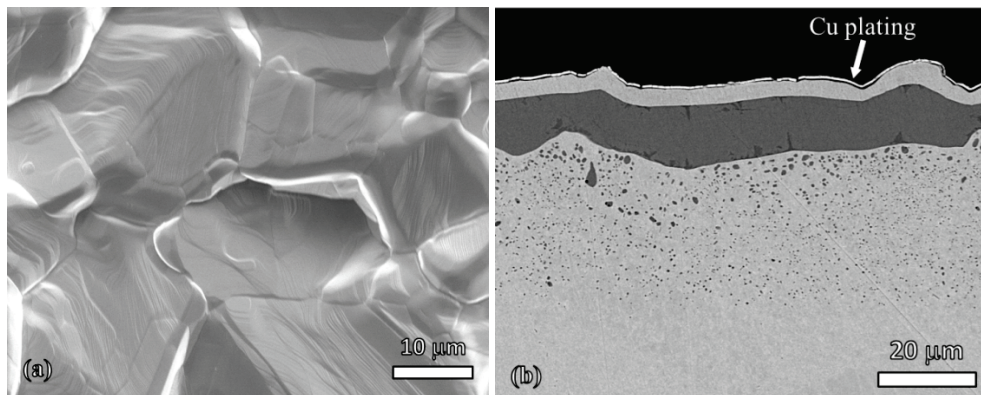


Figure 8.5: SEM images (secondary electrons (a), back scattered electrons (b)) of (a) surface and (b) cross-section of a Mn alloyed steel after first oxidizing at 950 °C for 8 hours in Ar + 33 vol.% CO<sub>2</sub> + 17 vol.% CO gas mixture and next reducing at 850 °C for 4 hours in Ar + 5 vol.% H<sub>2</sub> gas mixture.

The lattice parameters of  $\alpha$ -iron,  $\gamma$ -iron and  $\text{Fe}_{0.95}\text{O}$  at 910 °C are 0.2907, 0.3647 and 0.4363 nm, respectively [28]. Hence, reducing  $\text{Fe}_{0.95}\text{O}$  to iron results in volume shrinkage of about 42 %. However, the lattice misfit at the scale/iron interface can be much smaller. The orientation relationships at the iron/Wüstite interface is  $(100)_{\text{Fe}}\parallel(100)_{\text{FeO}}$  and  $[010]_{\text{Fe}}\parallel[011]_{\text{FeO}}$  for  $\alpha$ -iron, and  $(100)_{\text{Fe}}\parallel(100)_{\text{FeO}}$  and  $[100]_{\text{Fe}}\parallel[100]_{\text{FeO}}$  for  $\gamma$ -iron [28, 29]. Then the misfit relative to the Wüstite lattice at iron/Wüstite interface is about 5.7 and 16.4 % for  $\alpha$ -iron and  $\gamma$ -iron, respectively. In addition, dissolved oxygen is normally considered to be present at the interstitial sites of iron lattice due to its similar diffusion coefficient as nitrogen and carbon in iron [30]. Hence, the outward flux of dissolved oxygen atoms to the surface does not lead to counter flux of vacancies to the iron/Wüstite interface. Therefore, good adhesion between iron and Wüstite scale is expected.

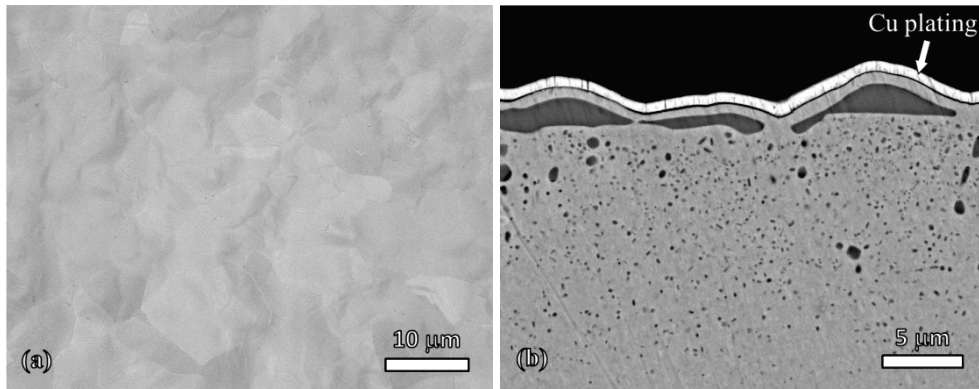


Figure 8.6: SEM images (back scattered electrons) of (a) surface and (b) cross-section of a Mn alloyed steel after first oxidizing in Ar + 33 vol.%  $\text{CO}_2$  + 17 vol.% CO gas mixture for 3 hours and then reducing in Ar + 10 vol.%  $\text{H}_2$  gas mixture at dew point of 10 °C for 15 minutes at constant temperature of 950 °C.

Reduction of  $\text{FeO}$  at 950 °C in Ar + 10 vol.%  $\text{H}_2$  gas mixture occurs at dew points below 36 °C, while reduction of  $\text{MnO}$  at the same temperature requires dew points below -75 °C. Thus, the  $\text{MnO}$  in the Wüstite scale formed on the Mn alloyed steel will not be reduced in an Ar +  $\text{H}_2$  gas mixture with a dew point of 10 °C. Nevertheless, an oxide-free surface of Mn alloyed steel is obtained by first forming and then reducing the Wüstite scale at 950 °C. This is because the  $(\text{Fe,Mn})_{1-\delta}\text{O}$  scale dissociates into iron alone instead of iron plus embedded  $\text{MnO}$  particles. The Mn still remains in the unreduced  $(\text{Fe,Mn})_{1-\delta}\text{O}$  scale and the Mn concentration in the unreduced  $(\text{Fe,Mn})_{1-\delta}\text{O}$  scale increases with reduction time. Apparently, transport of Mn occurs towards the remaining Wüstite. Figure 8.6 shows the surface and cross-section of the Mn-steel after, first oxidizing at 950 °C for 3 hours in Ar + 33 vol.%  $\text{CO}_2$  + 17 vol.% CO gas mixture and then reducing at same temperature for 15

minutes in Ar + 10 vol.% H<sub>2</sub> gas mixture at dew point of 10 °C, and no external MnO was observed. After reducing for 2.5 hours with the same annealing parameters, the Wüstite scale formed during the oxidation stage can be fully reduced; see Figure 8.7. The iron layer formed after the reduction of Wüstite scale is well adhered to the original steel matrix. The Mn concentration in the formed iron layer is practically zero. However, the Mn concentration in the remaining Wüstite scale increases with reduction time ( $x$  in (Fe<sub>1-x</sub>Mn<sub>x</sub>)<sub>1-δ</sub>O increases from 0.03 to 0.07 after 15 minutes of reduction). After full reduction of the oxide scale, the small amount of Mn dissolved in the Wüstite turns into internal (Mn,Fe)O precipitates underneath the surface; see Figure 8.7(b).

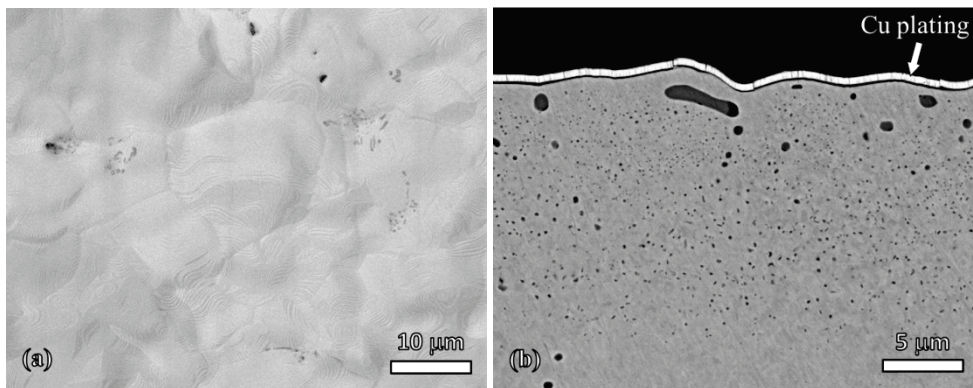


Figure 8.7: SEM images (back scattered electrons) of (a) surface and (b) cross-section of a Mn alloyed steel after first oxidizing in Ar + 33 vol.% CO<sub>2</sub> + 17 vol.% CO gas mixture for 3 hours and then reducing in Ar + 10 vol.% H<sub>2</sub> gas mixture at dew point of 10 °C for 2.5 hours at constant temperature of 950 °C.

### 8.4.3 Kinetics of Wüstite reduction

The reduction kinetics of the Wüstite layer by hydrogen can be predicted using Eq. (8.15) with the data summarized in Table 8.2. The temperature dependence of the parabolic rate constant is dominated by the temperature dependence of the oxygen diffusivity in iron. The activation energy for Wüstite reduction predicted using Eq. (8.15) is 104 kJ/mol if the formed iron layer is in the ferrite phase, while the activation energy for oxygen diffusion in ferrite equals 98 kJ/mol [18]. The parabolic rate constant for Wüstite reduction as a function of temperature in dry reducing atmosphere is presented in Figure 8.8. The parabolic rate constant of Wüstite reduction is determined experimentally with the approach illustrated in the Appendix E to this thesis. Comparison of these predicted values with experimentally determined parabolic rate constants for the reduction of Wüstite on both pure iron and the Mn alloyed steel shows good agreement; see Figure 8.8. This suggests that the kinetics of Wüstite reduction at steady state in Ar + H<sub>2</sub> gas mixture is indeed

controlled by the bulk diffusion of dissolved oxygen in the formed iron layer. Also it confirms that the rate of oxygen take-up by hydrogen at iron surface and the decomposition of Wüstite at scale-alloy interface are fast compared with the oxygen transport in the iron layer. Moreover, it suggests that the adopted data of oxygen diffusion in iron [18] as well as oxygen dissolution in iron [20] are valid.

Table 8.2: Summary of the data adopted for calculation of parabolic rate constant for Wüstite reduction.

Parameters	Values	Reference
$D_{\underline{O}}^0(\alpha)$ ( $\text{cm}^2 \text{s}^{-1}$ )	0.037	18
$Q(\alpha)$ ( $\text{J mol}^{-1}$ )	98000	18
$D_{\underline{O}}^0(\gamma)$ ( $\text{cm}^2 \text{s}^{-1}$ )	5.75	18
$Q(\gamma)$ ( $\text{J mol}^{-1}$ )	168000	18
$\Delta H_{\underline{O}}^0(\alpha)$ ( $\text{J mol}^{-1}$ )	-154834	20
$\Delta S_{\underline{O}}^0(\alpha)$ ( $\text{J mol}^{-1} \text{K}^{-1}$ )	-70.3	20
$\Delta H_{\underline{O}}^0(\gamma)$ ( $\text{J mol}^{-1}$ )	-173021	20
$\Delta S_{\underline{O}}^0(\gamma)$ ( $\text{J mol}^{-1} \text{K}^{-1}$ )	-86.5	20
$\Delta H_{\text{FeO}}^0$ ( $\text{J mol}^{-1}$ )	-264890	18
$\Delta S_{\text{FeO}}^0$ ( $\text{J mol}^{-1} \text{K}^{-1}$ )	-65.4	18
$\rho_{\text{Fe}}$ ( $\text{g cm}^{-3}$ )	7.9	21
$M_{\text{Fe}}$ ( $\text{g mol}^{-1}$ )	56	21
$M_{\text{O}}$ ( $\text{g mol}^{-1}$ )	16	21

Since the diffusion coefficient of oxygen for ferrite is much larger than for austenite [18], the parabolic rate constant for Wüstite reduction suddenly drops due to the phase transformation of iron from ferrite into austenite. Hence, the reduction of Wüstite is relatively faster when the formed iron layer is ferrite rather than austenite. Moreover, the Sievert's constant for oxygen dissolution in ferrite is slightly higher than that in austenite

[20], which also contributes to the decrease of the parabolic rate constant (see Eqs (8.1) and (8.14)) when the iron layer transforms from ferrite into austenite. This is in agreement with the experimental results that the observed parabolic rate constants for the reduction of Wüstite on pure iron and Mn alloyed steel at 950 °C (i.e. both in austenite state) are much lower than those predicted for a ferrite layer; see Figure 8.8.

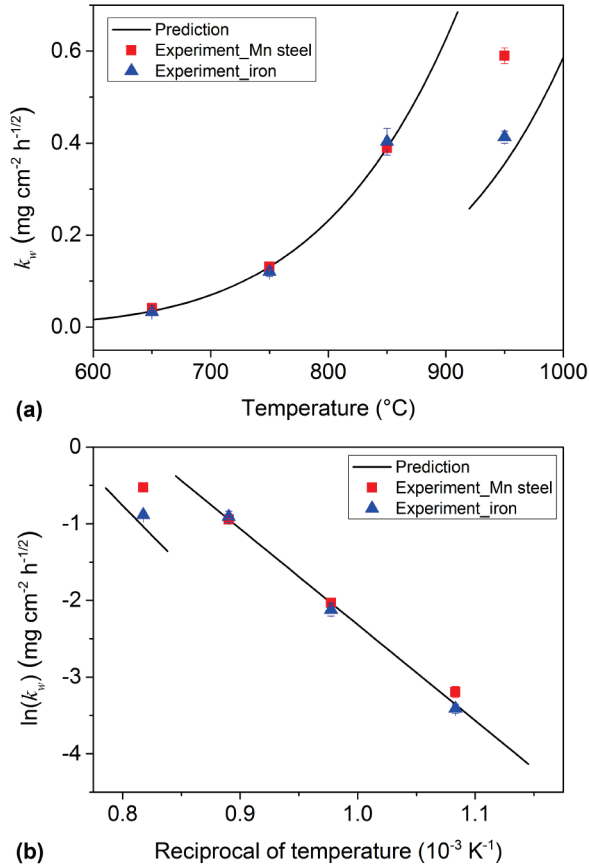


Figure 8.8: Comparison between the predicted (cf. Eq. (8.13)) and experimentally determined parabolic rate constants of reduction of Wüstite on pure iron and a Mn alloyed steel alloy at different temperatures; (a) normal plot and (b) Arrhenius plot. The formed iron layer is in ferritic phase below 912 °C and in austenitic phase above 912 °C. Note that the oxygen concentration at the iron/gas interface was taken zero, i.e.  $N_{\text{O}}^s = 0$ .

The kinetics of Wüstite reduction also depends on the oxygen partial pressure in the gas phase, which is related to dew point and H<sub>2</sub> partial pressure [19]. Increasing the oxygen partial pressure in the reduction atmosphere, increases the concentration of dissolved

oxygen at the iron surface ( $N_{\underline{O}}^s$ ) and thus reduces the parabolic rate constant for Wüstite reduction; see Eq. (8.13). As can be seen in Figure 8.9, at 850 °C the parabolic rate constant for Wüstite reduction is practically independent of oxygen partial pressures up to  $3 \times 10^{-20}$  atm., but decreases rapidly at higher oxygen partial pressures. At the dissociation oxygen partial pressure of Wüstite the reduction process does not take place and hence the parabolic rate constant for Wüstite reduction drops to zero. However, in an annealing atmosphere with a dew point lower than 10 °C and a  $H_2$  volume fraction larger than 5 %, the effect of oxygen partial pressure on the parabolic rate constant for Wüstite reduction is small compared with the effect of temperature.

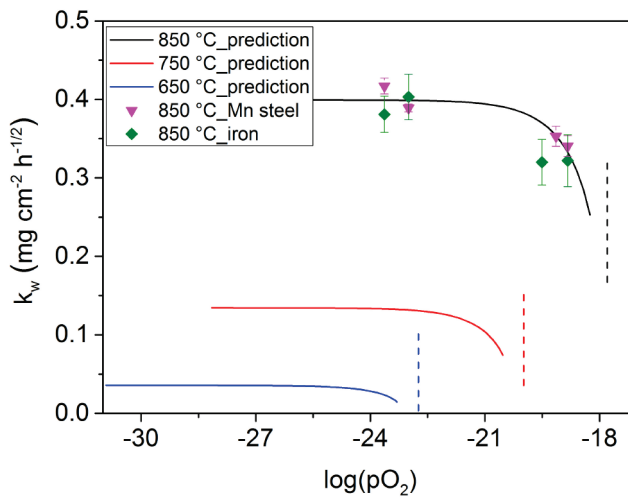


Figure 8.9: Effect of oxygen partial pressure on parabolic rate constant of Wüstite reduction at temperatures of 650, 750 and 850 °C. Dashed lines indicate the dissociation oxygen partial pressure of Wüstite. Note that the oxygen partial pressure in dry Ar +  $H_2$  gas mixture is calculated assuming a dew point of -45 °C.

The dissolution of Mn in the Wüstite scale with a concentration of 3 at.% may lower the parabolic rate constant for Wüstite reduction by about 1.7 % (cf. Eqs (8.1) and (8.14)), which is relatively small and neglected in this study. The dissociation oxygen partial pressure at the interface between iron layer and Wüstite scale decreases with Mn concentration in the Wüstite scale, because the activity of FeO in the (Fe,Mn)O solution is less than unity.

The dissociation of Wüstite scale occurs not only at the scale/iron interface, but also at the original steel/scale interface, because the oxygen activity in the steel is lower than the dissociation oxygen partial pressure of Wüstite. The predicted and measured parabolic rate

constants shown in Figures 8.8 and 8.9 only reflect the reduction process at scale/iron interface, since the reduction at steel/scale interface does not result in any weight change of sample. Hence, the total reduction rate of the Wüstite scale is higher than that determined from the measured mass loss. However, the amount of Wüstite reduced at the scale/steel interface is small compared with that at the scale/iron interface. The Wüstite dissociation at the steel/scale interface provides the oxygen source that allows inward oxygen diffusion and thus forms an internal oxidation zone (IOZ) beneath the Wüstite scale; see e.g. Figures 8.2 and 8.5. The rate of Wüstite dissociation at scale/steel interface equals to the flux of oxygen into the IOZ, and thus can be estimated from the kinetics of internal oxidation underneath the Wüstite scale. The gradient of dissolved oxygen in the IOZ is almost linear [18, 31], and the flux of oxygen into the steel at the steel/scale interface can thus be estimated with Fick's 1<sup>st</sup> law. Since the level of the oxygen partial pressure at steel/scale and scale/iron interfaces are almost the same and the oxygen concentration at the IOZ front equals zero, the ratio of the Wüstite reduction rate at scale/iron interface over that at scale/steel interface can be estimated with:

$$\frac{J_{\text{O}}^{\text{FeO/Fe}}}{J_{\text{O}}^{\text{FeO/steel}}} = \frac{N_{\text{O}}^e - N_{\text{O}}^s}{N_{\text{O}}^e} \frac{d}{X} \quad (8.16)$$

where  $d$  is the depth of IOZ underneath the Wüstite scale,  $J_{\text{O}}^{\text{FeO/Fe}}$  and  $J_{\text{O}}^{\text{FeO/steel}}$  represent the oxygen flux from Wüstite to the iron layer and from Wüstite to the steel substrate, respectively. The increase of the depth of IOZ ( $d$ ) during the reduction process can be estimated from the classical internal oxidation theory [18]. The thickness of the iron layer ( $X$ ) as a function of reduction time can be calculated using Eq. (8.4). The ratio of the amount of Wüstite reduced at scale/iron interface over the amount of Wüstite reduced at scale/steel interface equals to the ratio of the integration of the oxygen flux at the two interfaces, i.e.  $\int J_{\text{O}}^{\text{FeO/Fe}} dt / \int J_{\text{O}}^{\text{FeO/steel}} dt$ . Figure 8.10 shows the predicted fraction of the amount of Wüstite scale reduced at the scale/steel interface as a function of reduction time. The depth of IOZ before the start of reduction process was taken 10 or 20  $\mu\text{m}$ . The dew point in the reducing atmosphere was taken -70 and 5  $^{\circ}\text{C}$ . Although the fraction of the amount of Wüstite reduced at the scale/steel interface increases with reduction time, the dominant reduction process of Wüstite scale occurs at the scale/iron interface. For example, after oxidizing the Mn alloyed steel at 950  $^{\circ}\text{C}$  for 8 hours and then reducing in dry Ar + 5 vol.% H<sub>2</sub> gas mixture at 850  $^{\circ}\text{C}$  for 4 hours, the contribution of the amount of Wüstite reduced at the scale/steel interface to the total amount of Wüstite reduced is about 6 %. Thus, the calculated reduction kinetics of the scale/iron interface (see Section 8.2) provides a satisfactory estimate on the total reduction kinetics of the Wüstite scale.

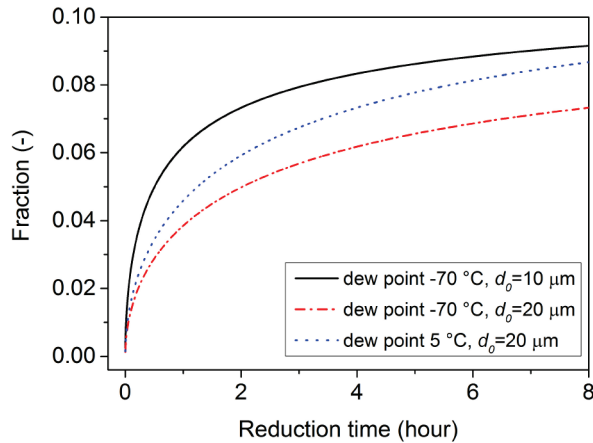


Figure 8.10: Fraction of Wüstite reduced at scale/steel interface at 850 °C in Ar + 5 vol.% H<sub>2</sub> gas mixture with dew point -70 or 5 °C. At the beginning of the reduction process, the depth of IOZ equals  $d_0$ .

## 8.5 Conclusions

Oxidizing pure iron and Mn alloyed steel in Ar + 33 vol.% CO<sub>2</sub> + 17 vol.% CO gas mixture forms a dense Wüstite scale. A dense and uniform layer of pure iron is formed at the surface of the Wüstite scale after reduction in Ar + H<sub>2</sub> gas mixtures. The reduction of the Wüstite scale follows a parabolic rate law at steady state. The parabolic rate constant of Wüstite reduction for Wüstite grown onto pure iron and the Mn-steel are the same. The kinetics of Wüstite reduction in Ar + H<sub>2</sub> gas mixtures is controlled by bulk diffusion of dissolved oxygen in the formed Fe layer. Mn is dissolved in the Wüstite scale formed during oxidation of Mn alloyed steel. Mn remains dissolved in unreduced Wüstite scale during reduction process. An oxide-free surface of Mn alloyed steel can be obtained by forming first a Wüstite scale that subsequently is reduced in a Ar + H<sub>2</sub> gas mixture.

## References

- [1] N. Fonstein, *Advanced High Strength Sheet Steels*, Springer International Publishing, Switzerland, 2015.
- [2] A.R. Marder, *Progress in Materials Science*, **45** (2000), 191.
- [3] G.M. Song, T. Vystavel, N. van der Pers, J.T.M. De Hosson and W.G. Sloof, *Acta Materialia*, **60** (2012), 2973.



- [4] E.M. Bellhouse and J.R. McDermid, *Metallurgical and Materials Transactions A*, **41** (2010), 1539.
- [5] H. Liu, Y. He, S. Swaminathan, M. Rohwerder and L. Li, *Surface and Coatings Technology*, **206** (2011), 1237.
- [6] V.A. Lashgari, C. Kwakernaak and W.G. Sloof, *Oxidation of Metals*, **81** (2014), 435.
- [7] M. Blumenau, C.O. Gusek, M. Norden and R. Schonenberg, *AISTech Conference Proceedings*, AIST, USA, 2012.
- [8] W. Liu, J.Y. Lim, M.A. Saucedo, A.N. Hayhurst, S.A. Scott and J.S. Dennis, *Chemical Engineering Science*, **120** (2014), 149.
- [9] P.C. Hayes, *Metallurgical Transactions B*, **10** (1979), 211.
- [10] R.A. Giddings and R.S. Gordon, *Journal of the American Ceramic Society*, **56** (1973), 111.
- [11] D.H.St. John, S.P. Matthew and P.C. Hayes, *Metallurgical Transactions B*, **15** (1984), 709.
- [12] A.M. Watts, D.H.St. John and P.C. Hayes, *Metallurgical Transactions B*, **14** (1983), 753.
- [13] M. Farren, S.P. Matthew and P.C. Hayes, *Metallurgical Transactions B*, **21** (1990), 135.
- [14] E.T. Turkdogan and J.V. Vinters, *Metallurgical Transactions*, **3** (1972), 1561.
- [15] P.C. Hayes, *Steel Research International*, **82** (2011), 480.
- [16] H.K. Kohl and H.J. Engell, *Archiv für das Eisenhüttenwesen*, **34** (1963), 411.
- [17] L. von Bogdandy and H.J. Engell, *The Reduction of Iron Ores*, Springer Berlin Heidelberg, Berlin, 1976.
- [18] D.J. Young, *High Temperature Oxidation and Corrosion of Metals*, Elsevier, Oxford, 2008.
- [19] D. Huin, P. Flauder and J.B. Leblond, *Oxidation of Metals*, **64** (2005), 131.
- [20] V.A. Lashgari, *Internal and External Oxidation of Manganese in Advanced High Strength Steels*, Ph.D Dissertation, Delft University of Technology, 2014.
- [21] D.R. Lide, *CRC Handbook of Chemistry and Physics*, 88th ed., Taylor & Francis, Florida, 2007.
- [22] J.T. Armstrong, *Electron Probe Quantitation*, Springer US, Boston, 1991.
- [23] W. Mao and W.G. Sloof, *Scripta Materialia*, **135** (2017), 29.
- [24] F.S. Pettit and J.B. Wagner Jr, *Acta Metallurgica*, **12** (1964), 35.
- [25] R. Bredesen and P. Kofstad, *Oxidation of Metals*, **36** (1991), 27.
- [26] R. Bredesen and P. Kofstad, *Oxidation of Metals*, **34** (1990), 361.
- [27] D.H.St. John and P.C. Hayes, *Metallurgical Transactions B*, **13** (1982), 117.

- 
- [28] D.H.St. John, S.P. Matthew and P.C. Hayes, *Metallurgical Transactions B*, **15** (1984), 701.
- [29] Y. Sasaki, M. Bahgat, M. Iguchi and K. Ishii, *ISIJ International*, **45** (2005), 1077.
- [30] C. Wagner, *Acta Metallurgica*, **21** (1973), 1297.
- [31] V.A. Lashgari, G. Zimbitas, C. Kwakernaak and W.G. Sloof, *Oxidation of Metals*, **82** (2014), 249.



## Appendix A

### Oxygen partial pressure in annealing atmosphere

The relation between dew point ( $DP$ ) and partial pressure of water vapour ( $p_{H_2O}$ ) was adopted from ref. [1]:

$$\log p_{H_2O} = \frac{9.8DP}{273.8 + DP} - 2.22 \quad DP \leq 0 \text{ } ^\circ\text{C}$$

$$\log p_{H_2O} = \frac{7.58DP}{240 + DP} - 2.22 \quad DP > 0 \text{ } ^\circ\text{C}$$

where the units of  $p_{H_2O}$  and  $DP$  are in atmosphere (atm.) and degree Celsius ( $^\circ\text{C}$ ), respectively. Then, the partial pressure of oxygen ( $pO_2$ ) at equilibrium can be calculated with the Gibbs free energy of formation of water vapour, namely [1]:

$$\log pO_2 = 6 - \frac{26176}{T} + 2 \log \left( \frac{p_{H_2O}}{p_{H_2}} \right)$$

in which  $T$  is absolute temperature in Kelvin and  $p_{H_2}$  is the partial pressure of  $H_2$  in atmosphere.

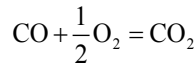
For the concentration of oxygen dissolved at the surface ( $N_O^s$ , in mole fraction) of iron with fcc crystal lattice in equilibrium with ambient gas mixture, it holds that [2]:

$$\log(N_O^s) = \log \left( \frac{p_{H_2O}}{p_{H_2}} \right) - \frac{4050}{T} - 1.52$$

While for iron with bcc crystal lattice in equilibrium with ambient gas mixture, it holds that [2]:

$$\log(N_O^s) = \log \left( \frac{p_{H_2O}}{p_{H_2}} \right) - \frac{5000}{T} - 0.67$$

The  $pO_2$  in a  $CO_2 + CO$  gas mixture can be calculated considering the following reaction:



with the standard Gibbs free energy (unit in J/mol) expressed as [3]:

$$\Delta G^0 = -282420 + 86.8T$$

At equilibrium, the relation between  $CO_2/CO$  ratio and the  $pO_2$  in the gas mixture can be calculated according to:

$$pO_2 = \left(\frac{p_{CO_2}}{p_{CO}}\right)^2 \exp\left(\frac{2\Delta G^0}{RT}\right)$$

## References

- [1] D. Huin, P. Flauder, and J. B. Leblond, *Oxidation of Metals*, **64** (2005), 131.
- [2] V.A. Lashgari, *Internal and External Oxidation of Manganese in Advanced High Strength Steels*, Ph.D. thesis, Delft University of Technology, 2014.
- [3] J. Xu, *Kinetics of Wüstite formation and reduction of Manganese alloyed steels*, Master thesis, Delft University of Technology, 2013.

## Appendix B

### Summary of classical Wagner internal oxidation theory

The classical Wagner theory of internal oxidation [1-3] quantitatively predicts the kinetics of internal oxidation as well as the concentration depth profiles of solute oxygen, alloying element that remains as solid solute and the oxide precipitates. Consider oxidation of an A-B (A is matrix and more noble than B) binary alloy and forms internal precipitate  $\text{BO}_v$ , the depth of internal oxidation zone (IOZ),  $\xi$ , can be expressed as a function of oxidation time  $t$  with the following equation:

$$\xi = 2\gamma\sqrt{D_O t} \quad (\text{B1})$$

where  $\gamma$  is a dimensionless kinetic parameter, and  $D_O$  is the diffusion coefficient of oxygen in alloy matrix. The value of  $\gamma$  can be obtained by numerically solving the equation

$$\frac{N_O^s}{vN_B^0} = \frac{\exp(\gamma^2)\text{erf}(\gamma)}{\varphi^{1/2} \exp(\gamma^2\varphi)\text{erfc}(\gamma\varphi^{1/2})} \quad (\text{B2})$$

in which  $N_O^s$  is the mole fraction of dissolved oxygen at alloy surface,  $N_B^0$  is the mole fraction of alloying element in the bulk alloy,  $v$  is the stoichiometry number of  $\text{BO}_v$ , and  $\varphi$  equals to the ratio between diffusion coefficient of oxygen and alloying element B, namely:

$$\varphi = \frac{D_O}{D_B} \quad (\text{B3})$$

The concentration depth profile of dissolved oxygen within IOZ is

$$N_O = N_O^s \left\{ 1 - \frac{\text{erf}(x/2\sqrt{D_O t})}{\text{erf}(\gamma)} \right\} \quad (\text{B4})$$

where  $x$  is the distance to the surface. The concentration of dissolved oxygen beyond IOZ is zero. The concentration of alloying element B within the IOZ is zero, while beyond IOZ is

$$N_B = N_B^0 \left\{ 1 - \frac{\text{erfc}(x/2\sqrt{D_B t})}{\text{erfc}(\gamma\varphi^{1/2})} \right\} \quad (\text{B5})$$

The mole fraction of internal oxide  $\text{BO}_v$  within the IOZ is constant, which equals:

$$N_{\text{BO}_v} = \frac{N_B^0}{\sqrt{\pi}\gamma\varphi^{1/2} \exp(\gamma^2\varphi)\text{erfc}(\gamma\varphi^{1/2})} \quad (\text{B6})$$

The concentration of  $\text{BO}_v$  drops to zero at internal oxidation front.

## References

- [1] C. Wagner, *Zeitschrift Fur Elektrochemie*, **63** (1959), 772.
- [2] R.A. Rapp, *Corrosion*, **21** (1965), 382.
- [3] D.J. Young, *High Temperature Oxidation and Corrosion of Metals*, Elsevier, Oxford, 2008.

## Appendix C

### Solubility product of oxides and nitrides in ideal Fe and Ni alloys

The solubility product ( $K_{sp}$ ) of precipitate  $BX_v$  in an A-B alloy is defined as the product of the mole fraction of solute B and X,  $N_B$  and  $N_X$ , respectively:

$$K_{sp(BX_v)} = N_B \times (N_X)^v \quad (C1)$$

This solid solubility product for ideal alloys equals:

$$K_{sp(BX_v)} = \exp\left(\frac{\Delta G^0}{RT}\right) \quad (C2)$$

where  $\Delta G^0$  is the standard free energy of the reaction  $\underline{B} + v\underline{X} = BX_v$  in which the underlining denotes that the element is dissolved in the alloy. Since  $\Delta G^0$  is usually a linear function of temperature, the  $K_{sp}$  of precipitate  $BX_v$  as a function of temperature can be described as:

$$K_{sp(BX_v)} = \exp\left(a + \frac{b}{T}\right) \quad (C3)$$

in which  $a$  and  $b$  are constants. The values of  $a$  and  $b$  can be obtained from the reported values of  $K_{sp}$ . Alternatively, the values of  $a$  and  $b$  for some oxides and nitrides in Fe and Ni alloys can be evaluated from solubility products at different temperatures computed with a thermodynamic tool [1]. A system that consists of a Fe - M or Ni - M binary alloy in equilibrium with Ar + N<sub>2</sub> or Ar + O<sub>2</sub> gas mixture was created. The thermodynamic data of the gas species were taken from the FactPS database [2]. The Fe - M and Ni - M binary alloys with BCC or FCC crystal lattice were created using the data from the FStel database [2]. The thermodynamic data of oxides and nitrides were taken from the FactPS database except for AlN and VN whose data were taken from the FStel database. The computed values of the solubility products as a function of reciprocal of absolute temperature were least-square fitted. The values of  $a$  and  $b$  for the interested nitrides and oxides in Fe and Ni alloys considering an ideal solid solution are listed in Tables C1 to C4.

Table C1: Values of  $a$  and  $b$  for oxides in Fe alloys with FCC crystal lattice from 950 to 1100 °C considering an ideal solid solution; cf. Eq. (C3).

Type of oxide	$a$	$b$	Ref.
MnO	-1.865	-24791	[1]
CrO <sub>1.5</sub>	-0.260	-36104	[3]
AlO <sub>1.5</sub>	0.823	-57539	[1]
SiO <sub>2</sub>	-2.629	-51374	[1]



## Appendices

Table C2: Values of  $a$  and  $b$  for nitrides in Fe alloys with BCC crystal lattice from 500 to 650 °C considering an ideal solid solution; cf. Eq. (C3).

Type of nitride	$a$	$b$	Ref.
AlN	3.484	-27460	[1]
VN	4.019	-26651	[1]
TiN	6.097	-39338	[1]
CrN	4.714	-20210	[1]

Table C3: Values of  $a$  and  $b$  for nitrides in Fe alloys with FCC crystal lattice from 950 to 1100 °C considering an ideal solid solution; cf. Eq. (C3).

Type of nitride	$a$	$b$	Ref.
AlN	-2.133	-24430	[1]
VN	2.199	-22871	[1]
TiN	2.466	-33537	[1]
CrN	0.864	-13208	[1]

Table C4: Values of  $a$  and  $b$  for nitrides in Ni alloys with FCC crystal lattice from 950 to 1100 °C considering an ideal solid solution; cf. Eq. (C3).

Type of nitride	$a$	$b$	Ref.
AlN	1.446	-23523	[1]
VN	4.952	-19642	[4]
TiN	-5.279	-20444	[5]
CrN	0.440	-16978	[1]
NbN	4.837	-20272	[4]

## References

- [1] C. Bale, P. Chartrand, S.A. Degterov, G. Eriksson, K. Hack, R. Ben Mahfoud, et al., *Calphad*, **26** (2002), 189.
- [2] Factsage Database Documentation, <http://www.crct.polymtl.ca/fact/documentation/>.
- [3] D.J. Young, *High Temperature Oxidation and Corrosion of Metals*, Elsevier, Oxford, 2008.
- [4] A.T. Allen and D.L. Douglass, *Oxidation of Metals*, **51** (1999), 199.
- [5] G.C. Savva, G.C. Weatherly and J.S. Kirkaldy, *Metallurgical and Materials Transactions A*, **27** (1996), 1611.

## Appendix D

### Coupled linear-parabolic kinetic model

The coupled linear-parabolic kinetic model for Wüstite formation on pure iron in  $\text{CO}_2 + \text{CO}$  gas mixtures was first reported in ref. [1]. The model can be also applied for Wüstite growth on pure iron in gas mixtures of  $\text{H}_2\text{O}$  and  $\text{H}_2$ . The mechanism of Wüstite growth described by the model is schematically represented in Figure 7.1 in Chapter 7. It is assumed that a uniform and dense layer of Wüstite is formed and fully covers the iron substrate during oxidation. The growth of the Wüstite scale is dominated by the diffusion of Fe cations from the iron-scale interface to the surface of the scale. Thermodynamic equilibrium between iron and Wüstite is established at the iron-scale interface, and the oxygen activity at the interface,  $a_{\text{O}}^{\text{Fe/FeO}}$ , is governed by the dissociation oxygen partial pressure of FeO. However, thermodynamic equilibrium is not established between the scale surface and the gas ambient. The oxygen activity at Wüstite surface ( $a_{\text{O}}^*$ ) is always lower than the oxygen activity in the gas ambient ( $a_{\text{O}}$ ), but higher than the oxygen activity at iron-scale interface. The oxygen activity at Wüstite surface increases as the oxidation process proceeds. During oxidation, mass balance at the scale-gas interface is established, i.e. the rate of oxygen incorporation,  $J_{\text{O}}$ , is balanced with the outward flux of Fe ions,  $J_{\text{Fe}}$ , according to [1]:

$$J_{\text{O}} = \frac{J_{\text{Fe}}}{1 - \tilde{\delta}} \quad (\text{D1})$$

where  $\tilde{\delta}$  denotes the average cation deficit in the Wüstite scale ( $\text{Fe}_{1-\tilde{\delta}}\text{O}$ ). The rate of oxygen incorporation at scale surface equals to [1]:

$$J_{\text{O}} = K_{\text{oxid}} (a_{\text{O}}^*)^{-n} \left(1 - \frac{a_{\text{O}}^*}{a_{\text{O}}}\right) p_{\text{oxid}} \quad (\text{D2})$$

in which  $K_{\text{oxid}}$  ( $\text{mol cm}^{-2} \text{s}^{-1} \text{atm}^{-1}$ ) is the rate constant of the overall surface reaction between Wüstite scale and  $\text{H}_2\text{O}$  vapour ( $K_{\text{H}_2\text{O}}$ ) or  $\text{CO}_2$  ( $K_{\text{CO}_2}$ ) in the gas.  $p_{\text{oxid}}$  (in atm.) is the partial pressure of the oxidant gas species in the gas mixture, namely  $\text{H}_2\text{O}$  vapour ( $p_{\text{H}_2\text{O}}$ ) or  $\text{CO}_2$  ( $p_{\text{CO}_2}$ ). Both oxygen activities  $a_{\text{O}}^*$  and  $a_{\text{O}}$  in Eq. (D2) are expressed in terms of  $p_{\text{H}_2\text{O}}/p_{\text{H}_2}$  or  $p_{\text{CO}_2}/p_{\text{CO}}$  ratio. The value of  $n$  ranges from 0 to 1 [2], depending on the mechanism of oxygen incorporation into the Wüstite surface.

Assuming that the concentration profile of Fe vacancies in the Wüstite scale is linear and the diffusion of Fe vacancies obeys Fick 1<sup>st</sup> law, the outward flux of cations at scale surface is given by:

$$J_{Fe} = \frac{D\delta^{Fe/FeO}}{xV} \left( \frac{\delta^*}{\delta^{Fe/FeO}} - 1 \right) \quad (D3)$$

where  $\delta^*$  and  $\delta^{Fe/FeO}$  denote the Fe deficiency at the scale surface and the scale-iron interface, respectively.  $V$  is the molar volume of oxide scale and  $x$  is the thickness of the scale.  $D$  is the diffusion coefficient of Fe vacancies in the Wüstite scale, and is considered to be a constant, independent of local defect concentration. The growth rate of Wüstite scale equals:

$$\frac{d(\Delta m / A)}{dt} = M_O J_O = \frac{M_O J_{Fe}}{1 - \tilde{\delta}} \quad (D4)$$

where  $M_O$  is the molar mass of oxygen atom, and the mass gain per unit area equals:

$$\frac{\Delta m}{A} = \frac{M_O x}{V} \quad (D5)$$

Yet, two dimensionless auxiliary variables are introduced, namely:

$$\xi = \frac{\Delta m / A}{(\Delta m / A)^*} \quad (D6)$$

and

$$\nu = \frac{t}{t^*} \quad (D7)$$

where

$$\left( \frac{\Delta m}{A} \right)^* = \frac{M_O D \delta^{Fe/FeO}}{K_{oxid} p_{oxid} V^2 (1 - \tilde{\delta})} \quad (D8)$$

and

$$t^* = \frac{D \delta^{Fe/FeO}}{(K_{oxid} p_{oxid} V)^2 (1 - \tilde{\delta})} = \frac{(\Delta m / A)^*}{M_O K_{oxid} p_{oxid}} \quad (D9)$$

$(\Delta m / A)^*$  and  $t^*$  are constants and their values are obtained in the following manner. When oxidizing iron in an atmosphere with high oxygen partial pressure (say pure oxygen gas), a layer of magnetite can be formed on top of the Wüstite scale. Assuming that the thermodynamic equilibrium is established at the magnetite-Wüstite interface, the growth of Wüstite layer follows parabolic rate law. Substituting  $\delta^*$  with the Fe deficiency at the magnetite-Wüstite interface ( $\delta^{FeO/Fe_3O_4}$ ) obtains (cf. Eqs (D3), (D4) and (D5)):

$$\frac{d(\Delta m / A)}{dt} = \frac{(M_0)^2}{1 - \tilde{\delta}} \frac{D\delta^{\text{Fe/FeO}}}{(\Delta m / A)V^2} \left( \frac{\delta^{\text{FeO/Fe}_3\text{O}_4}}{\delta^{\text{Fe/FeO}}} - 1 \right) \quad (\text{D10})$$

From Eq. (D10), the parabolic rate constant for the growth of Wüstite layer underneath magnetite can be given as:

$$k_{p,\text{O}_2} = \frac{d(\Delta m / A)^2}{dt} = \frac{2(M_0)^2}{1 - \tilde{\delta}} \frac{D\delta^{\text{Fe/FeO}}}{V^2} \left( \frac{\delta^{\text{FeO/Fe}_3\text{O}_4}}{\delta^{\text{Fe/FeO}}} - 1 \right) \quad (\text{D11})$$

Then, the  $(\Delta m / A)^*$  can be expressed as (cf. Eqs (D8) and (D11)):

$$\left( \frac{\Delta m}{A} \right)^* = \frac{k_{p,\text{O}_2}}{2M_0 K_{\text{oxid}} p_{\text{oxid}} \left( \frac{\delta^{\text{FeO/Fe}_3\text{O}_4}}{\delta^{\text{Fe/FeO}}} - 1 \right)} \quad (\text{D12})$$

To obtain  $(\Delta m / A)^*$  and  $t^*$ , the values of  $k_{p,\text{O}_2}$ ,  $K_{\text{oxid}}$ ,  $\delta^{\text{Fe/FeO}}$  and  $\delta^{\text{FeO/Fe}_3\text{O}_4}$  need to be determined experimentally. The temperature dependence of the parabolic rate constant for Wüstite growth on pure iron in oxygen is estimated from the experimental data in refs [3, 4], namely:

$$k_{p,\text{O}_2} = 132.8 \times \exp\left(\frac{-18800}{T}\right) \quad (\text{D13})$$

in which the unit of  $k_{p,\text{O}_2}$  is  $\text{g}^2\text{cm}^{-4}\text{min}^{-1}$ , and  $T$  is the absolute temperature. The reported temperature dependence of the surface reaction constants  $K_{\text{H}_2\text{O}}$  [5] and  $K_{\text{CO}_2}$  [1] are summarized in Table 7.2 in Chapter 7. The equilibrium Fe deficiency ( $\delta$ ) of Wüstite is a function of oxygen partial pressure ( $p_{\text{O}_2}$ , in atm.) according to [6]:

$$\log(p_{\text{O}_2}) = M \left( \frac{1}{1 - \delta} \right) + B \quad (\text{D14})$$

where  $M$  and  $B$  are constants depending on temperature. The temperature dependence of  $M$  and  $B$  from 700 to 1300 °C were evaluated from the experimental data reported in ref. [6] by least-square linear fitting, namely:

$$M = -\frac{7765.6}{T} + 29.4 \quad (\text{D15})$$

and

$$B = -\frac{19475.1}{T} - 24.1 \quad (\text{D16})$$

Then, the values of  $\delta^{\text{Fe/FeO}}$  and  $\delta^{\text{FeO/Fe}_3\text{O}_4}$  can be obtained once the equilibrium oxygen partial pressures for Fe-FeO and FeO-Fe<sub>3</sub>O<sub>4</sub> are known; cf. Eq. (D14).

The Fe deficiency at Wüstite surface ( $\delta^*$ ) as a function of oxygen activity ( $a_o^*$ ) is given by:

$$\delta^* = 1 - \frac{M}{2 \left[ \log(a_o^*) - 0.5B + \frac{\Delta G^0}{2.303RT} \right]} \quad (D17)$$

where the  $\Delta G^0$  is the standard Gibbs energy of the reaction  $\text{CO} + 1/2\text{O}_2 = \text{CO}_2$  or  $\text{H}_2 + 1/2\text{O}_2 = \text{H}_2\text{O}$ . Combining Eqs (D2), (D3), (D4), (D6) and (D8) obtains:

$$\xi = \frac{\left( \frac{\delta^*}{\delta^{\text{Fe/FeO}}} - 1 \right)}{(a_o^*)^{-n} \left( 1 - \frac{a_o^*}{a_o} \right)} \quad (D18)$$

Since each value of  $a_o^*$  correspond to a certain value of  $\xi$ , the  $a_o^*$  can be considered as a function of  $\xi$ , namely:

$$a_o^* = g(\xi) \quad (D19)$$

From Eqs. (D2), (D4), (D6), (D7) and (D9), the following equation can be derived:

$$\frac{d\xi}{d\nu} = \frac{t^*}{(\Delta m / A)^*} \frac{d(\Delta m / A)}{dt} = (a_o^*)^{-n} \left( 1 - \frac{a_o^*}{a_o} \right) \quad (D20)$$

Integrating Eq. (D20) gives:

$$\nu = \int_0^\xi \frac{1}{[g(\xi)]^{-n} \left[ 1 - \frac{g(\xi)}{a_o} \right]} d\xi \quad (D21)$$

The plot of  $\xi$  as a function of  $\nu$  can then be obtained numerically. Then the kinetics of Wüstite growth on iron (in terms of mass gain per unit area as a function of time) can be quantitatively predicted; cf. Eqs (D6) and (D7).

When the oxygen activity at Wüstite surface almost reaches the oxygen activity in the ambient gas (i.e. thermodynamic equilibrium is almost established between Wüstite surface and gas), the growth kinetics of Wüstite scale follow the parabolic rate law. According to the coupled linear-parabolic model, the parabolic rate constant of Wüstite growth on iron as a function of gas composition can be estimated according to:

$$k_w = \frac{k_{p,\text{O}_2}}{2 \left( \frac{\delta^{\text{FeO/Fe}_3\text{O}_4}}{\delta^{\text{Fe/FeO}}} - 1 \right)} \left( \frac{\delta^{\text{ambient}}}{\delta^{\text{Fe/FeO}}} - 1 \right) \quad (D22)$$

where  $\delta^{ambient}$  represents the Fe deficiency at Wüstite surface in equilibrium with the gas ambient. The value of  $\delta^{ambient}$  can be calculated from  $a_o$  according to Eq. (D17).

## References

- [1] F.S. Pettit and J.B. Wagner Jr, *Acta Metallurgica*, **12** (1964), 35.
- [2] H.J. Grabke, K.J. Best and A. Gala, *Werkstoffe und Korrosion*, **21** (1970), 911.
- [3] L. Himmel, R.F. Mehl and C.E. Birchenall, *Journal of Metals*, **5** (1953), 827.
- [4] D.J. Young, *High Temperature Oxidation and Corrosion of Metals*, Elsevier, Oxford, 2008.
- [5] E.T. Turkdogan, W.M. McKewan and L. Zwell, *Journal of Physical Chemistry*, **69** (1965), 327.
- [6] R.A. Giddings and R.S. Gordon, *Journal of the American Ceramic Society*, **56** (1973), 111.

## Appendix E

### Determination of steady state parabolic rate constant

The reduction kinetics of Wüstite in terms of the steady state parabolic rate constant is determined from the mass change observed with thermogravimetric analysis; see Section 8.3. First a Wüstite layer was formed by oxidizing in Ar + 33 vol.% CO<sub>2</sub> + 17 vol.% CO gas mixture and next this layer was reduced by switching the gas atmosphere to Ar + H<sub>2</sub>. Since purging of the reducing gas mixture takes time, the initial stages of Wüstite reduction cannot be captured. Hence, in order to obtain a value for the steady state parabolic rate constant, the observed reduction kinetics was fitted with:

$$y = A(x - x_0)^{0.5} + y_0 \quad (\text{E1})$$

where  $A$ ,  $x_0$  and  $y_0$  (representing the imaginary starting point of steady state reduction kinetics) are unknown and were obtained after fitting,  $x$  and  $y$  represent the reduction time and mass loss respectively. The value obtained for the coefficient  $A$  is the effective parabolic constant for Wüstite reduction. As an example, Figure E1 shows the thermogravimetric curve during the reduction of Wüstite scale for both pure iron and the Mn alloyed steel samples at 850 °C as well as the corresponding least-square fitted parabolic curve. The error in the determination of the effective parabolic constant was estimated by varying the range of data selected for the fitting.

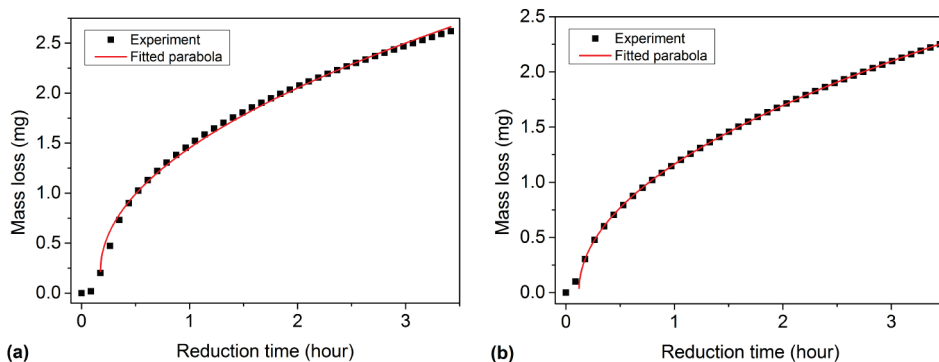


Figure E1: Mass change during the reduction in dry Ar + 5 vol.% H<sub>2</sub> gas mixture at 850 °C of Wüstite on (a) pure iron and on (b) a Mn alloyed steel. A parabolic rate law was fitted to the data (cf. Eq. (E1)).

# Summary

Nowadays, advanced high strength steels (AHSS) are extensively used for automotive applications. The common alloying elements in AHSS are Mn, Si, Cr and Al. To protect AHSS against corrosion, a zinc or zinc alloy coating is applied onto the steel surface usually by the continuous hot-dip galvanizing process in automotive steel industry. The steel strip passes through continuous annealing furnaces before entering a zinc bath in order to obtain certain microstructures and mechanical properties. However, the galvanizing quality is impaired to a large extent by the oxides of alloying elements formed at steel surface during the continuous annealing treatment. Fundamental knowledge on the high temperature oxidation behaviour of multi-element alloyed AHSS is rather limited, yet important for optimizing the annealing process and improving the quality of zinc-coated steel product. Therefore, in this thesis, the fundamental aspects of oxidation phenomena of selected advanced high strength steels during annealing process prior to galvanizing are studied.

In Chapter 1, the background of the galvanizing process in steel making industry is briefly introduced. The importance of understanding the oxidation phenomenon of advanced high strength steels to producing galvanized steel product with good quality is illustrated. The scope of the research as well as the outline of this thesis is clarified.

Chapter 2 focuses on the thermodynamic aspect of oxide formation in multi-element alloyed steels. The type of oxide phases formed upon annealing steel alloys is first predicted based on the phase diagrams computed with a thermodynamic tool for Fe-Mn, Fe-Mn-Cr and Fe-Mn-Cr-Si steel alloys in oxidizing environment. Then, to validate the predictions, steels alloyed with different concentrations of Mn, Cr and Si are annealed at temperatures of 750, 850 and 950 °C in gas mixtures of Ar with H<sub>2</sub> and H<sub>2</sub>O vapour with different oxygen partial pressure. The identified oxide phases formed during annealing are generally in good agreement with the predictions based on the computed phase diagrams, suggesting that thermodynamic equilibrium is established between the gas ambient and the steel surface. (Mn,Fe)O is the only type of oxide formed upon annealing of Fe-Mn binary steel alloys. Adding Cr to the Mn alloyed steels leads to the formation of (Mn,Cr,Fe)<sub>3</sub>O<sub>4</sub> spinel. The dissociation oxygen partial pressure of (Mn,Cr,Fe)<sub>3</sub>O<sub>4</sub> spinel is lower than that of (Mn,Fe)O. The Si in the steels alloyed with Mn and Cr results in the formation of Mn<sub>2</sub>SiO<sub>4</sub> whose dissociation oxygen partial pressure is lower than that of (Mn,Cr,Fe)<sub>3</sub>O<sub>4</sub>. Increasing the Si concentration in the Fe-Mn-Cr steel alloy suppresses the formation of



$(\text{Mn,Cr,Fe})_3\text{O}_4$  spinel and  $(\text{Mn,Fe})\text{O}$ . Increasing the Mn concentration in the steel alloy, however, promotes the formation of  $(\text{Mn,Cr,Fe})_3\text{O}_4$  spinel and  $(\text{Mn,Fe})\text{O}$ .

In Chapter 3, the effect of non-ideal behaviour of solution on the solubility product of oxide precipitates in steel alloys is studied. The change in the solubility product of a  $\text{B}_n\text{O}_v$  oxide precipitate with alloy composition is determined by the interaction parameters pertaining to solute B and O as defined according to the Wagner formalism. A generic approach for calculating the interaction parameters without any input of experimental data is developed based on the macroscopic atom model in conjunction with quasi-chemical description of alloys. The interaction parameters pertaining to nitrogen and carbon calculated with this approach for liquid and solid iron alloys show reasonable to good agreement with either experimental or computational results with thermodynamic tools. This indicates that our approach is promising for estimating the interaction parameters pertaining to oxygen for steel alloys.  $\text{Al}_2\text{O}_3$  is taken as an example to study the effect of alloying elements on the solubility product in steel alloys.

In Chapter 4, a generic multi-element and multi-phase coupled thermodynamic-kinetic model based on Fick's 1st law is developed for internal precipitation due to inward diffusion of a foreign element. The type, composition and amount of internal precipitates as a function of depth below the surface can be predicted considering annealing time, temperature and ambient activity of the foreign element. The prediction of the depth profiles of internal precipitation zone also includes the concentration of alloying elements and the foreign element as solid solute. Possible phase transformations of alloy matrix due to solute atom depletion during internal precipitation process are also well described with the model. This thermodynamic-kinetic model allows accounting for effects of non-ideal behaviour of a solid solution, i.e. solute atom interactions, on the kinetics of internal precipitation process. The effect of solute interaction between the foreign element and the precipitated alloying element depends on the solubility product of the precipitate as presented in Chapter 3. For steels alloyed with Mn, Si, Cr and Al, the solubility product of internal oxides are small and the effect of non-ideal behaviour of iron alloys can be practically ignored. However, the solute interaction can be significant when the solubility product of precipitates is large. For example, the interaction between nitrogen and the nitrided element in Ni alloys enhances internal nitridation and results in uphill diffusion of nitrogen solute in the internal nitridation zone. In the case of ternary alloys, the non-reacting alloying element can significantly affect the kinetics of internal precipitation by changing the solubility of the foreign element in the alloy.

Chapter 5 is on the investigation on the composition depth profile of internal  $(\text{Mn}_{1-x},\text{Fe}_x)\text{O}$  precipitates formed during internal oxidation of a Mn alloyed steel. The depth profile of oxygen activity within the internal oxidation zone of the Mn alloyed steel is obtained from the simulated concentration depth profile of solute oxygen. In equilibrium the composition of the  $(\text{Mn}_{1-x},\text{Fe}_x)\text{O}$  precipitates depends on the local activity of oxygen in the internal oxidation zone. Consequently, the concentration of Fe in the  $(\text{Mn}_{1-x},\text{Fe}_x)\text{O}$  precipitates decreases similar to the oxygen activity within the internal oxidation zone as a function of depth below the steel surface. The measured depth profile of Fe concentration in internal  $(\text{Mn}_{1-x},\text{Fe}_x)\text{O}$  in the annealed Mn alloyed steel matches with prediction. This demonstrates that local thermodynamic equilibrium is established in the internal oxidation zone of Mn alloyed steels during annealing in an oxidizing environment, which is a key assumption in the coupled thermodynamic-kinetic model.

In Chapter 6, the coupled thermodynamic-kinetic model is applied to predict the internal oxidation behaviour of Fe-Mn-Cr steel alloys. To validate the simulation results, selected Fe-Mn-Cr steel alloys are annealed at 950 °C for 1 to 16 hours in a gas mixture of Ar with 5 vol.%  $\text{H}_2$  and dew points of -30, -10 and 10 °C. Both MnO and  $\text{MnCr}_2\text{O}_4$  are formed during oxidation. The concentration depth profiles of internal oxides as well as the kinetics of internal oxidation are in good agreement with simulation results. Local thermodynamic equilibrium is established in the internal oxidation zone of Fe-Mn-Cr steel alloys during annealing. The internal oxidation zone of MnO has almost the same size as  $\text{MnCr}_2\text{O}_4$  when annealed at dew points of -10 and 10 °C. The growth of internal oxidation zone of Fe-Mn-Cr steel alloys is controlled by diffusion of solute oxygen, and hence follows parabolic rate law. Both MnO and  $\text{MnCr}_2\text{O}_4$  can be considered as low solubility product precipitates in steels. The extended Wagner internal oxidation theory for ternary alloys can be applied to estimate the parabolic rate constant of internal oxidation of Fe-Mn-Cr steel alloys annealed above dew point of -10 °C.

Chapter 7 is on the study of kinetics of Wüstite formation on pure iron and Mn alloyed steels in  $\text{H}_2\text{O} + \text{H}_2$  and  $\text{CO}_2 + \text{CO}$  gas mixtures. Thickness of Wüstite scale formed on pure iron in these gas mixtures can be well predicted as a function of annealing temperature, time and gas composition according to the classical coupled linear-parabolic model. The initial Wüstite growth on iron is controlled by gas-oxide boundary reaction, and the scale thickness increases linearly with time. As the oxide layer thickens, the transport of the reacting species through the oxide scale determines the growth rate and then a parabolic growth law is obeyed. However, the linear growth rate of Wüstite scale on Mn alloyed steels is much lower than that on pure iron. A possible explanation for the huge discrepancy in the scale growth rate between iron and Mn alloyed steels is the segregation of Mn cations

at the Wüstite scale surface. The reaction rate constant as a function of temperature for the reaction at the gas-oxide boundary follows Arrhenius relation.

Chapter 8 focuses on the reduction kinetics of Wüstite scale on pure iron and Mn alloyed steels in Ar plus H<sub>2</sub> gas mixture. The reduction kinetics are first predicted and then validated by experiments. Reducing the Wüstite scale in Ar plus H<sub>2</sub> gas mixture forms a dense iron layer on top of the remaining Wüstite scale, which separates the unreduced scale from the reduction atmosphere. The reduction rate of a Wüstite scale on pure iron and Mn alloyed steel are almost the same. The kinetics of Wüstite reduction by H<sub>2</sub> is controlled by the bulk diffusion of solute oxygen in the formed iron layer, and hence follows a parabolic rate law. The parabolic rate constant of Wüstite scale reduction as a function of temperature obeys an Arrhenius relation. The effect of gas composition of reducing atmosphere on the reduction kinetics of Wüstite scale is relatively small below an annealing dew point of about 5 °C. An oxide-free surface of Mn alloyed steel can be obtained successfully by first forming and subsequently reducing a Wüstite scale. Such a process will significantly improve the galvanizing quality.

# Samenvatting

Nieuwe staalsoorten met hoge sterkte worden toegepast in automobielen. Veel voorkomende legeringselementen in deze geavanceerde staalsoorten zijn Mn, Si, Cr en Al. Om het materiaal te beschermen tegen corrosie wordt de staalstrip voorzien van een zink coating. In een continu warmtebehandelingsproces wordt de staalstrip aan het einde door een vloeibaar-zink bad geleid. Met het warmtebehandelingsproces verkrijgt het staal de gewenste microstructuur en mechanische eigenschappen. Echter, de kwaliteit van het galvaniseren hangt in hoge mate af van de oxides die op het staaloppervlak zijn gevormd tijdens het warmtebehandelingsproces. Fundamentele kennis omtrent het oxidatiegedrag van het geavanceerde staal met meerdere verschillende legeringselementen ontbreekt. Deze kennis is onmisbaar voor het optimaliseren van het warmtebehandelingsproces alsmede de kwaliteit van de zink coating. In dit proefschrift worden de fundamentele aspecten van de oxidatie fenomenen tijdens het gloeien voorafgaand aan het verzinken van enkele geselecteerde staalsoorten behandeld.

In hoofdstuk 1, wordt het galvaniseerproces voor staal kort beschreven. De relevantie van het begrijpen van de oxidatie fenomenen voor het galvaniseren van de nieuwe geavanceerde staalsoorten wordt besproken. De reikwijdte van het onderzoek en de hoofdpijnen van dit proefschrift worden hier verduidelijkt.

Hoofdstuk 2 is gericht op de thermodynamica van de oxidatieproducten gevormd in staal met meerdere legeringselementen. Allereerst is het type oxide dat gevormd wordt tijdens het gloeien van staallegeringen voorspeld op basis van fase diagrammen van Fe-Mn, Fe-Mn-Cr en Fe-Mn-Cr-Si in een oxiderende omgeving. Deze fase diagrammen zijn berekend met behulp van een thermodynamische computerprogramma. Vervolgens zijn verschillende staallegeringen met verschillende gehalten Mn, Cr en Si gegloeid bij 750, 850 en 950 °C in gasmengsels van Ar, H<sub>2</sub> en H<sub>2</sub>O met verschillende zuurstof partiële druk. De gevormde oxides komen goed overeen met de oxides voorspeld op basis van de brekende fase diagrammen. Dit geeft aan dat er thermodynamisch evenwicht heerst tussen het staaloppervlak en de gasatmosfeer. Tijdens het gloeien van binaire Fe-Mn legeringen wordt er alleen (Mn,Fe)O gevormd. Als er ook Cr aan de Fe-Mn legering is toegevoegd, dan wordt er een (Mn,Cr,Fe)<sub>3</sub>O<sub>4</sub> spinel oxide gevormd. Het blijkt dat de dissociatie zuurstof partiële druk van het (Mn,Cr,Fe)<sub>3</sub>O<sub>4</sub> spinel lager is dan die van (Mn,Fe)O. Als er aan de Fe-Mn-Cr legering ook nog Si is toegevoegd, dan vormt zich Mn<sub>2</sub>SiO<sub>4</sub>. De dissociatie zuurstof partiële druk van Mn<sub>2</sub>SiO<sub>4</sub> is lager dan die van (Mn,Cr,Fe)<sub>3</sub>O<sub>4</sub>. Echter, als het Si gehalte toeneemt in de Fe-Mn-Cr legering, dan wordt de vorming van (Mn,Cr,Fe)<sub>3</sub>O<sub>4</sub> spinel

en (Mn,Fe)O onderdrukt. Maar als het Mn gehalte in deze legering wordt verhoogd, dan wordt de vorming van (Mn,Cr,Fe)<sub>3</sub>O<sub>4</sub> spinel en (Mn,Fe)O bevorderd.

In hoofdstuk 3, is het effect van niet-ideaal gedrag de oplosbaarheid van zuurstof en de legeringselementen op het oplosbaarheidsproduct van oxide precipitaten in de staallegering bestudeerd. De verandering van het oplosbaarheidsproduct van een B<sub>n</sub>O<sub>v</sub> oxide precipitaten als functie van de legeringssamenstelling is bepaald. Hiertoe zijn de interactieparameters met betrekking tot de elementen B en O in oplossing gedefinieerd volgens het Wagner formalisme. Voor het berekenen van deze interactieparameters is een algemene benadering ontwikkeld gebaseerd op het macroscopische atoom model en een quasi-chemische beschrijving van legeringen los van experimentele data. Ook de interactieparameters voor stikstof en koolstof in vloeibare en gestolde staallegeringen zijn berekend volgens deze benadering. Gebleken is dat deze interactieparameters goed overeenkomen met experimentele resultaten en/of berekende resultaten met thermodynamische computer programma's. Dit suggereert dat onze benadering is veelbelovend voor het bepalen van de interactieparameters voor zuurstof in staallegeringen. Als voorbeeld is Al<sub>2</sub>O<sub>3</sub> genomen om het effect van legeringselementen op het oplosbaarheidsproduct van dit oxide in staal.

In hoofdstuk 4 is een gekoppeld thermodynamisch en kinetisch model is beschreven dat is ontwikkeld voor multi-element en multi-fasen legeringen waarin precipitatie optreedt door inwaartse diffusie van een 'vreemd' element. Dit algemene model is gebaseerd op de 1e diffusie wet van Fick. Het type, de samenstelling en de hoeveelheid inwendige precipitaten kan worden voorspeld als een functie van de diepte onder het oppervlak van de legering voor iedere gloeitijd en temperatuur alsmede de activiteit het 'vreemde' element in de atmosfeer. De voorspelde diepte profielen voor de inwendige precipitatiezone omvat ook de concentraties van de legeringselementen alsmede de concentratie van het 'vreemde' element in oplossing. Eventuele fasetransformaties in de matrix van de legering door verandering van de samenstelling door het precipitatie proces wordt goed beschreven met het model. Verder, is het met dit thermodynamisch-kinetisch model mogelijk effecten van niet-ideaal gedrag van opgeloste elementen op de kinetiek van de het precipitatie proces in rekening te brengen. Het effect van de interactie tussen het opgeloste 'vreemde' element en het opgeloste legeringselement dat het precipitaat vormt hangt af van het oplosbaarheidsproduct zoals beschreven in hoofdstuk 3. Voor staallegeringen met Mn, Si, Cr and Al is het effect van het niet-ideale gedrag op het oplosbaarheidsproduct van oxide precipitaten erg klein en kan dus worden verwaarloosd. Echter, het effect van niet-ideale gedrag kan beduidend zijn als het oplosbaarheidsproduct groot is. Bijvoorbeeld, in het geval van nitreren van nikkellegeringen versneld de interactie tussen stikstof en het legeringselement dat het precipitaat vormt het nitreren en leidt tot opwaartse diffusie van

stikstof. In het geval van ternaire legeringen kan het legeringselement dat niet deelneemt aan het precipitatie proces de kinetiek beïnvloeden, doordat dit legeringselement de oplosbaarheid van het vreemde element kan vergroten.

Hoofdstuk 5 gaat over het samenstellingsdiepteprofiel van  $(\text{Mn}_{1-x},\text{Fe}_x)\text{O}$  precipitaten gevormd na inwendig oxideren van een staallegeringen met Mn. Het diepteprofiel van de zuurstofactiviteit in de inwendige oxidatiezone van een Mn staallegering is verkregen door berekening van de het opgeloste zuurstofconcentratieprofiel. Als er evenwicht heerst, dan hangt de samenstelling van de  $(\text{Mn}_{1-x},\text{Fe}_x)\text{O}$  precipitaten af van de lokale zuurstofactiviteit in de inwendige oxidatiezone. Dan neemt de concentratie Fe in de  $(\text{Mn}_{1-x},\text{Fe}_x)\text{O}$  precipitaten af als een functie van de diepte onder het oppervlak overeenkomstig de zuurstofactiviteit in de inwendige oxidatiezone. De experimentele bevestiging hiervan bewijst dat inderdaad lokaal thermodynamisch evenwicht is bereikt in de inwendige oxidatiezone tijdens het gloeien van het staal. Dit is de voornaamste aanname in het gekoppelde thermodynamisch-kinetisch oxidatie model.

In hoofdstuk 6, is het gekoppelde thermodynamisch-kinetisch oxidatie model toegepast om het inwendige oxidatie gedrag van Fe-Mn-Cr staallegeringen te voorspellen. Ter verificatie van hiervan, zijn er enkele Fe-Mn-Cr staallegeringen gegloeid op 950 °C gedurende 1 tot 16 uur in een gas mengsel van Ar met 5 vol.% H<sub>2</sub> en dauwpunten van -30, -10 en 10 °C. Zowel MnO als MnCr<sub>2</sub>O<sub>4</sub> precipitaten zijn gevormd in de inwendige oxidatiezone. De samenstellingsdiepteprofielen van de oxide precipitaten alsmede de groei van de inwendige oxidatiezone komen overeen met de voorspelde resultaten. Dit betekent ook dat er lokaal evenwicht heerst in de inwendige oxidatie zone tijdens het gloeien van de Fe-Mn-Cr staallegeringen. De afmeting van de MnO en de MnCr<sub>2</sub>O<sub>4</sub> inwendige oxidatiezone zijn vrijwel gelijk na gloeien met dauwpunten van -10 en 10 °C. De groei van de inwendige oxidatiezone in de Fe-Mn-Cr staallegeringen wordt beheerst door diffusie van het opgeloste zuurstof en volgt daarom een parabolische groei wet. Zowel MnO als MnCr<sub>2</sub>O<sub>4</sub> precipitaten hebben een laag oplosbaarheidsproduct in staal. Daarom is de uitgebreide Wagner theorie van toepassing om de parabolische groeiconstante te berekenen voor inwendige oxidatie van Fe-Mn-Cr staallegeringen.

Hoofdstuk 7 gaat over de studie van de Wüstite (FeO) groei op zuiver ijzer en mangaan gelegeerd staal door oxidatie in H<sub>2</sub>O + H<sub>2</sub> en CO<sub>2</sub> + CO gasmengsels. De Wüstite laagdikte na gloeien van zuiver ijzer in deze gasmengsels is goed te voorspellen als functie van temperatuur, tijd en gassamenstelling met het klassieke lineair-parabolisch model. De initiële groei van Wüstite op zuiver ijzer wordt beheerst door een reactie aan het oxide-gas grensvlak, waardoor de oxidelaagdikte lineair toeneemt met de gloeitijd. Met toenemende

oxidelaagdikte wordt het transport van de reactanten door de oxidelaag bepalend voor de groei en volgt dit een parabolische groei wet. Echter, de lineaire groeiconstante voor Wüstite op Mn gelegeerd staal is veel lager dan die voor Wüstite op zuiver ijzer. Een mogelijke verklaring hiervoor is de segregatie van Mn ionen aan het oxide oppervlak. De snelheidsconstante als een functie van de temperatuur voor de reactie aan het oxide-gas grensvlak betreffende de groei van Wüstite op Mn gelegeerd staal voldoet aan de Arrhenius vergelijking.

Hoofdstuk 8 behandelt de reductie van een Wüstite laag op zuiver ijzer en mangaan gelegeerd staal in Ar en H<sub>2</sub> gasmengsels. Allereerst is de kinetiek van het reductieproces voorspeld en vervolgens gevalideerd via experimenten. Door de reductie van Wüstite in een in een Ar met H<sub>2</sub> gasmengsel vormt zich een gesloten ijzer laag bovenop de resterende Wüstite laag, waardoor de nog niet gereduceerde oxide laag gescheiden wordt van de reducerende gasatmosfeer. De snelheid van de reductie van de Wüstite laag op zuiver ijzer en Mn gelegeerd staal is vrijwel gelijk. De kinetiek van de reductie van Wüstite door waterstofgas wordt beheerst door de diffusie van opgelost zuurstof in de gevormde ijzer laag en voldoet daardoor aan een parabolische groei wet. De parabolische groeiconstante als functie van de temperatuur kan beschreven worden met de Arrhenius vergelijking. De samenstelling van het reducerende gasmengsel heeft een geringe invloed op de Wüstite reductiekinetiek als het dauwpunt beneden de 5 °C is. Een oppervlak dat volledig vrij is van oxides kan met succes gerealiseerd worden door eerst een Wüstite laag te vormen en deze vervolgens te reduceren. Toepassing van dit proces zal de kwaliteit van de zinklaag na het galvaniseren van het staal ten goede komen.

# Acknowledgement

I would like to express my sincere gratitude to my daily supervisor Wim Sloof for offering me this valuable opportunity of being a PhD candidate in TU Delft. I am very grateful to him for giving me the freedom to decide research topics according to my own interest and plan my research activities based on my pace. I highly appreciate his dedicated guidance and support for my work during my PhD study. I am really thankful to his faith in me even when I was down. I will owe him all my life for passing me his craftsman's spirit. I am also very grateful to my promoter Barend Thijsse and my mentor John van den Dobbelsteen for the valuable and inspiring discussions.

My PhD research was carried out in the framework of the research program of the Materials innovation institute (M2i). Kind support from M2i program manager Bert van Haastrecht and M2i HR team are gratefully acknowledged.

I am indebted to Wanda Melfo, Marga Zuijderwijk, Henk Bolt and Peter Beentjes of Tata Steel IJmuiden for the kind and inspiring discussions during the progress meetings every three months. I am very grateful for their support as well as giving us the freedom to choose detailed research topics. I really appreciate their help in preparing steel samples, composition analysis and GDOES measurement, which significantly makes my life much easier. Furthermore, I am indebted to Frank Goodwin of International Zinc Association for his support for our research and fruitful discussions.

I would like to sincerely thank Hans Brouwer for facilitating my experimental work, such as designing and building the annealing setup, executing annealing experiments in infrared furnace, sample preparation by ion polishing and training on operation of all kinds of equipment. Moreover, I highly appreciate our talk during the break of experiments, reminding me to keep thinking logically and independently instead of blindly trusting the authorities, which is now a quality not so common among PhD students or even professors. To me, our talk is sometimes even more inspiring than my academic research. I am also indebted to Kees Kwakernaak for his help in many EPMA measurement and SEM training. I also owe thanks to Ruud Hendrikx, Niek van der Pers and Richard Huizinga for the numerous XRD measurement and data analysis. I am also grateful to Sander van Asperen for his help in the metallography lab as well as his assistance and encouragement in the basement fitness room.



I want to thank all my friends in Delft for your companionship during my stay here. I owe gratitude to our group members, present and past, Vahid, Ann-Sophie, Alexandra, Linda, Georgina, Zeynep, Yulia, Shunsuke, Toshio, Jeff Xu, Meng Zhao, Lu Shen, Lianshi Qu, Yuliu You, Guoping Bei and Xiaoming Duan, for being really nice and helpful to me and make my life in office and lab enjoyable every day. I also own special thanks to my master students Qiyu Lei and Yao Ma for tolerating my bad temper and not being irritated by my strict supervision. I am grateful to all other “fourth floor” members as well, such as Fengwei Sun, Xi Zhang, Casper, Neha, Robert-Jan, Astrid, Syam for the relaxing but cheerful discussions. I also want to express my gratitude to Zhaoxiang Chen, Yaxun Wu, Xiaohua Zhang and Hao Su for the accompany during my master study in Delft, attending the same courses and taking the same exams. And, I must also thank Zhaoxiang Chen (again), Xiaochen Che, Haiyang Cui and Ran An for repeatedly inviting me for dinner.

Last but not least, I would like to express my deepest gratitude to my family for always supporting my career. Without their support, my journey to the Netherlands would not happen in the first place. I am also deeply indebted to them for teaching me to be a responsible man dedicated to my job. Finally, special thanks to my fiancée Yue Du for her unwavering love, understanding and encouragement, which help me go through the most difficult time of my PhD study.

# List of publications

## Journal

W. Mao, Y. Ma and W.G. Sloof, *Internal oxidation of Fe-Mn-Cr steels, simulations and experiments*, Oxidation of Metals, 2018, DOI 10.1007/s11085-018-9836-7.

W. Mao, R.W.A. Hendrikx and W.G. Sloof, *Prediction of oxide phases formed upon internal oxidation of advanced high-strength steels*, Oxidation of Metals, 2017, DOI 10.1007/s11085-017-9815-4.

W. Mao and W.G. Sloof, *Reduction kinetics of Wüstite scale on pure iron and steel sheets in Ar and H<sub>2</sub> gas mixture*, Metallurgical and Materials Transactions B, vol. 48, p. 2707, 2017.

W. Mao and W.G. Sloof, *Relation between oxygen activity gradient in the internal oxidation zone of Mn alloyed steel and the composition of oxide precipitates*, Scripta Materialia, vol. 135, p. 29, 2017.

## Conference proceedings

W. Mao, J.C. Brouwer, W. Melfo, M. Zuijderwijk, J. Winter and W.G. Sloof, *Simulation of oxidation of selected advanced high strength steels during annealing prior to galvanizing*, Galvatech 2017, Tokyo, Japan.

W. Mao, V.A. Lashgari, W. Melfo and W.G. Sloof, *Effect of Cr on the oxidation of advanced high strength steels during annealing prior to galvanizing*, Galvatech 2015, Toronto, Canada.

# Curriculum vitae

## **Weichen Mao**

Born on February 02, 1989  
Nanjing, Jiangsu Province, China

### **September 2013 – present**

PhD candidate in Department of Materials Science and Engineering, Faculty of 3ME, Delft University of Technology, Delft, the Netherlands

### **September 2011 – August 2013**

Master of Materials Science and Engineering, Delft University of Technology, Delft, the Netherlands

### **September 2007 – July 2011**

Bachelor of Materials Science and Engineering, Beijing University of Aeronautics and Astronautics, Beijing, China

### **September 2001 – July 2007**

Shenzhen Senior High School, Shenzhen, China